



ISSN 0962-8428

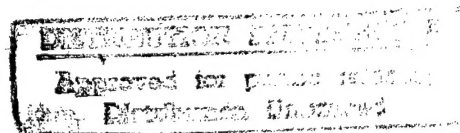
The Royal Society

Philosophical Transactions: Physical Sciences and Engineering

High-temperature structural materials

A Discussion organized and edited by
R. W. Cahn, A. G. Evans and M. McLean

Volume 351 Pages 417-632 Number 1697 15 June 1995



Philosophical Transactions of the Royal Society of London SERIES A

19980318 035

PHILOSOPHICAL TRANSACTIONS: PHYSICAL SCIENCES AND ENGINEERING

Editor: Professor F. T. Smith

Department of Mathematics, University College London, Gower Street, London WC1E 6BT

Editorial Board

Professor L. M. Brown, Cavendish Laboratory, Madingley Road, Cambridge CB3 9HE
Dr K. G. Cox, Department of Earth Sciences, Parks Road, Oxford OX1 3PR
Dr R. H. Friend, Cavendish Laboratory, Madingley Road, Cambridge CB3 9HE
Professor K. Glover, University Department of Engineering, Trumpington Street, Cambridge CB2 1PZ
Professor P. Gray, The Master's Lodge, Gonville and Caius College, Cambridge CB2 1TA
Professor H. E. Huppert, Institute of Theoretical Geophysics, Department of Applied Mathematics and Theoretical Physics, Silver Street, Cambridge CB3 9EW
Professor J. T. Stuart, Department of Mathematics, Imperial College of Science, Technology and Medicine, Huxley Building, 180 Queen's Gate, London SW7 2BZ
Professor J. M. T. Thompson, Department of Civil Engineering, University College London, Gower Street, London WC1E 6BT
Professor R. C. Vaughan, Department of Mathematics, Imperial College of Science, Technology and Medicine, Huxley Building, 180 Queen's Gate, London SW7 2BZ

NOTICE TO AUTHORS

Scope. *Philosophical Transactions* series A welcomes papers on any aspect of the physical sciences and engineering, including mathematics and Earth sciences.

Submission. Authors may send their papers direct to the Editorial Office, whose address is given below, or to the Editor or a member of the Editorial Board. Three copies of the typescript and figures are required, and originals of any figures should also be submitted. Papers should be prepared in accordance with the 'Instructions to authors' printed at the end of every volume of *Philosophical Transactions* A and available from the Editorial Office.

Editorial address: Editorial Office, *Philosophical Transactions* A, The Royal Society, 6 Carlton House Terrace, London SW1Y 5AG.

COPYRIGHT

© 1995 The Royal Society

Except as otherwise permitted under the Copyright, Designs and Patents Act, 1988, this publication may only be reproduced, stored or transmitted, in any form or by any means, with the prior permission in writing of the publisher, or, in the case of reprographic reproduction, in accordance with the terms of a licence issued by the Copyright Licensing Agency. In particular, the Society permits the making of a single photocopy of an article from this issue (under Sections 29 and 38 of the Act) for an individual for the purposes of research or private study.

SUBSCRIPTIONS

Philosophical Transactions of the Royal Society series A (ISSN 0962-8428) is published monthly. The subscription price for 1995, including postage, is £490 in the U.K. and £524 (U.S. \$891) overseas. Air-speeded post is available for overseas subscribers at a small extra charge. Full details of subscription rates may be obtained on request from the Publications Sales and Marketing Department, The Royal Society, 6 Carlton House Terrace, London SW1Y 5AG. The Royal Society is Registered Charity no. 207043.

REPORT DOCUMENTATION PAGE

Form Approved OMB No. 0704-0188

Public reporting burden for this collection of information is estimated to average 1 hour per response, including the time for reviewing instructions, searching existing data sources, gathering and maintaining the data needed, and completing and reviewing the collection of information. Send comments regarding this burden estimate or any other aspect of this collection of information, including suggestions for reducing this burden to Washington Headquarters Services, Directorate for Information Operations and Reports, 1215 Jefferson Davis Highway, Suite 1204, Arlington, VA 22202-4302, and to the Office of Management and Budget, Paperwork Reduction Project (0704-0188), Washington, DC 20503.

1. AGENCY USE ONLY (Leave blank)		2. REPORT DATE	3. REPORT TYPE AND DATES COVERED	
		15 June 1995	Conference Proceedings	
4. TITLE AND SUBTITLE			5. FUNDING NUMBERS	
Philosophical Transactions: Physical Sciences and Engineering High Temperature Structural Materials			F6170895W0025	
6. AUTHOR(S)				
Conference Committee				
7. PERFORMING ORGANIZATION NAME(S) AND ADDRESS(ES)			8. PERFORMING ORGANIZATION REPORT NUMBER	
Imperial College of Science, Technology & Medicine Prince Consort Road London SW7 2BP United Kingdom			N/A	
9. SPONSORING/MONITORING AGENCY NAME(S) AND ADDRESS(ES)			10. SPONSORING/MONITORING AGENCY REPORT NUMBER	
BOARD PSC 802 BOX 14 FPO 09499-0200			CSP 95-1003	
11. SUPPLEMENTARY NOTES				
Only pages 417-632 available.				
12a. DISTRIBUTION/AVAILABILITY STATEMENT			12b. DISTRIBUTION CODE	
Approved for public release; distribution is unlimited.			A	
13. ABSTRACT (Maximum 200 words)				
The Final Proceedings for High Temperature Structural Materials, 2 November 1994 - 3 November 1994				
14. SUBJECT TERMS			15. NUMBER OF PAGES	
Ceramics, Intermetallics, and Their Composites			215	
			16. PRICE CODE	
			N/A	
17. SECURITY CLASSIFICATION OF REPORT	18. SECURITY CLASSIFICATION OF THIS PAGE	19. SECURITY CLASSIFICATION OF ABSTRACT	20. LIMITATION OF ABSTRACT	
UNCLASSIFIED	UNCLASSIFIED	UNCLASSIFIED	UL	
NSN 7540-01-280-5500				

High-temperature structural materials

A DISCUSSION ORGANIZED AND EDITED BY R. W. CAHN,
A. G. EVANS AND M. MCLEAN

Discussion held 2 and 3 November 1994

CONTENTS

	PAGE
M. MCLEAN	
Nickel-base superalloys: current status and potential	419
<i>Discussion: G. A. WEBSTER, F. R. N. NABARRO, A. COTTRELL</i>	432
J. C. WILLIAMS	
Materials requirements for high-temperature structures in the 21st century	435
<i>Discussion: M. MCLEAN, A. COTTRELL, M. HARVEY, T. KHAN</i>	447
M. F. ASHBY AND C. A. ABEL	
Materials selection to resist creep	451
<i>Discussion: M. J. GOULETTE, A. COTTRELL, G. A. WEBSTER</i>	467
M. KNECHTEL, N. CLAUSSEN AND J. RÖDEL	
Reliability of structural ceramics	469
<i>Discussion: K. S. KUMAR, R. CAHN</i>	483
R. R. NASLAIN	
Ceramic matrix composites	485
<i>Discussion: T. KHAN, M. STEEN, P. HOLMES</i>	495
R. W. CAHN	
Multiphase intermetallics	497
<i>Discussion: D. R. F. WEST, D. J. DUNSTAN, M. MCLEAN, J. W. MARTIN, D. MORRIS</i>	508
A. G. EVANS	
Ceramics and ceramic composites as high-temperature structural materials: challenges and opportunities	511
<i>Discussion: J. RÖDEL</i>	527
D. NGUYEN MANH, A. M. BRATKOVSKY AND D. G. PETTIFOR	
Quantum mechanical predictions in intermetallics modelling	529
<i>Discussion: A. R. C. WESTWOOD, K. S. KUMAR, R. W. CAHN</i>	541
N. SAUNDERS	
Phase diagram calculations for high-temperature structural materials	543
<i>Discussion: R. W. CAHN, M. MCLEAN, M. RAPPAZ, D. G. PETTIFOR</i>	560

M. RAPPAZ AND CH.-A. GANDIN	
Process modelling and microstructure	563
<i>Discussion: A. M. STONEHAM, M. MCLEAN, M. S. LOVEDAY</i>	576
B. F. DYSON	
Mechanical testing of high-temperature materials: modelling data-scatter	579
<i>Discussion: P. HIRSCH, M. MCLEAN, R. C. THOMSON, M. S. LOVEDAY</i>	593
T. J. LU AND J. W. HUTCHINSON	
Effect of matrix cracking on the overall thermal conductivity of fibre-reinforced composites	595
<i>Discussion: D. J. RÖDEL</i>	610
F. A. LECKIE	
High-temperature mechanism-based design	611

Nickel-base superalloys: current status and potential

BY M. MCLEAN

*Department of Materials, Imperial College of Science, Technology and Medicine,
Prince Consort Road, London SW7 2BP, UK*

The evolution of nickel-base superalloys has occurred over about 50 years through a combination of alloy and processing developments to satisfy quite different service requirements of various components of the gas turbine. There is now a good general understanding of the mechanisms leading to the unusual mechanical properties of these precipitation strengthened materials. Although the scope for further significant improvements in the behaviour of nickel-base superalloys appears to be limited, it is unlikely that their full potential is yet being achieved in engineering applications. Progress towards the development and validation of constitutive laws describing fully anisotropic deformation is described.

1. Introduction

The development of nickel-base superalloys has, almost entirely, been motivated by the requirement to improve the efficiency, reliability and operating life of gas turbines. There have been other peripheral applications but, at present about 90% of superalloys produced are used in gas turbines for a range of applications, including aerospace, electricity generation, gas/oil pumping and marine propulsion. The differing requirements in specific parts of the engine and the different operating conditions of the various types of gas turbine have led to the development of a wide range of nickel-base superalloys with individual balances of high-temperature creep resistance, corrosion resistance, yield strength and fracture toughness. However, all of these materials have evolved from the Ni-Al-Ti-Cr precipitation strengthened alloy, Nimonic 80A, developed by Pfeill and his colleagues at the Mond Nickel Company around 1940 in response to Whittle's need for a suitable turbine blade material for the first British gas turbine for aircraft propulsion (Betteridge & Shaw 1987; Sims 1984).

The principal characteristics of nickel-base superalloys largely derive from the precipitation of an $L1_2$ ordered intermetallic phase, γ' $Ni_3(Al,Ti)$, that is coherent with the face-centred-cubic γ -nickel solid solution matrix (Stoloff 1987). The development of viable superalloys has been achieved by a combination of compositional modifications that control aspects of the γ/γ' relationship (γ' volume fraction, γ' solvus, γ/γ' lattice mismatch), the use of more conventional alloying approaches to solid solution strengthening and corrosion resistance, and the introduction of a range of novel processing techniques (directional solidification, single crystal technology, powder processing, mechanical alloying, HIPping, etc.). A full review of superalloy technology is beyond the scope of this paper which will present a personal view relating to the most important recent developments and future requirements.

2. Historical trends

The efficiency of operation of the gas turbine is largely determined by the combination of the temperature and pressure/volume of gas passing from the combustion chamber to the external environment to provide propulsion, or power to motivate other machinery. The materials available to be used in the turbine, particularly as turbine blades and discs, have to a large extent determined the operating conditions of gas turbines. The progressive improvement in the efficiencies of gas turbines has paralleled the increased temperature capabilities and strengths of successive generations of superalloys that have been specifically developed for these critical components, in particular turbine blades and discs. Indeed, much of the drive for superalloy substitutes, which is the major theme of the present meeting, derives from the same continuing requirement. We consider briefly the evolution of materials for turbine blade and turbine disc applications.

(a) *Turbine blades*

Materials for high-pressure turbine blades must be able to operate in the high-temperature gases emerging from the combustion chamber; they experience a combination of high temperatures and relatively low gas-bending and centrifugal stresses. In the half century since the development of the first precipitation strengthened superalloy (Nimonic 80) the temperature capability of nickel-base superalloys, as measured by the temperature at which a creep rupture life of 1000 h can be achieved with a tensile stress of 150 MPa, has progressively increased by about 7 K per year (figure 1a). The increase in the gas operating temperature has been much greater than this due to engineering innovations, such as blade and thermal barrier coatings, that allow the blades to operate in an environment in which the gas temperature exceeds the melting point of the alloys from which the blade is produced.

The strategies adopted in the development of turbine blade materials have depended on the service cycles for which specific engines were designed and where different failure mechanisms determine component life. However, there have been some common threads to this alloy development:

- increasing γ' volume fraction (Al, Ti);
- increasing γ' solution temperature (Co);
- minimization of the γ/γ' lattice parameter mismatch;
- solid solution strengthening (W, Mo, Ta, Re);
- ductilizing additions (Hf, B).

Alloys with high chromium contents have been developed to give the enhanced oxidation/corrosion behaviour required for marine and industrial applications, but this has usually been achieved at the expense of mechanical performance. The development of reliable corrosion resistant coatings is rendering less important the need for alloys that are inherently oxidation/corrosion resistant.

As the alloys have evolved to give increased high-temperature strength, it has been necessary to develop new processing techniques to produce the turbine blades to acceptable tolerances and to maintain the required levels of ductility. The principal stages in this development can be summarized as follows.

(i) Forged blades were produced, and still are from some alloys, while there was a sufficiently wide heat treatment window, between the γ' -solvus and liquidus temperatures to allow reliable thermo-mechanical processing.

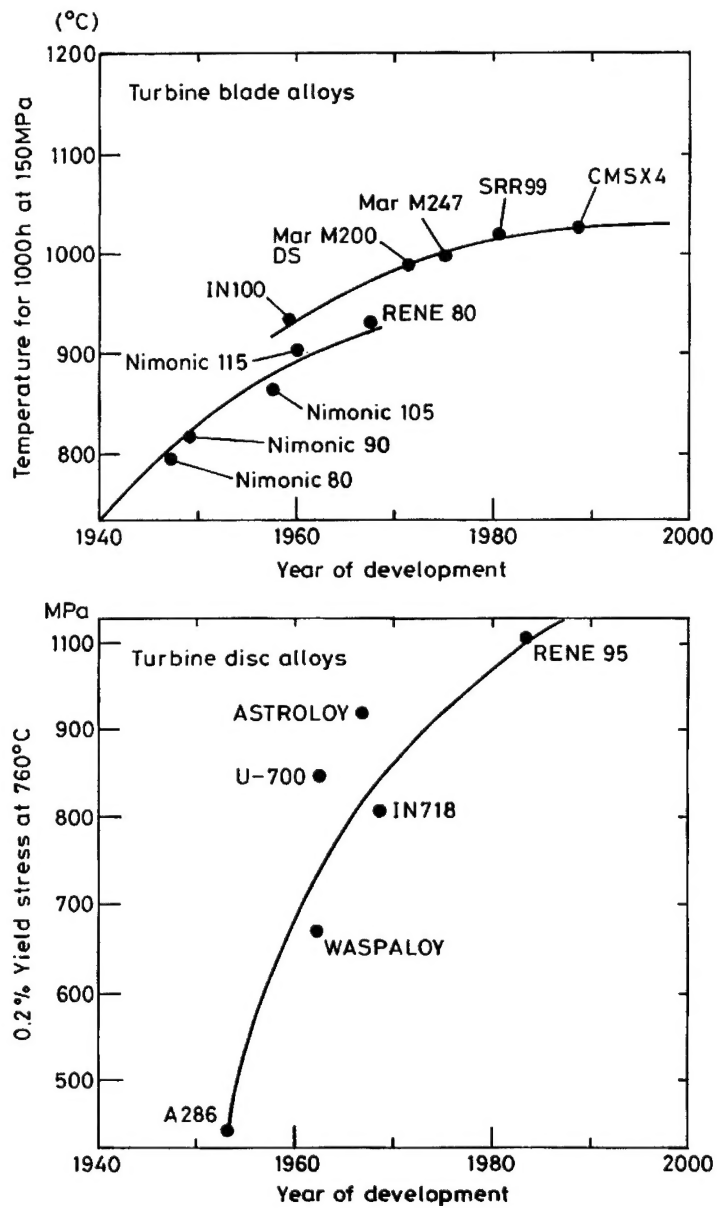


Figure 1. Trend in the improvement in superalloys for turbine blade and disc applications as a function of the year of introduction of the alloy. (a) Blade alloys temperature for 1000 h rupture life with 150 MPa stress. (b) Disc alloys. Yield stress at 850 °C.

(ii) Investment casting was introduced for alloys where forging was impracticable and where adequate ductility could be achieved. However, as the γ' volume fraction increased beyond about 50%, the ductilities became unacceptably low due to premature fracture at transverse grain boundaries.

(iii) Directional solidification, first used by Ver Snyder and co-workers by a modification of the investment casting process (see, for example, Ver Snyder *et al.* 1966), produced an elongated grain structure and a $\langle 001 \rangle$ crystal texture parallel to the solidification direction. The result has been an increase in creep

ductility from less than 1% to more than 25% and considerable enhancement of the thermal fatigue resistance for alloys such as MarM 200.

(iv) Single crystal superalloys result from a fairly simple variant of the directional solidification process and is now state-of-the-art for advanced aerospace applications and is also being considered for large electricity generating plant.

It should be noted that processing changes have not always been in response to alloy development. Rather, alloy chemistry has often been adjusted to produce alloys tailored to the available processing technology. For example, the introduction of hafnium was to reduce the occurrence decohesion of longitudinal grain boundaries during directional solidification (Lund 1972). There is little or no inherent advantage of single crystal versions of the alloys produced by directional solidification; indeed, Piercey *et al.* (1970) studied single crystal superalloys over twenty years ago. However, Gell *et al.* (1980) showed that by stripping the elements intended to modify the grain boundaries (C, B, Hf) it was possible to increase the liquidus temperature and allow more effective control of the γ' morphology through heat treatment. A wide range of superalloys specifically intended for use in the single crystal form has been and continues to be developed.

The most advanced single-crystal superalloy turbine blades are now operating at a homologous temperature $T/T_m > 0.85$. Although further developments will certainly take place, the melting point of nickel provides a natural ceiling for the temperature capability of nickel-base superalloys. Consequently, there is limited scope for further large increments in temperature capability of this class of alloys.

(b) *Turbine disc alloys*

The turbine disc operates at considerably lower temperatures than do the blades (about 850 °C compared to 1150 °C for blades in current aero-engines). Consequently creep deformation is relatively insignificant. The principal design requirements, to reduce engine weight and increase rotational speed, both lead to high stresses on the disc and alloy development has been designed to increase the yield strength and to inhibit crack initiation and growth, particularly in fatigue conditions. Figure 1b indicates the progressive increase in yield strength and fatigue resistance of this class of alloy.

With increasing yield strength there has been an associated decrease in fracture toughness. Some amelioration of this effect has been obtained through control of grain size; attempts at producing duplex grain morphologies (*necklace grain structures*) appear to have been abandoned as being impractical (Jeal 1986). However, in current advanced disc alloys the critical defect size for brittle fracture at service stresses is about 30 μm (Sczercenie & Maurer 1987). Since various inclusions or clusters of precipitate particles can constitute such a critical defect this places demands on non-destructive examination that are currently unattainable. The consequences of disc failure, particularly in aero-engines, require a viable quality assurance procedure.

Turbine discs are currently produced either by forging or by powder processing, although the former is more extensively used. In both cases quality is maintained through careful control of alloy cleanliness at each stage of the process. The use of different secondary melting processes, on bar-stock initially produced by vacuum induction melting, is now standard procedure to control inclusion content. Vacuum arc refining (VAR), electro-slag refining (ESR), electron beam cold hearth refining (EBCHR) are all currently available as commercial processes producing

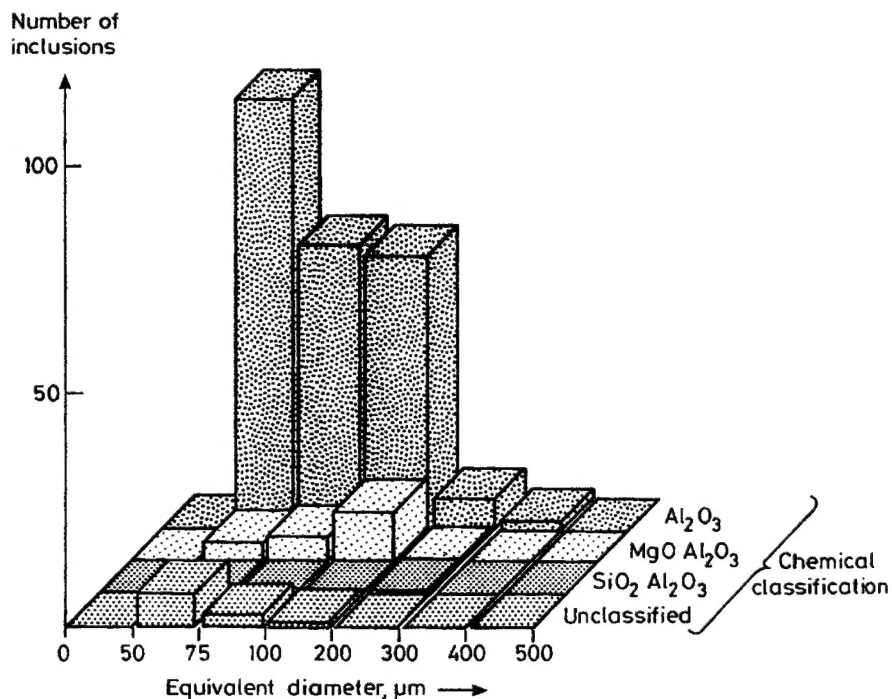


Figure 2. Size distribution of various types of inclusions found by analysis of the concentrated inclusions produced by electron beam button melting of the turbine blade alloy IN738LC (Chakravorty *et al.* 1987).

double, or triple, melted alloy (Patel & Siddal 1994). Because of the impracticality of characterizing the very low inclusion contents in these materials by conventional metallographic procedures or by mechanical tests on small specimens, novel approaches to evaluating very clean alloys are being developed. One such example is the electron beam button melting approach used by Quested & Hayes (1993) at the National Physical Laboratory which allows inclusions from 1 kg of alloy to be concentrated, identified and their size distributions determined (figure 2). A code-of-practice for use of the NPL approach to cleanliness evaluation has been agreed by the leading UK producers of turbine disc materials (Quested, personal communication).

If replacement materials for superalloys are developed that allow a significant increment in turbine operating temperature, there will be a corresponding increase in the service temperature of the disc. This will require new disc alloys. There is certainly scope for the further development of superalloys for this purpose. However, alternative materials, such as structural intermetallics, could well supersede superalloys because of the attractions of weight savings through reduced density. Superalloys for discs are at a less mature stage of development than are those for blade applications.

3. Fundamentals of mechanical behaviour

There can be no doubt that the attractive mechanical properties of nickel-base superalloys derive directly from the disposition of a high volume fraction of the

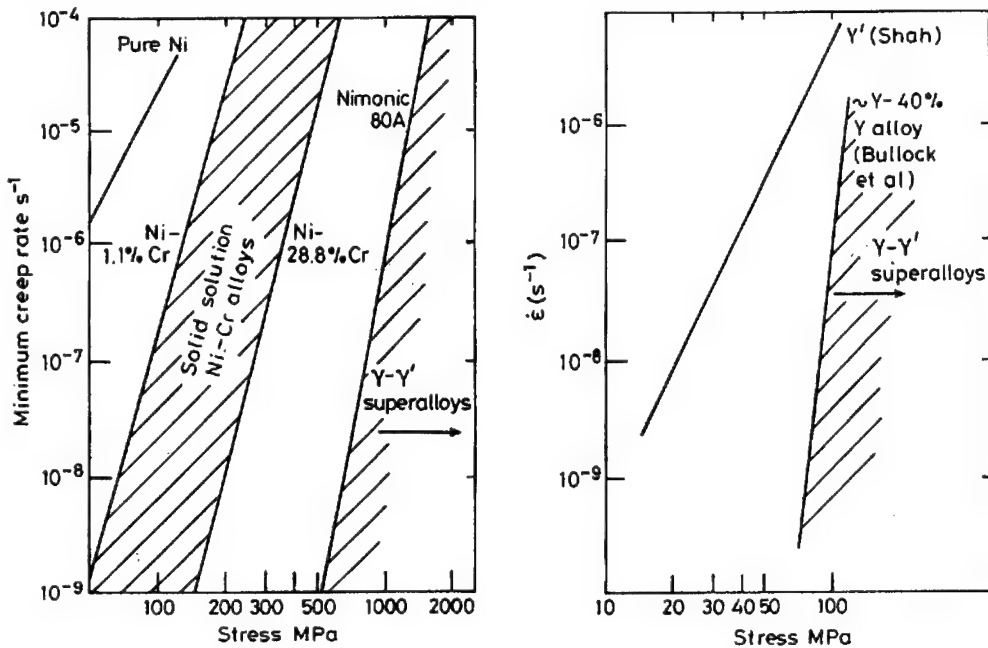


Figure 3. Comparison of the creep behaviour of (a) solid solution Ni-Cr alloys, (b) γ' $\text{Ni}_3(\text{Al},\text{Ti})$ intermetallic compounds and (c) γ/γ' nickel-base superalloys.

coherently dispersed γ' precipitate (up to 70% by volume) in the γ -nickel matrix. However, in spite of extensive fundamental studies there is still no clear consensus on the mechanisms controlling the engineering performance in service conditions. Here we focus on a limited number of aspects of the mechanical behaviour of these materials that have been thought to be of particular importance.

Superalloys with high volume fractions of γ' show a similar anomalous rise in yield strength with increasing temperature as is exhibited by the monolithic $\text{L}1_2$ intermetallic phase (Stoloff 1987). Detailed analysis of this phenomenon has been carried out by a large number of authors, notably Paidar *et al.* (1984), and there is now a general consensus that it is a consequence of thermally activated cross-slip onto cube planes that produces sessile dislocation segments that inhibit dislocation glide on octahedral planes. Hirsch (1992) has recently considered the detailed dislocation interaction that are occurring. Such considerations are likely to be important in service conditions where the yield stress is attained, or at least approached. However, design stresses will almost invariably be below the threshold for time-independent yield and γ' cutting is unlikely to be a significant factor during service.

In the sub-yield creep regime, relevant to turbine blades, it is clear that the creep performance of the duplex γ/γ' alloys is significantly superior either to (Ni,Cr) solid solution matrix or to the γ' $\text{Ni}_3(\text{Al},\text{Ti})$ precipitated phase (figure 3). Consequently, the γ' behaviour cannot be taken as a limit to the alloy performance. Rather, the coexistence of the two phases requires the operation of a radically different deformation mechanism than would occur in either individual phase. Indeed at stress levels below those required for γ' shearing it is likely that dislocation activity is largely restricted to the γ matrix and this is supported

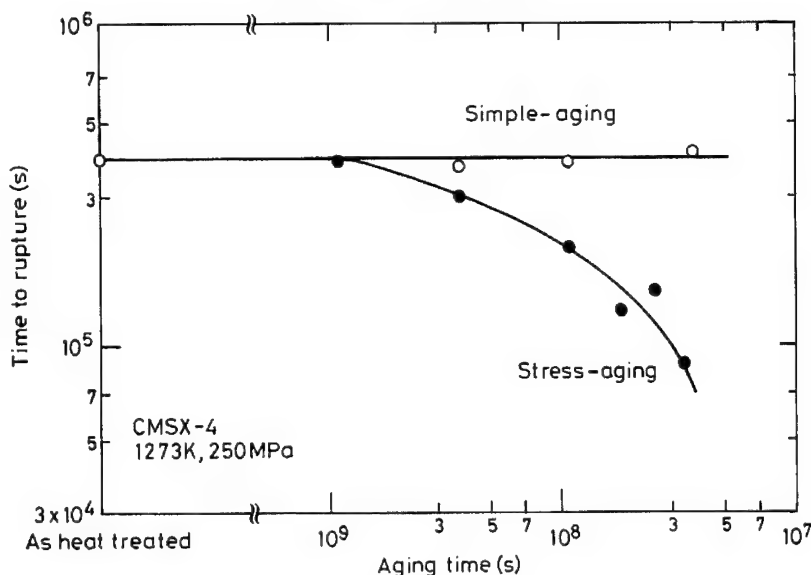


Figure 4. Comparison of the creep behaviour of the single crystal superalloy CMSX4 in two microstructural forms: (a) regular γ' morphology produced by commercial solution and ageing heat treatment and (b) rafted γ' morphology produced by heat treatment under stress (Kondo *et al.* 1994).

by transmission electron microscopy of creep deformed material (Henderson & McLean 1983). Dyson, McLean and co-workers (e.g. Ion *et al.* 1986; Dyson & McLean 1990) have developed a model of creep deformation that considers the dispersed particles to inhibit glide in the matrix: deformation occurs at a rate largely determined by dislocation climb and dislocations generated are mostly mobile leading to an increase in creep rate with accumulated plastic strain instead of the normal work-hardening exhibited by single-phase metals. This successfully accounts for a range of observations relating to the creep behaviour of superalloys that are not compatible with earlier models:

- (i) Creep in both tension and compression exhibits a progressively increasing creep rate, rather than a steady state deformation rate.
- (ii) Plastic prestrain of superalloys increases the creep rate relative to the unstrained material, rather than leading to strain hardening.
- (iii) There is little difference in creep curves of superalloys produced under constant load and constant stress conditions, indicating the dominance of an intrinsic strain softening mechanism over the effect of increased stress due to reduction in cross-sectional area during tensile deformation.

(a) Microstructural influences on mechanical behaviour

An interesting microstructural feature of single crystal superalloys is the directional coarsening of the γ' particles that occurs during high-temperature ageing (greater than 1000 °C) in the presence of a small stress (Tien & Copely 1971). Plausible explanations have been given of the effect due to stress gradients generated as a result of differences in elastic and lattice constants of the γ and γ' phases. The rafted microstructures that develop in most commercial single crystal superalloys under tensile stresses have often been cited as the reason for their un-

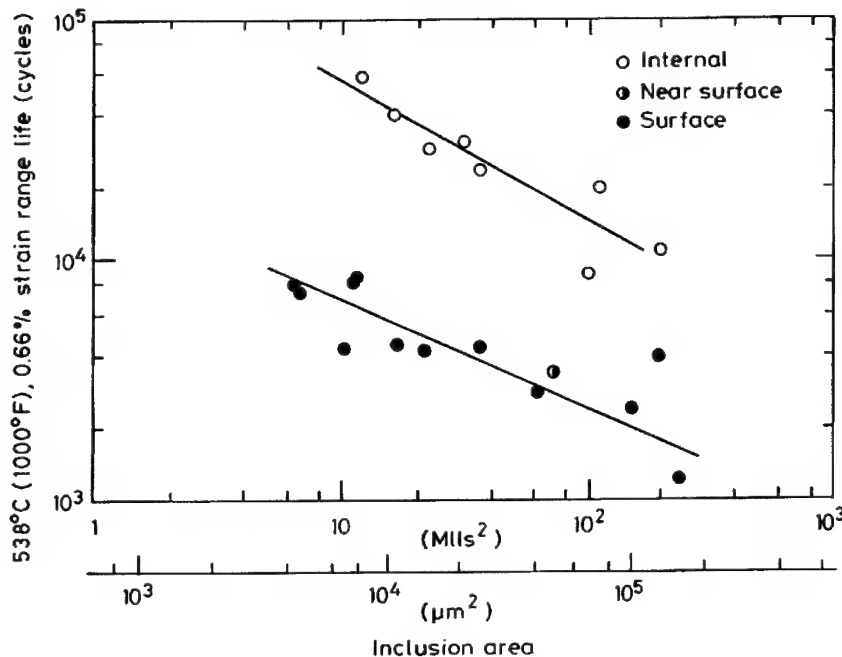


Figure 5. Variation in low cycle fatigue life with increasing volume fraction of inclusions in Rene 95 (Shamblen 1983).

expectedly good creep performance at temperatures in excess of about 1000 °C. However, it is now quite clear that the rafted γ' morphology is quite detrimental to the low and intermediate temperature creep behaviour (Caron *et al.* 1988; Kondo 1994). Figure 4, from the work of Kondo *et al.* (1994) clearly indicate that pre-rafting of the γ' reduces the rupture life relative to both the original material and that subject to conventional heat treatment. The benefits of a rafted γ' is now open to question particularly in the variable stress and temperature conditions likely to be experienced in service.

The importance of inclusions in controlling the low-cycle-fatigue life of turbine disc alloys has been demonstrated unambiguously in a number of studies. Shamblen (1993) for example, has deliberately added inclusions of known size and concentration to the alloy RENE95 and has shown a progressive decrease in cycles to failure with increasing inclusion volume fraction (figure 5). Pineau (1990) has paid particular attention to the problems of characterizing the fracture behaviour of materials with very low concentrations of defects. Mechanical testing of such materials must be carried out on a sufficiently large volume of material to ensure a high probability of the occurrence of defects characteristic of the component of interest.

4. Engineering considerations

The implementation of computer-aided design methods, to replace the traditional design codes, depends on there being a sufficiently sophisticated representation of the material behaviour. Whereas previous designs of gas turbine blades were based on simple measures of material performance, such as stress rupture

life and minimum creep rate, in the future attempts will be made to numerically simulate the performance of a component in likely service cycles that will inevitably involve multiaxial stresses and variable stresses and temperatures. It is unrealistic to collect an experimental database to cover all possible options, particularly in the case of anisotropic materials such as single crystal superalloys. It is necessary to devise a reliable approach to the extrapolation/interpolation of a restricted database through the use of appropriate constitutive equations that can be incorporated in the design calculations. Several empirical approaches (Graham & Walles 1955; Evans & Wilshire 1987) have been successful in representing uniaxial creep databases, but these are difficult to extend to variable and multiaxial loading conditions.

The mechanisms of creep deformation of superalloys, described in the previous section, have been translated into such a set of constitutive equations using the general formalism of continuum damage mechanics. Here, the uniaxial creep rate $\dot{\epsilon}$ is expressed as a function of state variables (or damage parameters) that represent the current condition of the material, in particular of the structural and microstructural features that control the strength of the alloy. For the isotropic form of the model appropriate to superalloys, an acceptable fit of creep data can be obtained by using two state variables; S is a dimensionless internal stress that increases to a steady-state value of S_{ss} leading to primary creep and $\omega = (\rho - \rho_i)/\rho_i$ represents the increasing density of mobile dislocations ρ (ρ_i is the initial value). The isotropic creep behaviour is represented by the following set of three equations involving the two variables S , ω and four constants $\dot{\epsilon}_i$, where $\dot{\epsilon}$ has dimensions of s^{-1} and H , S_{ss} , C are all dimensionless (Ion *et al.* 1986; Dyson & McLean 1990):

$$\dot{\epsilon} = \dot{\epsilon}_i(1 - S)(1 + \omega), \quad \dot{S} = H\dot{\epsilon}_i(1 - S/S_{ss}), \quad \dot{\omega} = C\dot{\epsilon}. \quad (4.1)$$

The model has been extended by Ghosh *et al.* (1990) to represent anisotropic creep of single crystals by considering creep deformation to be restricted to specific slip systems and computing the total strain resulting from each shear displacement. A set of equations equivalent to equations (4.1), but expressed in terms of shear, rather than tensile, strains γ^k is required for each family of slip systems. Then the total displacement ϵ_{ij} from all N components of shear on the allowed system $(n_1 n_2 n_3) \langle b_1 b_2 b_3 \rangle$ is given by

$$\epsilon_{ij} = \sum_{k=1}^N \gamma^k b_i^k n_j^k. \quad (4.2)$$

Here i, j represent the cube directions and k identifies one of the slip systems being considered: γ^k is the amount of shear on that system. An arbitrary crystal direction x will transform to a new orientation X , with a strain in that direction of $(\bar{X} - \bar{x})/\bar{x}$, where

$$\begin{bmatrix} X_1 \\ X_2 \\ X_3 \end{bmatrix} \begin{bmatrix} 1 + \epsilon_{11} & \epsilon_{12} & \epsilon_{13} \\ \epsilon_{21} & 1 + \epsilon_{22} & \epsilon_{23} \\ \epsilon_{31} & \epsilon_{32} & 1 + \epsilon_{33} \end{bmatrix} \begin{bmatrix} x_1 \\ x_2 \\ x_3 \end{bmatrix}. \quad (4.3)$$

In the analysis dislocation activity is taken to occur on two families of slip systems, $\{111\}\langle\bar{1}10\rangle$ and $\{100\}\langle011\rangle$. There is considerable evidence of the occurrence of

octahedral slip during creep, but only occasional observations of cube slip (Caron *et al.* 1988). However, elements of octahedral to cube cross-slip are also thought to occur.

For the simple axial orientations that are symmetrically disposed to the active slip systems there is no change in orientation during deformation and the tensile and shear formulations are totally equivalent being two different mathematical representations of the same physical model. The model can accurately represent individual creep curves, as can other more empirical approaches. However, the anisotropic model is also capable of representing (i) change in magnitude and order of creep anisotropy with stress and/or temperature; (ii) crystal rotations during creep; (iii) strain in any direction; (iv) change in material shape during deformation.

When combined with a representation of elastic anisotropy, a wide range of strain and load controlled types of deformation, such as stress relaxation and low cycle fatigue can also be simulated (Pan *et al.* 1993).

The success of such a model can only be assessed through searching validation and, as has been indicated above, comparison of measured and model-calculated creep curves does not constitute an adequate test. Here we indicate three quite different experimental validations of the predictions of the model.

(a) Low cycle fatigue

Figure 6 shows successive stress-strain loops for a strain controlled low-cycle fatigue test on SRR99 at 950 °C with a fixed tensile strain range between 0 and 0.75%. Here the loading is axial along the $\langle 001 \rangle$ direction. Model simulation has been carried out assuming that creep, as described by the parameters derived by analysis of a database of constant stress creep tests, is the dominant deformation mechanism; the only additional information required is the value of Young's modulus at the deformation temperature in order to account for elements of stress relaxation. Both measured and calculated behaviour show that individual cycles exhibit essentially elastic response, but there is a progressive shakedown due to stress relaxation with the maximum tensile stress decreasing from about 700 to 360 MPa and a compressive stress developing from 0 to about 300 MPa. Bearing in mind the relatively high stresses and strain rates in the LCF compared with those in the creep database, the prediction is remarkably accurate (Pan *et al.* 1994).

(b) Shape changes

A series of creep specimens of SRR99 tested to fracture with tensile loads along complex crystallographic directions have been examined to characterize the change in cross-sectional shape that develops along the necked portion of the fractured test pieces which were originally cylindrical: these measurements have been compared with computer simulations particular attention being paid to the crystallographic directions along which the maximum and minimum diameters develop (Pan *et al.* 1994). Figure 7 shows the different predictions of the shape development that would occur due either to octahedral or to cube shear deformation occurring alone; the experimental measurements for the example shown are clearly consistent with cube slip being dominant for that particular orientation. As expected from Schmid factor considerations orientations close to $\langle 001 \rangle$

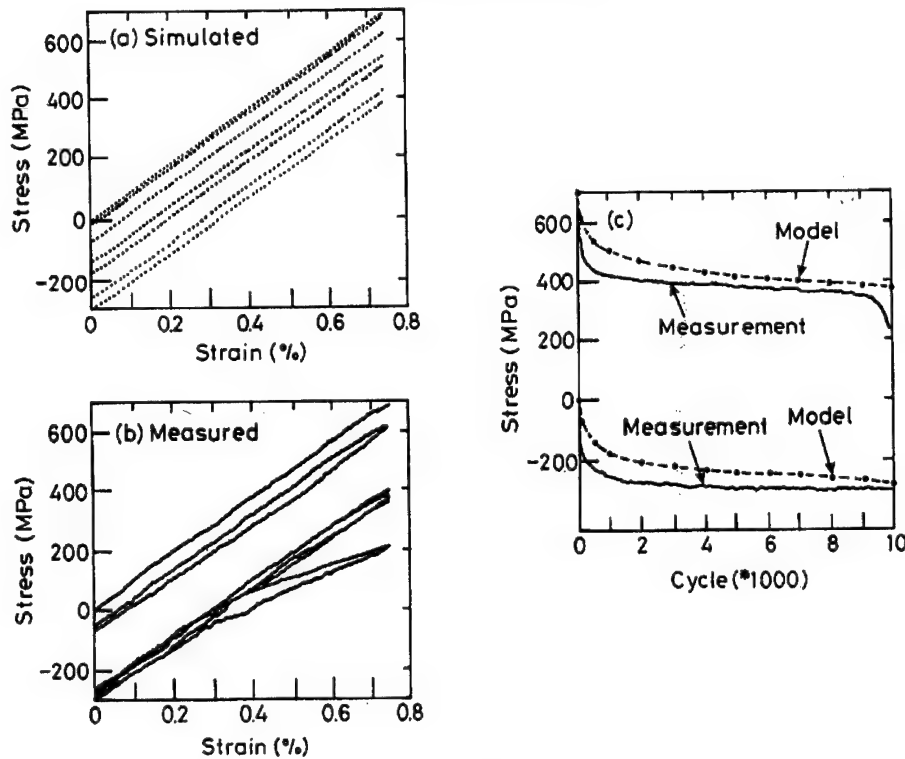


Figure 6. Simulated and measured low cycle fatigue behaviour for strain controlled cycling between 0 and 0.75% uniaxial tensile strain at 950 °C for $\langle 001 \rangle$ SRR99. (a) Simulated and (b) measured stress-strain curves for selected cycles, and (c) comparison of predicted and measured maximum and minimum stresses as a function of cycle number. (Pan *et al.* 1994.)

and $\langle 111 \rangle$ exhibit octahedral and cube slip dominance respectively, and give good agreement with the model predictions.

(c) Orientation changes

The same specimens used in the shape change measurements have been sectioned and the changes in orientation along the specimen length have been determined by using electron backscatter patterns produced in scanning electron microscopy (Dingley 1984). This technique has a high spatial resolution allowing local orientations to be determined on a scale of less than 1 μm . The results show an average drift of orientation that is largely consistent with the model simulation (figure 8) indicating dominant octahedral and cube shear near $\langle 001 \rangle$ and $\langle 111 \rangle$ orientations respectively, as was observed in the shape change experiments. However, deformation is highly heterogeneous leading to a growing spread of orientations, on a scale of a few micrometres, with increasing creep strain. High deformation is particularly associated with defects such as solidification porosity which in SRR99 aligns along the $\langle 001 \rangle$ solidification direction.

The design of discs using material with low fracture toughness is subject to the quite different problem of accounting for the possible presence of defects that can constitute, or grow to, a critical crack leading to brittle failure. Here, a probabilistic approach must be taken when, as is projected to be the case in the next generation of disc alloys, there is a sparse distribution of inclusions. Pineau

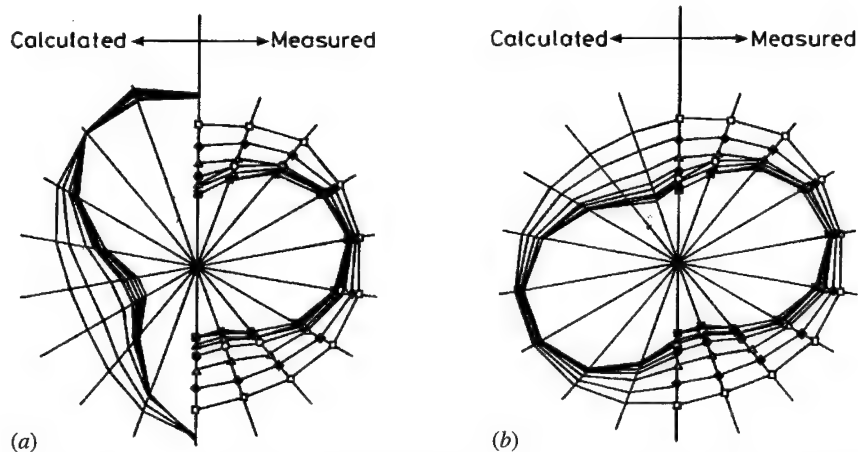


Figure 7. Comparison of the measured and predicted creep specimen cross-sections, shown as two halves of the same polar plot, at various values of reduction in area for a specimen of SRR99 of complex orientation after creep testing to fracture at 850 °C/450 MPa. (a) Octahedral slip and (b) cube slip. (Pan *et al.* 1995.)

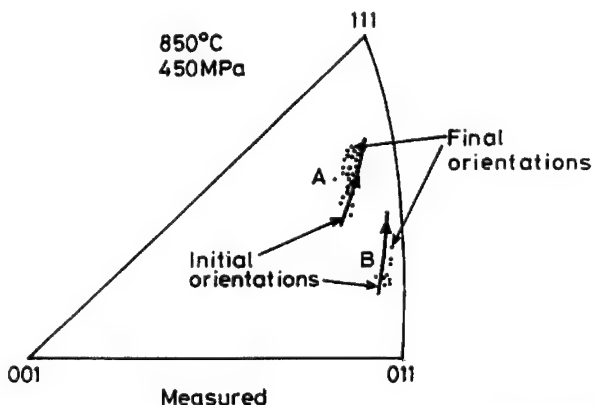


Figure 8. Change in orientation with creep strain for a specimen of SRR99 after tensile deformation at 950 °C/300 MPa showing model predictions and measurements using electron backscatter patterns.

(1990) has considered this problem in some detail showing the effect of component size on the design performance using such materials. The practical difficulty is in determining the probability distribution of defects when they are too dilute to be characterized by metallographic or conventional NDT techniques. Advanced methods, such as the EBBM approach developed at NPL, can be useful in providing a ranking of the general cleanliness of various materials, but they can only sample a small fraction of the alloys from which components are manufactured.

Because of the catastrophic implications of a disc failure, it is essential to develop a quality assurance and design strategy that will guarantee the component integrity. Since the resolution of available techniques for non-destructive evaluation is inadequate, attention has been focused on assuring material quality through control of the entire processing cycle. This has led to growing interest in modelling the critical parts of the process, such as VAR, ESR and EBBM, to

identify the optimum values of the process parameters required to achieve the desired microstructure.

5. Conclusions

The development of nickel-base superalloys has been one of the major successes of modern metallurgy. Over a period of 50 years or so very significant improvements have been achieved by a combination of alloy and process development, and these have rapidly been introduced into service. However, the scope for further substantial improvements in material properties, particularly for turbine blade alloys, is limited; here the most advanced materials are used in single crystal form at greater than $0.8T_m$.

By contrast, full exploitation of these materials has not yet been achieved. Two particular areas have been identified where substantial improvements in the engineering applications can be expected and which are at an early stage of development:

(i) Design procedures will be developed to make use of the constitutive laws accounting for the anisotropic mechanical behaviour single crystal superalloys. These should be capable of simulating component performance in realistic service conditions incorporating multiaxial stresses and variable loading conditions.

(ii) Control of the defect density in turbine disc alloys is required in order to achieve the loading conditions expected in future gas turbine designs. This is most likely to be achieved through process control informed by detailed process modelling.

Several colleagues have contributed significantly to the work reviewed in this paper; these include Dr M. B. Henderson, Dr R. N. Ghosh, Dr L. M. Pan and Dr B. A. Shollock. I also thank the Defence Research Agency for support of much of the work.

References

Betteridge, W. & Shaw, S. W. K. 1987 *Mater. Sci. Tech.* **3**, 682.
Caron, P., Ohta, Y., Nakagawa, Y. G. & Khan, T. 1988 In *Superalloys 1988* (ed. D. N. Duhl *et al.*), p. 215. Warrendale, PA: The Metallurgical Society.
Chakravorty, S., Quested, P. N. & McLean, M. 1987 In *Proc. Conf. on Advanced Materials and Processing Techniques for Structural Applications, ASM Europe Technical Conf.*, pp. 275-284.
Dingley, D. J. 1984 In *Scanning electron microscopy II*, p. 569. Chicago, IL.
Dyson, B. F. & McLean, M. 1983 *Acta metall. Mater.* **31**, 17.
Dyson, B. F. & McLean, M. 1990 *JISI Int.* **30**, 802.
Evans, R. W. & Wilshire, B. 1987 *Mater. Sci. Tech.* **3**, 701.
Gell, M., Giamei, A. F. & Duhl, D. N. 1980 In *Superalloys 1980* (ed. J. K. Tien *et al.*). Metals Park, OH: American Society of Metals.
Ghosh, R. N., Curtis, R. V. & McLean, M. 1990 *Acta metall. Mater.* **38**, 1977.
Graham, A. & Walles, K. F. A. 1955 *J. Iron Steel Inst.* **179**, 105.
Henderson, P. J. & McLean, M. 1983 *Acta metall. Mater.* **31**, 1203.
Hirsch, P. B. 1992 *Prog. Mater. Sci.* **36**, 63-88.
Ion, J. C., Barbosa, A., Ashby, M. F., Dyson, B. F. & McLean, M. 1986 NPL Report DMA A115. The National Physical Laboratory, Teddington.
Jeal, R. H. 1986 *Mater. Sci. Tech.* **7**, 721.
Kondo, Y., Kitazaki, N., Namekata, J., Ohi, N. & Hattori, H. 1994 *Testu To Hagane* **80**, 76.

Lund, C. 1972 US Patent nos 3 677 331 and 3 677 747.

Paidar, V., Pope, D. P. & Vitek, V. 1984 *Acta metall.* **32**, 435.

Pan, L. M., Ghosh, R. N. & McLean, M. 1993 *J. Phys., Paris, Colloque C7*, **3**, 629.

Pan, L. M., Scheibli, I., Shollock, B. A. & McLean, M. 1995 *Acta metall. Mater.*, **43**, 1375.

Pan, L. M., Ghosh, R. N. & McLean, M. 1994 In *Proc. of ICSMA 6*, p. 583.

Patel, S. J. & Siddall, R. J. 1994 In *Proc. of Vacuum Metallurgy Conference* (ed. A. Mitchell & J. Fernihaugh), p. 318. AIME.

Pearcey, B. J. 1970 US Patent no. 3 494 709.

Pineau, A. 1990 *High temperature materials for power engineering* (ed. E. Bachelet *et al.*), pp. 913–934. Dordrecht: Miner Academic.

Quested, P. N. & Hayes, D. M. 1993 *NPL Rep. DMM(A)130*. National Physical Laboratory, Teddington.

Sczercenie, F. & Maurer, G. 1987 *Mater. Sci. Tech.* **3**, 733.

Shamblen, C. E., Culp, S. L. & Lober, R. W. 1983 *Electron beam melting and refining-state of the art 1983* (ed. R. Bakish), pp. 61–94. Library of Congress ISSN 07408706.

Sims, C. T. 1984 In *Superalloys 1984* (ed. J. K. Tien *et al.*), p. 399. Warrendale, PA: The Metallurgical Society.

Stoloff, N. A. 1987 In *Superalloys II* (ed. C. T. Sims *et al.*). Wiley.

Tien, J. K. & Copeley, S. M. 1971 *Metall. Trans.* **2**, 543.

Ver Snyder, F. 1966 US Patent no. 3 260 505.

Discussion

G. A. WEBSTER (*Imperial College, London, UK*). I would like to comment on Professor McLean's remarks that alloy development is nearly complete, some process development is possible and that the biggest scope is for engineering exploitation. I agree with these views. Single crystals are being used for turbine blade applications and Professor McLean showed how behaviour in specific crystallographic orientations could be predicted for uni-axial stressing. The presence of thermal gradients in cooled blades will introduce a multi-axial stress state in these components and thorough understanding of the response of single crystals to multi-axial stress is needed before their full potential can be exploited. Also, there may be scope for deliberately introducing compressive residual stresses in engine discs to reduce the influence of small critical effects in high strength disc alloys.

M. MCLEAN. I fully agree with Professor Webster's initial remarks. Too much emphasis has been given in the past on the problems of extrapolating short-term data to long times; this is not a serious problem for aerospace applications. Rather, there is a need to predict multi-axial and cyclic loading responses from uniaxial data. I believe that the state-variable approach is beginning to allow us to do so. I am less sure of the viability of deliberately imposing compressive residual stresses; I would be concerned that they would relax during high-temperature service.

F. R. N. NABARRO (*CSIR, Pretoria, South Africa*). To use an analogy introduced by our chairman many years ago, the dislocations are moving in narrow channels, so flow is lamellar rather than turbulent. Only one family of dislocations is active, and these do not obstruct one another.

M. MCLEAN. This observation must be basically correct. One might debate if a

single set of dislocations will propagate along the cube-oriented channels between γ particles; perhaps there will be activity on two octahedral planes. However, clearly there will be little potential for work hardening.

A. COTTRELL (*University of Cambridge, UK*). Professor McLean said that nickel is near its limit of development as a high-temperature material. This must be so, since the working temperature of the nickel superalloys is so near the melting point of nickel. As well as its excellent mechanical properties, i.e. high-temperature creep strength and high fracture toughness, the nickel superalloy has another major property which is so good that it is often taken for granted and overlooked: its excellent oxidation resistance. I think that there is, and will be, great difficulty in moving beyond nickel to more refractory materials, because so few of them have good oxidation resistance at really high temperatures. If it were not for this we might now be using niobium or molybdenum blades in advanced gas turbines. The same problems are likely to apply generally to intermetallics and carbide ceramics. Probably the only way forward, beyond the nickel superalloys, for the very highest temperatures, is to develop refractory oxides into useful engineering materials.

M. MCLEAN. In terms of oxidation resistance, there is a compromise course of coating the nickel-base superalloys and this is already extensively used in practice. Ceramic coatings are used for their thermal-barrier qualities, as well as for oxidation resistance. I agree that oxide ceramics offer the potential of intrinsic strength and oxidation resistance. If their toughness can be improved to a sufficient level they will certainly find an application. It must also be borne in mind that ceramic turbine blades are unlikely to be cooled, as are nickel superalloy blades. Consequently, the comparison must be between the material operating temperature in the case of the ceramic, with gas temperature for the superalloy, which may be about 300 K in excess of the metal temperature.

Materials requirements for high-temperature structures in the 21st century

BY JAMES C. WILLIAMS

GE Aircraft Engines, Cincinnati, OH 45215, USA

The continued improvement in efficiency of high-temperature structures depends on improved materials and on designs that utilize these materials more effectively. This paper discusses the possibilities available to achieve these improvements. While the results are applicable to any high-temperature structure, the discussion focuses on gas turbine engines. This is because some of the most demanding requirements correspond to this application and the author is more familiar with this area.

Possible materials can be separated into distinct classes: evolutionary and revolutionary materials. The former represent incrementally improved materials, mostly metals. The latter represent intermetallic compounds, and metal, polymer and ceramic composites. An attempt is made to estimate the extent of improvements that can be realized from each class of material. In addition, the barriers to realization of the gains are outlined. Where possible, next steps in overcoming these are described.

Finally, non-technical issues such as material cost and availability are addressed and the growing importance of these factors is discussed.

1. Introduction

High-temperature structures operate under additional design constraints, compared to those intended for service at or near room temperature. Examples of these constraints are time dependent inelastic strain (creep), thermally induced stresses and environmental degradation of material properties. The efficiency of high-temperature structures depends on the ability of the designer to compensate for these and other effects of operating temperature. Detailed knowledge of the service domain and materials behaviour helps minimize the complications due to elevated temperature service. This knowledge is also helpful in minimizing the amount of conservatism that needs to be incorporated into designs to compensate for service environment uncertainty and unanticipated time dependence of materials behaviour. There are ultimate service temperature limits imposed by expected structural life and by the capability of the materials used in the structure. These limits also are determined by the consequence of structural failure if the service life is not achieved. Clearly, when the consequences of premature failure are economic, the implications are quite different than when there are possible safety related issues. The level of design conservatism reflects these differences. Among the most demanding structural applications for high-temperature materials are those in aircraft engines. The basis for this statement is a combination

of several factors: the operating temperatures are high, the expected structural lifetimes are long, the consequence of structural failure is extreme, and the weight critical nature of the product forces the design margins to be as small as possible, consistent with product safety.

Despite these significant constraints, there has been a steady improvement in the capability of aircraft engines with each successive product generation. There are several quantitative parameters that can be used as measures of performance of aircraft gas turbine engines. Perhaps the most important of these are thrust normalized by weight (thrust-to-weight ratio or T/W) and thrust-normalized fuel consumption (specific fuel consumption (SFC)). This paper summarizes the gains made in these performance indices over the past 40 years or so and examines the prospects for continued improvements. The past increases in materials capability are based on multiple generations of improved metallic alloys and on major improvements in processing technology. The future opportunities for continued improvements are much more limited and the rate of progress, going forward, cannot be sustained by improvements only in metals. The alternatives to metals have many other uncertainties and associated questions. Among these are cost and the existence of an industrial base capable of making materials such as ceramic and metal matrix composites in production quantities, assuming they can be made to work technically.

Today, as a combined result of the overcapacity for producing aircraft engines and their natural maturation as a product, these high technology machines have assumed many of the characteristics of a commodity. That is, they are selected by customers who assign a large weight to price in the decision process. The effect of this recent change in the market place is the further slowing of introduction of new technology and a greater focus on cost. This has the effect of restraining R&D budgets and dramatically reduces the ease with which new materials can be introduced into production engines. This is not to imply that no new technology is being developed or introduced into new or derivative engines. It is clear, however, that cost plays a much greater role in the early decision process regarding areas selected for investment in materials technology development.

The intent of this paper also is to describe the current environment for new technology introduction and discuss the effects it has on the future directions for engine materials technology. Some specific actions can be taken to increase the affordability of materials technology development. Included are the earlier use of cost models to estimate affordability and more productive pre-competitive cooperation between traditional competitors that have common needs. More discussion of this will follow.

2. Past materials developments and gas turbine engine performance characteristics

In addition to T/W and SFC, there are several other metrics that are useful to assess the performance of an aircraft engine. These metrics include the compressor exit temperature (T_3) and the turbine inlet temperature (T_{41}). These temperatures are related thermodynamically to the overall pressure ratio of the engine cycle. Cycles with higher overall pressure ratios are more efficient and thus desirable in modern turbofan engines. Another metric is the mass of air that the fan moves relative to that which passes through the engine core (the compres-

Table 1. Representative gas turbine characteristics as a function of time

service date	$T_3/^\circ\text{C}$ ($^\circ\text{F}$)	$T_{41}/^\circ\text{C}$ ($^\circ\text{F}$)	overall pressure ratio	by-pass ratio
1955	379 (715)	871 (1600)	10	< 2
1965	427 (800)	938 (1720)	12–13	2–3
1975	593 (1100)	1343 (2450)	14–16	5–6
1995	693 (1280)	1427 (2600)	35–40	8–9
2015 (est.)	816 (1500)	1760 (3200)	65–75	12–15

sor, combustor and turbine). This metric is another indicator of the propulsive efficiency of the engine. This measure is called the by-pass ratio. Table 1 summarizes the changes in these parameters over the past 40 years as new generations of products have been developed.

The steady increases in T_3 and T_{41} shown in table 1 have been possible because of the availability of higher-temperature alloys for the rotating machinery in the compressor and the turbine section of the engine. In the case of turbine airfoils, these increases have been partly due to improved alloys and partly due to new processing methods. The transition first from conventionally cast Ni base superalloys with equiaxed grain structures to directionally solidified superalloys with only longitudinal grain boundaries and then to monocrystals with no large angle grain boundaries is the result of processing capability improvements. These transitions in structure allowed by processing advances also have enabled alloy chemistries to be modified to delete grain boundary strengthening elements such as Hf and B. These elements had been necessary to impart the required ductility, but they reduced the melting point of the alloy and thus reduced the creep strength. The variation with time of the temperature capability of turbine blade materials, including the effects of processing is shown in figure 1.

In the case of discs, the higher-temperature alloys have a higher volume fraction of the γ' strengthening precipitate and also contain higher concentrations of refractory metal additions, both of which increase the creep strength. The most recent generation of alloys also are made with powder metallurgy methods because this is the surest means of obtaining segregation-free, large forgings. In some cases special processing has been used to create larger than normal grain sizes to further enhance the creep strength. Such changes also affect other properties such as static strength, low-cycle fatigue strength and fatigue crack growth resistance. The key has been to obtain a balance of these properties that enhances the overall structural efficiency of the discs. This has been successfully done and powder metallurgy discs with controlled grain diameters of the order of 45–90 μm diameter are regularly used today.

Other improvements in processing such as the use of clean melting technology also has improved the performance of disc alloys by eliminating inclusions that can be the source of early fatigue crack initiation. As a result, the stress levels at which the clean-melted alloys can be used with high confidence is increased and the rotor weight can be reduced accordingly. Concurrently, the cost of these improved materials has been held in check, relative to the level of performance, by the use of improved processes. These processes have higher yields and greater

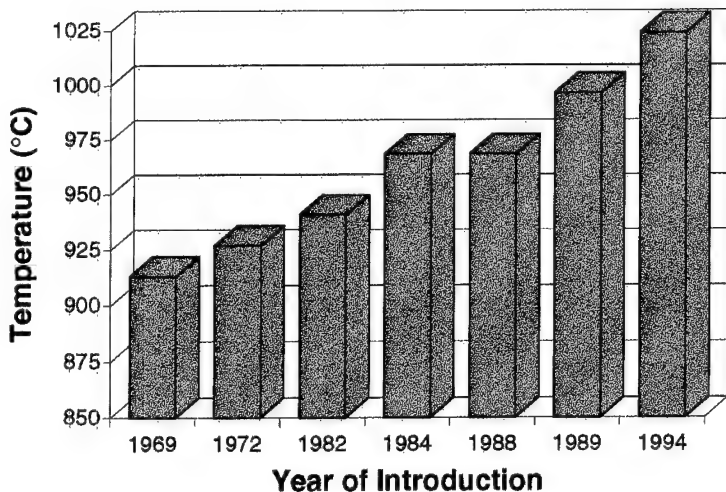


Figure 1. Bar chart showing the changes in temperature capability of cast turbine blade alloys as a function of time. The first three alloys in the series are equiaxed, conventional cast. The next one is a monocrystal alloy. The next is a directionally solidified alloy with comparable performance at lower cost. The last two are monocrystal alloys.

reliability as the result of the use of process modelling. Through improved process controls, made possible by concentrating on the critical process variables identified with modelling, the product of the process exhibits less variation and the occurrence of 'special cause' events is minimized. Finally, the increased use of net shape processing techniques such as casting and precision forging has reduced the cost of manufacturing components from these improved alloys. Without the improvements in processing capability, the cost of the improved materials would be much higher and their use would be much more limited.

3. Future generation metallic materials

The above summary describes, in general terms, the engine performance improvements that have been made and the role of materials as a key enabling technology. An important question with regard to expectations of future improvements is, 'How much more performance can be expected from metals?' Clearly, the rate of improvement is slowing and it is possible that the point of diminishing returns for metals is approaching. The more realistic challenges beyond the next one or two generations of metallic alloys may be the gains obtainable by tailoring existing alloys for particular application regimes and improving the life capability of existing materials. Schematically, this is depicted in figure 2, from which the concept of a performance asymptote or limit can be inferred. In this figure an index of material performance, e.g. creep strength, is shown as a time series. Clearly, the use of a smooth curve is only schematically correct, since the performance increments are achieved on a generation by generation basis. The more important point, however, is that the cost of each increment of performance is roughly the same, so the benefit/cost ratio is decreasing as the asymptote is approached. Barring a major (unlikely) breakthrough in high-temperature metallic alloy concepts, this asymptote is essentially fixed by material melting temperature. The time may be at hand that a logical and appropriate economic decision

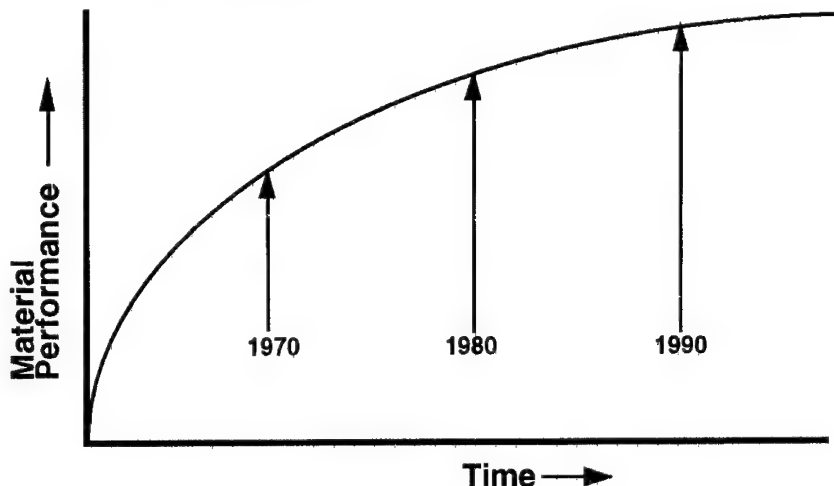


Figure 2. Schematic plot of evolutionary material capability as a function of time. The overall capability is approaching an asymptotic value, but each generation of material cost about the same to develop, making the benefit for unit cost less.

would be to concentrate future R&D efforts on adapting existing materials to serve well-defined niche applications.

One such application is the emerging high speed civil transport (HSCT) engine currently under development in the US. The operating temperatures for the turbomachinery in this engine are not much higher than that of current generation subsonic engines. The times at maximum temperature, however, are many times longer. The long time at high power levels, and therefore high temperatures, is required in the HSCT engine to sustain supersonic cruising speeds. These time-temperature combinations greatly exceed any experience that exists in the aircraft engine industry. Schematic time-temperature profiles for subsonic and HSCT engines are shown in figure 3. This application introduces time-dependence issues in materials performance that have not been addressed previously. These issues will require special attention from a materials standpoint but the maximum temperature capability requirement is not significantly increased in comparison to the recent subsonic transport engines (see table 1). The rotor materials for the HSCT engine thus will require tailoring of the properties to meet these requirements, but the upper boundary of the operating temperature domain need not be extended. These requirements, while challenging, do not call the asymptote (at least on a temperature axis) into question and there is a basis for optimism that the requirement can be met.

The asymptote suggestion also implies the following question: What can still be done to improve metals? This question is causing the engine materials community to more aggressively examine the viability of new classes of materials that have the capability of defeating the metals temperature barrier. These future materials have been separated into two classes, according to the magnitude of the potential performance increment. The classes are called evolutionary and revolutionary, respectively. High-temperature evolutionary materials are metals, almost by definition. Facing the evolutionary materials asymptote question becomes more pressing as the limits of metals are actually approaching and as

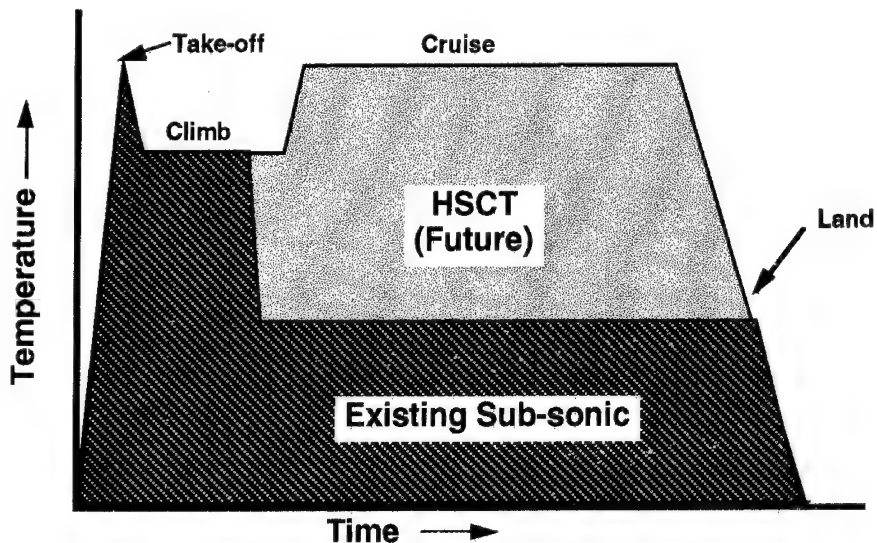


Figure 3. Schematic plots of turbomachinery temperature at various points in a flight cycle for typical subsonic transport engine and the proposed HSCT engine. Note the long exposures at high temperatures during cruise for the HSCT.

resources to explore alternatives become more limited. In the end, the decision will be one of comparing more certain modest gains obtainable from at least one more generation of evolutionary materials with the possibility of much larger gains obtainable from revolutionary materials but with higher risk. This question will be examined in more detail in the next section, but it is relevant to raise it here because these other materials are widely viewed as an apparent alternative to next generation metals. This is in part because of the diminishing benefit relative to cost that can be obtained from another generation of evolutionary metals.

Against this background, it is useful to examine the prospect for next-generation metallic engine components such as rotors (discs) and turbine blades. It appears that there is at least one more generation of turbine blade alloys that can be identified, developed and put into service. These will be investment cast monocrystal blades. The temperature capability and durability of this next alloy and of earlier generation alloys also can be enhanced through the use of ceramic thermal barrier coatings (TBCs). Between these two technologies, it appears that the gas temperature in the high-pressure turbine can be increased by about 100–125 °C in the foreseeable future while maintaining a constant cooling air flow. Conversely, the use of TBCs at a constant gas temperature allows the cooling flow to be reduced for improvement in SFC without raising the metal temperature. The impediment to development of TBCs is improving their current level of durability. If the temperature advantage that can be obtained through their use is incorporated into an airfoil design either through lower cooling air flows or higher gas temperatures, a breach in the coating due to spallation, either from impact or loss of adherence, will have serious consequences in airfoil life. The current generation of TBCs are durable enough to provide significant life extensions, but their use to accommodate increases in T_{41} is a higher risk proposition at present.

Regarding discs, the current T_3 limitations are mainly related to compressor rotor capability since these rotors are not cooled. The limitation for commercial transport applications is more closely related to the effects of dwell or hold time on fatigue crack growth (HTCG) than it is to creep strength. Fortunately, the effects of coarser grain size has a common benefit for both properties, so the use of processing methods that result in grain sizes in the ASTM 4–6 range improves both HCTG and creep strength. Low cycle fatigue (LCF) strength is reduced with increased grain size, but the limiting properties for most long-life commercial engine discs is fatigue crack growth or HCTG, not LCF. As T_3 increases in next-generation high-thrust commercial engines, creep may become a factor, but it is unlikely that LCF will be a life-limiting consideration. Thus alloys and processing methods that improve creep and HCTG will be the focus of most future disc development activities. It is likely that all next generation alloys that meet the strength requirements will be too solute rich to be producible by ingot metallurgy (also called cast and wrought) methods. This mainly is because of the difficulty in producing large, good quality ingots of these richer alloys. Thus powder metallurgy (PM), or its equivalent, will be the basic production method upon which higher temperature disc processing is built. This is an inherently more costly method which immediately raises questions in light of the new cost/performance paradigm. However, on the positive side, once the transition from cast and wrought to PM processing is a *fait accompli*, the incremental cost of special processing to achieve coarser grain size is small. There are several possibilities for higher temperature discs for use above 730 °C. The first is dual heat treatment (DHT) where the disc rim is selectively heat treated to have coarser grains than the bore. This yields better creep and HCTG in the hottest regions of the disc with minimal impact on LCF and tensile strength of the bore. The second method is a dual alloy disc (DAD) where the bore is made of a higher tensile strength, less creep- and HCTG-resistant alloy and the rim is made of a different alloy that has much better creep and HCTG resistance. Processes that prove technical feasibility of both of these approaches have been adequately demonstrated, but reduction to full scale production practice remains to be done. Both of these options raise the cost of discs. The DHT disc will cost less but will give a smaller increase in temperature capability than the DAD approach. Evaluating the trade-off of cost increment against performance improvement cannot be done in isolation. The author believes it is not likely that many applications will emerge where performance is so important that large cost increments will be acceptable. The question is whether, in the light of the newly recognized absolute cost constraints, there will ever be an application for DAD technology. Only the market place will answer this question.

Some actions that can be taken to reduce the barriers to implementing the next generation materials have been mentioned in the Introduction. Some of these are directly related to mitigation of cost barriers, others are more closely related to technical barriers, although this separation is somewhat artificial.

The first of these is the need to do a better job of pre-selecting the most likely materials and process candidates before initiating development. This implies that some rudimentary affordability analysis needs to be conducted before any technical work is initiated. Technologists of an earlier generation will not willingly accept this requirement, but this is a management issue that simply needs to be embedded in the organizational culture (it is an element of the new cost-driven realities). The net result of implementing this cost conscious practice is that fewer,

more promising technologies will be under development at any one time. This permits more resources to be focused on the most likely candidate technologies, with the likelihood of early realization in practice being significantly increased. It also is important to remain alert to opportunities to introduce new materials in low risk or limited use as early as possible to raise the awareness of their existence and potential. Even limited, but real, service experience has a disproportionately beneficial effect on the confidence designers have in a new material. Another way to reduce the cost of developing a new material is to engage in joint development projects with other companies that have common requirements. In earlier times, many companies viewed this approach with disdain because of perceived loss of competitive advantage. In reality, there is a great deal of development activity that can be done jointly even by direct competitors without compromising any potential advantage. More cooperation is emerging, but there is room for much more.

The technical barriers to higher temperature materials implementation include the need for a better fundamental understanding of time dependent materials behaviour, especially HTCG. If the understanding is based on principles instead of empirical data and information, the time-dependent behaviour of a range of alloys can be compared and contrasted without the need to generate large quantities of empirical test data for each alloy being examined. Another area for continued improvement, which is technical in nature, but which has potential for major cost impact is the development and use of realistic process models. Better models permit definition of processes that improve product quality and uniformity. Included are both materials and components such as forgings and castings.

The point of this discussion is to make it clear that new technology, both in materials and in processing, will be introduced into a future generation of new and derivative engines, but cost will play a more central role in the decision process. Just as this cost focus represents new thinking, there is new thinking that needs to be done to make new technology more affordable so as to prevent stagnation of product improvement. Product improvement driven by technology has been the characteristic that has differentiated the aircraft engine industry from, for example, the auto industry. Thus it appears that finding innovative ways of sustaining continued product improvements in a more cost conscious environment will be a key challenge for the industry.

4. The future of revolutionary materials

As mentioned earlier, a revolutionary material is one that has a large change (step function) in any particular property of interest. These materials have captured a great deal of interest among structural designers because of their potential for large gains in structural efficiency. Over the past 10–15 years a lot of effort has been devoted to reducing revolutionary materials to practice for inclusion in high-performance production military and commercial systems. It is fair to say that progress in reaching this objective has been slow. Today the only examples of these materials in significant use are polymer matrix composites. Other candidate classes of revolutionary materials are metal and ceramic matrix composites, and intermetallic compounds. The balance of this section will examine the status of each of these material classes and outline the prospects and timing for reducing them to practice.

(a) Polymer matrix composites (PMCs)

These materials are in use in a number of production systems, both in the air-frame structure and the engine. The largest volume of PMCs are used at or just above ambient temperature (less than 100 °C). There is a moderate amount of polyimide matrix, carbon fibre composite material (PMR-15) in use at temperatures up to about 275 °C, but this is small in an overall sense. Thus PMCs are not a mainstream topic of this article since they are not truly a high-temperature material. Nevertheless, a brief summary of the benefits and issues associated with the use of PMCs seems appropriate since this is the most mature class of revolutionary materials. PMCs are attractive because they provide major weight and durability advantages. They have specific stiffness and strength values of not less than twice that of metallic structures. They also have similar advantages in fatigue strength. They are considerably more costly to fabricate into components, compared to Al or Ti, and this has limited the extent of their use. Until quite recently, design methods to fully realize the benefits of PMCs have not been widely available. This deficiency has further limited their use in complex shaped structures. Compared to monolithic metals (as opposed fabricated metallic structures such as honeycomb core, metal face sheet), PMC structure is difficult and costly to repair. These two cost related factors are the subject of development effort and in time will be less troublesome. Today, however, these remain as issues that reduce the usage of PMCs. The industrial base for making PMC raw materials is reasonably mature, but the overcapacity, due in part to previous over-optimistic estimates of use levels, currently is creating major financial pressures for the materials suppliers. As a result there will be a shake-out in the supplier base, but the remaining companies should emerge healthier than they have been in several years.

(b) Metal matrix composites (MMCs)

Metal matrix composites have been in existence as a material concept for over 20 years. Laboratory quantities of these materials have been available for nearly as long. Today there are several distinct classes of MMCS. These can be distinguished by the nature of the reinforcement: continuous fibre, discontinuous fibre or particulate reinforced composites. There are markets identified for each of these classes of MMC, but the only class that will be discussed here are Ti matrix composites reinforced with continuous SiC fibres (known as TMCS). These composites have been shown to have very attractive properties as can be seen in table 2. These properties represent a two-fold increase in structural efficiency when compared to high strength Ti alloys. The reproducibility of the properties shown in table 2 has also been thoroughly demonstrated and TMCS are widely accepted as a technically feasible material system. These properties are very anisotropic, but this characteristic can be managed through better design methods that are available (but not widely used). The issue that has been restricting TMC use is cost and at present this barrier is great enough that these materials are not in use in any production system.

The principal issue that is impeding extensive use of TMCS in addition to cost is the lack of a production scale and style source of supply. In some regards this can be viewed as a chicken and egg situation. This epitomizes the dilemma that has plagued the reduction to practice of revolutionary materials. That is, the

Table 2. *One example of reproducible, longitudinal-orientation MMC properties*
(Material system: Ti 6Al 2Sn 4Zr 2Mo + Si, wt%; ca. 150 μm SiC fibres.)

ultimate tensile strength	1.9×10^3 MPa (276 ksi)
Young's modulus	226×10^3 MPa (32.8 msi)
fracture strain	0.95%
density (equivalent to Ti alloys)	4.43 g cm^{-3} (0.16 lb in^{-3})

cost becomes less as the usage volume increases, but there are few applications that are so performance limited that the early higher cost during the low-volume phase of reduction to practice can be justified. Without a well-defined market, capitalization to produce the materials in larger (lower cost) volumes typically is not available. There currently is a large cooperative programme in the US that is aimed at reducing the cost of TMCS. There are several aspects of this cost-reduction programme that make the outcome encouraging. Most important is the agreement among the users to focus on a single, lowest-cost process for making TMCS. This lowest-cost process will be selected after a careful evaluation phase. Further, the initial applications planned for production introduction are ones limited by low use temperature and stiffness. This increases the chances of success because it is less likely that an unforeseen problem will occur during service introduction. If the material cost targets are achieved, TMCS will likely see initial service in real products within the next four years. While this is encouraging, the overall time line from material concept to actual product use is considerably longer than was originally forecast.

(c) Ceramic matrix composites (CMCs)

CMCs are the most attractive material concept for defeating the metals use temperature asymptote defined by melting temperature. The fibre toughening of CMCS avoids many of the well-known brittleness issues associated with monolithic ceramics. However, it is essential that the toughness of CMCS that is derived from fibre-dominated behaviour is retained after long term, high-temperature service. This poses a potential problem that is still under evaluation and extensive study. The key to fibre dominated behaviour is retention of a fibre matrix interface that has intermediate strength. It is common for reactions to occur during elevated temperature service that either strengthen or weaken the interface, thereby changing the toughening behaviour. As service temperatures increase above the 1300–1350 °C range this matter becomes increasingly difficult. Today, it is accurate to say that there are no CMC systems that have the service capability for thousands of hours at or above 1300 °C. Development efforts are still underway to achieve this goal, but it is a daunting prospect. There are other issues that must be resolved before CMCS can reach their full potential at these very high temperatures. One is the availability of a high-temperature fibre that will have adequate creep resistance as service temperatures are raised. This limitation is less bothersome than the loss of fibre dominated behaviour because it gradually reduces the load bearing capacity of CMCS but does not result in the onset of potential for catastrophic failure. CMCS also have a limited industrial base for large scale production, although the situation is somewhat better than for TMCS. As in the case of TMCS, the absence of applications and little consensus among users

regarding preferred processing methods contributes to the high cost of CMCs. A cooperative programme of the type described for TMCS would be useful as a means of cost reduction. There is growing interest in CMCs for low-emission engine combustor liners. If this application is realized, the situation could change and applications in real products could develop relatively rapidly.

(d) *Intermetallic compounds*

Intermetallics also have been the object of study for more than 25 years as potential replacements for high-temperature alloys. In fact, some of these materials have excellent high-temperature strength. The major barrier to the use of intermetallics has been the inability or unwillingness, in a risk sense, to deal with the low temperature brittleness of literally all intermetallic compounds. Most intermetallics become more ductile at elevated temperature, but the low temperature brittleness poses severe problems, some real and some perceived. An additional attraction of intermetallics is their low density, because many compounds contain one or more light elements such as Al or Si. The intent of this section is not to review the status of the various intermetallics that are currently the subject of a large number of development programmes around the world. Rather, it is to describe the barriers to implementation that a component made from an intermetallic must overcome to achieve production status. Several conferences have been held on intermetallics and the proceedings of these are an excellent source of detailed technical assessments of particular compounds (Darolia *et al.* 1993).

The brittleness of intermetallics makes them difficult to design with because of increased risk of unanticipated fracture in service and increased manufacturing losses because of cracking during processing. The pay-off from these low density materials justifies coping with these issues. As a result, there are several intermetallics that are being actively studied. Among the most promising and widely studied is the compound based on TiAl. There are several ternary and quaternary alloy variants of this compound under intense evaluation. At GE Aircraft Engines, an entire last-stage wheel of low pressure turbine (LPT) blades has been made from cast Ti-48Al-2Cr-2Nb and run in a factory cyclic endurance test of a large commercial transport engine. The blades have performed perfectly, demonstrating that the concern about low ductility is not performance limiting. These results are very encouraging and provide the impetus to consider a field evaluation of LPT blades. This is expected to commence in 1995. The TiAl LPT blades can be directly substituted for cast equiaxed Ni base alloy blades at about 50% weight reduction. Later, if this evaluation is successful, additional weight savings can be achieved by re-designing the disc and static structures because of the lighter rotor weight. Still the practical issue with TiAl is cost, because of the higher degree of difficulty of fabricating components. Casting helps reduce the cost, but TiAl castings will be more expensive until there is more experience in the industry. In the future, TiAl should be less expensive than cast Ni-base alloys if the prices of Ni and Co continue to escalate. It is an unusual opportunity to contemplate a simultaneous reduction in weight *and* cost. Many issues must be resolved before this is realized, but there is good reason to believe that this will eventually happen. There also is interest in forged (wrought) TiAl, but there is little reason for optimism regarding cost of this processing method. Here, the low ductility increases the number of forging steps and reduces the yields because of cracking. It appears that the first production application of TiAl, if it occurs,

will be in cast form. It is conceivable that the first production introduction of low-risk cast TiAl components could occur as early as 1997.

5. The effect of business climate and product maturity on product development trends

The current business climate in the aircraft engine sector only sharpens the cost focus. It is clear that the prime means of differentiating a product in this market today is price, not performance. This is because of the maturation of subsonic engines and the current world overcapacity for aircraft engine production. Today, all engines in a given thrust class have comparable (but not identical) performance characteristics. The most certain means of increasing market share is to offer a competitive product at a lower selling price than that of the competition. This means that the cost of producing the product must be reduced and vigorously managed, both at the engine factory and at the raw materials and component suppliers plants. The concept of cost as the primary consideration represents a new paradigm in the engine industry. Adapting to this new way of life has produced some significant changes including new ways of working and significant reductions in work force size. In addition to competitive cost comparisons between engine makers, there has recently arrived an awareness of the importance of absolute costs. Several major airlines have recently said that they cannot foresee a realistic means of obtaining adequate return on investment from any aircraft that costs more than about \$200,000 per seat (in 1994 dollars). The basis for this is the analysis of anticipated revenues and operating costs including the cost of ownership. The significance of this position is not the accuracy of the \$200,000 figure, but the recognition of an absolute cost constraint in addition to a relative one that is the result of competitive analysis. This event will undoubtedly affect the rate that new technology can be introduced into future generation engines and airframes. In turn, this will influence the types of development projects that the engine manufacturers undertake and the rules of thumb that have been used to assess the value of new technology that enhances product performance. External factors such as large increases in fuel cost may change this matter, but for current planning purposes such increases do not appear likely.

Even the market analysis of the HSCT assumes very modest fare premiums (about 10–15%) in three-class service to make the market size large enough to allow the return of development cost. Such modest increases will not buy much technology beyond that needed to meet the range and emissions requirements. Thus the market in which commercial aircraft and engines operate appears to have permanently changed. The new competitive realities are based on cost, not technology. It is time that technologists recognize these realities and adjust their thinking and approach to their work.

6. Summary

This paper has described the development of aircraft engines as products of high technology. A few ideas that have been presented are worth repeating here in capsule form.

1. Materials have played a significant role in the performance improvements of aircraft engines during the past 40 years.

2. The temperature limits of metals are being approached, but the alternatives to metals raise several different, but equally difficult questions.
3. The development and implementation cycle for new materials is very long and needs to be reduced. This will reduce development cost and permit more rapid introduction of new materials.
4. The current market climate places an unprecedented emphasis on cost.
5. Performance parity with cost advantage will be the most certain way to win market share in future transactions.
6. The ability to introduce new materials will be paced by cost, more than anything else.

References

Darolia, R., Lewandowski, J., Liu, C., Martin, P., Miracle, D. & Nathal, M. (eds) 1993 *Structural intermetallics*. Warrendale: TMS-AIME.

Discussion

M. MCLEAN (*Department of Materials, Imperial College, London, UK*). Doctor Williams indicated that ceramic matrix composites show particular promise for aero-engine applications. Does he envisage that they will be used with cooling? If not, what material temperature advantage is required over existing metallic materials for which blade cooling is likely to be more efficient?

J. C. WILLIAMS. Ceramic matrix composites (CMC) appear to be attractive for combustor liners, turbine blades, and static exhaust structural parts. Clearly the use of cooling would further enhance the temperature benefit in the former two cases. Today, there is no proven way to put cooling passages in CMCs. There at least two barriers. First, severing the fibre reinforcement would reduce the structural efficiency of the materials. Second, even carbides or nitrides have much lower thermal conductivity than superalloys. Consequently, there would be steep temperature gradients between cooling holes. This would only serve to exacerbate the thermal fatigue problem that is recognized in elastically heterogeneous materials such as CMCs.

Calculation of the increase in temperature capability to make an uncooled CMC part comparable to a current cooled superalloy turbine airfoil is not straightforward because of the differences in thermal conductivity and the anisotropy in this property that the fibres introduce. In superalloy blades cooling can provide as much as 500 °C ΔT between the metal temperature and gas temperature. Using this as a rough approximation, it is fair to say that there are no CMC systems today, either production or developmental, that offer this temperature. Of course, the durability required or expected in commercial engines today is an additional question mark when the use of CMCs is contemplated.

A. COTTRELL (*Department of Materials Science, University of Cambridge, UK*). As befits the title of this Discussion, we are concentrating on the problem of raising the working temperatures of materials. But in, for example, gas turbine engines it can be just as important to aim at reducing the weight, the pursuit of which would lead the materials research in a quite different direction. Would Dr Williams care to comment on these possible alternative strategies?

J. C. WILLIAMS. It is always attractive to introduce lower density materials, or more accurately, materials which have better performance on a density corrected basis. However, the overall performance benefits of significantly reducing the operating temperatures in the hot sections of a turbine engine to permit use of lower density materials are fewer than those that can be gained by increasing the temperatures through incremental improvement of the currently used Ni-based alloys. The difficulty lies in achieving large enough reductions in the operating temperature to permit the use of lower density alloys based on Ti or even Al, while maintaining acceptable performance characteristics and not increasing the risk of fire. The remaining question is whether there are lower density materials with roughly Ni-based alloy temperature capability. There are a few, including C-C composites, ceramic composites and some intermetallic compounds such as NiAl and TiAl. Each of these classes of materials present several durability related questions that are so daunting as to currently preclude their use in any production engines. Engine tests have shown that the difficulty in applying these materials varies by material class, but the least likely appears to be C-C composites and the most likely is TiAl, at least for rotating components. There has been considerable work expended in reducing the weight of static structures, with the result that polymer matrix composites and cast Ti alloys are widespread use today. Al and Mg alloys may be possible for the cool, front end but these materials are not widely used in western world for large engines.

The greatest performance benefits have been realized through incremental improvements in the gas temperatures partly made possible through higher temperature materials and partly through the use of improved cooling technology. Lighter weight structures are attractive, but as a complement to higher temperature rotors.

M. HARVEY (*Department of Materials Science and Metallurgy, University of Cambridge, UK*). Ram Darolia, also of General Electric, has published some interesting results with regard to nickel aluminide, NiAl, as a possible replacement for existing superalloys in blade applications. What is the current state of research at GE concerning this particular intermetallic?

J. C. WILLIAMS. There has been a lot of work done on NiAl at GE Aircraft Engines over the last six years. This work has focused on several aspects of this material including processing to make large monocrystals, alloying to achieve better creep strength and ductility improvements, manufacturing methods for making turbine airfoils and design methods that permit the use of limited ductility materials such as NiAl in turbine components. It is fair to say this work has taught us a lot and that we are now in a much better position to contemplate a demonstrator engine test of this material. We also have learned how much more difficult, compared to superalloys, it would be to reduce NiAl to practice in a production engine.

We have an engine test scheduled for mid-1995 which contains a turbine nozzle with NiAl vanes. Our previous effort gives us reasonable confidence that this test will be successful, but the next steps are less clear. The benefits of a 35% less dense alloy with several fold increased thermal conductivity are very clear. The cost of introducing this material and the associated durability risk are much less clear and need to be resolved before a production commitment could be made.

T. KHAN (*Chatillon Cedex, France*). Which type of materials does Dr Williams

have in mind while projecting T_3 (compressor air temperature) temperature of about 815 °C in advanced subsonic engines of the future? Could he give an indication in the type of research work which should be carried out to meet this goal.

J. C. WILLIAMS. First let me re-emphasize that, currently, there are no known materials solutions to permit an engine to operate for long times at 815 °C T_3 values. The best candidates for somewhat lower temperatures (up to 760 °C) are Ni-based alloys used in narrower regimes that the current 'one size fits all' approach. By this I mean the bore of a very high-temperature rotor could be made of a high strength, fatigue resistant alloy, the web could be a medium strength, creep-resistant, coarse-grained alloy and the rim might be directionally solidified or even monocrystal pieces made from airfoil alloys chosen for their extreme creep resistance, but low tensile and fatigue strength.

There has been discussion of W wire reinforced structures but I, personally, am not optimistic about the ability to eliminate reactions between the Ni alloy and W wire. Clearly, there are a number of serious technical barriers to achieving an 815 °C disc. Even if these can be overcome, the costs of such a disc may prove prohibitive. The gas turbine industry has provided other examples of technical successes that are commercial failures. As the industry matures, these must be avoided through cost-conscious, decision-making processes in the early stages of a development project.

Materials selection to resist creep

BY M. F. ASHBY AND C. A. ABEL

*Engineering Design Centre, Cambridge University Engineering Department,
Trumpington Street, Cambridge CB2 1PZ, UK*

A design-led procedure is developed for the selection of materials to resist creep, creep fracture, creep relaxation and creep buckling. It is an extension of a successful procedure for room temperature design which uses performance indices and materials-selection charts. The extension requires the definition of a 'design strength', σ_D , which characterizes material response under conditions imposed by the design. Materials are ranked by an optimization procedure which combines σ_D with other properties (such as density, or cost, or stiffness) to isolate the subset which best meet the design specification.

1. Introduction

How are materials chosen to avoid failure by creep at high temperatures (figure 1)? Very largely by experience. Polymers can be used at room temperature, but, with only a few exceptions, not above 100 °C. The most creep resistant of aluminium alloys are good to about 200 °C; titanium alloys to 600 °C; stainless steels to 850 °C, and so on. But optimal selection requires much more than this. The choice depends not only on material properties, but on the mode of loading (tension, bending, torsion, internal pressure), on the failure criterion (excessive deflection, fracture, relaxation of stress, buckling, etc.) and on the optimization objective (minimizing weight, or cost, or maximizing life). A designer, not himself a specialist on creep, has no easy way to identify the subset of materials best suited to his needs, or to predict the ways in which a change in the design might influence the choice. In short, we lack a systematic procedure for selecting materials for use at high temperatures.

There is a systematic method for selecting materials for mechanical design at room temperature. Could it be extended to high? To answer this, we first examine how the method works.

2. Material selection for room temperature design

The method uses two key ideas: *performance indices* and *material-property space*.

A performance index is a group of material properties which characterizes some aspect of the performance of a component (Crane & Charles 1984; Ashby 1992). Selecting a material with the largest value of the appropriate index maximizes this aspect of performance. The indices are derived from models of the function of the component. The best materials for making a light strong *tie* (a tensile

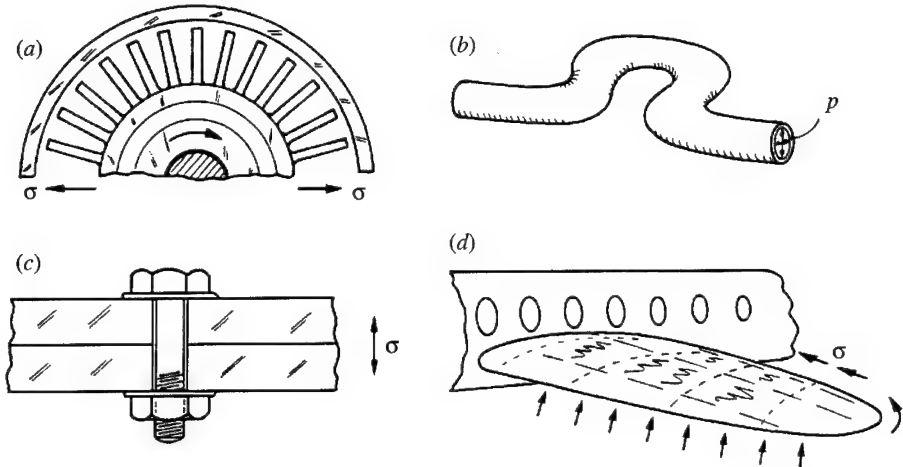


Figure 1. Creep is important in four classes of design: (a) displacement-limited, (b) failure-limited, (c) relaxation-limited and (d) buckling-limited.

member) are those which have the highest value of the specific strength:

$$M_1 = \sigma_y / \rho, \quad (2.1)$$

where σ_y is the yield strength and ρ is the density. This will appear obvious; it could have been guessed. But it is dangerous to guess indices. The best material for a light strong *beam*, i.e. a component loaded in bending rather than tension, is that with the greatest value of

$$M_2 = \sigma_y^{2/3} / \rho, \quad (2.2)$$

or, if the width of the beam is fixed but its height can be adjusted (when it is called a *panel*), that with the greatest value of

$$M_3 = \sigma_y^{1/2} / \rho. \quad (2.3)$$

Material indices such as these are derived from models which describe *function*, *objective* and *constraints*. Equation (2.2), for example, is derived as follows. A material is required for a light, strong beam. The beam has a specified length L and a rectangular cross section $b \times h$ such that $b = \alpha h$ (α also specified, so that the shape remains constant) as shown in figure 2a. Its function is obvious: it is that of supporting a bending moment. The objective is to minimize its mass m , given by

$$m = AL\rho, \quad (2.4)$$

where $A = bh = \alpha h^2$ is the area of the cross section and ρ is the density of the material of which the beam is made. There are constraints: first, the length L and the proportions α are specified, and second, the beam must not collapse plastically under the load F . Plasticity starts when the stress in the surface of the beam first reaches the yield strength σ_y of the material; plastic collapse occurs when this plasticity penetrates through the entire section to give a plastic hinge. The load F which will just cause collapse is

$$F = C_1 \sigma_y b h^2 / L, \quad (2.5)$$

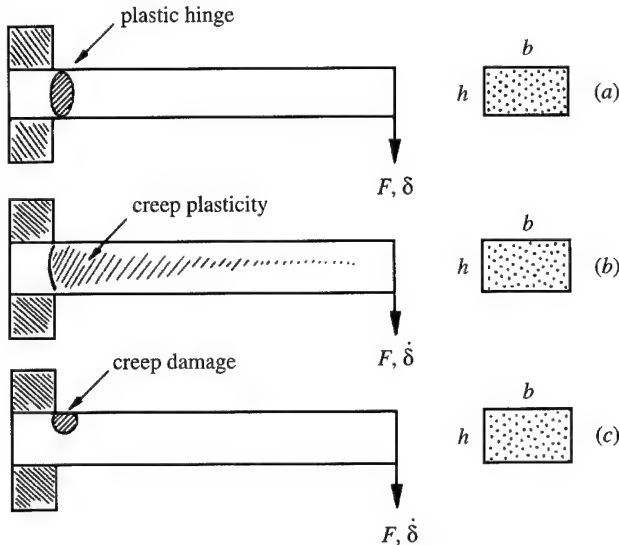


Figure 2. A cantilever beam loaded with an end load F . (a) At room temperature a plastic hinge forms where the bending moment is highest. (b) At high temperature creep plasticity is distributed. (c) Creep fracture starts where the local tensile stress is highest.

where C_1 is a constant which depends only on the load distribution; for the cantilever of figure 2, $C_1 = \frac{1}{4}$. Other supports or other distributions of load change C_1 but nothing else. The beam can be made lighter by reducing the area A of the cross section, but if it is reduced too much the beam will collapse under the load F ; we are free to choose A so as to reduce the mass, provided the constraint is still met. Substituting for A in (2.4) from (2.5) (and using $bh^2 = A^{3/2}/\alpha^{1/2}$ and $C_1 = \frac{1}{4}$) gives

$$m = \rho L \alpha^{1/3} \{4FL/\sigma_y\}^{2/3}. \quad (2.6)$$

In this equation the quantities L , α and F are fixed by the design. The mass m is minimized by minimizing the remaining term $\rho/\sigma_y^{2/3}$. It is convenient to restate this as a quantity to be maximized: the mass of the beam can be minimized (and performance maximized) by seeking the material with the largest value of the performance index of (2.2). Panels (plates of fixed width loaded in bending) gibe, by a similar route, (2.3).

The differences in the exponents that appear in the three index equations (1, 2/3, and 1/2) drastically change the choice of materials. This is where the idea of material-property space enters: a multi-dimensional space with values of material properties as axes. Sections though this space can be charted ('material-selection charts') and, on to these, the material indices can be plotted. In the example shown as figure 3, the axes are $\log(\sigma_y)$ and $\log(\rho)$. When data for a given material class – metals, for instance – are plotted on these axes, it is found that they occupy a field which can be enclosed in a 'balloon'. Ceramics as a class occupy a characteristic field, and so do polymers, elastomers and composites. The fields may overlap but are nonetheless distinct. Individual materials or subclasses (tungsten in the class of metals, or polypropylenes in the class of polymers) appear as little bubbles within each class-balloon, with dimensions defined by the ranges of their properties.

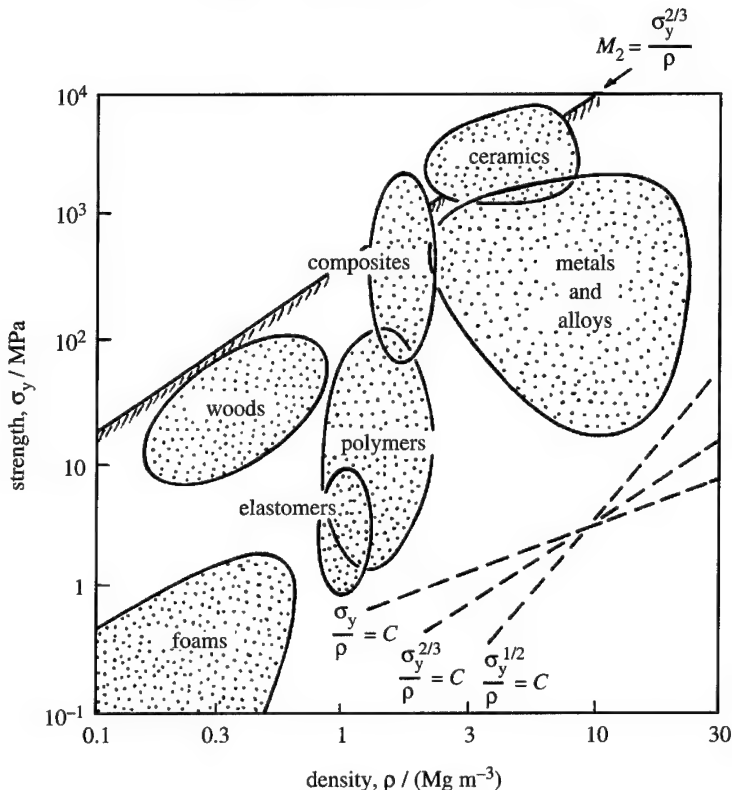


Figure 3. A selection chart for strength-limited design showing the yield strength σ_y plotted against the density ρ on logarithmic scales. A compilation of such charts for room temperature design is given by Ashby (1992).

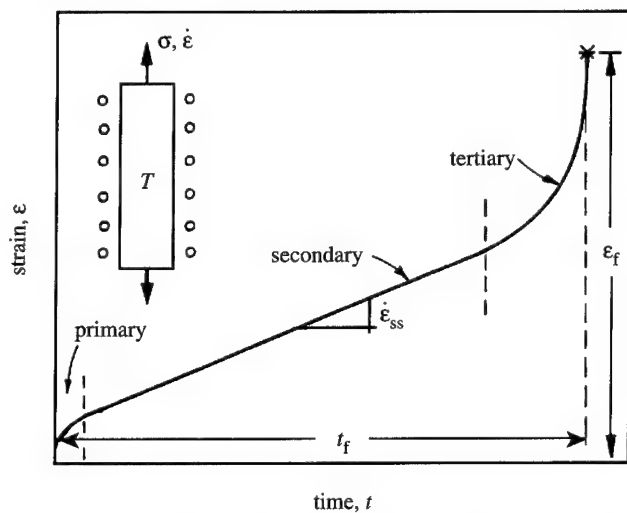


Figure 4. A typical creep curve showing the tensile strain ϵ plotted against time t . It shows the primary, secondary and tertiary stages, and the quantities ϵ_{ss} , ϵ_f and t_f .

The subset of materials with the greatest value of an index can be identified rapidly using such charts. Taking logarithms of (2.2), for instance, we find

$$\log(\sigma_y) = \frac{3}{2} \log(\rho) + \frac{3}{2} \log(M_2). \quad (2.7)$$

The equation defines a grid of lines of slope 3/2 on the chart, one for each value of M_2 . The construction is illustrated in figure 3, from which it can be seen that certain fibre-reinforced composites and ceramics have the particularly large values of M_2 and so are the best choice for a light, strong beam. The index M_1 plots as a line of slope 1; M_3 plots as a line of slope 2; they identify the best materials for light strong ties and panels. Plotting these on figure 3 identifies the best subset for each application. The chart plus the indices allow optimal selection for each combination of function, constraint and objective.

The method is fully developed in texts and software (Ashby 1992; Cebon & Ashby 1992; CMS software 1994). Multiple selection stages are possible by using different slices through property space, and the shape of the cross section (important in bending, torsion and in resisting buckling) can be included in the indices. But this is all for room temperature. We return to our earlier question: can the method be extended to high temperatures?

3. Material indices for high temperature, creep-limited design

In design against creep, we seek the material and the shape which will carry the design loads without failure, for the design life at the design temperature. The meaning of 'failure' depends on the application. We distinguish four types of failure, illustrated in figure 1.

1. Displacement-limited applications, in which precise dimensions or small clearances must be maintained (as in the discs and blades of turbines), when design is based on creep rates $\dot{\epsilon}$ or displacement rates $\dot{\delta}$.

2. Rupture-limited applications, in which dimensional tolerance is relatively unimportant, but fracture must be avoided (as in pressure-piping), when design is based on time-to-failure t_f .

3. Stress-relaxation-limited applications in which an initial tension relaxes with time (as in the pretensioning of cables or bolts) when design is based on a characteristic relaxation time t_r .

4. Buckling-limited applications, in which slender columns or panels carry compressive loads (as in the upper wing skin of an aircraft, or an externally pressurized tube), when design is based on critical time-to-instability t_b .

To tackle any of these we need constitutive equations which relate the strain rate $\dot{\epsilon}$ or time-to-failure t_f for a material to the stress σ and temperature T to which it is exposed.

(a) Constitutive equation for creep deflection

When a material is loaded at a temperature above about one third of its absolute melting point, T_m , it creeps. Figure 4 shows the shape of the tensile creep curve at constant stress, σ , and temperature T . A primary extension is followed by a stage of steady-state creep, which ends in an accelerating tertiary stage. The important parameters are marked: the steady-state creep rate $\dot{\epsilon}_{ss}$, the time to fracture, t_f , and the creep ductility, ϵ_f .

The characteristics of the curve and the way it changes with temperature and

stress are described mathematically by a constitutive equation (Finnie & Heller 1959; Hult 1966; Penny & Marriott 1971; Gittus 1975; Frost & Ashby 1972; Evans & Wilshire 1985). Many constitutive equations for creep-rate have been suggested, some purely empirical, some science-based; most are a mix of the two. Those most widely used in engineering design when deflection is important relate the steady-state strain rate $\dot{\epsilon}_{ss}$ to the tensile stress σ and the temperature T thus:

$$\dot{\epsilon}_{ss} = Af(\sigma)e^{-Q/RT}. \quad (3.1)$$

where A is a kinetic constant, Q an activation energy, R the gas constant and $f(\sigma)$ means 'a function of stress σ '. The function $f(\sigma)$ can be approximated, over restricted ranges of stress, by a power law (an approximation associated with the name of Norton), giving

$$\dot{\epsilon}_{ss} = A \left(\frac{\sigma}{\sigma_0} \right)^n e^{-Q/RT} = \dot{\epsilon}_0 \left(\frac{\sigma}{\sigma_0} \right)^n. \quad (3.2)$$

where the constant A , the activation energy Q , the exponent n and the characteristic strength constant σ_0 are material properties. Considerable experience has accumulated in the use of Norton's law, which has the appeal that it allows analytical solutions to a wide range of engineering problems (see, for instance, Finnie & Heller 1959; Hult 1966; Penny & Marriott 1971). For this reason we shall use it even though, from a scientific point of view, it lacks a completely respectable pedigree.

(b) Constitutive equation for creep fracture

When fracture rather than deflection is design-limiting, creep is characterized instead by the time to fracture, t_f . It, too, can be described by a constitutive equation with features like those of (3.1). Here, again, a power law gives an adequate description over a restricted range of σ and T :

$$t_f = B \left(\frac{\sigma}{\sigma_f} \right)^q e^{Q_f/RT} = t_{f0} \left(\frac{\sigma}{\sigma_f} \right)^q. \quad (3.3)$$

with its own values of kinetic constants B , activation energy Q_f , exponent q and characteristic strength σ_f .

(c) Constitutive equation for creep relaxation

Creep relaxation requires a constitutive equation which combines creep and elastic response. For tension, and neglecting transient creep, it takes the form:

$$\dot{\sigma}/E = -\dot{\epsilon}_{ss} = -\dot{\epsilon}_0 \left(\frac{\sigma}{\sigma_0} \right)^n. \quad (3.4)$$

where E is Young's modulus, $\dot{\epsilon}_{ss}$ is given by (3.2) and $\dot{\sigma}$ is the rate of change of stress with time. For the bending of a beam (as in figure 2) the equation becomes, instead

$$\dot{F}/S = \dot{\delta}_c, \quad (3.5)$$

where \dot{F} is the rate of change of force F , S is the bending stiffness and $\dot{\delta}_c$ is the creep deflection rate of the beam. Similar expressions describe torsion and compression.

4. Material selection in the creep regime

We wish to derive indices which parallel those of § 2, but for design when creep takes place. The immediate difficulty is that the 'strength' is now no longer a fixed material property, but depends on temperature and on the strain rate. The treatment below is kept as brief as possible. Fuller details can be found elsewhere (Abel & Ashby 1994).

(a) Deflection-limited design

Consider first the trivial case of a tensile member – a tie – of minimum weight, designed to carry a load F for a life t without deflecting more than δ at a temperature T . If the tie has length L , the steady strain rate must not exceed

$$\dot{\epsilon} = \delta/Lt. \quad (4.1)$$

Inserting this into the constitutive (3.2) for tensile creep and inverting gives

$$\sigma = F/A = \sigma_0(\delta/\dot{\epsilon}_0 Lt)^{1/n}. \quad (4.2)$$

The objective is to minimize the mass of the tie. Solving for A and substituting this into (2.4) gives

$$m = L\rho F/\sigma_D$$

with

$$\sigma_D = \sigma_0(\delta/\dot{\epsilon}_0 Lt)^{1/n}. \quad (4.3)$$

Thus the lightest tie which meets the constraints of F , T , t and δ is that made of the material with the largest value of

$$M = \sigma_D/\rho. \quad (4.4)$$

This is just (2.1) with σ_y replaced by σ_D , defined above; it contains both temperature and time.

The analysis of beams, shafts, pressure vessels (and such like) is a little more complex, but follows the same pattern. Consider, as an illustration, the cantilever beam of figure 2b carrying a load F , but now at a temperature such that it creeps. The objective, as before, is to make the beam as light as possible; the constraints (again as before) are that its length L and the proportions α of its cross section are fixed, and that it must support the load F for a time t at temperature T without deflecting more than δ . The design specification constrains the deflection rate, $\dot{\delta}$: it must not exceed δ/t . The deflection rate δ for a cantilever beam with end load F , creeping according to the constitutive (3.2) is

$$\dot{\delta} = \frac{2}{n+2} \dot{\epsilon}_0 L^2 \left\{ \frac{4FL}{\sigma_0} \left(\frac{2n+1}{2n} \right) \frac{1}{bh^{(2n+1)/n}} \right\}^n. \quad (4.5)$$

Eliminating b and h between the equations (2.4) and (4.5), using $b = \alpha h$, gives

$$m = \rho L^{(3n+3)/(3n+1)} \alpha^{(n+1)/(3n+1)} \left[\left(\frac{2n+1}{2n} \right) \frac{4FL}{\sigma_D} \right]^{2n/(3n+1)}. \quad (4.6)$$

with σ_D , which we call the *design strength*, given by

$$\sigma_D = \sigma_0 \left(\frac{n+2}{2} \frac{\dot{\delta}}{L\dot{\epsilon}_0} \right)^{1/n}. \quad (4.7)$$

Table 1. Creep deflection

(Time to deflect through δ ('life') = t ; $\dot{\delta} \propto \delta/t$, $n \gg 1$. To minimize cost, replace ρ by $C_m \rho$ in the expressions for M ; to minimize energy content, replace ρ by $q_m \rho$.)

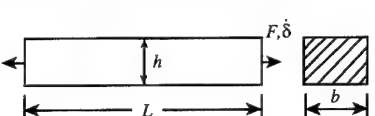
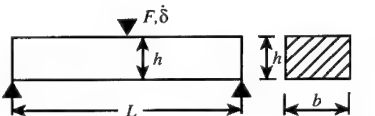
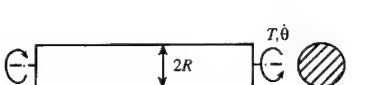
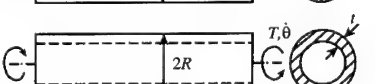
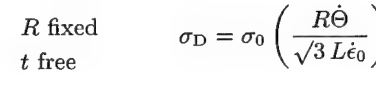
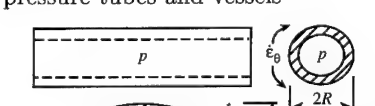
mode of loading	geometry	design strength	index
tension; centrifugal loading			
		any b and h	$\sigma_D = \sigma_0 \left(\frac{\dot{\delta}}{L\dot{\epsilon}_0} \right)^{1/n}$
bending			
	$b = \alpha h$	$\sigma_D = \sigma_0 \left(\frac{\dot{\delta}}{L\dot{\epsilon}_0} \right)^{1/n}$	$M = \sigma_D^{2/3}/\rho$
		b fixed h free	$M = \sigma_D^{1/2}/\rho$
		h fixed b free	$M = \sigma_D/\rho$
torsion			
		solid R free $t = \alpha R$	$\sigma_D = \sigma_0 \left(\frac{\dot{\Theta}}{\sqrt{3}\dot{\epsilon}_0} \right)^{1/n}$
		t fixed R free	$M = \sigma_D^{2/3}/\rho$
		R fixed t free	$\sigma_D = \sigma_0 \left(\frac{R\dot{\Theta}}{\sqrt{3}L\dot{\epsilon}_0} \right)^{1/n}$
			$M = \sigma_D^{1/2}/\rho$
pressure tubes and vessels			
		R fixed t free	$\sigma_D = \sigma_0 \left(\frac{\dot{R}}{R\dot{\epsilon}_0} \right)^{1/n}$
			$M = \sigma_D/\rho$

Table 2. Creep fracture

(Time to fracture ('life') = t_f ; $n \gg 1$. To minimize cost, replace ρ by $C_m \rho$ in the expressions for M ; to minimize energy content, replace ρ by $q_m \rho$.)

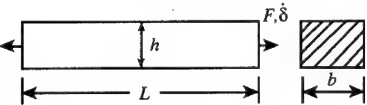
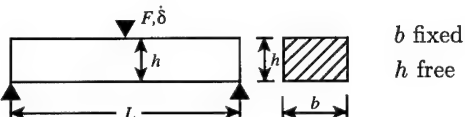
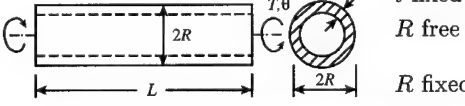
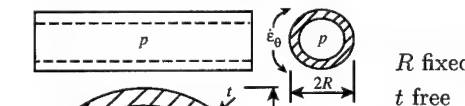
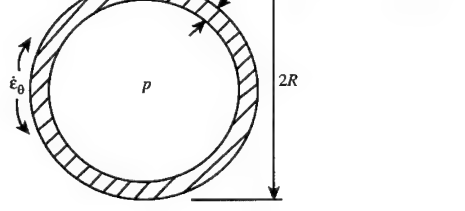
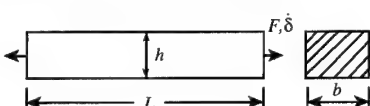
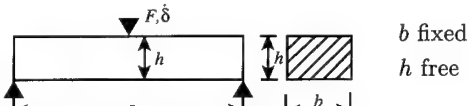
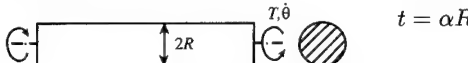
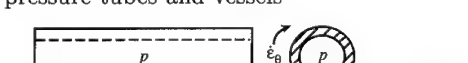
mode of loading	geometry	design strength	index
tension; centrifugal loading			
		$\sigma_D = \sigma_{f0} \left(\frac{t_{f0}}{t_f} \right)^{1/q}$	$M = \sigma_D / \rho$
bending			
	$b = \alpha h$	$\sigma_D = \sigma_{f0} \left(\frac{t_{f0}}{t_f} \right)^{1/q}$	$M = \sigma_D^{2/3} / \rho$
		h fixed h free	$M = \sigma_D^{1/2} / \rho$
	h fixed b free		$M = \sigma_D / \rho$
torsion			
		$t = \alpha R$	$\sigma_D = \sigma_{f0} \left(\frac{t_{f0}}{t_f} \right)^{1/q}$
		t fixed R free	$M = \sigma_D^{2/3} / \rho$
		R fixed t free	$M = \sigma_D^{1/2} / \rho$ $M = \sigma_D / \rho$
pressure tubes and vessels			
		R fixed t free	$\sigma_D = \sigma_{f0} \left(\frac{t_{f0}}{t_f} \right)^{1/q}$
			$M = \sigma_D / \rho$

Table 3. Creep relaxation

(Time to relax to $\frac{1}{2}F_i$ or $\frac{1}{2}T_i$ ('life') = t_r ; $n \gg 1$. To minimize cost, replace ρ by $C_m\rho$ in the expressions for M ; to minimize energy content, replace ρ by $q_m\rho$.)

mode of loading	geometry	design strength	index
tension; centrifugal loading		any b and h $\sigma_D = \sigma_0 \left(\frac{\sigma_0}{E\dot{\epsilon}_0 t_r} \right)^{1/n-1}$	$M = \sigma_D / \rho$
bending		$b = \alpha h$ $\sigma_D = \sigma_0 \left(\frac{\sigma_0}{E\dot{\epsilon}_0 t_r} \right)^{1/n-1}$	$M = \sigma_D^{2/3} / \rho$
			$M = \sigma_D^{1/2} / \rho$
		h fixed b free	$M = \sigma_D / \rho$
torsion		solid R free $t = \alpha R$ $\sigma_D = \sigma_0 \left(\frac{\sigma_0}{2\sqrt{3}\pi\dot{\epsilon}_0 G t_r} \right)^{1/n-1}$	$M = \sigma_D^{2/3} / \rho$
		t fixed R free $\sigma_D = \sigma_0 \left(\frac{R\dot{\Theta}}{\sqrt{3}L\dot{\epsilon}_0} \right)^{1/n}$	$M = \sigma_D^{1/2} / \rho$
		R fixed t free	$M = \sigma_D / \rho$
pressure tubes and vessels		R fixed t free $\sigma_D = \sigma_0 \left(\frac{\dot{R}}{R\dot{\epsilon}_0} \right)^{1/n}$	$M = \sigma_D / \rho$
			

Equation (4.6) looks messy, but it is not as bad as it seems. We examine first the fully plastic limit, found by setting $n = \infty$. The equation now simplifies to

$$m = \rho L \alpha^{1/3} (4FL/\sigma_D), \quad (4.8)$$

which is identical with (2.6) if σ_D is replaced by σ_y . The design strength in creep, then, plays the same role as the yield strength in room-temperature plasticity. In fact, (4.8) is a good approximation to the more complex result of (4.6) over the entire range of values of the exponent n ($3 < n < 20$) normally encountered in metals and alloys. Inspection shows that the mass is minimized by maximizing the index M_2 given earlier (equation (2.2)) with ρ replaced by (remember that contains temperature and deflection rate).

A parallel calculation for a panel (flat plate in bending) gives (2.3), again with σ_y replaced by σ_D , appropriately defined. Similar expressions are derived for torsion and for internal pressure (tables 1-3). Selection with the objective of minimizing cost rather than weight lead to identical results with ρ replaced by $C_m \rho$, where C_m is the material cost per kilogram; and the objective of minimizing energy content is achieved by replacing this by $q_m \rho$, where q_m is the energy content per kilogram.

(b) Fracture-limited design

Consider next an application in which fracture, not deflection rate, is design limiting (figure 1b). For a bending beam the largest stresses appear, and creep fracture starts, in the outer fibres at the place where the bending moment M is greatest (figure 2c). The time t to the onset of failure of the cantilever, using the constitutive relation of (3.3), is

$$t = t_{fo} \left(\frac{2q+1}{2q} \frac{4FL}{\sigma_{fo} b h^2} \right)^q. \quad (4.9)$$

Writing $b = \alpha h$, solving for the area $A = bh$ and substituting in (2.4) gives

$$m = \rho L \alpha^{1/3} \left[\left(\frac{2q+1}{2q} \right) \frac{4FL}{\sigma_D} \right]^{2/3}. \quad (4.10)$$

with the design strength

$$\sigma_D = \sigma_{fo} (t_{fo}/t)^{1/q}. \quad (4.11)$$

The parallel with deflection-limited design is obvious; and once again the result reduces to that for full plasticity in the limit $q = \infty$. The mass is minimized, as before, by maximizing the index of (2.2), with σ_y replaced by this new, fracture-related σ_D which depends on design life, t , and on temperature, T . Analogous calculations for ties and panels give (2.1) and (2.3) again; only the definition of σ_D is different. Similar expressions describe torsion and internal pressure (table 1), and are modified for cost or energy content by replacing ρ by $C_m \rho$ or $q_m \rho$, as before.

(c) Relaxation-limited design

A tensile cable or a bolt, pretensioned to provide a bearing or clamping force F at an elevated temperature, relaxes with time by creep. The calculation is a standard one; elastic strain σ/E is replaced over time by creep strain. The total change in strain in the cable or bolt is zero, since its ends are fixed. The governing

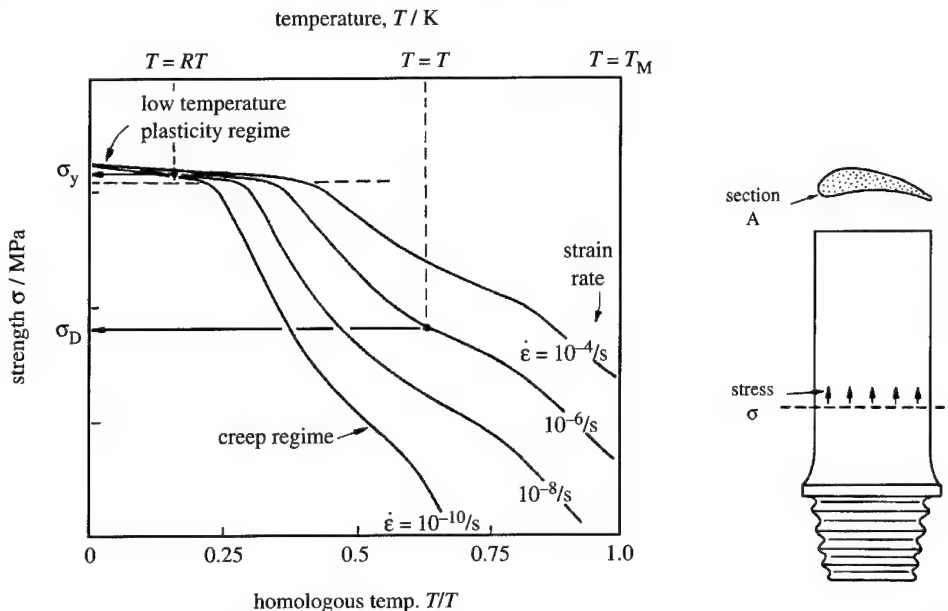


Figure 5. The strength, at room temperature, is measured by the yield strength σ_y , which has a small temperature dependence that is often ignored. At high temperatures, the strength σ_D depends strongly on temperature and strain rate.

Figure 6. A turbine blade.

equation for the stress in the component was given earlier as (3.4). Integrating this with the boundary condition $\sigma = \sigma_i$ at $t = 0$, gives

$$\left(\frac{\sigma_0}{\sigma}\right)^{n-1} - \left(\frac{\sigma_0}{\sigma_i}\right)^{n-1} = (n-1) \frac{E\dot{\epsilon}_0 t}{\sigma_0}, \quad (4.12)$$

where σ_i is the stress to which the cable or bolt was originally tightened, and σ is the stress to which it has relaxed in time t . In this case a constraint is specified by defining a characteristic relaxation time, t_r , as the time required for the stress to relax to a specified fraction of its initial value. Inverting (4.12) gives:

$$t_r = \left[1 - \left(\frac{\sigma}{\sigma_i} \right)^{n-1} \right] \frac{\sigma_0^n}{(n-1)E\dot{\epsilon}_0 \sigma^{n-1}}. \quad (4.13)$$

We take this fraction σ/σ_i , to be 0.5, for the purpose of illustrating the method. The result is independent of the choice of value. For $n > 3$ the term in square brackets is then close to unity; for simplicity we shall neglect it. The design specifies the minimum bearing or clamping load F . Writing $\sigma = F/A$, and substituting for A in (2.4), gives the mass of the cable or bolt which will safely provide a clamping load greater than F for a life t_r :

$$m = L\rho F/\sigma_D \quad (4.14)$$

with

$$\sigma_D = \sigma_0 \left(\frac{\sigma_0}{(n-1)E\dot{\epsilon}_0 t_r} \right)^{1/(n-1)}. \quad (4.15)$$

The mass is minimized by selecting the material with the greatest value of σ_D/ρ , that is, the material index is once more that of (2.1) with σ_y replaced by this new σ_D .

Springs, too, relax their tension with time. Most are loaded in bending, when the constitutive behaviour is that of (3.5). Taking a beam of length L as an example, we write, for the stiffness S :

$$S = C_2 EI/L^3, \quad (4.16)$$

where I is the second moment of its area and C_2 is a constant. Integrating with the boundary conditions $F = F_i$ at $t = 0$ gives a result with the form of (4.12). Proceeding as before, we find for the minimum weight design of a leaf spring (or any spring loaded in bending), which must not relax its restoring force in time t_r at temperature T , the index M_2 of (2.2), with σ_D (when $n > 3$) given by

$$\sigma_D \approx \sigma_0 \left(\frac{\sigma_0}{E\dot{\epsilon}_0 t_r} \right)^{1/(n-1)}. \quad (4.17)$$

Table 1 lists results for other modes of loading. Similar calculations for ties and panels give (2.1) and (2.3) again; only the definition of σ_D is different. The earlier adaptations to cost or energy apply here too.

5. The selection procedure

Expressions for the indices M and the associated design strengths σ_D are summarized in table 1. The close parallel between these results and those for room temperature plasticity (equations (2.1), (2.2) and (2.3)) suggests a selection procedure. The design temperature T and acceptable deflection rate $\dot{\delta}$, or life t , or relaxation time t_r are identified. Using this information, values for the appropriate σ_D are calculated from a database of creep properties for materials (it is necessary to cap the value of σ_D at the value σ_y to allow for the change of deformation mechanism to yielding at low temperatures). These are used to construct a chart of $\log(\sigma_D)$ against $\log(\rho)$; it is the creep equivalent of figure 3, but is specific to the particular temperature, deflection rate or life required by the design since these appear in the definition of σ_D . The indices M_1 , M_2 and M_3 can be plotted onto it, allowing optimum selection for each application.

The easiest way to see how all this works is through examples. Those of the next section are deliberately simplified to avoid unnecessary digression. The method remains the same when the complexity is restored.

6. Specific applications

The examples below illustrate the selection of materials for structures loaded at elevated temperatures, and which are limited by deflection, by fracture or by stress relaxation. The selection is based on a single criterion: that of best dealing with one or other of these creep-related limits. Many other considerations enter the selection of materials for high-temperature use: resistance to oxidation, to thermal shock, and so on. Here we consider the selection for the initial shortlist, to which these other considerations can then be applied.

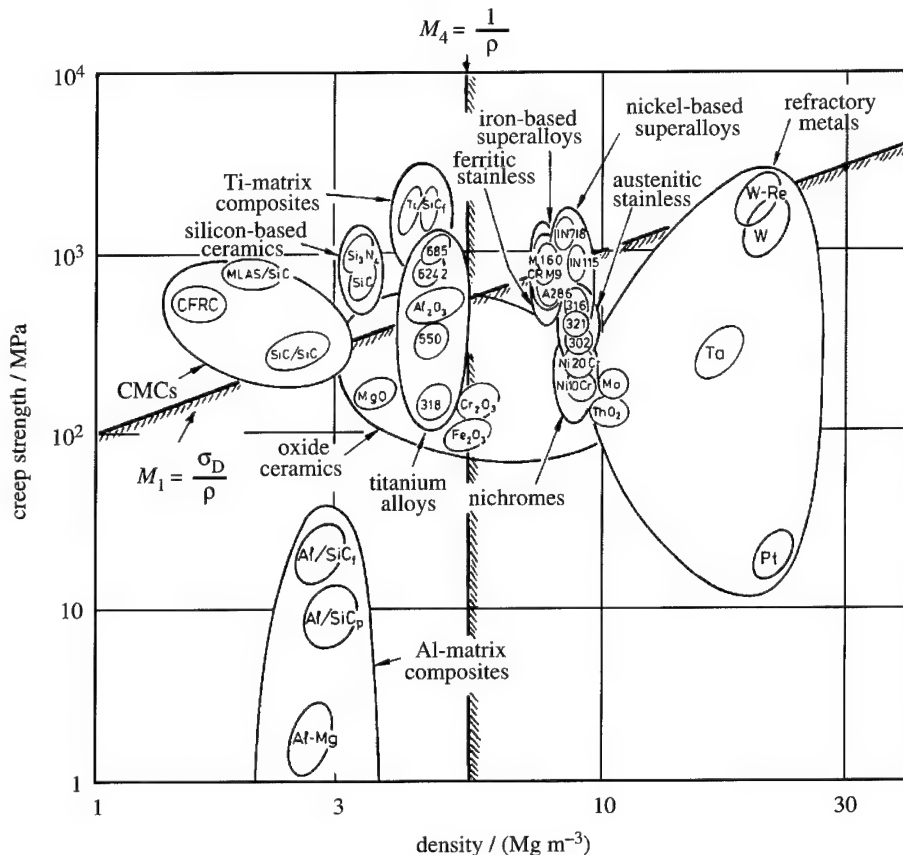


Figure 7. A selection chart for deflection-limited design at 400 °C for a life of 1000 h.

(a) *Fan and turbine blades for gas turbines*

A rotating blade of an aircraft turbine is self-loaded (figure 1a and 5); the centrifugal force caused by its own mass is much larger than that exerted by the gases which propel it. Adiabatic compression of the intake air can heat the compressor-fan blade to 400 °C or more. The dominant mode of steady loading, therefore, is tensile, and proportional (for fixed blade proportions) to the density of the material of which the blade is made. It could, then, be anticipated that the appropriate index is that for tensile loading, M_1 of (2.1), with the design strength for tensile loading, (4.3). More detailed analyses add complexity, but confirm this result (Able & Ashby 1994). The turbine blade is loaded in the same way, but is hotter: designers would like to go to 1000 °C. Concepts for new turbines push this temperature to 1500 °C. The task is to select materials to maximize the safe angular velocity of the fan or turbine blade, designed to operate for a life $t = 1000$ h without extending by more than δ , which is required to be 1.0% of its length, for each of these temperatures, and at the same time to minimize the weight.

The profile and section are determined by the blade design; neither is free. The mass is minimized by minimizing

$$M_4 = 1/\rho. \quad (6.1)$$

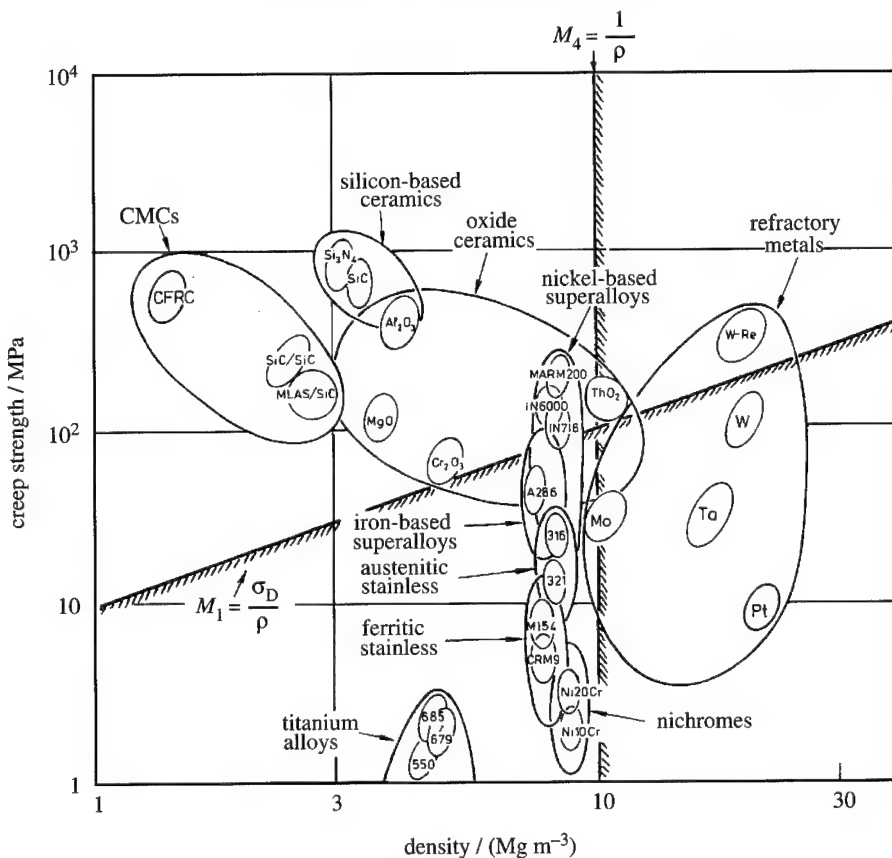


Figure 8. A selection chart for deflection-limited design at 1000 °C for a life of 1000 h.

Table 4. Materials for fan blades at 400 °C

material	comment
Ti-matrix composites (Ti/SiC _f)	the ultimate in performance, but very expensive
Ti alloys (e.g. Ti 685, 6242)	high creep strength and low density makes these the best choice
Ni-based superalloys (e.g. IN738)	excellent creep strength, but both indices M_1 and M_4 inferior to Ti alloys
iron-based superalloys, stainless steels	less good than nickel-based alloys, but cheaper
ceramics and CMCs	excellent values of M_1 and M_4 but brittleness is a problem

Figures 6, 7 and 8 show σ_D , calculated for 400 °C, 1000 °C and 1500 °C, with a value of δ/L and T corresponding to the design specification, plotted against density, ρ . Selection lines plotting the appropriate indices are shown. The selections are listed in tables 4, 5 and 6.

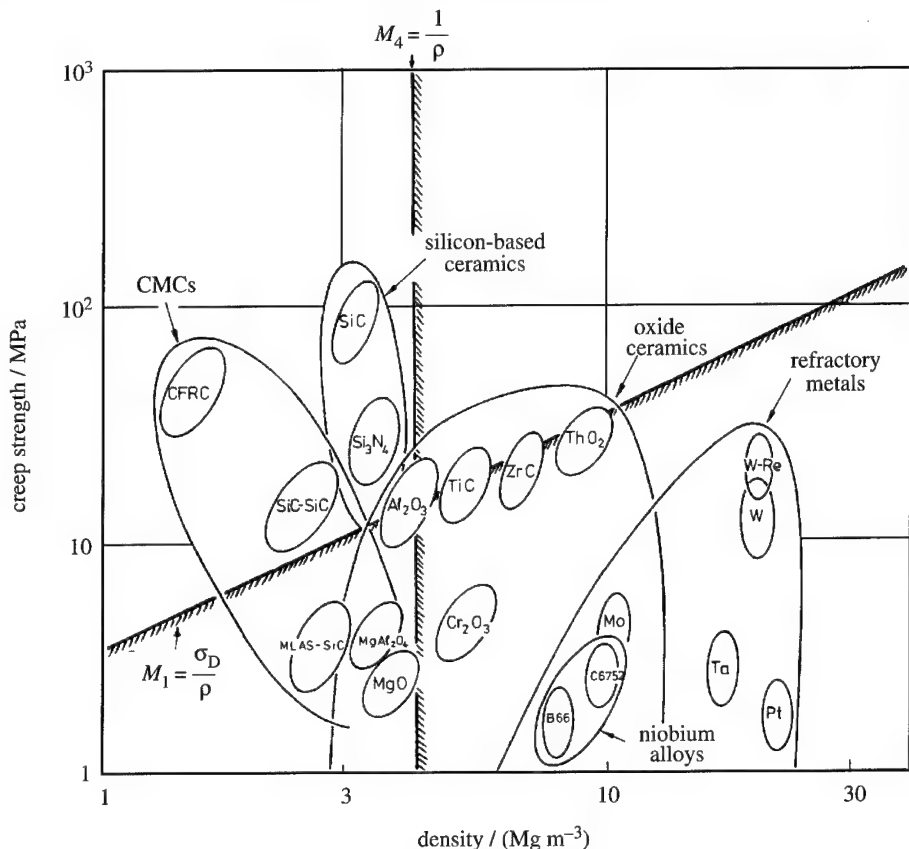


Figure 9. A selection chart for deflection-limited design at 1500 °C for a life of 1000 h.

Table 5. Materials for fan blades at 1000 °C

material	comment
Ni-based superalloys	among metallic alloys, these have the highest values of M_1 , but heavy
refractory metals	W-Re alloys offer high M_1 but very heavy
oxide ceramics and silicon-based ceramics, CMSs	large weight saving possible if design can accommodate brittleness

7. Summary and conclusions

A design-led procedure is proposed for the selection of materials to resist creep deflection, creep fracture, buckling and stress relaxation. It is an extension of a successful procedure for room temperature design which couples performance indices with materials-selection charts to identify an optimum subset of candidate materials for a given design. The extension requires the definition of a 'design strength', σ_D , which characterizes material response under conditions imposed by the design: the temperature, and the acceptable creep deflection, life or relaxation

Table 6. Materials for fan blades at 1500 °C

material	comment
oxide and silicon-based ceramics (SiC, Al ₂ O ₃)	offer high values of M_1 and M_4 but design must accommodate brittleness
refractory metals	W-Re creep resistant, but heavy
ceramic composites (SiC-SiC; carbon-carbon)	potential for gains in performance, but brittleness and chemical stability require attention

time. Materials are ranked by an optimization procedure which combines σ_D with other properties (such as density, or cost, or stiffness) to isolate the subset which best meet the design specification.

The paper concludes with examples of the application of the method, which, when implemented in software, gives an efficient way of identifying promising candidates for a wide range of creep-limited application.

This work was supported by the Defence Advanced Research Project Agency through the University Research Initiative under Office of Naval Research Contract No. N-00014-92-J-1808.

References

Abel, C. A. & Ashby, M. F. 1994 Materials selection to resist creep and creep rupture. Report CUED/C-EDC/TR18, June, pp. 1-32. Engineering Department, Cambridge University.

Ashby, M. F. 1992 *Materials selection in mechanical design*. Oxford: Pergamon Press.

Cebon, D. & Ashby, M. F. 1992 Computer-aided materials selection for mechanical design. *Metals Mater.*, pp. 25-30.

CMS Software, Granta Design, 20 Trumpington Street, Cambridge CB2 1QA, UK.

Crane, F. A. A. & Charles, J. A. 1984 *Selection and use of engineering materials*. London: Butterworths.

Evans, R. W. & Wilshire, B. 1985 *Creep of metals and alloys*. London: The Institute of Metals.

Finnie, I. & Heller, W. R. 1959 *Creep of engineering materials*. New York: McGraw-Hill.

Frost, H. J. & Ashby, M. F. 1982 *Deformation mechanism maps*. Oxford: Pergamon Press.

Gittus, J. 1975 *Creep, viscoelasticity and creep fracture*. London: Elsevier.

Hult, J. 1966 *Creep in engineering structures*. London: Baisdell Press.

Penny, R. K. & Marriott, D. L. 1971 *Design for creep*. Boston, MA: McGraw-Hill.

Discussion

M. J. GOULETTE (*Rolls-Royce plc, Derby, UK*). The linkage of design systems and materials selector proposed by Professor Ashby may not be useful for final designs of gas turbines because the choice of materials for a specific component is very limited at this stage. It should prove to be useful, however, at earlier stages in the technology acquisition processes when choices have to be made about which competing material systems will be scaled up and fully characterized. At this stage the design linkage is vital so that choices which are correct both technically and commercially can be made.

M. F. ASHBY. I agree; the procedure outlined here helps with the early stages of the design process.

A. COTTRELL (*Department of Materials Science, University of Cambridge, UK*). It seems to me that Professor Ashby's excellent system for inter-relating material properties with engineering design, could be useful particularly for the designer who is aiming at revolutionary new engineering systems, as for example when the gas turbine was introduced in place of the piston engine, because with such radically new and unexplored engineering it will be important to know what materials might be most useful and there may be no previous experience in these cases to guide the design engineer. Professor Ashby's logical system of analysis would be a good way of making initial entries into such pioneering and unexplored fields.

G. A. WEBSTER (*Department of Mechanical Engineering, Imperial College, London, UK*). I would like to relate Professor Ashby's procedure for selecting materials to resist creep deformation and failure to Professor McLean's remarks about there being significant scope for engineering exploitation in achieving optimum high-temperature designs. Professor Ashby illustrated the procedure using components of fixed dimensions. It may be possible to further refine materials choice by allowing the component dimensions to be altered. For example, turbine blades could be tapered and different disc profiles examined. Is it possible to incorporate these features into the selection procedure?

M. F. ASHBY. Coupled selection of material and shape is possible: see Ashby (1992).

Reliability of structural ceramics

BY M. KNECHTEL¹, N. CLAUSSEN¹ AND J. RÖDEL²

¹*Advanced Ceramics Group, ²Ceramics Group, Technische Hochschule
Darmstadt, D-64295 Darmstadt, Germany*

In this study the influence of *R*-curve effects on reliability are investigated assuming natural flaws as being peripherally cracked spherical voids. Various experimental literature as well as own results are presented, including Al_2O_3 , Si_3N_4 , ZrO_2 and Al reinforced Al_2O_3 .

1. Introduction

A variety of engineering ceramics can be used for structural applications such as silicon carbide for heat exchangers, silicon nitride for turbochargers, zirconia for extrusion dies and alumina for cutting tools. For their commercial use, good mechanical reliability and predictable performance is required, especially when designed for engine or turbine components where failure of a part may cause fatal damage of the whole device. Although numerous extrinsic and intrinsic reinforcing mechanisms have been developed to diminish the brittleness of ceramic materials the fracture toughness of most ceramics does not exceed values of $10 \text{ MP am}^{1/2}$. However, the application of sophisticated processing techniques, limiting typical flaw sizes and inhomogeneities to a micrometre scale, allows attainment of high flexural strengths up in the GPa range. The limited resistance to crack propagation imparts a sensitive strength dependence of ceramics on defect population. Thus, in contrast to fracture toughness, strength is a statistical property which is mathematically described by the well-known Weibull distribution function. This article examines the efficiency of various reinforcing mechanisms in enhancing the reliability of structural ceramics.

2. Fracture mechanics background

(a) Weibull distribution function

Since the brittleness of ceramics implies that stress concentrations can not be relieved via plastic flow, the largest flaw is the failure site of the material. In this context, the fracture is induced by an applied stress that causes a stress intensity factor at the largest flaw higher than the critical value (K_{Ic}) of the material. Thus the most appropriate statistical description is the weakest link model, from which a three parametric strength distribution function, at first introduced by Weibull based on a heuristic approach (Weibull 1951), can be derived (Freudenthal 1968):

$$P(\sigma) = 1 - \exp \left\{ - \left(\frac{\sigma - \sigma_u}{\sigma_0} \right)^m \right\}. \quad (2.1)$$

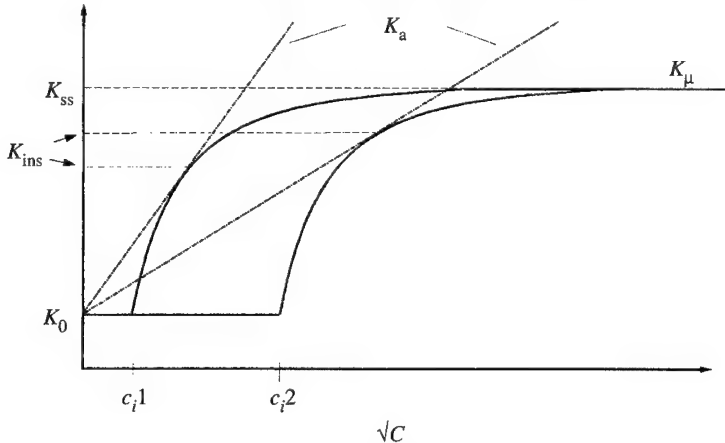


Figure 1. Schematic R-curves starting at two different penny-shaped cracks of length c_i1 and c_i2 .

The probability of fracture (P) at a stress level (σ) is determined by the threshold stress (σ_u), below which no fracture occurs, a scaling parameter (σ_0) and a shape parameter (m). σ_0 is usually called the characteristic stress and m the Weibull modulus. In nearly all practical cases σ_u can be set to zero resulting in a two parametric distribution. Various numerical techniques can be applied (Bergmann 1986; Dortmanns & de With 1991; Steen *et al.* 1992) determining the shape and scaling parameter from a given number N of specimens tested with the maximum likelihood method being the most reliable one. As an estimator (h_i) for the failure probability of i th ranked sample, a widely used and efficient expression is $(i - 0.5)/N$.

(b) Influence of R-curve effects on strength variability

It has been pointed out by previous authors that the existence of a rising crack-growth resistance, i.e. R-curve behaviour, leads to a narrowing of strength distribution (Cook & Clarke 1988; Shetty & Wang 1989). The basic mechanism reducing the effect of flaw size in R-curve materials is due to stable crack growth before fracture. Crack advancement occurs when the applied stress intensity (K_a) equals the crack tip toughness (K_0) which is independent on initial crack length c_i . However, the point of unstable propagation (K_{ins}), where the crack resistance of the material (K_μ) increases less than K_a with further crack extension, is shifted higher up the R-curve with increasing c_i (figure 1). Thus toughness at instability is increased with rising flaw size which imparts a diminished strength sensitivity on c_i . The impact of a rising crack resistance on strength distribution becomes less pronounced if the extent of stable crack growth is limited by a steep initial slope of the R-curve. The same is true for very shallow R-curves that reach their plateau value at extremely large crack lengths, which are far beyond the instability point.

Various experimental results support the fact that materials exhibiting pronounced R-curve behaviour reveal a narrow strength distribution. Improved flaw tolerability has been reported for transformation toughened zirconia (Kendall *et al.* 1987; Ready *et al.* 1993) which is well known for its crack-growth resistance. The dependence of strength distribution on R-curve has been pointed out for

ceria-stabilized zirconia (Pross *et al.* 1992) as well as magnesia-stabilized zirconia (Ramachandran *et al.* 1993). A significant reduction of Weibull modulus was observed when bend tests were carried out above the transformation temperature. A decrease of m from 92 down to a value of 9 was reported for Ce-TZP when tested at room temperature and 600 °C respectively (Hartsock & McLean 1984) and a reduction of a value of 20 in Mg-PSZ by a factor of 2 when tested at 400 °C (Ramachandran *et al.* 1993). Other examples are metal infiltrated ceramics where m is increased by a factor of two when compared to the porous preform (cf. ch. 4.4) or coarse-grained silicon nitride that exhibits higher m values when compared to the fine-grained material (Dressler 1993).

The following ceramic materials will be classified with respect to different mechanisms of strength control and the validity of these above mentioned correlations will be critically examined.

3. Theoretical evaluations and predictions

Determining the strength of a composite containing flaws requires the knowledge of flaw geometry, loading configuration and the stress-displacement relation of the reinforcing phase. As proposed by several authors (Evans & Davidge 1970; Rice 1984; Uematsu *et al.* 1993), natural flaws can be assumed as being spherical voids of radius r with a circumferential crack of length L (figure 2). For this case the fracture mechanical weight function under uniform loading conditions has been presented in the literature (Fett 1994). Besides the fact that experimental data can be reasonably well explained, it allows the accurate description of model composites containing spherical voids (Chao & Shetty 1992). Calculating the R -curve for an arbitrary stress-displacement relation of the reinforcing phase requires the knowledge of the crack opening displacement. This can be obtained from numerically solving an integral equation (Uematsu *et al.* 1993). In some special cases these integral equations exhibit a particularly simple form, especially if the bridging stresses remain constant at any crack length. Then an analytical expression for the crack resistance curve $K_\mu(c)$ can be derived:

$$K_\mu(c) = K_0 + p_{\max} \beta(c, r) \sqrt{\frac{2}{\pi}} \left(2\sqrt{(c-d)} + 0.4098 \frac{\sqrt{(c-d)^3}}{c} + 0.1001 \frac{\sqrt{(c-d)^5}}{c^2} + 1.4142(1 - \beta(c, r)) \frac{\sqrt{[(c+d)^2 - (d+r)^2]}}{\sqrt{(c+r)}} \right), \quad (3.1)$$

$$\beta(a, r) = (1 + c/r)^{-2}, \quad (3.2)$$

where K_0 is the crack tip toughness, p_{\max} the closure stress and d the mean distance between the reinforcing elements, i.e. the crack length at which the R -curve starts from a pore of radius r . Usually the length of the circumferential crack is estimated to be of the order of a few grains (e.g. 10 µm).

For a typical monolithic alumina ceramic with a mean strength and fracture toughness of 400 MPa and 3.5 MP am^{1/2} respectively, the application of Baratta's solution (Baratta 1981) for the stress intensity factor yields a value of 20 µm for r . Figure 3 shows resulting R -curves for an unbridged crack length of 5 µm in a range of crack lengths relevant for strength determination. The crack resistance curves were calculated for two bridging stresses. One R -curve is shown for a p_{\max}

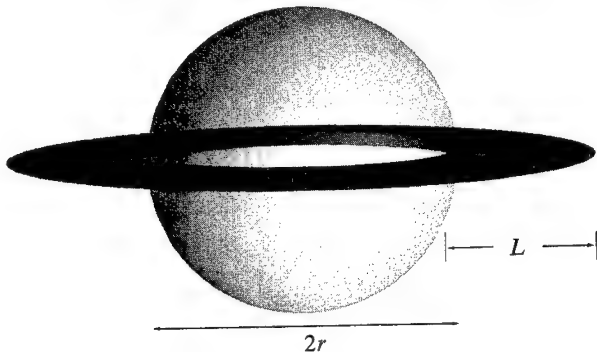


Figure 2. Natural flaw modelled as a spherical void of radius r and circumferential crack of length L .

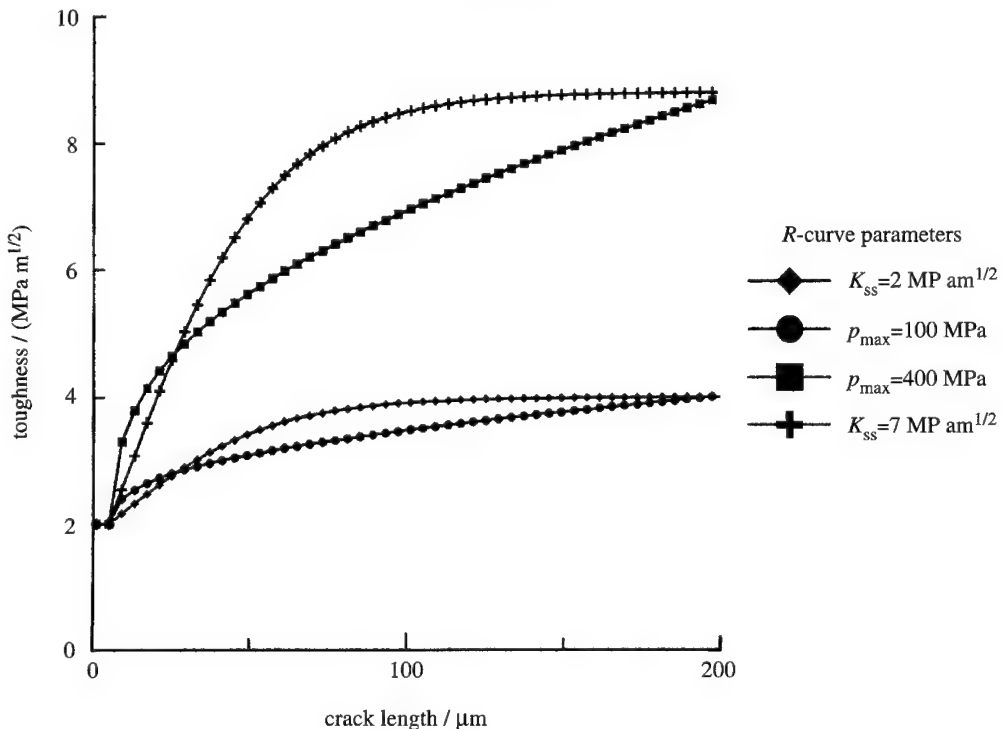


Figure 3. R -curves according to (3.2) (solid line) and (3.3) (solid line with rectangles) starting from a flaw as shown in figure 2 with radius of 20 μm and unbridged crack length of 5 μm .

of 100 MPa which corresponds to typical bridging stresses exerted by interlocking grains in alumina. Another crack resistance curve is shown for a bridging stress of 400 MPa, which results in a crack-growth resistance similar to silicon nitride (Schneider & Petzow 1994). The assumption of a Dugdale zone (i.e. constant bridging stresses) implies that the R -curve rises monotonically for any crack length. This can be used as a reasonable approximation, since some R -curve materials, like alumina, attain their steady-state toughness at a crack length far beyond the instability point. However, some materials such as silicon nitride can exhibit R -curves with very short bridging lengths where the plateau toughness is reached in the 100 μm range (Schneider & Petzow 1994). To take this fact into

account, a hypothetical R -curve was designed according to:

$$K_{\text{hyp}}(c) = K_0 + K_{\text{ss}} \tanh\left(\frac{c - c_{\text{in}}}{c_{\text{max}}}\right) \Phi(c - c_{\text{in}}), \quad (3.3)$$

where K_{ss} is the steady-state toughness at the plateau of the R -curve, c_{max} a bridging length parameter, c_{in} the initial flaw size and Φ the Heavyside step function, which equals unity for positive and zero for negative arguments. The corresponding R -curves of (3.3) with plateau toughness of 2 and 7 MP am^{1/2} are shown in figure 3.

For the monolithic material the dependence of strength on flaw size c is given by Griffith's equation:

$$\sigma_b = Y K_{\text{Ic}} / \sqrt{c}, \quad (3.4)$$

with K_{Ic} being the critical stress intensity factor and Y a numerical factor dependent on flaw geometry. Assuming strength being distributed according to the two parametric Weibull function and the peripheral crack length to be constant, the distribution of sphere sizes can be expressed as

$$P(r) = 1 - \exp[-(r_0/r)^{m/2}], \quad (3.5)$$

with r_0 being a characteristic radius. The numerical solution of the equations for unstable crack propagation,

$$K_a = K_\mu \quad \text{and} \quad \frac{dK_a}{dc} \geq \frac{dK_\mu}{dc}, \quad (3.6)$$

results in a strength distribution as depicted in figure 4, where the R -curves of (3.2) and (3.3) were used with the parameters according to figure 3. Included in this plot is the strength distribution for the unreinforced material. In the case of the material exhibiting a rising crack resistance the strength distribution shows a rather linear relation for limited R -curve effects, but deviation from the Weibull distribution becomes more pronounced for higher crack resistance. From the strength distributions for a set of 25 samples calculated with various bridging stresses, a linear regression was applied to obtain m and σ_0 . The result of this calculation shows an increase of m and σ_0 with increasing bridging stresses and plateau toughness respectively (figure 5a, b). The R -curve for constant bridging stresses (p_{max}) exhibits a steeper slope at short crack lengths making it less efficient in increasing reliability at low p_{max} . However, when p_{max} rises above a certain value, e.g. 600 MPa, the amount of stable crack growth becomes less limited and the m values exceed even those of the hypothetical R -curve. In that regime the deviation from the Weibull distribution becomes more pronounced, making its applicability questionable. In a similar manner, the characteristic strength of the Dugdale type R -curve is lower than the one of the hypothetical R -curve but experiences a higher increase with closure stresses above 350 MPa. It should be pointed out that the absolute values for m and σ_0 depend on the special choice of the characteristic sphere radius r_0 , e.g. the Weibull modulus at 600 MPa closure stresses is enhanced by roughly a factor of two when r_0 is increased from 20 to 30 μm , whereas the characteristic stress is reduced by 30%.

These results, which involve sample numbers common in testing on a laboratory scale may be insufficient from the manufacturer's point of view. Particularly in cases where large numbers of components are involved the probability of very

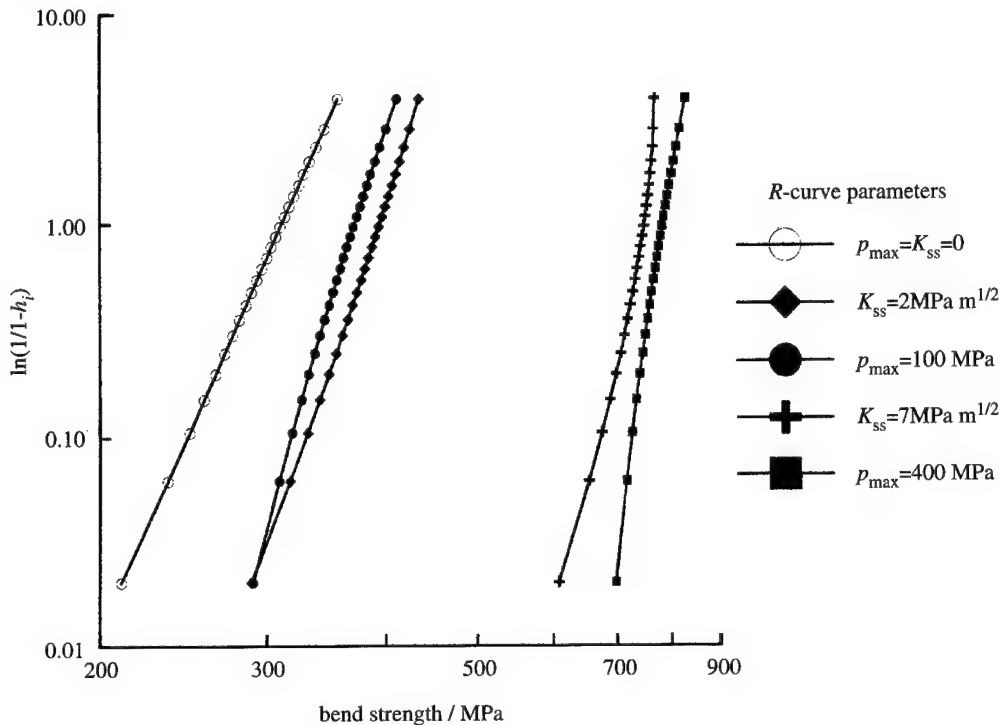


Figure 4. Strength distribution calculated for a sphere size distribution according to (3.4) without *R*-curve effects (open circles) and with *R*-curves of figure 3.

large flaw sizes increases. For these large flaws, instability occurs at large crack lengths where the *R*-curve flattens and does not lead to an effective strength enhancement. A calculation for fracture probabilities down to 1 in 10^7 demonstrates the deviation from the Weibull distribution (figure 6).

The fact that the slope of the strength values for the constant-bridging stress case is increased at low fracture probability is due to two facts. One is that the defect model of a peripherally cracked spherical void exhibits the deficiency that strength dependence on applied load is diminished asymptotically at high r/d ratios, i.e. for large pore radii if the circumferential crack length is kept constant (figure 7, where r_{\max} corresponds to a fracture probability of 10^{-7}). The other is the monotonic increase of K_{μ} which leads to unrealistic crack lengths at instability.

4. Case studies

(a) Alumina: defect controlled reliability

The reliability and strength of monolithic alumina ceramics can be effectively improved with a large variety of advanced processing techniques, such as slip, pressure and centrifugal casting as well as numerous other sophisticated powder processing techniques. Due to mechanically interlocked grains, alumina exhibits rising crack resistance that increases with grain size (Chantikul *et al.* 1990) and achieves values as high as $6 \text{ MPa m}^{1/2}$ at crack extensions of several millimetres (Steinbrech *et al.* 1990). Nevertheless no significant dependence of Weibull mod-

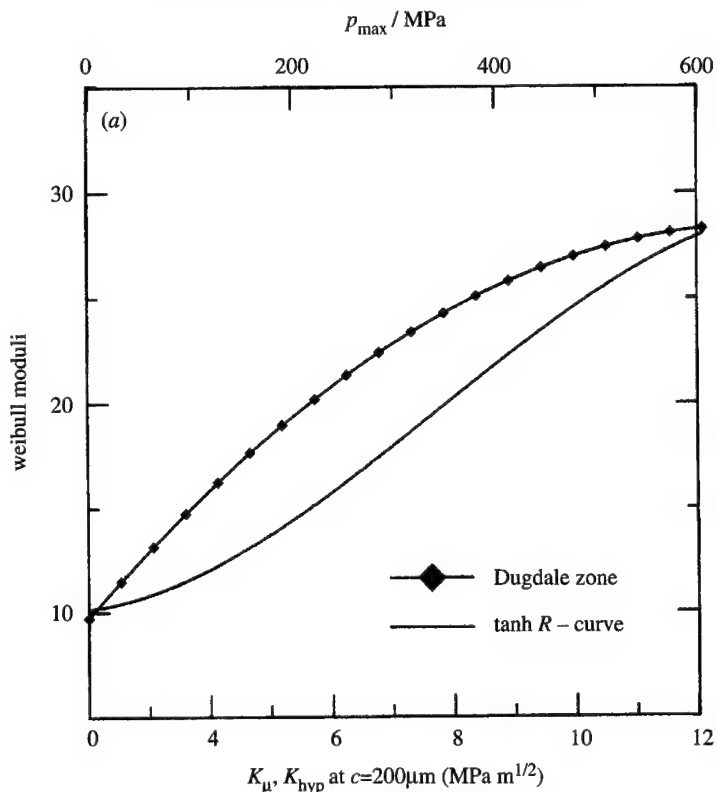


Figure 5. (a) Weibull moduli calculated for a set of 25 samples applying R -curves according to (3.2) and (3.3) as a function of crack resistance values at 200 μm crack length and closure stresses respectively.

ulus on grain size can be observed (figure 8) (Seidel *et al.* 1995). The R -curve of (3.2) was used by Seidel *et al.* to model the experimental results with reasonable agreement. Due to the moderate bridging stresses present in alumina (ranging between 30 and 120 MPa), the R -curve is too shallow to provide a significant narrowing of strength distribution.

(b) Silicon nitride: defect/ R -curve controlled reliability

A relatively high fracture toughness value for silicon nitride containing rod-shaped grains was reported by Lange more than 20 years ago (Lange 1973). R -curve measurements on silicon nitride using radial indentation cracks have demonstrated that the toughness rises from $4.3 \text{ MP am}^{1/2}$ at a crack length of 50 μm to $9 \text{ MP am}^{1/2}$ at 600 μm for the particular material investigated (Li *et al.* 1992). Since fine-grained silicon nitride has a fracture toughness of $1.8 \text{ MP am}^{1/2}$, it was speculated that the crack tip toughness for the R -curve material may still lie well below $4 \text{ MP am}^{1/2}$ (Rödel 1992), which would necessitate a steeply rising crack resistance for the regime of very short cracks. Silicon nitride with strong R -curve should therefore be a prime candidate for low strength variability due to stable crack growth.

A frequently quoted result for a high Weibull modulus is described by Dressler (1993). In figure 9 the strength distribution for a fine grained silicon nitride (sin-

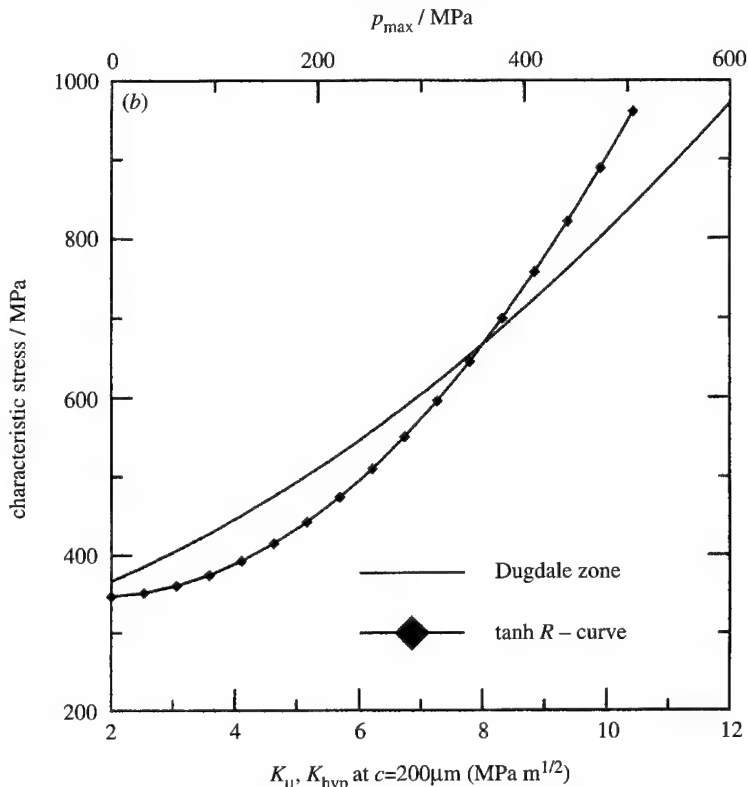


Figure 5. (b) Characteristic stresses calculated for a set of 25 samples applying R -curves according to (3.2) and (3.3) as a function of crack resistance values at 200 μm crack length and closure stresses respectively.

tered at 0.14 MPa N_2 for 20 min at 1780 $^{\circ}\text{C}$ and tempered at 1835 $^{\circ}\text{C}$ for 30 min at 10 MPa N_2) is compared to a coarse-grained silicon nitride (same sintering conditions, but tempering at 1900 $^{\circ}\text{C}$ for 6 h at 10 MPa N_2). The coarse-grained material has a very high Weibull modulus (46), but a comparatively low strength (902 MPa), whereas the fine-grained material has a mean strength of 1134 MPa and an m value of 14. The Weibull modulus appears to be a result of a general weakening of the material with the strongest specimen seeing a comparatively high strength reduction. This supposition is supported by the fact that the fracture origin in the fine-grained Si_3N_4 shifted from pores to large grains in the coarse-grained material (Dressler 1993). While an increasing grain diameter leads to an increase in steady-state toughness (Dressler 1993), but not in slope of the R -curve, we suggest that this increase in m with coarsening treatment is predominantly due to a change in defect population with a minor contribution arising from the change of R -curve behavior with microstructural scale.

(c) Zirconia: plasticity/ R -curve controlled reliability

According to Swain & Rose (1989), transformation toughened zirconia shows either transformation or R -curve limited strength or a combination of both. A plot of strength versus peak toughness exhibits therefore a maximum at intermediate toughness values where the transformation has not lead to premature microcrack formation, but provides a strength enhancing steep R -curve (Swain & Rose 1989).

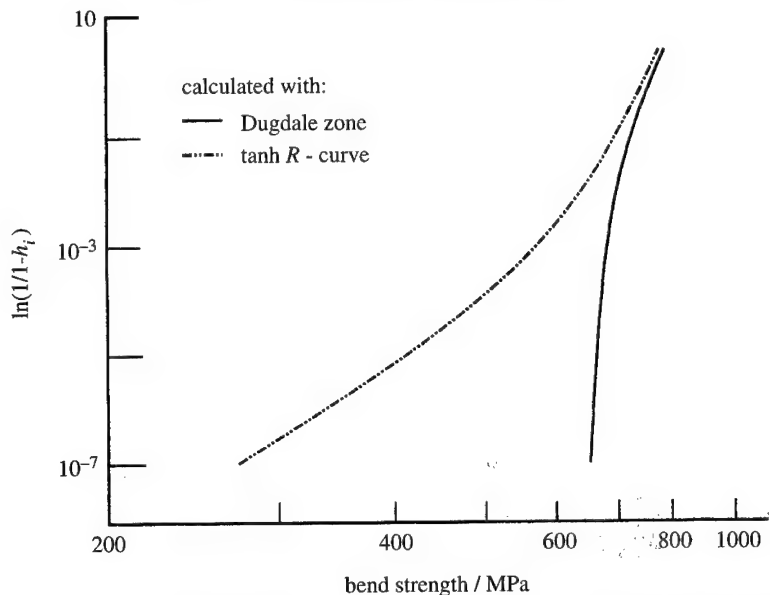


Figure 6. Strength distribution for a large set of samples corresponding to fracture probabilities down to 10^{-7} .

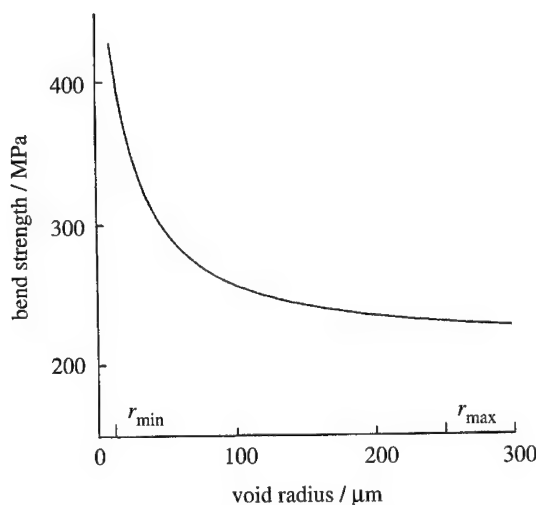


Figure 7. Dependence of strength on void diameter at a constant fracture toughness of $3.5 \text{ MPa} \text{ am}^{1/2}$ and circumferential crack length of $10 \mu\text{m}$.

This duality can be followed in recent evaluations of the Weibull modulus for Ce-TZP at room temperature and 600°C (where the chemical driving force for transformation is effectively reduced) as provided in figure 10 (Pross *et al.* 1992). In this case it is speculated that, at the critical transformation stress, microcrack formation begins and subsequent stable crack growth up the *R*-curve leads to high strength values as compared to the result obtained at 600°C .

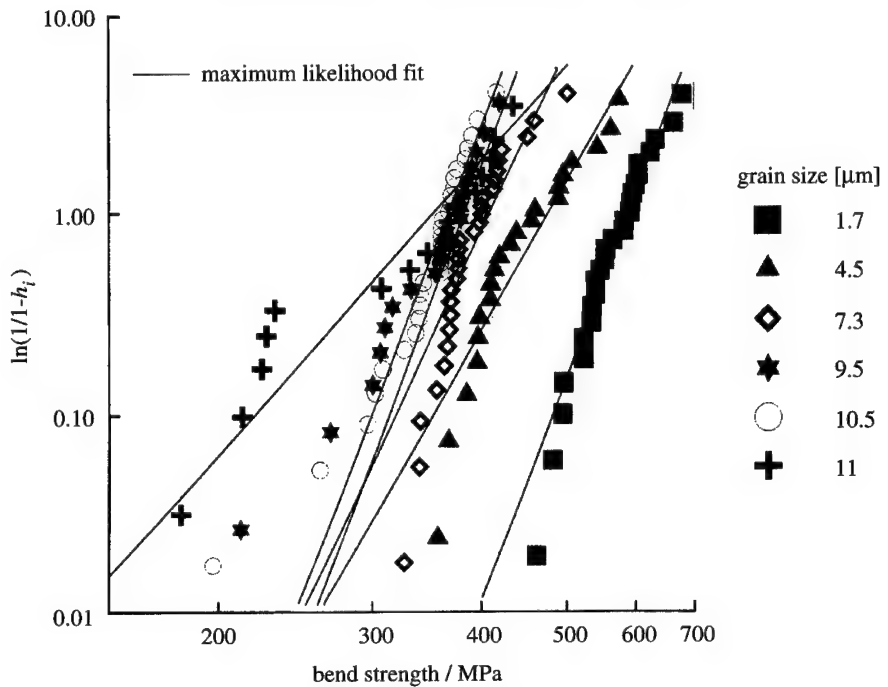


Figure 8. Strength distribution of alumina with various grain sizes.

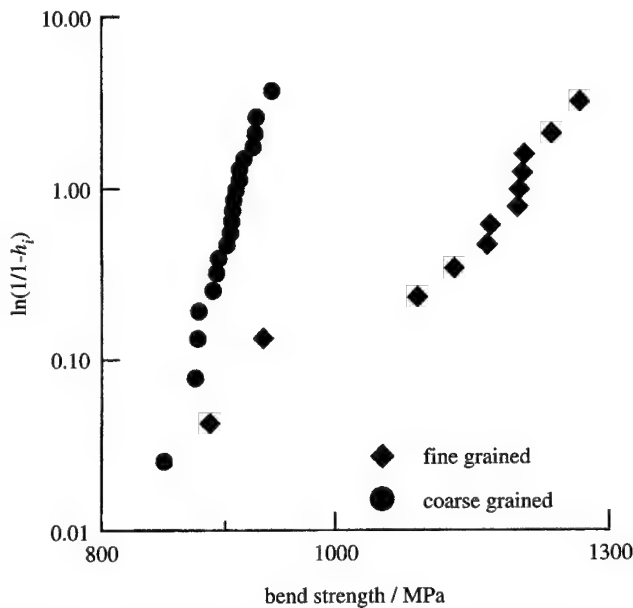


Figure 9. Strength distribution of silicon nitride with two different grain sizes (courtesy of W. Dressler).

(d) *Metal-reinforced ceramics: reduced flaw size/R-curve controlled reliability*

Various methods can be applied to fabricate metal-reinforced ceramics, such as squeeze casting (Lange *et al.* 1990), directed melt oxidation (Newkirk *et al.*

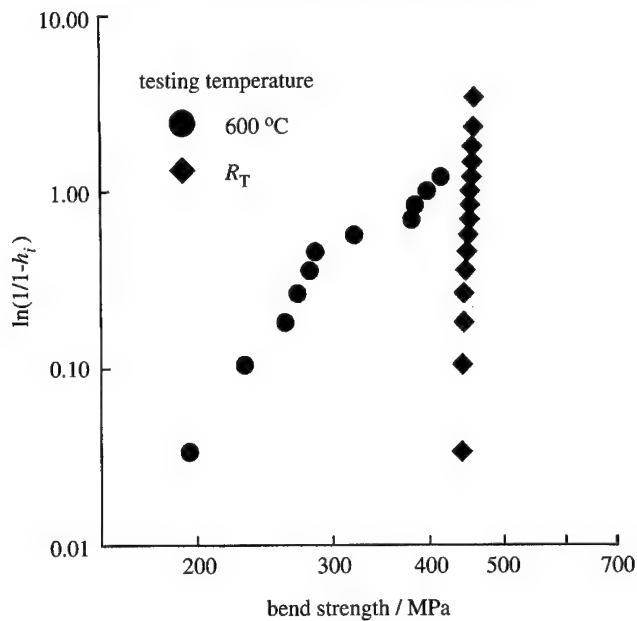


Figure 10. Strength distribution of Ce-stabilized zirconia at room temperature and 600 °C (Pross *et al.* 1992).

1986) and infiltration with (Travitzky & Claussen 1992) and without gas pressure (Toy & Scott 1990). Gas-pressure infiltration is successfully applied in a variety of metal-ceramic compositions including materials for high temperature applications like $\text{Ni}_3\text{Al}-\text{Al}_2\text{O}_3$ (Rödel *et al.* 1995). Porous ceramic preforms are obtained from sintering alumina green bodies to densities between 60 and 90% of theoretical density. The mechanical properties of the infiltrated composites are governed by metal content as well as microstructure (Priellip *et al.* 1995). The distribution of strength for three different microstructures (termed small (S), medium (M) and coarse (C)) of an $\text{Al}-\text{Al}_2\text{O}_3$ composite at a metal content of 25 vol% is depicted in figure 11, another for the medium microstructure at three different metal contents in figure 12. The Weibull moduli exhibit an increase by a factor of two when compared to the porous preforms for all cases except the one of the fine microstructure at 25 vol% metal content where no increase of m was observed. Due to the very small pore channel size of the preforms (0.08 μm), the stress-displacement relation of the metal ligaments bridging an advancing crack, reaches high closure stresses (Nohara 1982) at small crack openings, but is effective only up to an opening comparable to the ligament diameter (Ashby *et al.* 1989). Thus the resulting R -curve is believed to exhibit a very steep slope, therefore being ineffective in narrowing the strength distribution of the S composite. In contrast the coarse composite exhibits a mean pore channel size nearly an order of magnitude larger (0.75 μm) than the S composite, which imparts a more shallow R -curve thus resulting in reduced strength but enhanced reliability. Since the pore channel size remains essentially constant in the range of preform porosities applied, the shape of the crack resistance curve can be considered as being invariant of metal content. However, it has been demonstrated that K_{ss} is increased with metal content for a given microstructure, thus improving strength and narrowing strength distribution (figure 12).

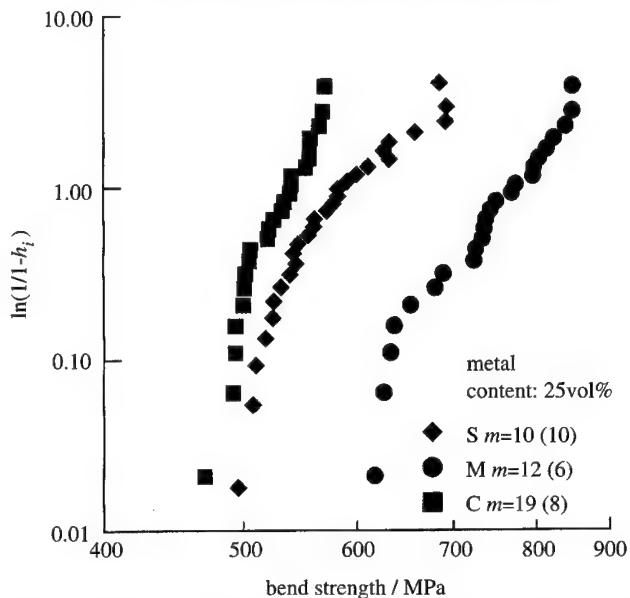


Figure 11. Strength distribution of Al infiltrated Al_2O_3 for three different microstructures. The values in parentheses correspond to the Weibull moduli of the uninfiltrated preforms.

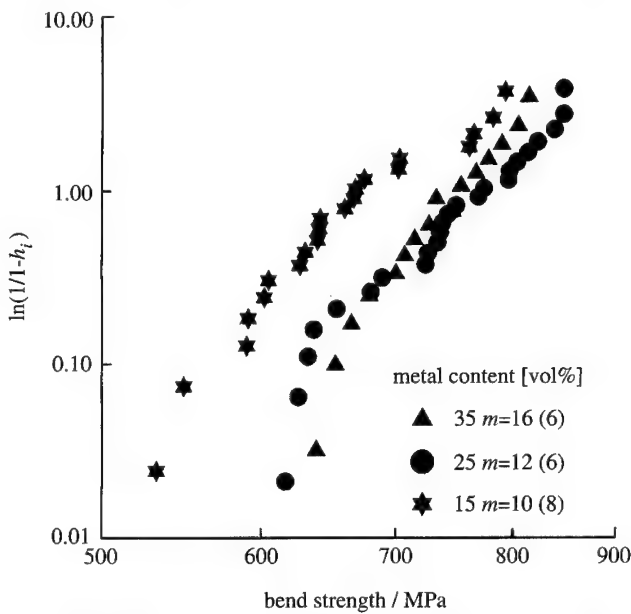


Figure 12. Strength distribution of an Al infiltrated Al_2O_3 with medium microstructure for three different metal contents. The values in parentheses correspond to the Weibull moduli of the uninfiltrated preforms.

Normalizing strength and toughness of all composites investigated so far to the data of the uninfiltrated matrices revealed a higher increase in strength than toughness (Priellip *et al.* 1995). Thus a diminished flaw size in the infiltrated composites has to be taken into account. Assuming the largest pore or pore agglomerate being the fracture origin, this effect can be explained by the fact that

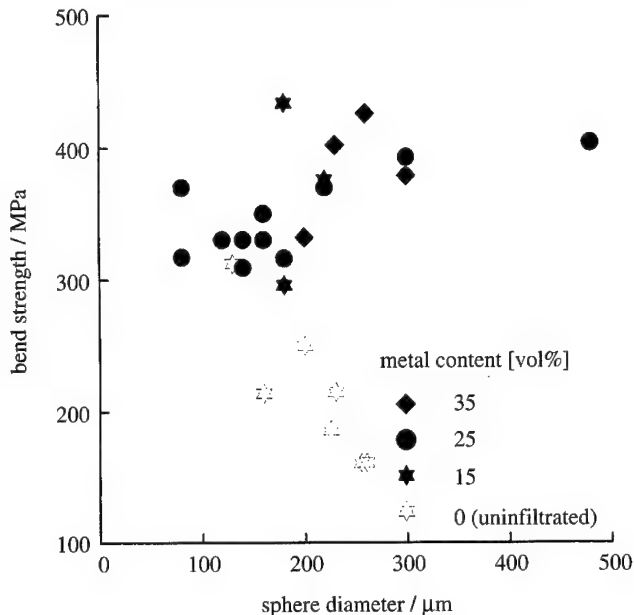


Figure 13. Strength of an Al-Al₂O₃ composite containing aluminium spheres of various diameter, acting as artificial flaws.

infiltrated pores act as single bridging elements. A further proof for this assumption can be given by the results of a model experiment, where bend bars with controlled defects were prepared incorporating polystyrene spheres in the green body. The polymer was burned out during sintering and the specimens were subsequently infiltrated with metal. Figure 13 depicts the equatorial bend strength of an Al-Al₂O₃ composite where failure occurred from the aluminium spheres for different metal contents and sphere diameters. No decrease in strength with increasing sphere diameter can be observed demonstrating the effectiveness of crack bridging. A more detailed analysis of strength distribution would therefore have to incorporate the effect of a rising crack resistance as well as the inhomogeneous distribution of bridging stresses.

5. Conclusions

It was demonstrated that reliability of structural ceramics can be controlled by at least four mechanisms with different degrees of efficiency, such as the distribution of defect size, *R*-curve effects, stress induced plasticity and reduced flaw size.

The influence of *R*-curve effects on strength distribution was modelled assuming natural flaws as being peripherally cracked spherical voids. For closure stresses in the range between 100 and 600 MPa, a maximum Weibull modul about three times higher than of the unreinforced reference case was predicted. Therefore the opportunity arises of further improving reliability through a combination of effective green forming techniques that narrow flaw size distribution with suitable crack-growth resistance imparting reinforcements.

The experimental data for strength and strength distribution presented were in the range of prediction except in the case of Ce-stabilized zirconia.

References

Ashby, M. F., Blunt, F. J. & Bannister, M. 1989 *Acta metall.* **37**, 1847–1857.

Baratta, F. I. 1981 *J. Am. Ceram. Soc. C* **64**, 3–4.

Bergmann, B. 1986 *J. Mater. Sci. Lett.* **5**, 591–619.

Chantikul, P., Bennison, S. J. & Lawn, B. R. 1990 *J. Am. Ceram. Soc.* **73**, 2419–2427.

Chao, L.-Y. & Shetty, D. K. 1992 *J. Am. Ceram. Soc.* **75**, 2116–2124.

Cook, R. F. & D. R. Clarke, D. R. 1988 *J. Am. Ceram. Soc.* **36**, 555–562.

Cox, B. N. & Marshall, D. B. 1994 *Acta metall. mater.* **42**, 341–363.

Dortmanns, L. J. M. G. & de With, G. 1991 *J. Am. Ceram. Soc.* **74**, 2293–2294.

Dressler, W. 1993 Ph.D. thesis, University of Stuttgart.

Evans, A. G. & Davidge, R. W. 1970 *J. nucl. Mater.* **5**, 314–325.

Fett, T. 1994 *Int. J. Fract.* **67**, R41–R47.

Freudenthal, A. M. 1968 In *Fracture* (ed. H. Liebowitz), vol. 2. Academic, 592–619.

Hartsock, D. L. & McLean, A. F. 1984 *Am. Ceram. Soc. Bull.* **63**, 266–270.

Kendall, K., McNALford, N. & Birchall, J. D. 1987 *Mater. Res. Soc. Proc.* (ed. P. F. Becher, M. V. Swain & S. Somiya), vol. 78, p. 189. Pittsburgh: MRS Press.

Lange, F. F. 1973 *J. Am. Ceram. Soc.* **56**, 518–522.

Lange, F., Velamakanni, B. V. & Evans, A. G. 1990 *J. Am. Ceram. Soc.* **73**, 388–393.

Li, C.-W. & Yamanis, J. 1989 *Ceram. Engng Sci. Proc.* **10**, 632–645.

Li, C.-W., Lee, D.-J. & Lui, S.-C. 1992 *J. Am. Ceram. Soc.* **75**, 1777–1782.

Newkirk, M. S., Urquhart, A. W., Zwicker, H. R. & Breval, E. 1986 *J. Mater. Res.* **1**, 81–89.

Nohara, A. 1982 *Jap. J. appl. Phys.* **21**, 1287–1292.

Priellip, H., Knechtel, M., Claussen, N., Streiffer, S. K., Müllejans, H., Rühle, M. & Rödel, J. 1995 *J. Mater. Sci. Engng.* (In the press.)

Pross, J. 1992 Ph.D. thesis, MPI Stuttgart.

Pross, J., Schneider, G. A., Schubert, H. & Petzow, G. 1992 In *Verstärkung Keramischer Werkstoffe* (ed. N. Claussen). Oberursel: Informationsgesellschaft.

Ramachandran, N., Chao, L.-Y. & Shetty, D. K. 1993 *J. Am. Ceram. Soc.* **76**, 961–969.

Ready, M. J., McCallen, C. L., McNamara, P. D. & Lawn, B. R. 1993 *J. Mater. Sci.* **28**, 6748–6752.

Rice, R. W. 1984 *J. Mater. Sci.* **19**, 895–914.

Rödel, J. 1992 *J. Eur. Ceram. Soc.* **10**, 143–150.

Rödel, J., Priellip, H., Sternitzke, M., Claussen, N., Alexander, K., Becher, P. & Schneibel, J. 1995 *Scr. metall.* (In the press.)

Schneider, G. A. & Petzow, G. 1994 *Key Engng Mater.* **89–91**, 563–568.

Seidel, J., Claussen, N. & Rödel, J. 1995 *J. Eur. Ceram. Soc.* **26**. (In the press.)

Shetty, D. K. & Wang, J.-S. 1989 *J. Am. Ceram. Soc.* **72**, 1158–1162.

Steen, M., Sinnema, S. & J. Bressers, J. 1992 *J. Eur. Ceram. Soc.* **9**, 437–445.

Steinbrech, R. W., Reichl, A. & Schaarwächter, W. 1990 *J. Am. Ceram. Soc.* **73**, 2009–2015.

Swain, M. V. & Rose, L. R. 1989 *J. Am. Ceram. Soc.* **69**, 511–518.

Toy, C. & Scott, W. D. 1990 *J. Am. Ceram. Soc.* **73**, 97–101.

Travitzky, N. & Claussen, N. 1992 *J. Eur. Ceram. Soc.* **9**, 61–65.

Uematsu, K., Sekiguchi, M., Kim, J.-Y., Saito, K., Mutoh, Y., Inoue, M., Fugino, M. & Miyamoto, A. 1993 *J. Mater. Sci.* **28**, 1788–1792.

Weibull, W. 1951 *J. appl. Mech.* **18**, 293–297.

Discussion

K. S. KUMAR (*Martin Marietta Laboratories, Baltimore, USA*). In the case-study relating to the intermetallic-infiltrated composite, Ni_3Al was selected as the intermetallic. Would it not be better to select a Ni-base superalloy or a refractory metal such as Nb or Ta to play the role that Ni_3Al is expected to, and realize significantly better improvements?

J. RÖDEL. A Ni-base superalloy will provide cavitation sites for premature cavity formation at the interface between intermetallic and ceramic if under tensile stress. Refractory metals will increase the density (as in Nb or Ta) of the composite.

R. CAHN (*Cambridge University, UK*). With regard to the experiments on alumina infiltrated with Ni_3Al minispheres, since weak alloy-ceramic interfaces were found, might I suggest two variants. (1) Try one of Liu's 'advanced aluminides', essentially Ni_3Al heavily alloyed with Cr, creating a highly oxidation-resistant intermetallic; this might bond better to alumina. (2) Try NiAl , which forms essentially an alumina layer on the surface when oxidized; indeed, it might be effective if it were to be preoxidized before infiltrating!

J. RÖDEL. We will try the Ni_3Al with Cr, since a strong bond is required for high strength. Experiments with NiAl are also planned, but of course we need a higher infiltration temperature still, which may technologically be not straightforward.

Ceramic matrix composites

BY R. R. NASLAIN

*Laboratoire des Composites Thermostructuraux, UMR 47 CNRS-SEP-UB 1,
Domaine Universitaire, 3 Allée de La Boëtie, 33600 Pessac, France*

SiC–SiC composites exhibit a non-brittle behaviour when the fibre–matrix bonding is controlled by the use of an interphase with a layered structure or microstructure, such as pyrocarbon, hex-BN or $(\text{SiC}-\text{PyC})_n$ multilayers. The best mechanical properties are achieved when there is a balance between the crack deflection and load transfer functions of the interphase. SiC–SiC composites are sensitive to oxidation but their stability in oxidizing atmospheres can be improved by tailoring their composition and microstructure.

1. Introduction

Ceramic matrix composites (CMCs), which consist of a ceramic matrix reinforced with ceramic fibres, are potential candidate materials for structural applications at high temperatures owing to their non-brittle mechanical behaviour and to the well-established thermal stability and high melting points of most ceramics. The CMCs which have been the most studied during the past two decades are the carbon–carbon (C–C), the SiC–matrix composites (i.e. the C–SiC or SiC–SiC, where the nature of the fibres is indicated first) and the oxide–matrix composites (such as the SiC–silica-based glass–matrix composites).

C–C composites have been designed initially to withstand short exposures at extremely high temperatures (e.g. in rocket engines or re-entry thermal protection), during which part of the material is usually consumed. More recently, their use has been extended to applications of longer duration but at much lower temperatures (e.g. in brake discs). Despite several outstanding advantages, the C–C composites suffer from a high sensitivity to oxidation even at very low temperatures (e.g. 500 °C). Their oxidation resistance has been improved by incorporating oxidation inhibitors to the matrix or/and adding external protective coating to the composite. However, these solutions might not be efficient enough for very severe use conditions (e.g. repeated load/temperature cycling under oxidizing atmospheres).

The best choice in terms of long-duration compatibility with chemically aggressive environments would be all-oxide composites. However, in the present state of knowledge and technology, some of their constituents, namely, the fibres and the interphases (used to bond in an appropriate manner the fibres to the matrix, as will be discussed later), have not been yet fully identified. Conversely, various oxide matrices with melting points close to or higher than 2000 °C (e.g. mullite, α -alumina, yttria, stabilized zirconia) have already been studied and processing techniques are available.

SiC-matrix composites seem to be an acceptable compromise with a view to medium-temperature range applications (i.e. at 1000–1500 °C) in oxidizing atmospheres. The SiC-matrix can be formed, as can its carbon counterpart, by both gas or liquid phase routes. High-performance SiC fibres (in terms of strength and creep resistance at 1000–1500 °C) are already studied at the laboratory scale. The weak point of the SiC–SiC composites might be the interphase material (presently, an anisotropic carbon). However, recent research results suggest that the situation could be significantly improved.

The aim of the present contribution is to show the potential of SiC–SiC composites as high-temperature structural materials, and to discuss the improvement which has been achieved during the past few years as well as the weak points which still limit their applications.

2. The CMC concept

It is known from the early work of Aveston *et al.* (1971) that a CMC can exhibit non-brittle mechanical behaviour (although all its constituents are intrinsically brittle), provided the fibre volume fraction is high enough and the fibres are not too strongly bonded to the matrix. Under such conditions, the brittle matrix (which fails first since its failure strain is much lower than that of the fibres, typically 0.1 and 1% respectively, for a SiC–SiC composite) undergoes microcracking up to a saturation state beyond which the load is carried by the fibres alone. In this process, each matrix microcrack is deflected parallel to the fibre surface by the weak interface which acts thus as a fuse (protecting the fibre from an early failure). Conversely, when the fibre–matrix (FM) bonding is too weak, the fibre is debonded over a very considerable length and the debonded interface no longer exhibits enough load transfer ability. Thus there should be a balance between the crack deflection and the load transfer functions. When this requirement is fulfilled, CMCS exhibit nonlinear stress–strain behaviour under tensile loading up to failure strains close to that of the fibres, i.e. typically 0.5–1%, which is an outstanding feature for a ceramic material.

The FM bonding mainly stems from thermal residual stresses (TRS) coupled to fibre surface roughness as well as from chemical bonds. The residual stresses are generated, during cooling from processing-temperature (typically, about 1000 °C) to ambient, as a result of coefficient of thermal expansion (CTE) mismatch. The TRS are compressive when $\alpha_m > \alpha_m^r$ (α_m being the matrix CTE and α_m^r the radial CTE of the fibre). The latter result from interdiffusion phenomena occurring at the FM interface during processing.

To control the FM bonding, an interphase (often referred to as the third constituent of the CMCS) is generally used. The interphase consists of a submicrometre thin film of a compliant material with a low shear stress, which is usually deposited at the fibre surface before composite processing (it can also be formed *in situ* during processing). The interphase has several key functions. First, it should properly deflect the matrix microcracks while providing enough load transfer, as previously mentioned. Second, it may also at least partly absorb the TRS (present when $\alpha_m \neq \alpha_m^r$), thus acting as a buffer and requiring a minimum thickness of interphase material. Third, the interphase may play the role of a diffusion barrier when the FM couple is very reactive. Finally, the interphase should be compatible with the fibres, the matrix and the environment.

From the present status of knowledge and technology, the best interphases are those with a layered crystal structure or microtexture (e.g. pyrocarbon, hexagonal-BN or mica-type oxides) (Naslain 1993), the layers being oriented parallel to the fibre surface and weakly bonded to one another. Other interface/interphase concepts have been suggested but have not yielded high-performance CMCS, up to now (Kerans 1993).

3. Fabrication of SiC–SiC composites

The SiC–SiC composites considered here are fabricated from continuous SiC-based fibres, according to a low-temperature/low-pressure gas phase route, the chemical vapour infiltration (CVI) process, which has been described in detail elsewhere (Naslain 1992). In a first step, the interphase material, i.e. pyrocarbon (PyC) or hex-BN, is deposited within the fibre preform, from gaseous precursors (respectively, a hydrocarbon or a $\text{BF}_3\text{--NH}_3$ mixture) at about 1000 °C and under a pressure of a few kPa or 10 kPa. Interphase thickness ranges from 0.1 to 1 μm . In a second step, the SiC-matrix is infiltrated according to a similar method, from a mixture of methyltrichlorosilane CH_3SiCl_3 (MTS) and hydrogen (Naslain & Langlais 1986). SiC–SiC composites processed by CVI exhibit some residual open porosity (typically, 10–15%). This feature has both some advantages and drawbacks. On the one hand, the residual pores which are regularly distributed in the material, act as crack initiators and contribute to yield homogeneous microcracking of the intertow SiC-matrix. On the other hand, the residual pores, being interconnected, favour the in-depth diffusion of oxygen when the composite is exposed to oxidizing atmospheres. For this reason, an external coating (consisting of a glass-forming material such as SiC) is usually deposited, in a last step, on the composite surface by chemical vapour deposition (CVD) in order to seal the residual pores. Finally it is worth noting that the SiC-matrix deposited by CVD/CVI is textured (with the $\langle 111 \rangle$ direction of the cubic SiC-crystals perpendicular to the substrate) and contains residual stresses due to crystal growth defects (Bobet *et al.* 1993).

4. Mechanical behaviour and effect of the interphase texture

The mechanical behaviour of two-dimensional SiC–SiC composites, e.g. under tensile loading along one of the two fibre directions, has been significantly improved over time as the processing conditions, the texture of the PyC-interphase and the FM bonding, came to be better controlled (figure 1).

The first two-dimensional SiC–SiC composites, fabricated from Si–C–O fibres (e.g. Nicalon, from Nippon Carbon) with no pyrocarbon coating, were essentially brittle, owing to the too strong FM bonding (Naslain 1993) (composite of type D, inset in figure 1). Later, the use of a pyrocarbon coating yielded composites exhibiting some nonlinear stress-strain behaviour (composites of type C). However, the poor control of the FM interfacial zone in terms of the texture of the PyC interphase and bonding between the PyC interphase and the fibre, resulted in limited matrix microcracking and early failure of the fibres and composite (with typically, $\sigma^R \approx 180 \text{ MPa}$ and $\epsilon^R \approx 0.2\%$).

The role played by the PyC-interphase has been clearly established in more recent materials, namely composites of type A and B, corresponding respectively

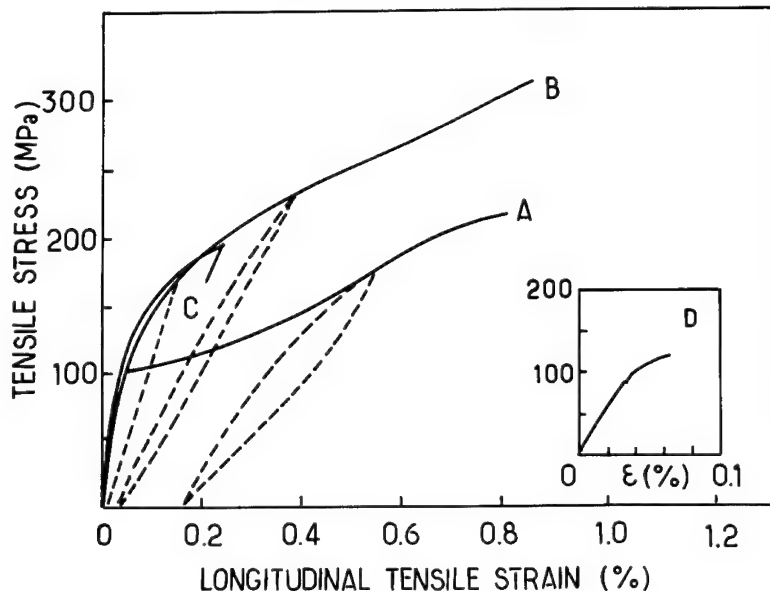


Figure 1. Tensile curves at ambient for various as-processed two-dimensional SiC-PyC-SiC composites fabricated by CVI from Nicalon fibres. After Cojean (1991) and Naslain (1993).

to a weak and a stronger FM bonding (figure 1). In composite A, as soon as matrix microcracking starts, the fibres are debonded over long distances owing to the weak FM bonding (figure 2a) with several important consequences: (i) a strong decrease in the load transfer capability of the FM interfacial zone (since the fibres are rapidly debonded from the PyC-interphase) at the beginning of the nonlinear σ - ϵ domain and (ii) a rapidly achieved matrix microcracking saturation state, the microcracks being very few, limited to the intertow SiC and widely spaced. These features are responsible for the 'plateau-like' aspect of the σ - ϵ tensile curve (figure 1). Beyond microcrack saturation, the applied load is essentially carried by the fibres (almost totally debonded from matrix), the matrix microcracks becoming more and more widely opened. Finally, failure occurs at a high strain (0.8–1%) and with extensive fibre pull-out. In such composites, microcrack deflection (the fuse function) occurs near the interface between the Si–C–O fibre and the PyC interphase. It is related to a thin bilayer (thickness of a few 10 nm) consisting of a sublayer of a silica-based glass on the fibre side and a sublayer of strongly anisotropic pyrocarbon (with the atomic planes parallel to the fibre surface) on the PyC interphase side (Cojean 1991; Droillard 1993). It is generally accepted that the silica sublayer results from a surface decomposition/oxidation of the metastable Si–C–O fibres.

The mechanical behaviour of composite B is very different, owing to the occurrence of a different deflection mode of the matrix microcracks itself related to an improved structure of the FM interfacial zone and to better processing conditions (figure 2b). In composite B, the PyC interphase is now strongly bonded to the fibre (i.e. the fibre–PyC interface is no longer the weakest link) and still consists of an anisotropic pyrocarbon whose atomic layers are parallel to the fibre surface without being continuous (as they are in graphite). A key difference between composites A and B is that the matrix microcracks are deflected within

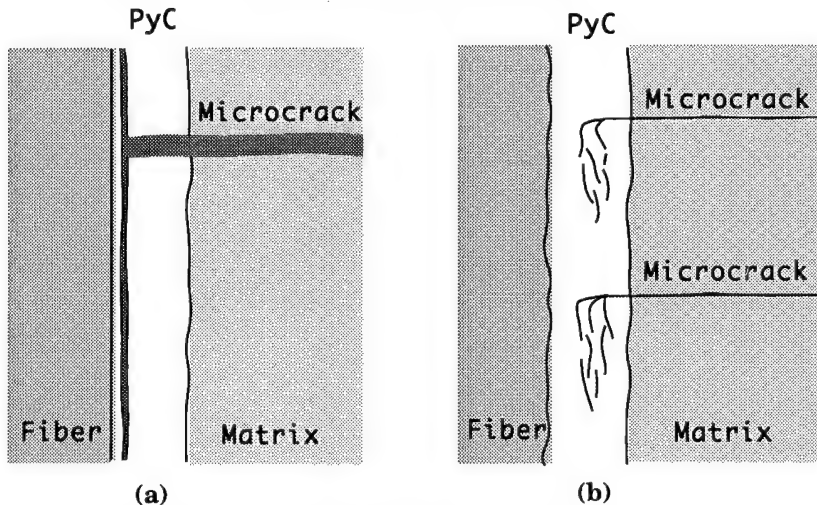


Figure 2. Microcrack propagation paths (schematic) near the fibre-matrix interfacial zone in two-dimensional SiC-PyC-SiC composites fabricated by cvi from Nicalon fibres: (a) composites of type A and (b) composites of type B. After Droillard (1993).

the PyC-interphase (and not at the fibre surface) in B. Each microcrack is deflected in an infinity of nanocracks formed between the carbon atomic planes, i.e. it is here the whole interphase which is acting as a fuse (whereas in A it is a weak interface at the fibre surface) (Droillard 1993). This new crack deflection mechanism has very important consequences: (i) the FM bonding is not totally destroyed, i.e. as the matrix microcracks are deflected within the interphase, the FM interphase zone keeps enough load transfer ability, thus (ii) matrix microcracking can proceed further (i.e. it occurs both within the SiC intertow matrix (as in A) but also within the SiC-matrix in the 0° tow), the saturation state being only achieved near composite failure, the cracks being numerous and weakly opened (Aubard 1992). Finally, failure occurs at a high failure stress (close to 400 MPa) and high failure strain but with very limited fibre pull-out (since the FM bonding is stronger, as is confirmed by the narrow unloading/reloading loops and by fibre push-out data).

These results clearly show that the best material in terms of mechanical properties is that, composite B, corresponding to the stronger FM bonding (and not, as often reported in the literature, that with the weaker FM bonding exhibiting extensive fibre pull-out) in which an appropriate balance between the crack deflection and load transfer functions of the FM interfacial zone has been achieved during processing.

5. Effect of the environment

SiC is known to have an excellent resistance to oxidation up to about 1500 °C as long as the oxidation regime remains passive (i.e. with the formation of a protective scale of glassy silica). However, even under such conditions, SiC-PyC-SiC composites have at present two weak points: (i) the fibres which do not consist entirely of SiC (Nicalon-type fibre also contains some free carbon and a metastable ternary phase $\text{SiO}_{2x}\text{C}_{1-x}$) (Bodet *et al.* 1995) and (ii) the pyrocarbon interphase.

(a) *Effect of an inert environment*

As shown in figure 3, two-dimensional SiC-PyC-SiC composites (type C), fabricated from Si-C-O fibres (Nicalon-type) and aged under vacuum or argon, exhibit a decrease in their mechanical behaviour at ambient temperature. This decrease is observed for ageing treatments performed beyond about 1100 °C and is related to the decomposition of the fibres. At $T > 1100$ °C, the $\text{SiO}_{2x}\text{C}_{1-x}$ phase decomposes with an evolution of CO and SiO, the latter reacting with the free carbon of the fibres and the interphase, with two important consequences: (i) grain growth of the SiC-nanocrystals of the fibres (since they are no longer separated from each other by the silicon oxycarbide amorphous phase), resulting in a weakening of the fibres and, more importantly, (ii) a weakening of the load transfer capability of the FM interfacial zone (since the PyC-interphase is progressively consumed and replaced by a void), as supported by TEM analysis and push-out data (Labrugère *et al.* 1993).

The thermal stability of two-dimensional SiC-PyC-SiC composites in vacuum or inert atmospheres could be improved in two ways. First and as mentioned in § 3, a SiC seal-coating can be applied to the composite. Under such conditions, the decomposition of $\text{SiO}_{2x}\text{C}_{1-x}$ is slowed down by an internal pressure of CO and SiO. However, this solution might become ineffective under load cycling (with microcracking of the seal-coating). A better alternative would be to use fibres which no longer contain the $\text{SiO}_{2x}\text{C}_{1-x}$ phase, such as the Si-C fibres obtained by an electron beam curing/pyrolysis process, from polycarbosilane precursors. Such fibres (in which the oxygen content is only 0.5 wt%) are stable up to about 1500 °C (Takeda *et al.* 1992).

(b) *Effect of an oxidizing environment*

In an oxidizing atmosphere (e.g. the air), the weak point of SiC-PyC-SiC composites is the pyrocarbon interphase (assuming that the problem related to the stability of the fibres has been solved, as discussed in § 5 a). However, under specific conditions, SiC-PyC-SiC composites behave as self-healing materials.

When, say, a rectangular sample of one-dimensional SiC-PyC-SiC composite (with a SiC seal-coating on the four faces parallel to the fibre direction) is submitted to an oxidation treatment, chemical reactions occur according to the following overall equations:



Since, in this example, the oxidation process is a one-dimensional phenomenon, an annular pore is formed around each fibre as the PyC-interphase is progressively consumed (equations (1) or/and (1')) (figure 4a). Thus oxygen (and in the opposite direction CO or/and CO_2) has to diffuse along the pore to react with the PyC-interphase. During this diffusion, oxygen reacts with the pore wall (i.e. the fibre and the matrix) to give a silica scale (equation (2) and (2')). All these phenomena can be modelled, in this simple case, the results depending mainly on the temperature and the PyC interphase thickness. An example of a simulation is

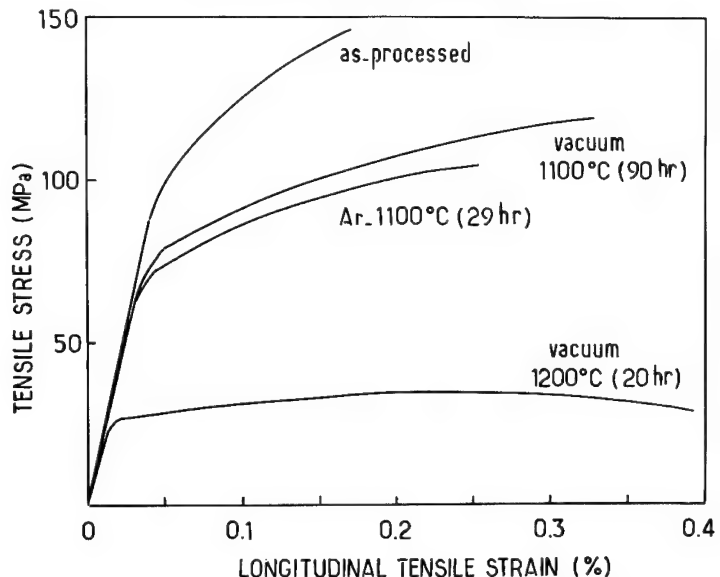


Figure 3. Effect of ageing treatments on the tensile curve at ambient of two-dimensional SiC-PyC-SiC composites (type C) fabricated by CVI from Nicalon fibres. After Labrugère *et al.* (1993).

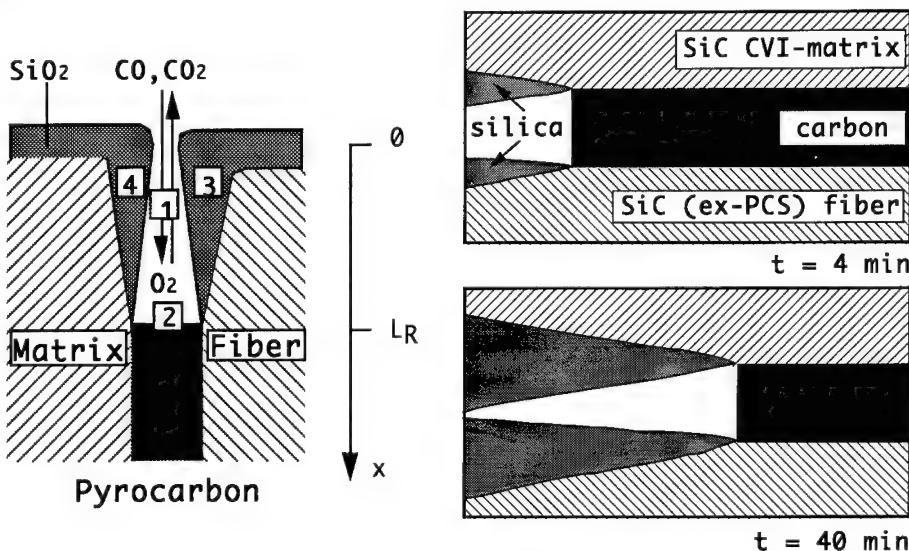


Figure 4. Effect of an oxidizing atmosphere on one-dimensional SiC-PyC-SiC model composites: (a) elementary phenomena involved (1: diffusion of O_2 , $CO-CO_2$; 2: oxidation of the carbon interphase; 3, 4: oxidation of the fibre surface and matrix), (b) simulation of the oxidation phenomena for an oxidation performed in pure oxygen ($P = 100$ kPa) at 1200 °C. After Filipuzzi & Naslain (1994).

shown in figure 4b (Filipuzzi *et al.* 1994). When the temperature is high enough and the PyC interphase thin, the silica scales seal the pore and the oxidation stops.

The effect of both the temperature and the interphase thickness on the length of carbon l_r which is consumed as a function of time is shown in figure 5. For

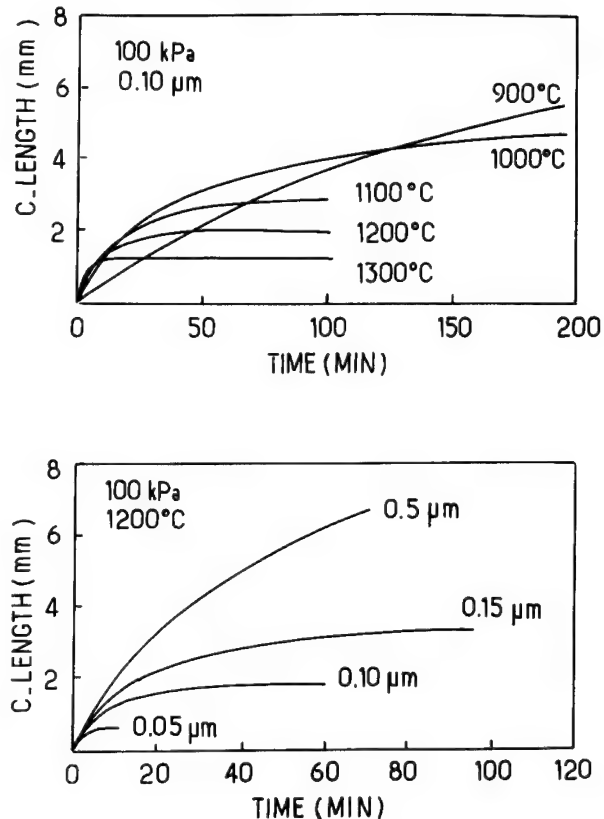


Figure 5. Effect of temperature (a) and interphase thickness (b) on the kinetics of oxidation of the PyC interphase in model one-dimensional SiC-PyC-SiC composites, as derived from simulation. After Filipuzzi & Naslain (1994).

a given interphase thickness, oxidation proceeds in-depth at low temperatures (since the formation rate of silica is too low) and, conversely, it is limited to near the external surface at high temperatures (figure 5a). A similar effect is observed at constant temperature when the PyC-interphase is varied (figure 5b).

Thus the effect of an oxidizing atmosphere on SiC-PyC-SiC composites is more dramatic at low temperatures ($500 < T < 1000$ °C) than at higher temperatures where the material is self-healing.

The compatibility of SiC-PyC-SiC composites with oxidizing atmospheres could be improved at least in two directions. One way is to replace the PyC interphase by, for instance, a multilayered $(\text{SiC-PyC})_n$ interphase where the thickness of each PyC sublayer is reduced to a few nm or 10 nm (see figure 5b and 6) (Droillard 1993). Another way is to replace pyrocarbon by hex-BN which has a similar layered crystal structure (and thus can act as a fuse) but exhibits a much higher oxidation resistance (figure 7) (Economy & Lin 1977). The oxidation of hex-BN starts at *ca.* 850 °C (instead of *ca.* 450 °C for PyC) and yields an oxide, B_2O_3 , which is liquid in a wide temperature range ($500 < T < 1100$ °C), wets SiC and is known for its healing properties. SiC-BN-SiC composites have been prepared and characterized. However, in the present status of the research, their mechanical properties are not yet as good as those of their SiC-PyC-SiC counterparts.

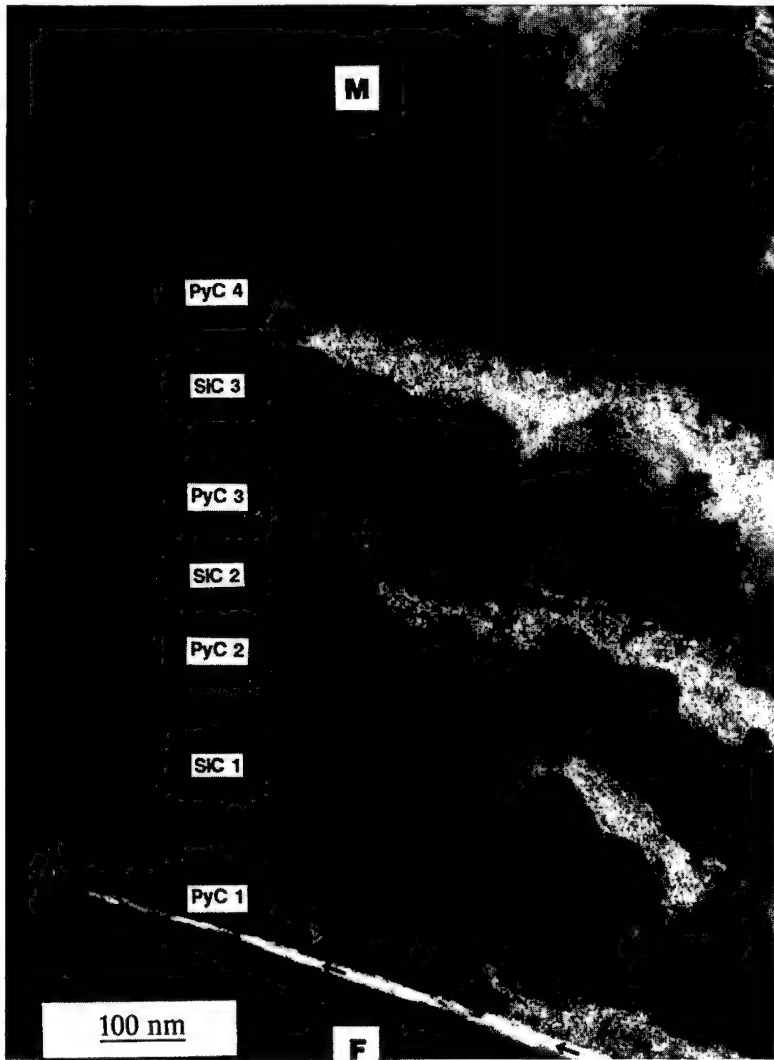


Figure 6. TEM image of the fibre-matrix interfacial zone in a two-dimensional SiC-SiC composite with a multilayered $(\text{PyC-SiC})_n$ interphase. After Droillard (1993).

Additionally, very little is known about their mechanical behaviour in oxidizing atmospheres (Naslain *et al.* 1991; Prouhet *et al.* 1994).

6. Conclusion

SiC-SiC composites exhibit a non-brittle mechanical behaviour when the fibre-matrix bonding has been properly controlled during processing via the use of an interphase. Efficient interphase materials are those with a layered crystal structure or/and microtexture, such as pyrocarbon, hex-BN or $(\text{SiC-PyC})_n$ multilayers.

The nonlinear mechanical behaviour and the high toughness of SiC-SiC composites are related to the occurrence of damaging phenomena including matrix microcracking. The best mechanical properties (in terms of failure stress, failure

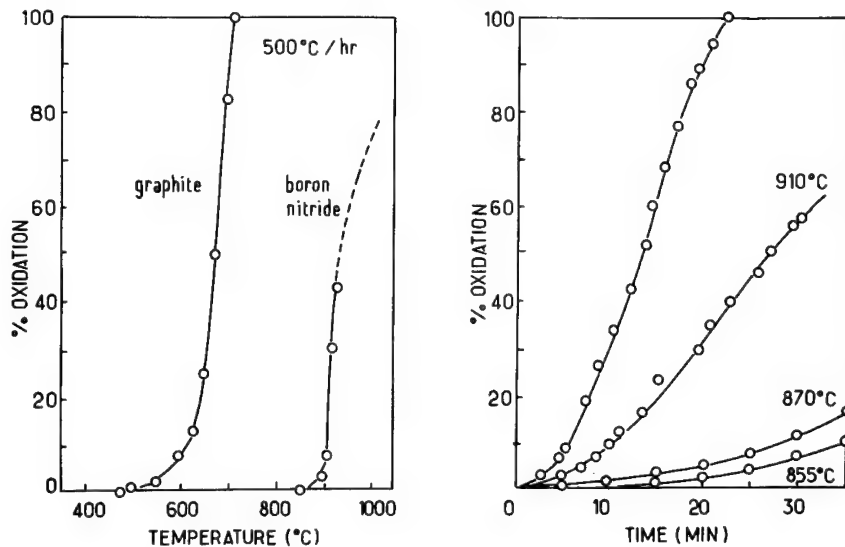


Figure 7. Oxidation of BN-fibres: (a) as compared to that of carbon fibre, (b) kinetics of oxidation for various temperatures. After Economy & Lin (1977).

strain, energy release rate and fatigue resistance) are achieved for rather strong fibre-matrix bonding (i.e. when there is a balance between the crack deflection and load transfer functions of the fibre-matrix interfacial zone). Under such conditions, failure occurs with limited fibre pull-out.

SiC-SiC composites are still sensitive to the effect of the environment by the fibres (which are often not stable enough at high temperatures) and the interphase (particularly, pyrocarbon). The use of more stable fibres (e.g. fibres without oxygen and whose composition is close to C/Si = 1), seal-coating and hex-BN interphase would undoubtedly significantly increase the compatibility of SiC-SiC composites with oxidizing atmospheres in the 1000–1500 °C temperature range.

This article has been written on the basis of the research performed at LCTS during the past few years with the support of SEP. The author acknowledges the contribution, among others, of J. Lamont, A. Guette, X. Bourrat, G. Camus, C. Robin-Brosse, F. Lamouroux and S. Goujard.

References

Aubard, X. 1992 Modélisation et identification du comportement mécanique des matériaux composites 2D-SiC-SiC. Thèse de doctorat, Université de Paris VI, France.

Aveston, J., Cooper, G. A. & Kelly, A. 1971 Single and multiple fracture. In *Proc. Conf. on the Properties of Fibre Composites*, National Physical Laboratory, 4 November 1971, pp. 15–26. Guildford, UK: IPC, Science and Technology Press.

Bobet, J. L., Lamont, J. & Lebrun, J. L. 1993 In *Proc. Int. Conf. on High Temperature Ceramic Matrix Composites* (ed. R. Naslain, J. Lamont & D. Doumeingts), pp. 515–522. Abington, Cambridge: Woodhead Publishing.

Bodet, R., Lamont, J., Jia, N. & Tressler, R. E. 1995 Microstructural stability and creep behaviour of Si-C-O (Nicalon) fibres in carbon monoxide and argon environments. *J. Am. Ceram. Soc.* (In the press.)

Cojean, D. 1991 Composites SiC-C-SiC: relation entre les propriétés mécaniques et la microtexture des interphases. Thèse doctorat, Université de Pau et des Pays de l'Adour, France.

Droillard, C. 1993 Elaboration et caractérisation de composites à interphases séquencées PyC-SiC. Thèse doctorat, Université de Bordeaux, France.

Economy, J. & Lin, R. 1977 Boron nitride fibres. In *Boron and refractory borides* (ed. V. I. Matkovich), ch. D III, pp. 552–564. Springer.

Filipuzzi, L. & Naslain, R. 1994 Oxidation mechanisms and kinetics of one-dimensional SiC–C–SiC composite materials. 2. Modeling. *J. Am. Ceram. Soc.* **77**, 467–580.

Kerans, R. J. 1993 Control of fibre–matrix interface properties in ceramic composites. *Proc. Int. Conf. on High Temperature Ceramic Matrix Composites* (ed. R. Naslain, J. Lamon & D. Doumeingts), pp. 301–312. Abingdon, Cambridge: Woodhead Publishing.

Labrugère, C., Guette, A. & Naslain, R. 1993 Comportement mécanique et évolution microstructurale de composites 2D-SiC (ex-PCS)–C–SiC (cv1) vieillis thermiquement. In *Microstructure, comportements thermomécaniques et modélisation des composites céramique–céramique à fibres* (ed. J. L. Chermant & G. Fantozzi), pp. 91–111. Paris: Hermès.

Naslain, R. 1992 cv1 composites. In *Ceramic matrix Composites* (ed. R. Warren), ch. 8, pp. 199–244. Glasgow and London: Blackie.

Naslain, R. 1993 Fiber–matrix interphases and interfaces in ceramic matrix composites processed by cv1. *Composite Interfaces* **1**, 253–286.

Naslain, R. & Langlais, F. 1986 CVD processing of ceramic–ceramic composite materials. In *Tailoring multiphase and composite ceramics* (ed. R. E. Tressler, G. L. Messing, C. G. Pantano & R. E. Newnham). *Mater. Sci. Res.* **20**, 145–164. Plenum Press.

Naslain, R., Dugne, O., Guette, A., Sèvely, J., Robin-Brosse C., Rocher, J. P. & Cotteret, J. 1991 Boron nitride interphase in ceramic matrix composites. *J. Am. Ceram. Soc.* **74**, 2482–2488.

Prouhet, S., Camus, G., Labrugère, C., Guette, A. & Martin, E. 1994 Mechanical characterization of Si–C (O) fibre–SiC (cv1) matrix composites with a BN-interphase. *J. Am. Ceram. Soc.* **77**, 649–656.

Takeda, M., Imai, Y., Ichikawa, H., Ishikawa, T., Kasai, N., Seguchi, T. & Okamura, K. 1992 Thermal stability of the low oxygen silicon carbide fibres derived from polycarbosilane. *Ceram. Engng Sci. Proc.*, pp. 209–217. Westerville: The American Ceramics Society.

Discussion

T. KHAN (*Onera, Chatillon, France*). There is another potentially interesting class of CMCS, i.e. the glass matrix composites. Some of these materials seem to have a temperature capability of up to 1200 °C. Can these materials be compared with the SiC–SiC in terms of limitations, advantages and cost?

R. R. NASLAIN. The glass (or glass-ceramic) matrix composites have been designed for long-duration applications at medium temperatures (typically 600–1000 °C) in oxidizing atmospheres. Several factors seem to limit the high-temperature capability of these materials, including (i) the creep of the matrix (which still contains some amorphous and viscous phase even ceramization) and (ii) the nature of the *in situ* formed interphase (whose main constituent, carbon, is sensitive to oxidation at very low temperatures). In contrast, the SiC–matrix in SiC–SiC composites is more resistant to creep (it is fully crystalline and SiC melts with decomposition only at about 2500 °C). Additionally, the interphase in SiC–SiC composites is not formed *in situ* as the result of a fibre–matrix chemical reaction. It is deposited on the fibre before the infiltration of the matrix. Thus it is not necessarily carbon (hex-BN has already been successfully used and other interfacial materials and/or concepts are presently studied). The advantages of glass–matrix composites may be in (i) the rapidity of their processing, (ii) the variety of composition of the matrix, and (iii) the absence of significant residual porosity (they are gas and liquid tight). Very large structural parts (such as those used for the thermal protection of spacecraft) can be fabricated with SiC–

SiC composites (in the 2 m size) and their high-temperature capability seems to be much higher. Finally, the main part of the cost of both composites is related to the fibres. The processing time of SiC-SiC composites is higher but a very large number of parts can be treated simultaneously and as a result the processing time per part is probably of the same order not to say lower. It is noteworthy that C-C is competitive with steel in brake disks.

M. STEEN (*Institute of Advanced Materials, Joint Research Centre, European Commission, Petten, The Netherlands*). How may thermal cycling affect the oxidation resistance of SiC-SiC composites? Is it possible to integrate the isothermal oxidation kinetics over the temperature range of interest to obtain the cyclic oxidation rate, or is there an acceleration effect to be considered?

R. R. NASLAIN. Two factors control the overall oxidation kinetics of SiC-SiC composites: (i) the intrinsic oxidation kinetics of the components (the fibres, the interphase and the matrix), and (ii) the rate of the in-depth diffusion of oxygen (and in the opposite direction, that of the carbon oxides). During a thermal cycling test, there is no obvious reason that could justify a change in the intrinsic oxidation kinetics of the constituents. Conversely, thermal cycling may enhance the microstructural damage stage of the composite: (i) new microcracks could be formed, and (ii) the pre-existing microcracks could be periodically re-opened. As a result, the overall oxidation rate can be accelerated (remembering that the oxidation of SiC-SiC composites with pyrocarbon interphase is much more severe at low temperatures, i.e. 400–700 °C, if the external coating undergoes microcracking, since, under such conditions, the rate of formation of the silica protective layer is extremely slow). The effect of thermal cycling on the lifetime of SiC-SiC composites in air is indeed an issue, on which a large effort of research is currently being expended.

PETER HOLMES (*ABB Management AG, Baden-Dättwil, Switzerland*). Can the model of oxidation loss of the carbon interface and formation of a silica plug be used to predict the length of fibre interface lost before the plugging occurs at various temperatures of exposure?

R. R. NASLAIN. Yes, the model of oxidation loss of the carbon interphase and formation of silica plug can be used (and has already been used) to predict the length of interphase consumed before plugging occurs, in SiC-PyC-SiC unidirectional composites, at various temperatures, for PyC interphases of different thicknesses and in atmospheres with different oxygen partial pressures. For more details see Filipuzzi & Naslain (1994) or Filipuzzi (1991).

Additional references

Filipuzzi, L. 1991 Ph.D. thesis, no. 593, University of Bordeaux.

Multiphase intermetallics

BY R. W. CAHN

*Department of Materials Science and Metallurgy, University of Cambridge,
Pembroke Street, Cambridge CB2 3QZ, UK*

Ordered intermetallic compounds, notably the aluminides of nickel, titanium, iron and niobium, have been under intensive investigation for the past two decades as prospective load-bearing materials for high temperatures, with special emphasis on aerospace applications. The stronger of these phases are all catastrophically brittle at and near ambient temperature and this difficulty has proved obdurate. A promising solution appears to be to alloy such phases in such a way that the result is a two-phase or multiphase material. The extra phases may be disordered and intrinsically ductile: the presence of such phases lowers the high-temperature strength but is apt to enhance the plastic deformability of the material even at ambient temperature. There are also instances of multiphase alloys in which all the phases are ordered intermetallics, some stronger and more brittle, others weaker and more ductile, and the end-result can be a promising combination of strength and ductility, as well as good creep resistance.

1. Introduction

An intermetallic, an abbreviated term which has come into universal use, is an ordered compound between two or more metals, in simple numerical atomic proportions. Intermetallics fall into two large families: weakly ordered ('reversible') ones like Cu_3Au or CuZn which become disordered on heating before they melt, and strongly ordered ('permanent') ones like NiAl , TiAl or Nb_3Al which remain ordered up to the melting temperature. The physical features of such phases, and the ordering transformation, have been investigated since the 1930s, but mechanical properties and their relation to microstructure have only been studied since the 1950s; at first, reversibly ordered phases were examined so that ordered and disordered states of the same compound could be compared, then attention shifted to permanently ordered ones, the aluminides of nickel, titanium, iron and niobium in particular. This latter kind of research became intensive in the mid-1970s and nowadays is probably the most active branch of physical metallurgy. The motive force for this great flood of research has been the hope that certain permanently ordered intermetallics might become prime contenders for high-temperature structural applications, in jet engines in particular, with a view to raising service temperatures and reducing weight. This kind of application is my main concern in this paper: it requires a high creep resistance at temperatures well above 700°C with reasonable resistance to brittle failure at ambient temperature.

Westbrook (1993), who has worked on intermetallics since the 1950s, has published a systematic account of the history of these researches in the context of

their times. The complex crystal chemistry of intermetallics has been surveyed by Ferro & Saccone (1993). A good account of the early studies of the plastic behaviour of intermetallics was published by Lawley (1967). Among the numerous overviews of recent researches on the mechanical behaviour of potentially usable, permanently ordered intermetallics, the following can be recommended as being particularly informative: the single articles by Fleischer *et al.* (1989), Yamaguchi & Umakoshi (1990), George *et al.* (1994) and Sauthoff (1995); the multiauthor compilations by Liu *et al.* (1992) and Fleischer & Westbrook (1994); and the conference proceedings in which Westbrook's (1993) paper appears. Fleischer & Westbrook's recent two-volume work is the most comprehensive, while Sauthoff's book chapter is the most thorough overview by a single author or group of authors. All of these treatments cover a wide range of intermetallics; there are many others that focus on particular families of compounds, such as the titanium aluminides, and there are also numerous conference proceedings from 1985 onwards, several of which (e.g. Whang *et al.* 1990; Izumi 1991) contain important overview papers. A fine critical survey, by a panel of experts, of current scientific issues in connection with the mechanical behaviour of intermetallics has been published by Yoo *et al.* (1993).

As a broad generalization, it is safe to say that the strength and also the resistance to high-temperature creep of intermetallics increases as the ordering energy increases. This quantity is a measure of the energy required to destroy the long-range order and replace it by a random distribution of atoms on the lattice. The reversible intermetallics all *ipso facto* have small ordering energies; FeAl, Ti₃Al and the very important Ni₃Al phase have intermediate ordering energies; phases such as NiAl, TiAl and Nb₃Al have high ordering energies. At the same time (and subject to complications arising from environmental effects), the brittleness, especially at ambient temperatures, increases in line with the ordering energies, and a great deal of recent research has been addressed to this problem, as it affects NiAl and TiAl in particular. This paper focuses on one promising approach for moderating the brittleness of strongly ordered intermetallics, which is the replacement of single-phase (also called 'monolithic') intermetallics by multiphase alloys.

2. Some practically important intermetallic phases

I shall emphasize two phases: Ni₃Al and NiAl. The first of these has received more attention than any other intermetallic, though its intrinsic importance for aerospace uses is now seen to be slight; NiAl has recently moved to the top of the agenda as a possible base intermetallic for jet engine blades and discs, while TiAl is seen as increasingly promising for other jet engine components and possibly for discs; it is also under development for automotive 'supercharger' turbine blades. Iron aluminides, though they have received much attention, are not strongly enough ordered to be of interest for jet engine temperatures and they are primarily targeted at terrestrial uses at modest temperatures, while the niobium aluminides, (with or without titanium added) though very strongly ordered and recently much studied, have not yet reached the stage at which their promise can be reliably assessed (see brief overviews by George *et al.* (1994) and Dimiduk *et al.* (1993)). TiAl, possibly the most important phase in present estimation, is briefly treated in a separate section.

Ni_3Al This cubic phase, with $\text{L}1_2$ structure, is the ordered component of conventional superalloys (see McLean's paper in this collection): such superalloys consist principally of an oriented, coherent and stable dispersion of Ni_3Al cuboids in a disordered matrix of almost the same lattice parameter. Ni_3Al has the striking property of a yield stress that rises with increasing temperature up to about 650°C (the anomalous yield point effect). This important characteristic has been the subject of a great deal of theory based on dislocation dynamics, and while the general outlines of an interpretation are agreed, details are still being vigorously debated. Experimental facts are set out in a general survey of the properties of Ni_3Al (Stoloff 1989) while the development of theoretical models is mapped out by Yamaguchi & Umakoshi (1990). A very clear early joint survey of both experimental and theoretical aspects of anomalous yield was published by two of the principal investigators in this field, Pope & Ezz (1984).

There are several other important aspects of this phase. Single crystals have long been known to be ductile, but polycrystals were perceived as intrinsically brittle until in 1978, in a study which has become a classic, Aoki & Izumi in Japan discovered that doping with small amounts of boron, which segregates to grain boundaries, can confer ductility on Ni_3Al polycrystals; later it was found that this benefit only obtains when there is a little more nickel than corresponds to stoichiometry. The origin of this ductilizing effect, and the related question whether grain boundaries in the pure compound are *intrinsically brittle*, has generated a huge literature, which is excellently summarised in the review by George *et al.* (1994). George *et al.* (1993), as part of an extensive research on environmental effects, found a way of making wholly uncracked Ni_3Al polycrystals and were able to prove that these were highly ductile in a high vacuum, but if moisture was present at a partial pressure of as little as a millionth of an atmosphere, atomic hydrogen was generated by seepage along grain boundaries and reaction with Al, which embrittles the grain boundaries. (This phenomenon of environmental embrittlement was found by Liu to be common to several intermetallics). Substantial chromium additions overcome the problem. Alloying with iron reduces the ordering energy and enhances the ductility (Horton *et al.* 1987); in fact, Flinn took out a patent as long ago as 1962 for a Ni_3Al alloy ductilized by iron (Flinn 1962).

The upshot of all this is that with proper precautions, Ni_3Al is intrinsically ductile in both single crystal and polycrystalline form. Its intrinsic strength as a single phase is insufficient for most uses beyond about 600°C , though as remarked it is the crucial constituent in (always multiphase) superalloys. A family of advanced nickel aluminides was developed by Liu and his colleagues in the early 1980s by alloying the binary phase with Cr, Fe and small amounts of several other metals. These are stronger, as well as being reasonably ductile; they have found several applications, including use in fuselage fasteners in aircraft. The real value of Ni_3Al will probably be recognised as residing in its potential for conferring some ductility on other, stronger phases.

NiAl This very strongly ordered cubic phase (the *virtual* critical temperature for disordering, far above the melting temperature, has been estimated as being above 4000°C), with the simple $\text{B}2$ structure, has excellent high-temperature strength and a considerably lower density than both Ni_3Al and superalloys, and so (after many years of mild academic concern) it has received an unparalleled measure of attention during the last decade, especially since the late 1980s. The

outcome of this research has been collected in an outstanding review by Miracle (1993), which incorporates 337 literature citations. While strong, light, oxidation-resistant and with good creep resistance and outstanding heat conductivity, the phase is extremely brittle at and some way above ambient temperature. Much of the recent research has addressed this recalcitrant problem. Darolia in America has been the industrial leader in this research; his large team at GE's engine factory has aimed directly at the production of *single-crystal* gas-turbine blades, as set forth in a very informative overview (Darolia *et al.* 1992). Single-crystal applications are immune from the generalization that multiphase alloys are to be preferred to single-phase ones.

Single crystals of favourable orientations show some ductility even at room temperature, and this ductility is considerably enhanced by small (*ca.* 0.1 at%) alloying additions of Fe, Mo or Ga; at larger solute contents the benefit disappears. The preferred interpretation of this at present is that the solute acts as a scavenger of unintended, embrittling interstitial solutes.

Polycrystalline NiAl in general is brittle, but in an important study, Hahn & Vedula (1989) discovered that very close to stoichiometry only, some 2% of tensile ductility can be achieved even at ambient temperature; the reasons remain mysterious. One tentative suggestion is that interstitial solute content is apt to be smaller for the stoichiometric alloy, and interstitials have also been adduced to account for indications that brittleness can be reduced by low-temperature heat-treatment. The normal brittleness of the polycrystalline alloy is attributed to the prevalence of $\langle 100 \rangle$ slip vectors, which imply that insufficient independent slip systems are available to enable individual grains to follow an externally imposed shape change; sustained attempts to alter the preferred slip vector by alloying have been unsuccessful. $\langle 111 \rangle$ slip is possible but suffers from a very high critical shear stress; it is not clear whether the problem is one of a lack of dislocation sources with this geometry or whether the Peierls–Nabarro stress for dislocation propagation is very high. Grain sizes below 20 μm also create some ductility.

Cotton *et al.* (1993a, b) have systematically studied the effect of various solutes on the behaviour of NiAl; substantial further hardening was found for some solutes, but no ductilization.

In the next section, various efforts to alleviate the brittleness of NiAl by introducing other, less brittle, phases will be outlined.

3. Multiphase alloys: generalities

Apart from the brittleness problem, there is a further crucial reason for preferring the multiphase version of an intermetallic to the monolithic (single-phase) form. When the microstructure is right, the creep resistance of the multiphase form (and this is what matters most in jet engine applications) is much better than that of the monolith. This is, after all, why the standard γ/γ' superalloy structure has held its own for so many years. The essential microstructural feature is the stable dispersion of small ordered γ' particles in an epitaxial relationship to a disordered γ matrix; dislocations are restricted to the narrow matrix channels between the particles. Naka *et al.* (1992) demonstrated the superiority of such a microstructure very clearly with the measurements in figure 1, taken from their paper. A 'single crystal' of an advanced superalloy, CMSX-2 (consisting actually of a single orientation of disordered matrix with a dispersion of γ' particles all in

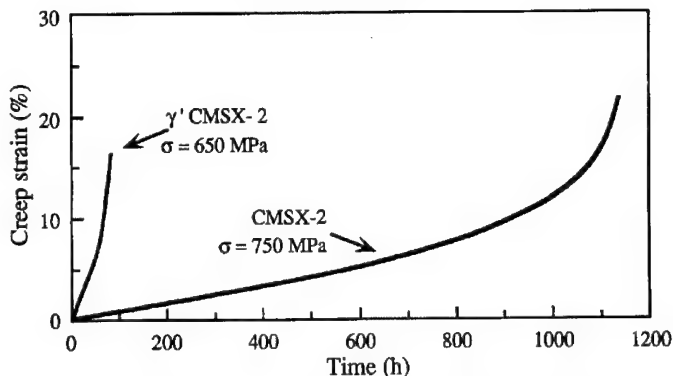


Figure 1. Creep curves at 760 °C for [001]-oriented single-phase CMSX-2 and two-phase γ' /CMSX-2 single crystals. After Naka *et al.* (1992).

parallel orientation) is compared in creep with another crystal consisting of monolithic γ' , at 760 °C. Although the stress acting on the superalloy crystal is 15% higher, yet its creep rate is much lower than that of the monolithic γ' crystal. (The tensile strengths of the two crystals at the same temperature are virtually identical.) In their investigation, Naka *et al.* go on to examine other, novel alloy systems which have similar microstructures (dependent on having almost the same lattice parameter for the two epitaxial phases), but use a (disordered) body-centred cubic matrix instead of the usual face-centred cubic one. They obtained interesting high-temperature properties for Fe–Ni₂AlTi and Nb(+Cr)–Ti₂AlMo alloys which possess this type of microstructure. This paper deserves careful study.

In a very recent paper, entitled 'The superiority of superalloys', Nabarro (1994) makes essentially the same point, though his argument is centred on TiAl–Ti₃Al alloys, which are to be discussed below. He cites an excellent paper (Nathal *et al.* 1989) which presents extensive evidence for Ni-base alloys along the same lines as that in figure 1. In his paper, he discusses at some length the deformation mechanisms which confer upon superalloys their exceptional creep resistance.

The general point can be made, in the light of Naka's and Nabarro's arguments, that the strategy of replacing monolithic by multiphase alloys does not necessarily entail a sacrifice of high-temperature creep resistance for the prize of enhanced room-temperature ductility. It is quite possible in principle to design alloys which combine both these benefits. One might object that the end-result of many years' research on intermetallics might then merely be a renewed emphasis on two-phase (disordered + ordered) alloys; the chemistry but not the microstructural principle would change from traditional superalloys. This is not necessarily so: as we shall see in the next section, improved alloys can consist of two or more ordered intermetallic phases, or of two ordered intermetallic phases plus one disordered phase. Indeed, most such alloys have an *ordered (o) matrix*; if such a matrix were associated with a disordered (d) epitaxial dispersoid, the result would be a mirror-image of a traditional superalloy, but quite generally, it is appropriate to regard an alloy with an ordered matrix as an intermetallic.

4. Multiphase alloys based on NiAl

No one has yet made a multiphase alloy with a NiAl matrix combined with a parallel epitaxial dispersion of another phase, but several alloys with other kinds

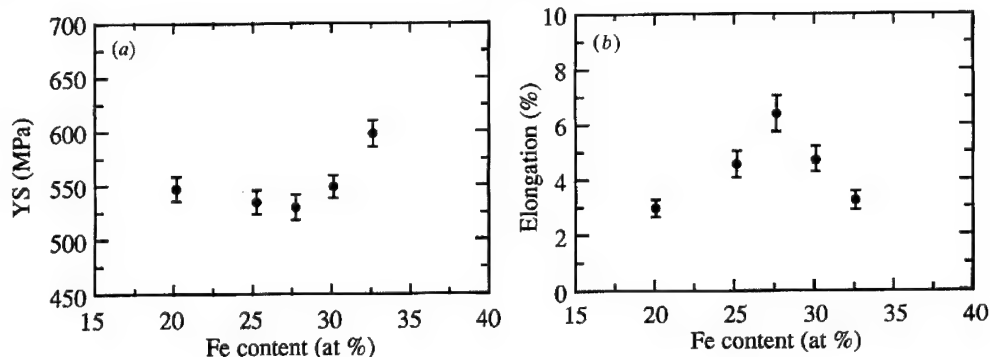


Figure 2. Plots of (a) yield stress and (b) elongation as a function of iron content for Ni(Al,Fe) alloys. After Tsau *et al.* (1992).

of epitaxy have been reported. Numerous metallurgists have examined multiphase alloys based on a major NiAl constituent, and some of them have most interesting properties—good strength combined with some ductility at ambient temperature. Few creep tests have been done as yet. The alloys examined hitherto fall into the following categories: (1) $\beta + \gamma'$; (2) $\beta + \gamma + \gamma'$; (3) $\beta + \beta'$; (4) $\beta + \beta' + \gamma'$. Here β represents (o) NiAl, γ represents a (d) FCC phase, γ' represents an (o) Ni₃Al-type phase, and β' represents an (o) Heusler phase such as Ni₂AlTi. Here there is space to mention only a few of the studies published in recent years.

(1) $\beta + \gamma'$ and (2) $\beta + \gamma + \gamma'$. If some of the aluminium in NiAl is replaced by iron, the alloy can have one or other of these phase structures, according to the iron content. Emphasis has been on Ni-20 at%Al-30 at%Fe, which consists of roughly equal amounts of rather finely divided β and ($\gamma + \gamma'$), the latter being a dispersion of minute γ' particles in a disordered matrix; there is some disagreement between investigators concerning the amount of disordered γ in this alloy, and this may depend upon details of heat treatment. The most detailed and recent study is by Guha *et al.* (1991). They compared the Ni-20Al-30Fe alloy with Ni-30Al-20Fe and with Ni-12Al-40Fe. The first had an ambient yield strength of 850 MPa (compared with a typical value of 250-450 MPa for pure polycrystalline NiAl) with up to 20% elongation; the second (an almost single-phase β alloy) had 800 MPa but only 2% elongation; the third (very like a normal γ/γ' superalloy) had 500 MPa and 28% elongation.

Figure 2 shows yield strength and elongation values measured for similar alloys by Tsau *et al.* (1992). They agree with Guha *et al.* in observing maximum elongation near 30 at% Al, but find lower yield stresses. The latter clearly depend upon the processing: Guha's alloys had been extruded, Tsau's were in cast form. These various alloys, incidentally, contain considerably more iron than Flinn's early patented alloys.

An earlier study (Pank *et al.* 1990) focused on ($\gamma + \gamma'$) alloys made by replacing Al in NiAl with 8-9 at%Co. Their alloys contain 'necklaces' of γ' surrounding the β grains and these alloys had 3-4% of elongation at room temperature. This kind of necklace structure is clearly not as effective as the more intimate phase mixture of the Ni-Al-Fe alloys.

Gibala and his collaborators have made important contributions to an understanding of how the extra phases in Ni-Al-Fe alloys are able to ductilize the alloys. Two important papers (Noebe *et al.* 1990; Misra *et al.* 1991) start from

research done in the 1970s in Gibala's laboratory on the enhancement of ductility of BCC metals by the use of surface films and also by preparing BCC and FCC two-phase alloys. They are among the very few who have examined Ni-Al alloys between 25 and 50 at% Al: they directionally solidified ($\beta + \gamma'$) $\text{Ni}_{70}\text{Al}_{30}$ and $\text{Ni}_{60}\text{Al}_{40}$ alloys and obtained up to 10% elongation as well as substantial strength rising with temperature to 600 °C, the best qualities of the two phases combined. They showed that the β phase contains many more dislocations than in single-phase β because of injection of dislocations from the γ' phase. Similar enhancement of dislocation populations in the β phase in $\text{Ni}_{50}\text{Al}_{30}\text{Fe}_{20}$ was also observed. Likewise, oxide surface films on single-phase NiAl crystals injected additional mobile dislocations into the bulk. This injection was recognized to be facilitated in the Ni-Al-Fe alloy because the β and ($\gamma + \gamma'$) phase fields were mutually oriented according to the Kurdjumov-Sachs relationship and this caused the glide planes in adjacent phase fields to be virtually parallel. Finally, the fine dispersion of γ' in the ($\gamma + \gamma'$) phase field served to arrest cracks originating from the β phase. (Guha *et al.* had also shown this.)

There is one other remarkable study of the behaviour of multiphase Ni-Al-Fe alloys, this time with Fe contents between 50 and 85 at%Fe. Jung & Sauthoff (1989) examined creep in alloys containing various Ni/Al/Fe proportions. Some of these were single-phase β (B2), others had either an α -iron matrix with β precipitates or else a β matrix with almost pure α -iron precipitates. An alloy of the latter kind was compared with a single-phase β alloy of the same composition as the matrix in the two-phase alloy (an interpolation method was used to make the comparison). The creep resistance of the ($\beta + \alpha$) alloy was higher than that of the single-phase β alloy, even though the α -iron precipitates were much softer than the β phase! The two-phase alloy was found to possess a threshold stress for creep: this threshold was successfully interpreted in terms of a model according to which the dislocation energy of a climbing matrix dislocation near the particle is reduced in the matrix-particle interface because of relaxation processes in the interface. This implies that the dislocation is attracted by the particle, and the overcoming of this attraction results in the threshold stress. Thus a soft disordered phase can enhance the creep resistance of an intermetallic matrix.

Generally, creep of intermetallics, especially multiphase alloys, has had rather less than the degree of attention it merits, and a recent critical overview of the theme by Sauthoff (1993) is therefore particularly welcome.

(3) ($\beta + \beta'$) and (4) ($\beta + \beta + \gamma'$). Many years ago, Polvani *et al.* (1976a, b) discovered what was in effect a superalloy based on a BCC lattice, but with both matrix and dispersoid in the form of ordered intermetallics, in the Ni-Al-Ti system. The matrix was β , that is, $\text{Ni}(\text{Al}, \text{Ti})$, while the dispersoid consisted of the strongly ordered Heusler phase, Ni_2AlTi , also denoted β' , which has the L2₁ structure. The high-temperature creep resistance of the dispersion was much greater than that of either constituent in single-phase form, consistently with the generalization made later by Nathal, Naka and Nabarro (quoted above). However, the alloy was hyperbrittle and development was soon aborted.

Recently, Yang *et al.* (1991, 1992a, b†) embarked on an alloy development pro-

† A very recent study related to Yang *et al.* (1992b) by Hsiung & Bhadeshia (1995) has shown that the ductility of these alloys can be further improved by extruding mixtures of the three single-phase powders.

gramme, based upon the hypothesis that the incorporation of a third, weaker and more ductile intermetallic phase, the γ' phase based on Ni_3Al , might serve to ductilize the $(\beta + \beta')$ $\text{Ni}-\text{Al}-\text{Ti}$ alloy without weakening it much. (Small amounts of quaternary additions (B or Cr or Fe) were also tried.) Figure 3a shows the three-phase $(\beta + \beta' + \gamma')$ field at 900 °C as determined in the 1992a paper, while figure 3b shows the room-temperature stress-strain characteristics in compression, compared with the unimproved $(\beta + \beta')$ alloys, and with a 'state-of-the-art' disc superalloy, U 720. The combination of strength and moderate ductility of the three-phase alloys, one of the most effective to be made up entirely of intermetallic phases, is clear. Several of the three-phase alloys proved to remain stronger than the U 720 up to about 650 °C (the anomalous yield characteristic of γ' helped in bringing this about). Figure 4 shows an example of the three-phase microstructure: this one has a β' matrix with β dispersoid; other alloys, nearer the NiAl corner of the three-phase triangle, have a β matrix with β' dispersoid. The β and β' are in parallel epitaxy, while the γ' is in Nishiyama-Wassermann orientation relationship with the matrix; this is not very different from the Kurdumov-Sachs relationship found by Gibala's team in $\text{Ni}-\text{Al}-\text{Fe}$ alloys. Microstructural analysis showed two things: dislocations were injected from the γ' into the β or β' phase, helped by a favourable orientation relationship (figure 5), and dislocations were more mobile in the very hard β' phase when it was in the form of a fine dispersoid than in the massive β' phase. No tensile or creep tests have as yet been performed.

The studies on the various $\text{Ni}-\text{Al}-\text{Fe}$ and on $\text{Ni}-\text{Al}-\text{Ti}$ alloys together make it clear that the strategy of marrying strong and brittle intermetallics with weaker and more ductile phases, in an intimate phase mixture to combine high-temperature strength with reasonable ambient ductility, works effectively. The Jung & Sauthoff paper suggests also that this strategy can be effective in enhancing creep resistance.

5. Multiphase alloys based on TiAl

Three titanium aluminides, all non-cubic, have all been intensively examined in recent years: Ti_3Al (reversibly ordered), TiAl and TiAl_3 (both permanently ordered). The view has gradually gained ground that alloys based on TiAl have the best overall prospects. In the very limited space available, it is only possible to make a few short comments on the multiphase aspects of TiAl .

TiAl has the $\text{L}1_0$ structure characteristic of CuAu . If the Al content is reduced slightly below 50 at%, then a two-phase structure including the hexagonal phase, Ti_3Al results. Such an alloy can either form a lamellar ('polysynthetic') structure, in which the two phases are in epitaxy within each grain, or by different heat treatments the alloy can be turned into a divorced, 'equiaxed' form. Other heat treatments can produce an intermediate structure. Grain size can also be varied within wide limits. The balance of ductility, toughness, strength and creep resistance varies according to the microstructure type, and recent researches have examined these trade-offs in great detail; thus, lamellar microstructures have better creep resistance and also higher toughness than equiaxed ones, in spite of having a lesser ductility. Dislocation 'injection' does not seem to have been specifically examined. The most recent concise survey is in George *et al.* (1994). An excellent survey of the effect of processing, and especially of heat-treatment,

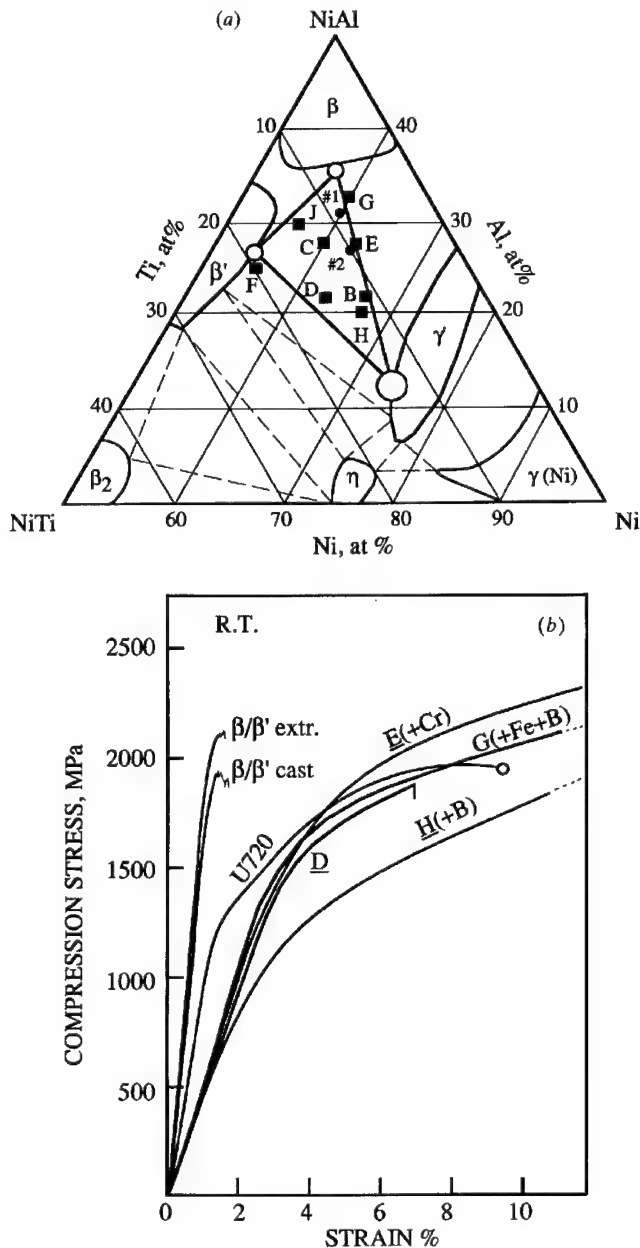


Figure 3. (a) The three-phase ($\beta + \beta' + \gamma'$) field in the Ni-Al-Ti system at 900 °C; the circles represent estimates of experimental inaccuracy in locating the corners of the three-phase triangle. Compositions of alloys examined are shown. After Yang *et al.* (1992a). (b) Compressive stress-strain curves at room temperature for several Ni-Al-Ti alloys, binary and ternary, and of a commercial superalloy (U 720). Some of the alloys contain small quaternary additions of other elements. After Yang *et al.* (1992b).

on the microstructure of ($\text{TiAl} + \text{Ti}_3\text{Al}$) alloys is by Martin *et al.* (1993), while a paper by Yamaguchi & Inui (1953) focuses on properties. Nabarro (1994) has examined in detail the ways in which $\text{TiAl}-\text{Ti}_3\text{Al}$ alloys resemble conventional

Figure 4

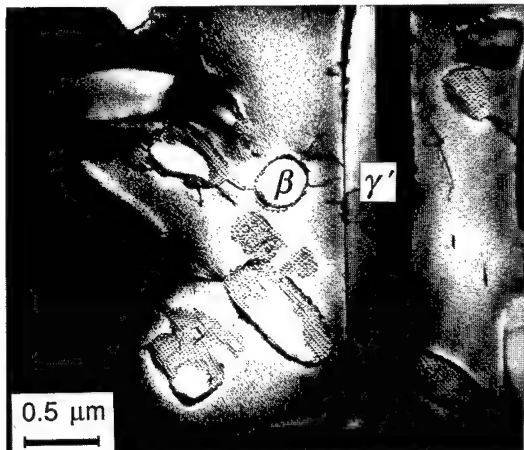


Figure 5

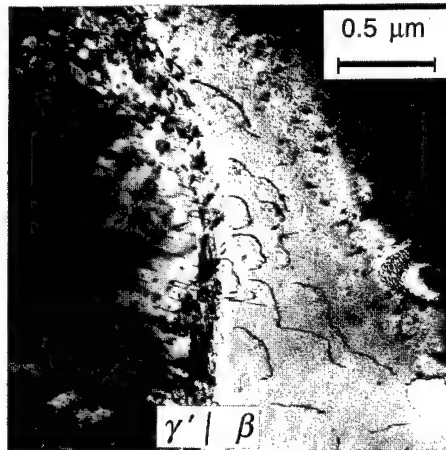


Figure 4. Electron micrograph of alloy D (see figure 2a) showing a twinned γ' lath and β islands (in parallel epitaxy) in a β' matrix. After Yang *et al.* (1992b).

Figure 5. Dislocations 'injected' from the γ' phase into the β' phase across a semicoherent boundary. After Yang *et al.* (1992b).

superalloys. The emphasis on the effects of minutely varied heat treatments, as noted in recent TiAl research, has yet to be seen in research on NiAl-based multiphase alloys.

References

Cotton, J. D., Noebe, R. D. & Kaufman, M. J. 1993a The effects of chromium on NiAl intermetallic alloys: Microstructures and mechanical properties. *Intermetallics* **1**, 3–20.

Cotton, J. D., Noebe, R. D. & Kaufman, M. J. 1993b Ternary alloying effects in polycrystalline β -NiAl. In *Structural intermetallics* (ed. R. Darolia, J. J. Lewandowski, C. T. Liu, P. L. Martin, D. B. Miracle & M. V. Nathal), pp. 513–522. Warrendale, PA: The Minerals, Metals and Materials Society.

Darolia, R., Lahrman, D. F., Field, R. D., Dobbs, J. R., Vhang, K. M., Goldman, E. H. & Konitzer, D. G. 1992 In *Ordered intermetallics: physical metallurgy and mechanical behaviour* (ed. C. T. Liu, R. W. Cahn & G. Sauthoff), pp. 679–698. NATO ASI Series, vol. 213. Dordrecht: Kluwer.

Dimiduk, D. M., Mendiratta, M. G. & Subramanian, P. R. 1993 Development approaches for advanced intermetallic materials – historical perspective and selected successes. In *Structural intermetallics* (ed. R. Darolia, J. J. Lewandowski, C. T. Liu, P. L. Martin, D. B. Miracle & M. V. Nathal), pp. 619–630. Warrendale, PA: The Minerals, Metals and Materials Society.

Ferro, R. & Saccone, A. 1993 Structure of intermetallic compounds and phases. In *Structure of solids* (ed. V. Gerold), pp. 123–215. *Materials science and technology*, vol. 1 (ed. R. W. Cahn, P. Haasen & E. J. Kramer). Weinheim: VCH.

Fleischer, R. L., Dimiduk, D. M. & Lipsitt, H. A. 1989 Intermetallic compounds for strong high-temperature materials: status and potential. *A. Rev. Mater. Sci.* **19**, 231–263.

Flinn, P. A. 1962 US Patent 3 021 211, for high-temperature nickel base alloys.

George, E. P., Liu, C. T. & Pope, D. P. 1993 Intrinsic ductility and environmental embrittlement of binary Ni_3Al . *Scr. metall. Mater.* **28**, 857–862.

George, E. P., Yamaguchi, M., Kumar, K. S. & Liu, C. T. 1994 Ordered intermetallics. *A. Rev. Mater. Sci.* **24**, 409–451.

Guha, S., Munroe, P. R. & Baker, I. 1991 Room temperature deformation behavior of multiphase Ni–20 at%Al–30 at%Fe and its constituent phases. *Mater. Engng A* **131**, 27–37.

Hahn, K. H. & Vedula, K. 1989 Room temperature tensile ductility in polycrystalline NiAl. *Scr. metall.* **23**, 7–12.

Horton, J. A., Liu, C. T. & Santella, M. L. 1987 Microstructures and mechanical properties of Ni₃Al alloyed with iron additions. *Metall. Trans. A* **18**, 1265–1277.

Hsiung, L. C. & Bhadeshia, H. K. D. H. 1995 *Metall. Trans. A*. (In the press.)

Izumi, O. (ed.) 1991 *Proc. Int. Symp. on Intermetallic Compounds – Structure and Mechanical Properties* (JIMIS-6). Sendai: The Japan Institute of Metals.

Jung, I. & Sauthoff, G. 1989 Creep behaviour of the intermetallic B2 phase (Ni,Fe)Al with strengthening soft precipitates. *Z. Metallk.* **80**, 484–489.

Lawley, A. 1967 In *Intermetallic compounds* (ed. J. H. Westbrook), pp. 464–490. New York: Wiley.

Liu, C. T., Cahn, R. W. & Sauthoff, G. (eds) 1992 *Ordered intermetallics: physical metallurgy and mechanical behaviour*. NATO ASI Series, vol. 213. Dordrecht: Kluwer.

Martin, P. L., Rhodes, C. G. & McQuay, P. A. 1993 Thermomechanical processing effects on microstructure in alloys based on gamma-TiAl. In *Structural intermetallics* (ed. R. Darolia, J. J. Lewandowski, C. T. Liu, P. L. Martin, D. B. Miracle & M. V. Nathal), pp. 177–186. Warrendale, PA: The Minerals, Metals and Materials Society.

Miracle, D. B. 1993 The physical and mechanical properties of NiAl. *Acta metall. Mater.* **41**, 649–684.

Misra, A., Hartfield-Wünsch, S. & Gibala, R. 1991 Ductility enhancement of Ni–Fe–Al B2 ordered alloys from dislocation sources provided by surface films and internal interfaces. In *Proc. Int. Symp. on Intermetallic Compounds – Structure and Mechanical Properties* (JIMIS-6) (ed. O. Izumi), pp. 597–601. Sendai: The Japan Institute of Metals.

Nabarro, F. R. N. 1994 The superiority of superalloys. *Mater. Sci. Engng A* **184**, 167–171.

Naka, S., Thomas, M. & Khan, T. 1992 Potential and prospects of some intermetallic compounds for structural applications. *Mater. Sci. Technol.* **8**, 291–298.

Nathal, M. V., Fiaz, J. O. & Miner, R. V. 1989 High temperature creep behavior of single crystal gamma prime and gamma alloys. *Mater. Res. Soc. Symp. Proc.* **133**, 269–274.

Noebe, R. D., Bowman, R. R., Kim, J. T., Larsen, M. & Gibala, R. 1990 The potential for ductility enhancement from surface and interface dislocation sources in NiAl. In *High temperature aluminides and intermetallics* (ed. S. Whang, C. T. Liu, D. P. Pope & J. O. Stiegler), pp. 271–300. Warrendale, PA: The Minerals, Metals and Materials Society.

Pank, D. R., Nathal, M. V. & Koss, D. A. 1990 Microstructure and mechanical properties of multiphase NiAl-based alloys. *J. Mater. Res.* **5**, 942–949.

Polvani, R. S., Tzeng, W.-S. & Strutt, P. R. 1976 High temperature creep in a semi-coherent NiAl–Ni₂AlTi alloy. *Metal. Trans. A* **7**, 33–40.

Pope, D. P. & Ezz, S. S. 1984 Mechanical properties of Ni₃Al and nickel-base alloys with high volume fraction of γ' . *Int. Metals Rev.* **29**, 136–167.

Sauthoff, G. 1993 The high temperature deformation of intermetallic alloys. In *Structural intermetallics* (ed. R. Darolia, J. J. Lewandowski, C. T. Liu, P. L. Martin, D. B. Miracle & M. V. Nathal), pp. 845–860. Warrendale, PA: The Minerals, Metals and Materials Society.

Sauthoff, G. 1995 Intermetallics. In *Structure and properties of nonferrous alloys* (ed. K. H. Matucha). Materials Science and Technology, vol. 8 (ed. R. W. Cahn, P. Haasen & E. J. Kramer). Weinheim: VCH.

Stoloff, N. S. 1989 Physical and mechanical metallurgy of Ni₃Al and its alloys. *Int. Mater. Rev.* **34**, 153–183.

Tsau, C. H., Jang, J. S. C. & Yeh, J. W. 1992 Microstructures and mechanical behaviors of Ni–Al–Fe intermetallic compounds. *Mater. Sci. Engng A* **152**, 264–268.

Westbrook, J. H. 1993 Intermetallics: their origins, status and future. In *Structural intermetallics* (ed. R. Darolia, J. J. Lewandowski, C. T. Liu, P. L. Martin, D. B. Miracle & M. V. Nathal), pp. 1–15. Warrendale, PA: The Minerals, Metals and Materials Society.

Westbrook, J. H. & Fleischer, R. L. 1994 *Intermetallic compounds: principles and practice*. New York: Wiley.

Whang, S. H., Liu, C. T., Pope, D. P. & Stiegler, J. O. (eds) 1990 *High temperature aluminides and intermetallics*. Warrendale, PA: The Minerals, Metals and Materials Society.

Yamaguchi, M. & Umakoshi, Y. 1990 The deformation behaviour of intermetallic superlattice compounds. *Prog. Mater. Sci.* **34**, 1–148.

Yamaguchi, M. & Inui, H. 1993 TiAl compounds for structural applications. In *Structural intermetallics* (ed. R. Darolia, J. J. Lewandowski, C. T. Liu, P. L. Martin, D. B. Miracle & M. V. Nathal), pp. 127–142. Warrendale, PA: The Minerals, Metals and Materials Society.

Yang, R., Leake, J. A. & Cahn, R. W. 1991 A microstructural study of a Ni_2AlTi – $\text{Ni}(\text{Al},\text{Ti})$ – $\text{Ni}_3(\text{Al},\text{Ti})$ three-phase alloy. *J. Mater. Res.* **6**, 343–354.

Yang, R., Saunders, N., Leake, J. A. & Cahn, R. W. 1992a Equilibria and microstructural evolution in the $\beta/\beta'/\gamma'$ region of the Ni–Al–Ti system: modelling and experiment. *Acta metall. Mater.* **40**, 1553–1562.

Yang, R., Leake, J. A. & Cahn, R. W. 1992b Three-phase ($\beta + \beta' + \gamma'$) Ni–Al–Ti–(Cr,Fe) alloys for high-temperature use. *Mater. Sci. Engng A* **152**, 227–236.

Yoo, M. H., Sass, S. L., Fu, C. L., Mills, M. J., Dimiduk, D. M. & George, E. P. 1993 Deformation and fracture of intermetallics. *Acta metall. Mater.* **41**, 987–1002.

Discussion

D. R. F. WEST (*Imperial College, London, UK*). In the TiAl-based alloys there is considerable interest in the addition of other elements in relatively small amounts. Is there beginning to emerge a clearer role of such additions and how they act to influence alloy properties?

R. W. CAHN. Yes, a picture is beginning to emerge about the role of ternary or quaternary additions to TiAl. For an excellent, concise discussion of this see Huang & Chesnutt (1994). The efficacy of any alloying additions depends on careful control of the Ti/Al ratio, to ensure the right two-phase microstructure. When this is right, V, Mn, and Cr generally enhance ductility. Arguments based on stacking-fault energy or c/a ratios do not seem to be helpful, and the most convincing arguments bear on the tendency of these additives to substitute preferentially for Al, thereby ‘reducing the covalency of the Ti–Al bond’, especially when there is a two-phase microstructure. Other additives, Nb in particular, help to enhance oxidation resistance, while still others (notably Er) mop up excessive dissolved oxygen. One has to hope that the different functions of additives do not interfere with each other!

D. J. DUNSTAN (*University of Surrey, UK*). Professor Cahn remarks that it is surprising that the iron dispersoid strengthens the material because the iron would be very soft. Could there not, however, be size effects? Semiconductors which are very soft at crystal growth temperatures can support high elastic strains (over 1%), provided the strained layer is very thin. Perhaps similar size effects strengthen the iron?

M. MCLEAN (*Imperial College, London, UK*). Professor Cahn suggests that intermetallics can be strengthened by the incorporation of entrained soft, disordered phases. The ultimate soft, disordered phase is a gas (or void). Is there evidence that a porous intermetallic is stronger than the fully dense material?

J. W. MARTIN (*Oxford University, UK*). There are two further points about strengthening by voids: firstly, in the absence of applied tensile stress they are essentially soluble at high temperature and will slowly disappear by sintering.

Secondly, in the presence of a sufficient tensile stress they will grow, possibly until the specimen fractures by void coalescence. So their presence in a microstructure may lead to impaired creep ductility. The presence of a dispersion of an insoluble soft phase will not necessarily be deleterious to creep ductility in the same way, as the particles, when sheared, would be unlikely to fracture and thus generate a microvoid. Only when particle-matrix decohesion occurred would impairment of ductility be a possibility by this mechanism.

R. W. CAHN. Voids can certainly strengthen a metal or alloy if they are small enough, and they are able to trap grain boundaries and prevent softening by recrystallization. If they are coarse, they are bad news: thus in intermetallics made by self-sustaining high-temperature synthesis, incomplete densification is apt to embrittle the product beyond its normal degree. But as voids become smaller, the extreme is reached when a void becomes a lattice vacancy. Recently, Chang *et al.* (1993) demonstrated that the hardness and the (unusually large) vacancy concentration in FeAl are closely correlated.

D. MORRIS (*University of Neuchâtel, Switzerland*). We should note that most probably useful intermetallics are multiphase, but not all. The multiphase concept is perhaps required for strengthening but most probably for ensuring creep resistance and toughening. For iron aluminides, however, the situation is different. While not aerospace materials, these have high potential, and indeed are already being used, as high-temperature, oxidation- and corrosion-resistant structural steels. The materials under development, whether disordered Fe/16%Al, DO_3 ordered Fe/25–28%Al or B2-ordered Fe/35+%Al, are essentially single-phase alloys, where strengthening is achieved by the ordered state, by grain refinement, and by solute additions (including perhaps vacancies). At the same time, dislocation multiplication and mobility is sufficiently good that plasticity, including at notch tips, is sufficient for the single-phase materials to be used as engineering materials.

R. W. CAHN. Yes, indeed, I quite agree. But then, the iron aluminides are relatively weakly ordered, and the brittleness problem is apt to be really obstinate only in those intermetallics which are strongly ordered, so then the multiphase solution becomes imperative.

Additional references

Chang, Y. A., Pike, L. M., Liu, C. T., Bilbrey, A. R. & Stone, D. S. 1993 *Intermetallics* **1**, 107–115.
Huang, S. C. & Chesnutt, J. C. 1994 Gamma TiAl and its alloys. In *Intermetallic compounds, principles and practice* (eds J. H. Westbrook & R. L. Fleischer), vol. 2, pp. 73–90. Wiley.

Ceramics and ceramic composites as high-temperature structural materials: challenges and opportunities

BY A. G. EVANS

*Division of Applied Sciences, Harvard University, Cambridge, MA 02138, USA
and Materials Department, University of California, Santa Barbara,
CA 93106, USA*

Perspectives are presented on the development of ceramics and ceramic matrix composites (CMCs) for high-temperature structural components. The emphasis is on design requirements and their role in directing research toward actual products. An important theme concerns the relative roles of fracture toughness and inelastic strain (ductility) in the application of materials in primary structures. Ceramics with high toughness have been developed, but macroscopic inelasticity has not been achieved. Robust design procedures have yet to be developed for such materials. This deficiency, as well as relatively high manufacturing and qualification costs, has retarded their commercial exploitation. Strategies for addressing this problem are considered.

CMCs are more 'design friendly' because they exhibit appreciable inelastic strain, in shear and/or in tension. Such strain capacity is an efficient means of redistributing stress and eliminating stress concentrations. The design process thus has commonality with that used for metallic components. Also, processing approaches that provide acceptable manufacturing costs have been devised. The sources of the inelastic strain are examined and models that lead to a constitutive law are described. Some examples are given of its FEM implementation for design calculations.

A limitation on the extensive exploitation of CMCs in high temperature systems has been the existence of degradation mechanisms. These include a 'pest' phenomenon, manifest as oxidation embrittlement in non-oxide CMCs, as well as excessive creep in oxide-oxide CMCs. These degradation mechanisms are discussed, and pathways to affordable high-temperature CMCs are analysed.

1. Introduction

A high-temperature materials research goal for over 20 years has been the creation of structural materials capable of reliable operation, in oxidizing conditions, under tensile stress, at temperatures in the 1200–1400 °C range. This goal has yet to be realized. The strategy has been to begin with materials inherently stable and also deformation resistant at these temperatures, typically ceramics or intermetallics. Components made from such materials are brittle and cannot be used reliably when subject to tensile stress. The addition of reinforcements is

envisioned as the means of introducing damage tolerance without compromising stability and deformation resistance. In practice, various approaches have been found that provide damage tolerance, but the stability and deformation resistance have always been detrimentally affected. Moreover, at least one property of such materials has invariably been found deficient: either toughness or creep strength or embrittlement sensitivity. High manufacturing costs are also problematic in many cases. The consequence is that comparisons with existing metallic systems, on a cost/benefit basis, are not favorable. The result has been a dearth of applications. An alternative research and development strategy is needed if such materials are to be implemented on a large scale in commercial systems. The ingredients include an intelligent processing regimen along with a cost estimation methodology, as well as robust performance models to supplement the manufacturing and design engineering.

The initial goal of the research on monolithic ceramics during the 1960s was to create 'ductile' ceramics by inducing plasticity. This goal did not have a meaningful technological outcome for one principal reason. Even when some ductility was achieved, the materials still had a low fracture toughness and were prone to catastrophic rupture (Clarke *et al.* 1967; Wiederhorn *et al.* 1970). This seeming paradox arose because cracks remained sharp instead of exhibiting plastic blunting. A complete theory describing this phenomenon has yet to be developed, although recent progress has been considerable (Rice & Beltz 1994; Xu *et al.* 1995; Hirsch & Roberts 1991).

The practical consequence of the early work on ceramics was a change in emphasis toward research on *toughening mechanisms*. The effort on 'toughened' ceramics resulted in major discoveries of mechanisms with robust theories capable of characterizing the principal effects. However, the technological ramifications have still been minimal. The lack of a translation of the physics and mechanics to the technology seems to reside in two deficiencies. (1) The high-toughness materials, when tested in tension, are still macroscopically linear. The consequence is that strain concentration sites are also regions of high stress. That is, the material has no mechanism for redistributing stress. The importance of this 'deficiency' has been highlighted as a result of the development of ceramic matrix composites. (2) The implications of the toughening to the design of ceramic components has not been formulated in a manner that can be explicitly used by the design engineer. (Note that the toughness does not appear as a parameter in design codes used for metals, ceramics or composites.)

The development of continuous fibre-reinforced ceramics (ceramic matrix composites (CMCs)) was instituted as a means of obviating the limitations associated with the 'toughened' monolithic materials. Following some crucial discoveries in the 1970s (Phillips 1974; Aveston *et al.* 1971) a large effort was made starting in the 1980s (Prewo 1987; Naslain, this volume). The major finding during this period was that composites can be microstructurally designed to induce inelastic deformation mechanisms in either tension or shear (Evans & Zok 1994). These provide sufficient strain to enable extensive stress redistribution at strain concentration sites, such as slots, joints and attachments (Cady *et al.* 1994; Mackin *et al.* 1995). This capability has allowed a design strategy similar to that used with metals. These advantages have given a stimulus to the continued development of composites. However, there are performance limitations governed by high-temperature degradation mechanisms.

2. Technology for design

(a) Monolithic ceramics

(i) Stochastic principles

There have been two complementary philosophies for implementing ceramics (Lange 1989; Evans 1982). One approach has been to elevate the fracture toughness. The other has emphasized a reduction in the size of the flaws introduced by processing and machining. Neither approach has had a profound effect on the technology, despite major scientific and engineering advances in both areas. Designing a load-bearing component using a linear material requires the following steps. (1) An elastic analysis is performed to obtain the stresses. (A problem arises for zones having high localized strain. Then there are mesh effects and sometimes singularities, particularly at joints, attachments and contacts. A design decision must be made about how to address these regions. Some approaches have been recommended, but software has not been made available. While these areas remain problematic, they are not given further consideration.) (2) The survival probability of each element within the finite-element mesh is evaluated using the principles of weakest link statistics (Freudenthal 1967; Matthews *et al.* 1976). The procedure required for this purpose is understood and has been implemented in software programs, CARES (among others), compatible with finite-element codes. The programs calculate the survival probability ϕ_s of volume elements, δV , using

$$\phi_s = 1 - \delta V \int_0^{\bar{\sigma}} g(S) dS, \quad (2.1)$$

where $g(S) dS$ is the number of flaws in unit volume having strength between S and $S + dS$, and $\bar{\sigma}$ is the average stress within the element at the design load. There is a corresponding formula for the surface elements. The survival probability of the component is the product of the survival probabilities of all of the elements (volume plus surface), $\Pi(\phi_s)$. Usually, $g(S) dS$ is approximated by a power law (Weibull distribution) with a scale parameter, S_0 , and a shape parameter, m . When the element size is small (of order the separation between the large extreme of the flaws in the population), this takes the form (Weibull 1939),

$$g(S) = mS^{m-1}/S_0^m. \quad (2.2)$$

The CARES software has the capability of performing these evaluations for any multiaxial state of stress.

The limitation on the practical utilization of the code is in the means for obtaining the data. It is crucial to note that the integration of (2.1) is between zero and the design stress. However, data are normally obtained using flexure tests or tension tests on small specimens. The consequence is that, because of the volume scaling inherent in weakest link statistics (2.1), these tests provide information about the flaw population at stresses above the design stress. An extrapolation of the data is implied (figure 1a). A robust procedure for conducting the extrapolation of the available data and for evaluating the confidence limits has not been made accessible to the design engineer. It is usually asserted that the scale and shape parameters obtained from laboratory data apply with high confidence at stresses below the design stress. Such assertions are not valid. Moreover, since (2.2) has no fundamental basis. A polynomial fit to the data could be made

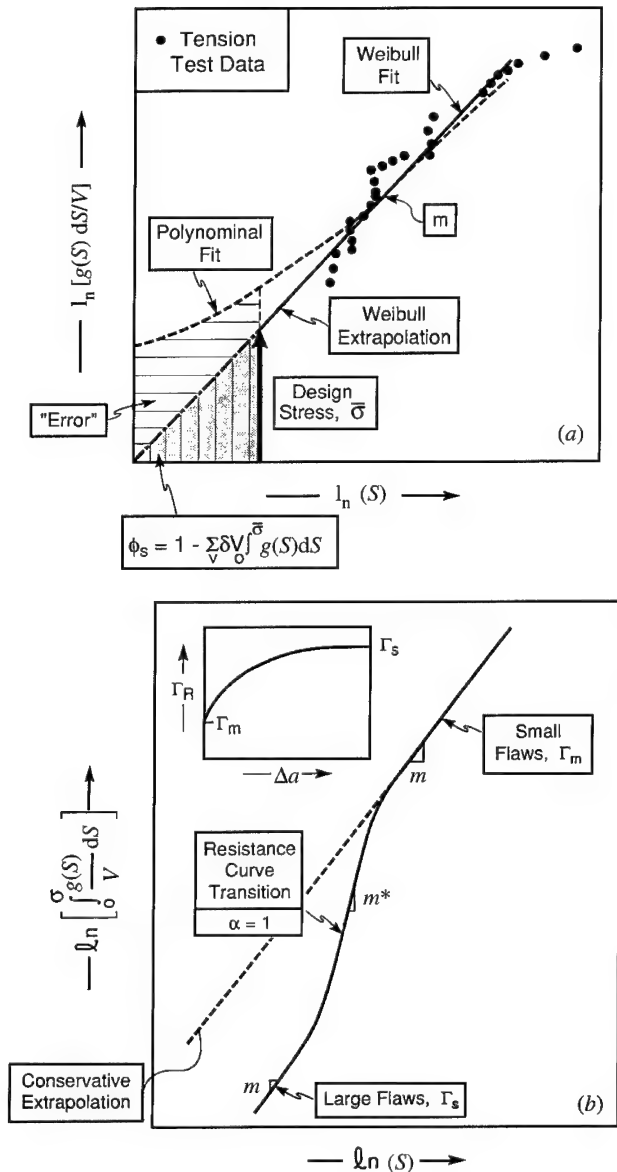


Figure 1. (a) Typical statistical data obtained upon tension testing of ceramics. The extrapolation from the (linear) Weibull fit is shown, as well as the extrapolation from a polynomial fit. These indicate the large difference in the projected survival probability (note that the axes are logarithmic). (b) Superior confidence associated with extrapolation when a toughened ceramic is used at the optimum value of the strengthening index, α . Note that there is a change in slope from m to m^* when $\alpha \approx 1$. This change enables a larger survival probability for the same flaw population. It is important to appreciate that levels of toughening having smaller values of α do not improve the survival probability.

with equal fidelity, resulting in substantial differences in the predicted survival probability (figure 1a).

To obviate this problem and to assure that an acceptable level of confidence is attributed to m and S_0 , tests should be performed on relatively large tension specimens to obtain data close to the design stress (figure 1a). The gathering of

such data is costly. The costs can probably be justified when the processing and machining have been standardized and subjected to a rigorous control regimen, such that the flaw populations are stable and consistent. In this case, results from proof tests and field tests augment the laboratory data and greatly enhance the confidence levels assigned to the design. Otherwise, batch-to-batch variations and deviations among machining runs result in flaw population changes that have to be recalibrated to provide the level of confidence required for design. The associated costs are usually prohibitive. There is a clear opportunity to implement a processing regimen using a control strategy that regulates the scale and shape parameters that characterize the flaw population.

(ii) *Toughness in design*

An early discovery in the quest for toughening mechanisms was the prevalence of resistance-curve behaviour (McMeeking & Evans 1982; Green *et al.* 1989; Evans 1990; Stump & Budiansky 1988). The main focus of the subsequent research was on the quantification of the resistance through a mechanism-based development of bridging laws and inelastic constitutive laws. However, all of the approaches still resulted in linear stress-strain characteristics upon tensile testing. Since non-linearity was not achieved, the elastic design strategy described above must still be implemented. The toughness itself does not enter the design code. Only its influence on the stochastic strength parameters, m and S_0 is relevant to design (Kendall *et al.* 1986; Cooke & Clarke 1988). This influence can be characterized by a non-dimensional strengthening index, designated α , given by

$$\alpha = (a_0/h_s)(\Delta\Gamma_s/\Gamma_m)^2, \quad (2.3)$$

where a_0 is the initial flaw size, $\Delta\Gamma_s$ is the steady-state toughness elevation, Γ_m the reference toughness in the absence of the toughening mechanism, and h_s is the crack extension needed to reach steady state. This index is a measure of the toughening rate, as the crack extends. Its effect is reflected in the magnitude of the ensuing strength, S , given by

$$\frac{S}{S_*} = \left\{ \frac{\alpha\sqrt{(1+\alpha)}}{\alpha + (\sqrt{(1+\alpha)} - 1)^2} \right\}^{1/2}, \quad (2.4)$$

where S_* is the strength at toughness Γ_m , in the absence of toughening.

The key result provided by this analysis is illustrated in figure 1b. When the flaws are very small ($\alpha \ll 1$), fracture occurs unstably and the strength is unaffected by the toughening. Conversely, larger flaws are able to experience stable crack growth and the strength may substantially exceed the untoughened magnitude. The transition between the small and large crack regions has particular significance (figure 1b). In this region, the effective shape parameter m^* becomes relatively large ($m^* > m$). The consequence is that the survival probabilities, estimated by extrapolation from the small flaw data obtained in typical laboratory tests would be conservative, provided that the processing and machining flaws that dictate the strength near the design stress satisfy, $\alpha \approx 1$. An evident goal for toughening and processing research is to identify and incorporate mechanisms that enable α to be of order unity at the design stress. Such optimization alleviates (but does not solve) the extrapolation problem.

(b) *Ceramic matrix composites*(i) *Stress redistribution*

Ceramic matrix composites (CMCs) have two characteristics that greatly facilitate their use as structural materials. (1) Their microstructural design imparts macroscopic inelastic deformation modes. These modes are very efficient at redistributing stress. The important consequence is that stress concentrations are largely eliminated at locations subject to large local strains. Sufficient understanding of the deformation has been gained to enable the development of constitutive laws which have already been implemented in finite-element codes such as ABAQUS (Xia & Hutchinson 1994; Xia *et al.* 1993; Genin & Hutchinson 1995). The calculations demonstrate that the inelastic strain allows the stresses to spread out and have relatively low peak magnitudes.

(2) The design procedure compares the peak stresses to the ultimate strengths, in tension (UTS) and shear, as governed by the *in situ* fibre bundle strength. The stochastic parameters that govern the fibre bundle strength are 'design friendly'. In particular, the shape parameter, m , is quite large (small variability) because the strength is controlled by multiple fibre failures, rather than the weakest link (Curtin 1991). This distribution approaches a Gaussian form (as in metals) and designers use standard deviations to obtain design allowables, enabling a high confidence level to be assigned to the survival probability.

(ii) *Inelastic strains*

The inelastic deformation of woven or laminated 0/90 CMCs in both tension and shear, occurs in accordance with one of two behaviours, designated class II and class III (Evans & Zok 1994). The former, are 'matrix dominated'. The inelastic strains are largely determined by matrix cracking, with interface debonding and frictional slip. The UTS is dictated by the fibre failure characteristics. In the class III, 'fibre dominated' CMCs, the inelastic tensile strains are controlled by the fibres, whereas the inelastic shear strains are governed by matrix damage. In both types of CMC, stress redistribution is dominated by the inelastic strains arising from matrix damage, particularly those in shear and in ± 45 tension, which occur at the lowest stress levels (figure 2).

(iii) *Design calculations*

Representative design calculations for CMCs are used to illustrate the importance of stress redistribution mechanisms. Calculations have been performed for tensile plates containing holes or slots. Others have been conducted for pin-loaded holes in order to simulate mechanical attachments made to either superalloy or Ti alloy supports (figure 3). Experimental comparisons obtained using Moire interferometry substantiate the fidelity of the calculations (Cady *et al.* 1994; Mackin *et al.* 1995; Genin & Hutchinson 1995). These measurements give the full strain distribution around the hole.

Both the calculations and Moire measurements illustrate the difference between class II and class III CMCs. For the former, strain concentrations persist. Yet, the stress concentration is small because the inelastic deformation caused by matrix cracking provides an effective means of redistributing stress. Conversely, for class III CMCs, the shear strain localizes into bands, causing both the strain and stress concentrations to be substantially reduced.

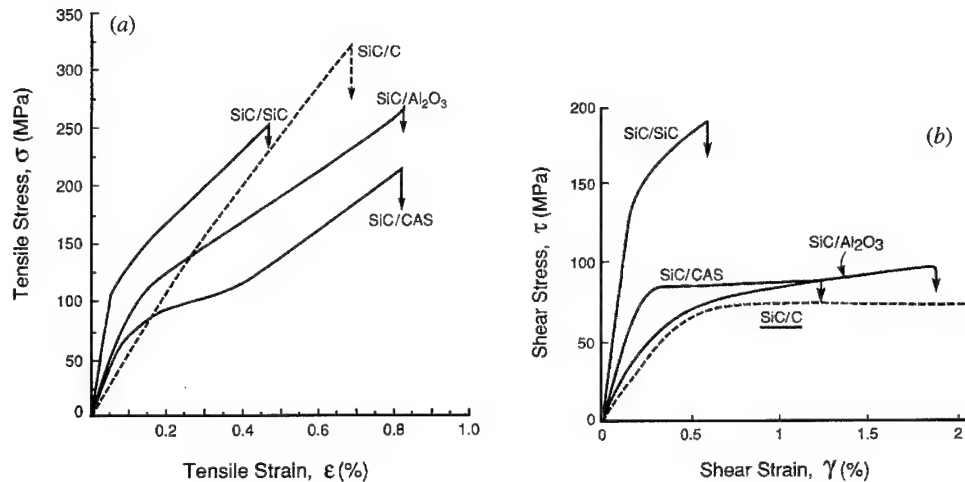


Figure 2. Typical stress-strain curves for CMCs: (a) tension; (b) shear. The class II CMCs are represented by the solid lines and the class III CMCs by the dotted lines.

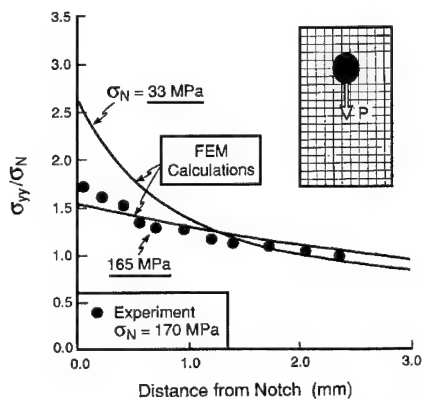


Figure 3. A pin loaded hole test performed on SiC-CAS showing the stress across the net section. The calculated and measured values are indicated. The stresses are obtained from the strains by Moire interferometry. This can be done because the lateral strains are essentially zero.

The stress-strain calculations and measurements are not in complete accordance with other experimental findings for sharp notches. Tension tests reveal notch insensitive strengths, indicative of the material's ability to completely eliminate stress concentrations (figure 4). Such behavior is not predicted by inelastic FEM calculations. The implication is that another stress redistribution mechanism operates in CMCs. It is believed that fibre pull-out is the operative mechanism (figure 4). When fibres begin to fail near the slot, their stochastics dictate a spatial distribution of fibre failure sites. This causes pull-out to occur at the matrix cracks, which reduces the stress on the intact fibres and enables additional load to be imposed before catastrophic failure occurs in the composite (Bao & Suo 1993). A complete simulation capability for design purposes requires that this pull-out effect be included. This implementation is in progress.

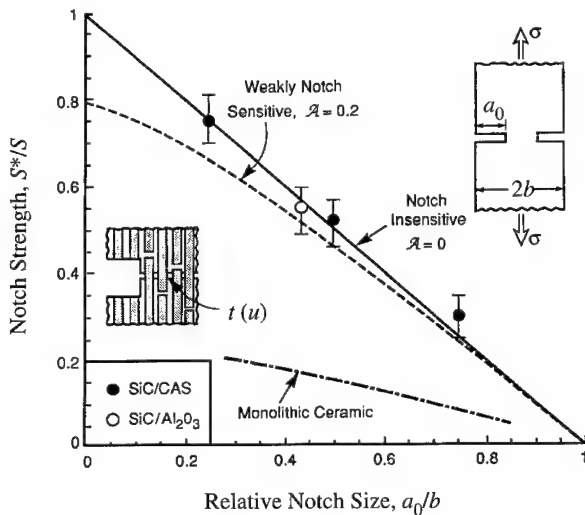


Figure 4. The notch insensitive behaviour found for two class II CMCs. The inset shows the pull-out mechanism. This combines with the inelastic strain mechanism provided by matrix cracking to eliminate the stress concentration at the notch.

3. Inelastic deformation mechanisms

(a) Basic concepts

Brittle matrix composites exhibit inelastic deformations when microcracks are stabilized. This is achieved by using either fibre coatings or porous matrices to deviate cracks toward the loading axis (figure 5), in accordance with the concept originally proposed by Cook & Gordon (1968). The resultant composite microstructure and the ensuing mechanical responses (Tu *et al.* 1995) resemble those found in various naturally occurring materials, such as wood. The fundamental requirement is that the crack deviating sites be homogeneously dispersed and have a low shear debond energy Γ_i relative to the fracture energy Γ_s of the fibre bundles. The most stringent stabilization requirement arises when there are no residual stresses. It is given by (He & Hutchinson 1989)

$$\Gamma_i < \frac{1}{4}\Gamma_s. \quad (3.1)$$

Residual compression in the deviation zone facilitates crack stabilization (figure 5). Once the deviation criterion has been satisfied, the extent of the inelastic strain is governed primarily by the number density of deviation sites and the friction stress that operates along the debonded surfaces. Two cases have been considered. (1) Composites that use a fibre coating to deviate the cracks – designated CMC-Cs. (2) Composites that use a porous matrix for crack deviation purposes – designated CMC-Ms (figure 5).

The inelastic strain of woven or laminated 0/90 CMCs increases and the flow stress decreases as the principal stresses deviate from the fibre axis (Cady *et al.* 1995). The lowest strains and the largest stresses obtain for 0/90 tensile loading. The largest strains and smallest stresses occur for shear loading: although off-axis tensile loading between 30 and 45° induces similar large strains. Fibre failure only contributes to the inelastic strains upon 0/90 tensile loading.

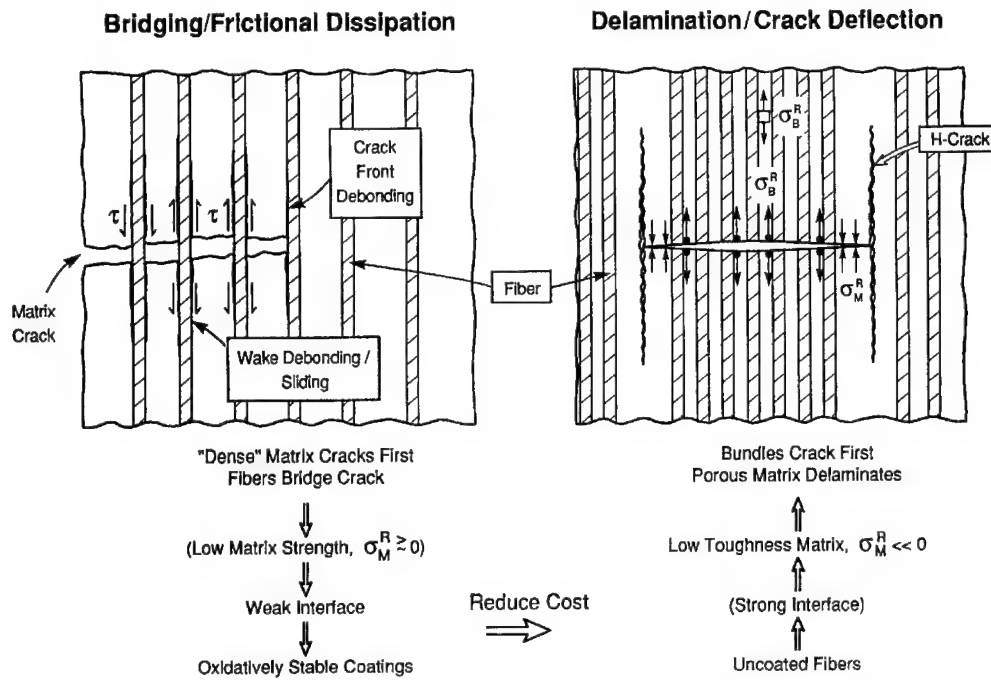


Figure 5. The two concepts for deviating cracks and inducing frictional dissipation along the debonded surfaces. (a) The use of a fibre coating to give an interphase capable of debonding, followed by friction. (b) A porous matrix, combined with residual compression, that causes debonding by H-cracking, with subsequent friction.

(b) Debonding and friction

Shear debonding is commonly encountered in thin brittle layers. It comprises the formation and eventual coalescence of microcracks *en échelon* within a cohesive zone. The associated fracture energy is (Xia *et al.* 1994) $\Gamma_i \approx 4\Gamma_0$, where Γ_0 is the mode I fracture toughness of the material in the layer. Recall that for debonding, inequality (3.1) must be satisfied, (3.5). This very stringent requirement eliminates all but a few debond concepts (Davis *et al.* 1993; Kerans 1994). The microcracks behind the debond coalescence and fragment the layer. This process induces friction at contacting asperities, resulting in a slip zone subject to a friction stress, τ . This stress is found to have essentially constant magnitude within the slip zone, although it varies among the different CMCs, from about 2 MPa in SiC-LAS to about 100 MPa in SiC-SiC (Evans & Zok 1994). It also diminishes upon cyclic loading and increases upon oxidation.

Qualitative models indicate that τ is affected primarily by the roughness amplitude behind the debond (Parthasarathy *et al.* 1994). The residual stress, the elastic compliance of the circumventing material and the friction coefficient may also be important. Present understanding is sufficient to allow τ to be systematically varied when fibre coatings are used. This is achieved by adjusting the coating thickness, its porosity and the matrix compliance.

(c) Stochastic fibre failure

In CMCs having fibre coatings, the stochastics of fibre failure are well established (Curtin 1991). When the debond and friction stresses are both relatively

low, the stress concentration that would otherwise develop in the circumventing material is eliminated. This feature enables fibre failures to occur in a spatially uncorrelated manner, resulting in global load sharing (GLS) characteristics. In such cases, friction allows stress transfer between the fibre and the matrix. The consequence is that, beyond a slip length l , the stress in the fibre is unaffected by the existence of the failure and l dictates the gauge length governing the fibre bundle strength. The ultimate tensile strength is given by

$$S_u = f S_c F(m), \quad (3.2)$$

where f is the fibre volume fraction, S_c is the characteristic strength and $F(m) \approx 0.7$. The fibre failures also produce a small inelastic strain upon loading along the fibre axis. This strain has some importance in class III CMCS.

Stress concentrations in the fibres caused by unbridged matrix cracks may reduce the UTS below the GLS level. The extent of such stress concentrations is governed by a stress concentration index, η , in accordance with the relation (Budiansky & Cui 1994; Xia *et al.* 1994),

$$S/S_u = \sqrt{[1 + (\eta\beta)^{2/3}]}, \quad (3.3)$$

with

$$\eta = \frac{3\pi f^2 E_f E^2 a \tau}{(1-f)^2 E_m^2 \bar{E} R S A},$$

where a is the size of the largest unbridged crack or manufacturing flaw, f is again the fibre volume fraction and A is an anisotropy coefficient. The quantity β , which depends on f , and E_f/E_m is a large-scale slip coefficient. For typical f and E_f/E_m , $\beta \approx \frac{1}{3}$. In 0/90 CMCS, a is typically the ply dimension, h , although manufacturing flaws could cause a to exceed h in severe cases. Note that η must exceed unity before there is a significant reduction in the UTS below the GLS value. Imposing this condition yields a maximum acceptable τ that ensures the GLS strength, $\tau_{\max} \approx 50$ MPa. Otherwise the strength will be lower than the GLS magnitude and the material would have a diminished inelastic tensile strain capacity.

(d) Matrix cracking

An understanding of the important role of matrix cracking has been gained from studies performed on 0/90 composites having fibre coatings that control debonding and friction. These have mostly been class II CMCS that exhibit considerable inelastic strain in both tension and shear. However, the resulting methodology appears to be more general, though phenomenological.

Two-cell models represent most of the features found upon loading class II CMCSs in the 0/90 orientation (Xia *et al.* 1994; Hutchinson & Jensen 1990). One model is for cracks that first form in the 90° plies (figure 6a). The other represents cracks that penetrate the 0° plies (figure 6b). Cracks in either woven or laminated 0/90 CMCSs form first in the 90° plies by tunnelling at a critical strain ϵ_t , given by

$$\epsilon_t E_T = g \sqrt{(E \Gamma_m / h) - \sigma_R}, \quad (3.4)$$

where Γ_m is the matrix fracture energy, σ_R is the ply level residual stress, E is the composite Young's modulus, E_T is the transverse Young's modulus, h is the ply thickness and g is a coefficient of order unity that depends on the transverse

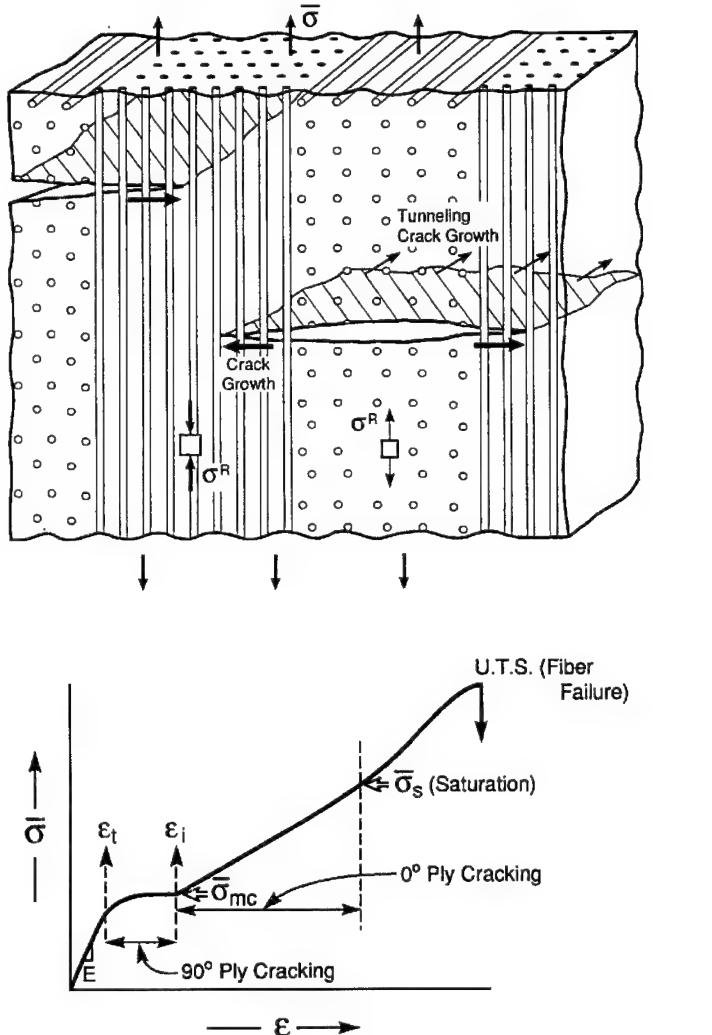


Figure 6. (a) The ply cracking model for a 0/90 CMC tested in tension. The associated stress-strain curve indicates the inelastic strains from sequential matrix cracking of the 90° and 0° plies, with the fibres intact.

attachment between the fibres and the matrix. At strains just above this critical condition there is a rapid change in the inelastic strain (figure 6a).

Upon subsequent loading, as the cracks penetrate the 0° plies, they interact with the fibres and the coating. When debonding and slip occur within the coating, the inelastic strain may be characterized by two stresses: a friction stress τ , and a debond stress σ_i . The latter is related to the debond toughness for the coating (Hutchinson & Jensen 1990; Budiansky *et al.* 1995). The strain ϵ depends on the stress σ acting on the 0° plies, in accordance with (Domergue *et al.* 1995)

$$\epsilon = 2L\sigma^2(1 - \Sigma_i)(1 + \Sigma_i + 2\Sigma^T) + (1 + \Sigma^T)\sigma/E_* - \sigma^T/E, \quad (3.5)$$

where Σ_i is the non-dimensional debond stress, $\Sigma_i = \sigma_i/\sigma$, E_* is the diminished elastic modulus caused by matrix cracking and L is an interface friction index,

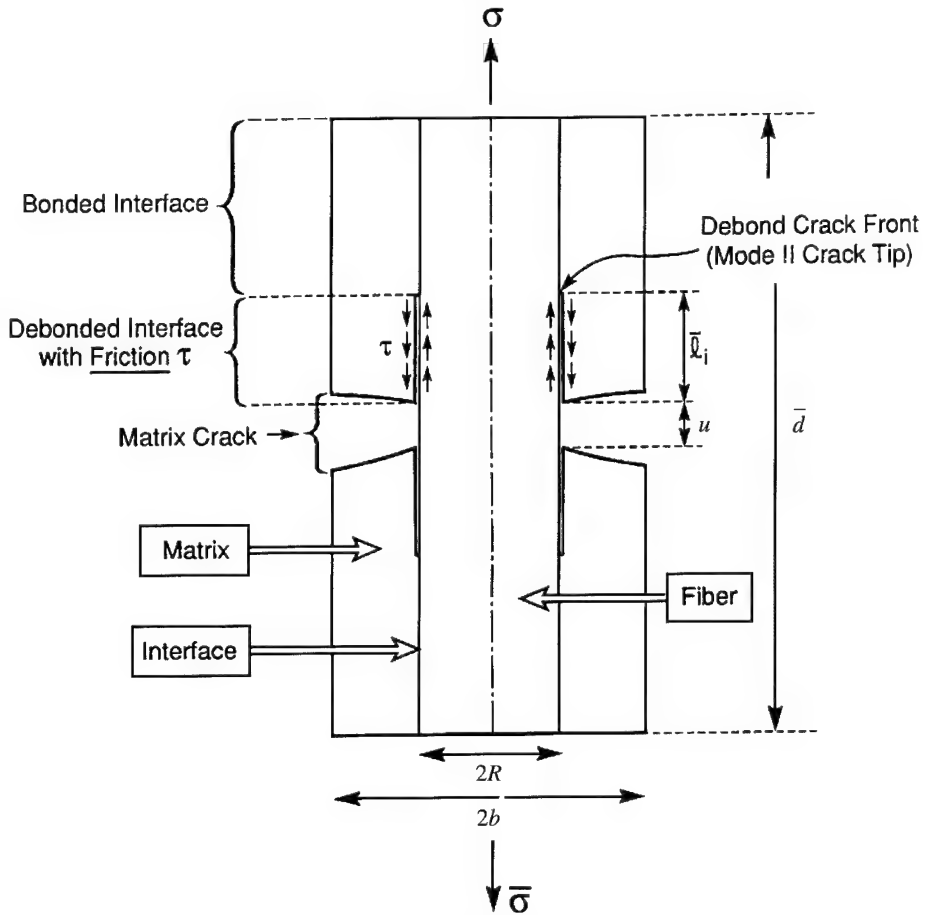


Figure 6. (b) The cell model for cracking of the 0° plies. The interface responses are characterized by a debond energy and a friction stress. These determine the inelastic strain in the presence of a matrix crack.

given by

$$L = \frac{b_2(1 - a_1 f)^2 R}{4f^2 \tau d E_m}$$

with d being the crack spacing and the coefficients a_1 and b_2 are of order unity (defined in the paper by Hutchinson & Jensen (1990)). Note that the influence of friction on the strain appears as a product, τd , of the friction stress and the crack spacing. Separate determination of τ is not required for simulation of the strains.

It has been demonstrated that E_* , L and Σ_i can be evaluated by using hysteresis strain measurements, upon plotting the tangent compliance as a function of stress (Pryce & Smith 1993; Domergue *et al.* 1995; Cady *et al.* 1995). L is obtained from the slope, E_* from the intercept and Σ_i from the slip-no-slip transition stress. With these parameters determined, σ^T can be evaluated from the remanent strain. The parameters obtained directly from the hysteresis measurements enable

the strains to be simulated. Such simulations have two roles. (1) They afford a consistency check on the methodology.

(2) They provide understanding about the separate influences on the strain provided by debonding, friction and matrix cracking.

4. Degradation by oxidation embrittlement

All non-oxide CMCS are susceptible to a 'pest' phenomenon that operates at intermediate temperatures, between 500 and 900 °C (figure 7). The degradation happens most readily at strain concentration sites, where matrix cracks have been created upon loading. These matrix cracks become pathways for the relatively rapid ingress of oxygen into the material (Brennan 1986; Heredia *et al.* 1995; Naslain, this volume). When the fibres and the coatings are non-oxides, the oxygen reacts to form both solid and gaseous products (Raj 1993). There are two consequences. (1) The fibres are weakened, because of flaws and residual stresses induced by the solid reaction product. (2) The friction stress changes and increases the stress concentration on the fibres at the perimeter of the cracks in the 90° plies (equation (3.3)). The degradation in the fibre strength combines with the increase in stress concentration to embrittle the composite. Typically, the embrittlement commences at the external surface and progressively extends inward, manifest as a region exhibiting negligible fibre pull-out. When the embrittled region has progressed to a sufficient extent, the remaining composite is unable to sustain the load.

Three approaches are being used to address this debilitating problem: (1) an all oxide composite, (2) multiple fibre coatings, and (3) kinetic retardation through coating and fibre chemistry selection.

(a) Oxide composites

Three different oxide CMCS have been devised. Two are fibre-coated CMC-Cs that use either a fugitive carbon coating (Davis *et al.* 1994) or a low toughness LaPO_4 coating (Morgan *et al.* 1994). The carbon coating protects the fibre upon matrix infiltration and may then be eliminated to form a gap. The gap is chosen to be small enough to allow asperity contact between the fibres and matrix to provide the requisite friction, which then controls the inelastic strains. Such CMCS gradually degrade at high homologous temperatures because the matrix sinters to the fibres and introduces flaws that cause weakening.

The third is a CMC-M concept (figure 5) that relies upon a porous matrix to deviate cracks (facilitated by residual compression). A fibre coating is not required (Tu *et al.* 1995). Such composites, exemplified by alumina-mullite, exhibit class III deformation characteristics. That is, stress redistribution is provided by the inelastic shear strain, enabled by two key requirements. (1) The matrix infiltration and heat treatment are performed at a sufficiently low temperature to ensure that fibre degradation is suppressed. (2) The porosity of the matrix and the residual stress are controlled at levels that satisfy debonding requirements.

A present performance limitation arises because all commercial oxide fibres are based on alumina. Such fibres have relatively low creep strength at temperatures above about 1000 °C. Moreover, these polycrystalline oxides have low thermal conductivities, leading to poor heat dissipation from regions subject to high heat flux. This induces high temperatures in the CMC causing an exacerbation of the

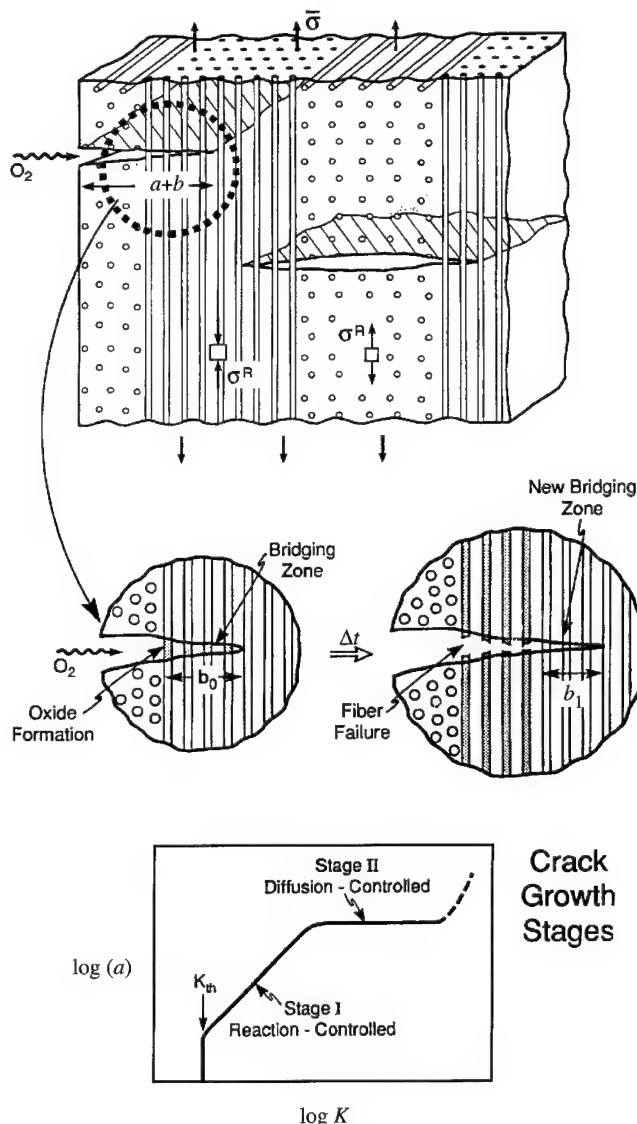


Figure 7. The phenomena that occur during oxidation embrittlement. The top view illustrates that O_2 diffuses through the matrix cracks and reacts with the exposed non-oxide fibres in the bridging zone, within the 0° plies, to form an oxide. This oxide layer weakens the fibres and causes them to fail. The crack then extends and the process repeats. The phenomenon is similar to high temperature stress corrosion cracking. It can be characterized in the same manner, shown on the bottom, through reaction and diffusion controlled regimes of crack propagation, dependent on the stress intensity factor, K .

fibre creep problem. Because of these limitations, the development of creep resistant oxide fibres continues.

(b) Multiple coatings

Multiple coating concepts have been suggested that have the potential for eliminating embrittlement in non-oxide CMCS (Kerans 1995; Naslain, this volume). One such concept proposes a triple coating. Two of the coatings would be comprised of

mullite, which is chemically compatible with SiC. The third, located between the other two, is a fugitive C coating. In principle, the thickness of this coating could be chosen to control the friction stress, but the concept has yet to be tried. A SiC–SiC composite with such a coating system should exhibit attractive thermal properties.

(c) Kinetic retardation

By understanding the embrittlement mechanism, its kinetics could be specified and lifetime predictions used to evaluate the acceptability of each CMC for specific applications. The phenomena that govern the embrittlement are illustrated on figure 7. Oxygen from the environment migrates into the narrow matrix cracks. Some of the oxygen diffuses into the fibres and forms an oxide reaction product. This reaction consumes some of the incoming oxygen. The consequence is a time evolution of the oxygen concentration in the cracks. When the oxide reaches a critical thickness, all of the exposed fibres within the crack fail and the crack extends by an amount equal to the fibre bridging zone size. A new bridging zone of pristine fibres is then exposed and the process repeats. Analysis of this phenomenon (Evans *et al.* 1995) has indicated a power law dependence of the failure time on the applied stress. However, the major material factor affecting the embrittlement kinetics is the diffusivity in the oxide, D_0 . This is dramatically influenced by purity, especially if it is silica-based. Small amounts of B and alkalies (Ca, Mg, etc.), profoundly increase D_0 . High-purity fibres thus provide an opportunity to retard embrittlement and enhance the life expectancy of non-oxide CMCs.

5. Opportunities

Ceramics have the disadvantage that weakest link statistics must be used for design. It is crucially important that the survival probabilities associated with design stress levels be specified with high confidence. In turn, this requires an intelligent processing regimen, using a control model that regulates the stochastic strength. Applying such a regimen has particular advantages when a toughened ceramic is used, because of the diminished variability and the greater confidence associated with data extrapolation.

The research challenges for CMCs are quite different. Their inelastic deformation enables the application of 'Gaussian' statistics, enabling the implementation of familiar design rules used for metal and polymer composites. The problems concern high temperature degradation. For non-oxide CMCs, oxidation embrittlement is the most debilitating. Retarding the degradation requires research on multiple coating concepts as well as on the development of fibres having high purity and acceptable manufacturing costs. High-purity SiC fibres appear to be the only realistic material. However, embrittlement would still be life limiting and its kinetics ultimately govern the applications.

Oxide–oxide CMCs present different challenges. In these materials, fibre creep limits performance. Affordable single crystal fibre growth is impractical. Among the affordable polycrystalline oxides, mullite is the material of choice. However, greater understanding is needed to project the behaviour of oxide fibres having high creep strength.

References

Aveston, J., Cooper, G. A. & Kelly, A. 1971 Single and multiple fracture. In *Properties of Fiber Composites: Conf. Proc. National Physical Laboratories*, pp. 15–26. Surrey, UK: IPC Science and Technology Press.

Bao, G. & Suo, Z. 1992 *Appl. Mech. Rev.* **45**, 355–66.

Brennan, J. J. 1986 *Tailing of multiphase ceramics* (ed. R. Tressler), p. 549. New York: Plenum.

Becher, P. F. & Tiegs, T. N. 1987 *Am. Ceram. Soc.* **70**, 651–654.

Budiansky, B. & Cui, L. 1994 *J. Mech. Phys. Solids* **42**, 1–19

Budiansky, B., Evans, A. G. & Hutchinson, J. W. 1995 *Int. J. Solids Struct.* **32**, 315–328.

Cady, C., Heredia, F. E. & Evans, A. G. 1995 *J. Am. Ceram. Soc.* (In the press.)

Cady, C., Mackin, T. E. & Evans, A. G. 1995 *J. Am. Ceram. Soc.* **78**, 77–82.

Clarke, F. J. P., Sambell, R. A. J. & Tattersall, H. G. 1962 *Phil. Mag.* **7**, 393–413.

Cooke, R. F. & Clarke, D. R. 1988 *Acta metall.* **36**, 555.

Curtin, W. 1991 *J. Am. Ceram. Soc.* **74**, 2837.

Davis, J. B., Lofvander, J. P. A. & Evans, A. G. 1993 *J. Am. Ceram. Soc.* **76**, 1249–1257.

Domergue, J.-M., Vagaggini, E., Evans, A. G. & Parenteau, J. 1995 *J. Am. Ceram. Soc.* (In the press.)

Evans, A. G. 1982 *J. Am. Ceram. Soc.* **65**, 127–137.

Evans, A. G. 1990 *J. Am. Ceram. Soc.* **73**, 187–206.

Evans, A. G. & Zok, F. W. 1994 *J. Mater. Sci.* **29**, 3857–3896.

Evans, A. G., Zok, F. W. & McMeeking, R. M. 1995 *Acta metall. Mater.* (In the press.)

Freudenthal, A. 1967 *Fracture* (ed. H. Liebowitz), pp. 341–345. New York: Academic Press.

Genin, G. & Hutchinson, J. W. 1995 *J. Am. Ceram. Soc.* (In the press.)

Gordon, J. E. 1968 *The new science of strong materials*. London: Penguin.

Green, D. J., Hanninck, R. H. & Swain, M. V. 1989 *Transformation toughening of ceramics*. Boca Raton, FL: CRC Press.

He, M. Y. & Hutchinson, J. W. 1989 *Int. J. Solids Struct.* **25**, 1053–1067.

Hirsch, P. B. & Roberts, S. G. 1991 *Phil. Mag. A* **64**, 55.

Hutchinson, J. W. & Jensen, H. 1990 *Mech. Mater.* **9**, 139.

Kendall, K., McNalford, N., Tan, S. R. & Birchall, J. D. 1986 *J. Mater. Sci.* **1**, 120.

Kerans, R. 1994 *Scr. metall. Mater.* **31**, 1075.

Lange, F. F. 1989 *J. Am. Ceram. Soc.* **72**, 1.

Mackin, T. J., Perry Jr, K. E., Epstein, J. S., Cady, C. M., He, M. Y. & Evans, A. G. 1995 *J. Am. Ceram. Soc.* (In the press.)

McMeeking, R. M. & Evans, A. G. 1982 *J. Am. Ceram. Soc.* **65**, 242–247.

Matthews, J. R., Shack, W. J. & McClintock, F. A. 1976 *J. Am. Ceram. Soc.* **59**, 304.

Morgan, P. E. D. & Marshall, D. B. 1995 *J. Am. Ceram. Soc.* (In the press.)

Parthasarathy, J. A., Marshall, D. B. & Kerans, R. 1994 *Acta metall. Mater.* **42**, 3773–3784.

Prewo, K. M. 1987 *J. Mater. Sci.* **22**, 2595.

Pryce, A. W. & Smith, P. A. 1993 *Acta metall. Mater.* **41**, 1269.

Phillips, D. C. 1974 *J. Mater. Sci.* **9**, 1874.

Raj, R. 1993 *J. Am. Ceram. Soc.* **76**, 2147.

Rice, J. R. & Beltz, G. E. 1994 *J. Mech. Phys. Solids* **42**, 333.

Stump, D. M. & Budiansky, B. 1988 *Int. J. Solid Struct.* **25**, 635.

Tu, W., Lange, F. F. & Evans, A. G. 1995 *J. Am. Ceram. Soc.* (In the press.)

Wiederhorn, S. M., Moses, R. L. & Bean, B. L. 1970 *J. Am. Ceram. Soc.* **53**, 18–23.

Weibull, W. 1939 *Ingénjörsvetenskapakademiens* (Handlingar Nr:), p. 153.

Xia, C. & Hutchinson, J. W. 1994 *Acta metall. Mater.* **42**, 1935–1945.
Xia, C., Carr, R. R. & Hutchinson, J. W. 1993 *Acta metall. Mater.* **41**, 2365.
Xia, C., Hutchinson, J. W., Budiansky, B. & Evans, A. G. 1994 *J. Mech. Phys. Solids* **42**, 1139–1158.
Xu, G., Argon, A. S. & Ortiz, M. 1995 *Phil. Mag.* (In the press.)

Discussion

J. RÖDEL (*GDP, Darmstadt, Germany*). Is really large-scale ductility – in the sense of an irreversible displacement in the stress–strain curve – needed, or just a local ductility to mitigate damage in a local scale, by, say, an incoming particle?

A. G. EVANS. If you think of large structural components with holes the size of millimetres, large-scale ductility is needed, but not a lot. Ductility less than 1% is sufficient.

Quantum mechanical predictions in intermetallics modelling

BY D. NGUYEN MANH, A. M. BRATKOVSKY AND D. G. PETTIFOR

*Department of Materials, University of Oxford,
Parks Road, Oxford OX1 3PH, UK*

Materials modelling involves research that spans the very broad spectrum of length scales from quantum mechanical calculations at the Å level all the way through to finite-element or finite-difference modelling at the continuum level. This paper reviews the role that quantum mechanics plays in the modelling hierarchy with particular reference to the titanium and nickel aluminides.

1. Introduction

The prediction of the properties of high-temperature intermetallics involves research that spans the very broad spectrum of length scales from quantum mechanical calculations at the Å level all the way through to finite-element or finite-difference modelling at the continuum level. The spectrum divides naturally into four different hierarchies or levels, namely the electronic, atomistic, microstructural, and continuum as shown in figure 1. We can loosely think of these as embracing the domains of the physicist and chemist (the solution of the Schrödinger equation and the nature of the chemical bond describing the interaction between the atoms respectively), the materials scientist (the evolution of microstructure), and the engineer (the modelling of processing). In this paper we are interested in bridging the gap between the electronic and atomistic hierarchies. In a following paper Rappaz (this volume) will address the question of how the gap is bridged between the microstructural and continuum hierarchies.

In intermetallics the unsaturated covalent bonds between different atomic species result in several important properties. First, perhaps the most important, they tend to be very strong and stiff, their strength and stiffness being maintained up to high temperature. Moreover, some intermetallics such as Ni_3Al show an anomalous sharp rise in strength with increasing temperature. Such a unique property makes intermetallics even more attractive as high-temperature materials. Second, they often show good oxidation resistance. For example, in the case of NiAl which has a higher melting point than those of the constituent elements, strong bonds between aluminium and nickel make their aluminium reservoir stable up to a high temperature and result in a remarkable high-temperature oxidation resistance. Third, those compounds based on light elements, such as TiAl and Ti_3Al , can have very low densities. The low density combined with the high strength and stiffness give rise to very attractive specific properties, which are especially important for rotating machinery and aerospace applications (Yamaguchi & Inui 1993). Unfortunately, at the same time, the directional nature of

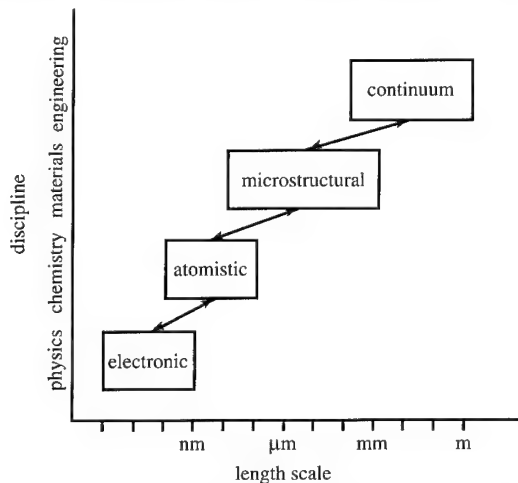


Figure 1. Hierarchy of models in materials research.

the covalent bond between different atomic species tends to cause intermetallics to be brittle at low temperatures. Therefore they are unlikely to find extensive engineering application, unless ways can be found to overcome this brittleness. Because of their great promise, there is a lot of effort to understand the origin of their brittleness.

A fundamental study of the deformation behaviour of intermetallics requires a realistic description of the bonding between the different constituent atoms. Simple pair potentials or the more recently developed embedded atom or Finnis-Sinclair potentials cannot explain the origin of the brittleness since the explicit *directional* character of the bonding is neglected. To solve this problem we are required to bridge the gap between the electronic and atomistic levels in the modelling hierarchies and to derive interatomic potentials that are firmly based on the quantum mechanical predictions of the Schrödinger equation. Recently, a novel angular-dependent interatomic potential has been obtained within the two-centre tight-binding approximation in which the directional character of the bonding is included explicitly from the outset (Pettifor 1989). Moreover, the many-atom expansion for this so-called bond order potential (BOP) has been shown to be not only exact but also rapidly convergent (Aoki 1993). The BOP scheme is an $O(N)$ method, in which the number of arithmetic operations grows *linearly* with the system size N . The BOPs may be used therefore for the atomistic modelling of very large systems in the studies of defects such as dislocation cores and interfaces.

The development of the BOP for a given system requires the appropriate tight-binding parameters as input. Since the two-centre, orthogonal tight-binding approach is semi-empirical the tight-binding parameters and their distance dependence must be *fitted* to theoretically predicted local density functional band structure and binding energy curves of both the ground state and metastable phases, as has been done with great success for silicon (Goodwin *et al.* 1989).

The purpose of this paper is to make a systematic first-principles study of the bonding of the 3d and 4d transition metal aluminides and to generate an *ab initio* database by solving the Schrödinger equation at the electronic level. Particular attention will be paid to possible competing phases with respect to the

ground state structures L1₀ for TiAl and B2 for NiAl which are the promising candidates for new high-temperature structural materials (Darolia 1991; Dimiduk 1992). This database will then be used to fit reliable transferable tight-binding parameters for TiAl and NiAl to perform defect simulations at the atomistic level using the novel angularly dependent BOPS (Pettifor *et al.* 1995).

2. Ab initio binding energy database

(a) Local density functional theory

Application of electron theory to understanding and predicting the properties of metals and alloys needs a reliable method for computing the stability of an arbitrary collection of atomic nuclei and electrons from first principles, that is, without resorting to experimental input other than universal constants. As one of the first-principles approaches, density functional theory is an exact theory for the total ground state energy of a system of electrons and fixed nuclei (Hohenberg & Kohn 1964; Kohn & Sham 1965). Within the so-called local density approximation (LDA), the exchange-correlation energy density is assumed to be that of a homogeneous electron gas with the same density as that seen locally by the electron. The total LDA energy is then a unique functional of the electron density $n(\mathbf{r})$, namely

$$U_T[n] = \sum_{i,\text{occ}} E_i - \frac{1}{2} \iint d\mathbf{r} d\mathbf{r}' \frac{n(\mathbf{r})n(\mathbf{r}')}{|\mathbf{r} - \mathbf{r}'|} - \int d^3r n(\mathbf{r})\mu_{xc}(\mathbf{r}) + U_{xc}[n] + U_{\text{ion-ion}}. \quad (2.1)$$

The first contribution, the band energy, is the sum of occupied eigenvalues E_i obtained by solving the one-electron Schrödinger equation with an effective potential V_{eff} given by

$$V_{\text{eff}}(\mathbf{r}) = V_{\text{ext}}(\mathbf{r}) + \int d\mathbf{r}' \frac{n(\mathbf{r}')}{|\mathbf{r} - \mathbf{r}'|} + \mu_{xc}(\mathbf{r}). \quad (2.2)$$

V_{eff} comprises three terms: the external potential due to the positive nuclei, the averaged electrostatic potential of the electron gas or Hartree potential, and the exchange-correlation potential (which is the functional derivative of U_{xc} with respect to n). The electronic density can be constructed from the eigenfunctions $\psi_i(\mathbf{r})$ of the Schrödinger equation by using

$$n(\mathbf{r}) = \sum_{i,\text{occ}} |\psi_i(\mathbf{r})|^2. \quad (2.3)$$

The second, third and fourth contributions to (2.1) correct for the double-counting of the electrostatic and exchange-correlation energies, respectively, because the eigenvalue E_i contains the potential energy of interaction with the j th electron and vice versa. The last contribution represents the ion-ion Coulomb interaction.

All the calculated results using self consistent LDF theory must be regarded as essentially the solution to the many-body quantum mechanical problem of a system of electrons and nuclei in a solid. The solution of the one-electron Schrödinger equation can be obtained numerically through one or other of the many, well developed band structure methods. They involve expanding the eigenfunctions $\psi_i(\mathbf{r})$ in basis set functions (e.g. plane-waves, muffin-tin orbitals, etc.). The cal-

Table 1. Characterization of twelve different structure types

	structure	spacegroup		local coordination
L1 ₀	CuAu	P4/mmm	123	(8Al+4TM) + 6TM
40	Kanamori	I4 ₁ /amd	141	(8Al+4TM) + (2Al+4TM)
L1 ₁	CuPt	R̄3m	166	(6Al+6TM) + 6Al
B19	AuCd	Pmma	51	(8Al+4TM) + 6TM
B2	CsCl	Pm̄3m	221	8Al + 6TM
B32	NaTl	Fd3m	227	(4Al+4TM) + 6Al
B11	CuTi	P4/nmm	129	(4Al+4TM) + (2Al+4TM)
B33	CrB	Cmcm	63	7Al + 10TM
B20	FeSi	P2 ₁ 3	198	7Al + 6TM
B27	FeB	Pmna	62	7Al + 10TM
B8 ₁	NiAs	P6 ₃ /mmc	194	(6Al+2TM) + 6TM
B1	NaCl	Fm3m	225	6Al + 12TM

culations in this section are made by using the full-potential linear muffin-tin orbitals (FP-LMTO) method (Methfessel 1988) which provides the smallest basis set with a precision of about 10^{-4} Ry for the total energy U_T . This accuracy is needed for determining structural energy differences which are often of the order of mRy per atom. Since the total energy U_T is of the order of 10^4 Ry per atom this requires a convergence of 1 part in 10^7 .

(b) Binding energy curves

In this study the choice of the competing structure-types within the transition metal aluminides is guided by the two dimensional AB structure maps where the observed ground state structures of neighbouring AB compounds to TiAl and NiAl are displayed (Pettifor 1992). We find, as expected, that TiAl takes the tetragonal L1₀ (CuAu) structure type which, neglecting the tetragonal distortion, results from ordering the titanium and aluminium atoms with respect to an underlying FCC lattice so that each atom is surrounded by a local coordination polyhedron of twelve atoms. On the other hand, we find that NiAl takes the cubic B2 (CsCl) structure type which results from ordering the nickel and aluminium atoms with respect to an underlying BCC lattice so that each atom is surrounded by a local coordination polyhedron of fourteen atoms comprising eight first and six second nearest neighbours. Importantly we find that if the 3d element Ti is replaced by isovalent 4d-Zr or 5d-Hf then the most stable structure is not tetragonal CuAu but orthorhombic CrB. Similarly, we find if the 3d element Ni is replaced by isovalent 4d-Pd or 5d-Pt then the most stable structure is not cubic CsCl but cubic FeSi with only seven unlike nearest neighbours in a distorted first neighbour shell rather than the eight of CsCl.

In our investigations, we have included the twelve different structure types listed in table 1. We have grouped these structure according to whether they are close packed FCC-like, HCP-like, BCC-like or some other more open structure type, respectively. For FCC-like structures, the following structures were included: L1₀ (CuAu), L1₁ (CuPt) and 40 (Kanamori phase) which correspond to stars

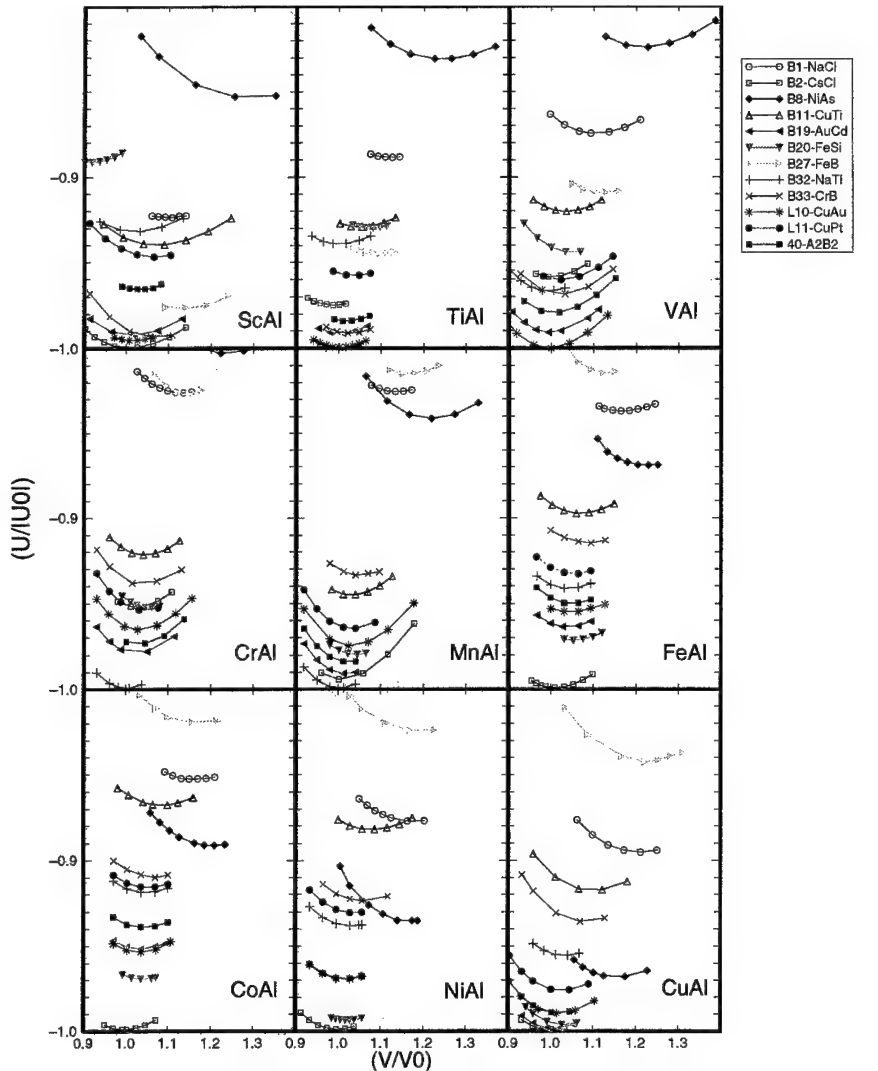


Figure 2. Self-consistent FP-LMTO binding energy-volume curves amongst the 3d transition metal aluminides with respect to twelve different structure types.

$\langle 100 \rangle$, $\langle \frac{1}{2}, \frac{1}{2}, \frac{1}{2} \rangle$ and $\langle 1, \frac{1}{2}, 0 \rangle$ respectively within the FCC Brillouin zone. For HCP-like structures, we included the only one that is observed for AB compound structures, namely B19 (AuCd). For the BCC-like structures, we include the B2 (CsCl), B32 (NaTl) and B11 (γ -CuTi) structures which correspond to the stars $\langle 100 \rangle$, $\langle \frac{1}{2}, \frac{1}{2}, \frac{1}{2} \rangle$ and $\langle \frac{1}{2}, \frac{1}{2}, 0 \rangle$, respectively, within the BCC Brillouin zone. The other structures we included are: B1 (NaCl), B8₁ (NiAs), B20 (FeSi), B27 (FeB) and B33 (CrB) which are commonly occurring structure types for the pd-bonded AB compounds (Pettifor & Podloucky 1986). The local coordination polyhedron that surrounds each transition metal atom is given in the last column of table 1 for each structure-type. The details of the FP-LMTO calculations for all the 3d and 4d transition metal aluminides will be analysed elsewhere. Here we give only some results concerning the prediction of structural trends within the transition metal aluminide compounds.

Table 2. Equilibrium volume per unit formula and bulk modulus of ground state for 3d and 4d transition metal aluminides
(B_{theor} is the result from other first-principle calculation.)

material (structure)	volume/Å ³		bulk modulus/Mbar	
	V_{cal}	$V_{\text{cal}}/V_{\text{exp}}$	B_{cal}	$(B_{\text{exp}} \text{ or } B_{\text{theor}})$
ScAl-(B2)	38.96	0.95	0.62	—
TiAl-(L1 ₀)	30.96	0.95	1.29	1.26
VAl-(L1 ₀)	27.20	—	1.59	—
CrAl-(B32)	24.56	—	1.89	—
MnAl-(B32)	23.39	—	1.91	—
FeAl-(B2)	22.99	0.94	1.88	1.52, 1.83
CoAl-(B2)	22.19	0.95	1.92	1.62
NiAl-(B2)	22.90	0.96	1.84	1.57, 1.87, 1.93
CuAl-(C2/m)	26.98	0.96	1.65	—
YAl-(B33)	47.41	0.97	0.66	—
ZrAl-(B33)	37.93	0.98	1.08	—
RuAl-(B2)	26.19	0.94	2.23	2.20
RhAl-(B2)	25.93	0.97	2.16	—
PdAl-(B20)	28.11	0.98	2.07	—

The complete set of binding energy curves for the 3d transition metal aluminides is given in figure 2 where the curves plotted have been scaled with respect to the calculated energy and volume of the most stable structure. We see that the ground states of the observed transition metal aluminides are predicted correctly: ScAl in the B2 structure, TiAl in the L1₀ structure, FeAl, CoAl and NiAl in the B2 structure. The B2 structure is shown in this figure to be most stable for CuAl as well, but this phase in fact is predicted to become unstable with respect to the monoclinic phase C2/m, which has a binding energy of about 4 mRy per atom lower than the B2 phase. If vanadium and chromium aluminides were to exist in the 50–50 stoichiometry then we would predict VAl to be L1₀ whereas CrAl would be B32. We predict that ferromagnetic state of L1₀–MnAl is more stable than nonmagnetic B32 which is also consistent with experimental observation (see, for example, Zhang & Soffa 1994).

In table 2 we give the calculated equilibrium volume and bulk modulus of the ground state for 3d and 4d transition metal aluminides. We see that the theoretical predictions compare very well with the experimental data where available. As expected, the lattice expands when going from 3d to 4d transition metal aluminides. The structural stability of the transition metal aluminides is presented in figure 3 where the structural energy difference relative to B2 is plotted as a function of the average number of valence electron per atom. We note that the changes in energy ΔU between competing structure-types are indeed varying from 10^{-3} to 10^{-2} Ry per atom as mentioned in the previous section. We find the structural trend from B2 (BCC-like) to L1₀ (FCC-like) to B19 (HCP-like) to B2 (BCC-like) as function of the average number of electrons per atom. This trend is different

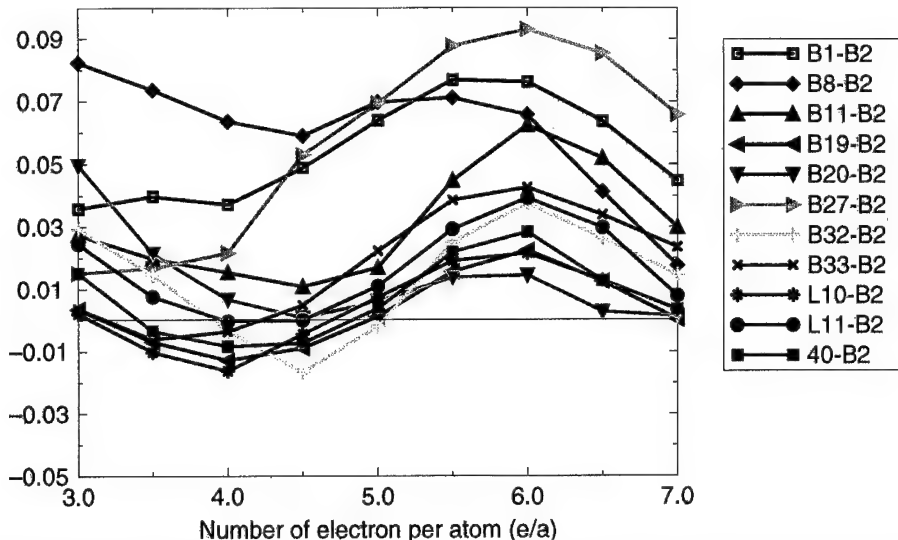


Figure 3. Structural energy differences relative to the B2 structure for the 3d-transition metal aluminides.

from that for the pure nonmagnetic transition metals where we go from HCP to BCC to HCP to FCC across the series. Thus, the structural stability depends on the angular character of the valence orbitals taking part in the bonding. We will explain the origin of the structural trend across the transition metal aluminides in the next subsection.

(c) Focus on TiAl and NiAl

Titanium aluminide and nickel aluminide are the two representative compounds at the beginning and end of the transition metal aluminides. The binding energy curves of these two compounds and also those of corresponding 4d compounds ZrAl and PdAl are shown in figure 4. We see that B33 (CrB) is predicted to be the closest metastable phase to the L1₀ ground state of TiAl, being about 3 mRy per atom higher in energy. Other nearby competing phases are B19 (AuCd), an ordered structure type with respect to the HCP lattice, being 3.4 mRy per atom higher in energy and the Kanamori phase labelled 40 which is an ordered structure type with respect to the FCC lattice. We observe that the LDA calculations predict correctly that ZrAl take the B33 (CrB) structure with L1₀ as the closest metastable phase. On the other hand, at the end of a series we see that B20 (FeSi) is the closest metastable phase to the B2 ground state of NiAl, being only about 3 mRy per atom higher in energy. Again when the 3d-Ni is replaced by isovalent 4d-Pd, our LDA calculations predict correctly that PdAl takes the B20 (FeSi) structure type with B2 as the closest metastable phase.

The prediction that the B33 and B20 structure-types are the nearest competing phases to the L1₀ of TiAl and the B2 of NiAl, respectively, is interesting because the structural stability of these phases is determined explicitly by the directional d(TM)-p(Al) bonding which is well described by the tight-binding model (Pettifor & Podloucky 1986). A dramatic example of the importance of directional bonding in determining intermetallic structure and properties is provided by RuAl₂ which takes the TiSi₂ structure type. This intermetallic was predicted to be a semicon-

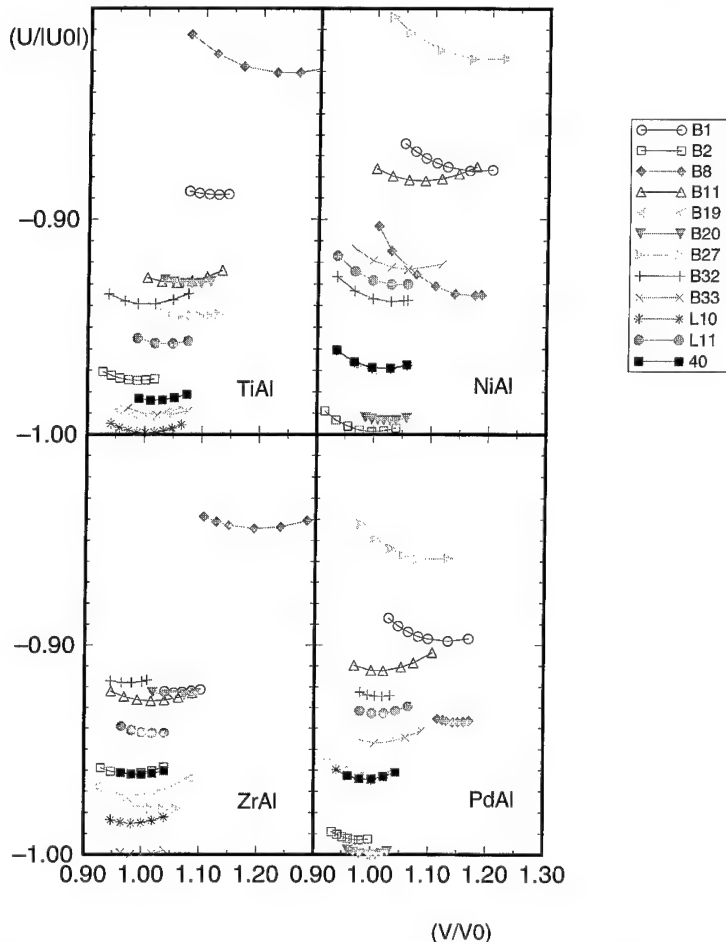


Figure 4. Binding energy curves for TiAl, NiAl, ZrAl and PdAl with respect to twelve different structure types.

ductor with the hybridization gap resulting directly from the angular character of pd bonding orbitals which separates the pd bonding from pd antibonding states, a theoretical result (Nguyen Manh *et al.* 1992) later confirmed by experiment (Pierce *et al.* 1993).

The structural stability in these phases is controlled mainly by the band structure energy contribution in (2.1) whose magnitude depends on the shape of the density of states. Figures 5a-c show the densities of states of the three competing phases L1₀, B33 and B19, respectively, at the fixed equilibrium volume for titanium aluminide from which we can deduce the relative stability within a non-self-consistent ‘frozen-potential’ approach (Nguyen Manh *et al.* 1995). It is clear that the hybridization between Ti and Al states has a very *similar* character for the three competing structures. The same conclusion can be made from figures 5d, e where the calculated density of states for the ground state B2 and its competing metastable phase B20 are shown.

An estimate of the energy difference between two structures can be obtained

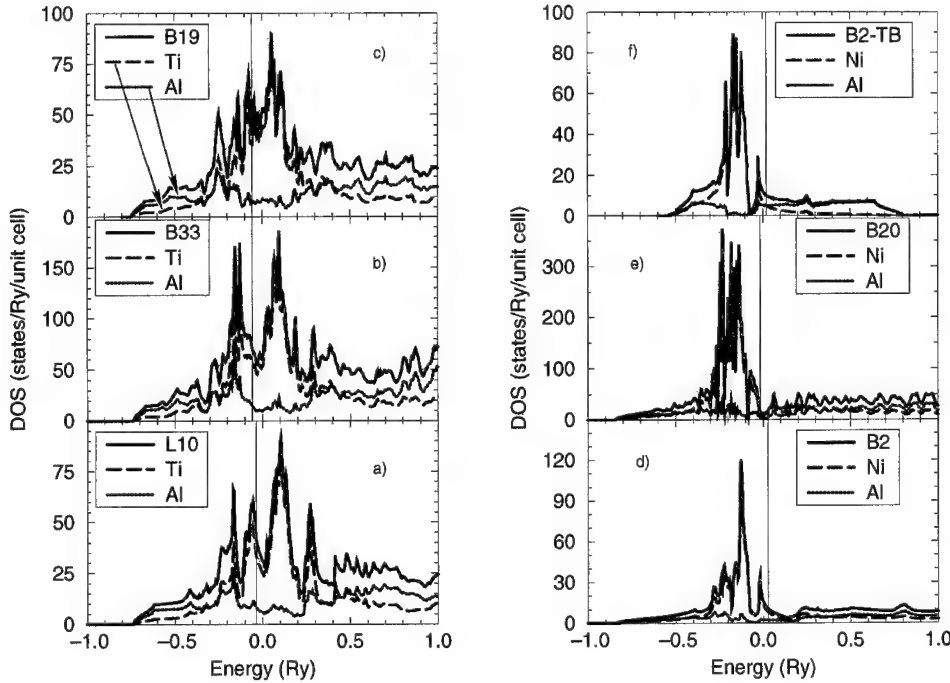


Figure 5. The calculated density of states for TiAl in the three competing phases: (a) $L1_0$, (b) B33 and (c) B19. The calculated density of states for NiAl in the two competing phases: (d) B2 and (e) B20. (f) Tight-binding density of states for NiAl in the p(Al)-d(Ni) model.

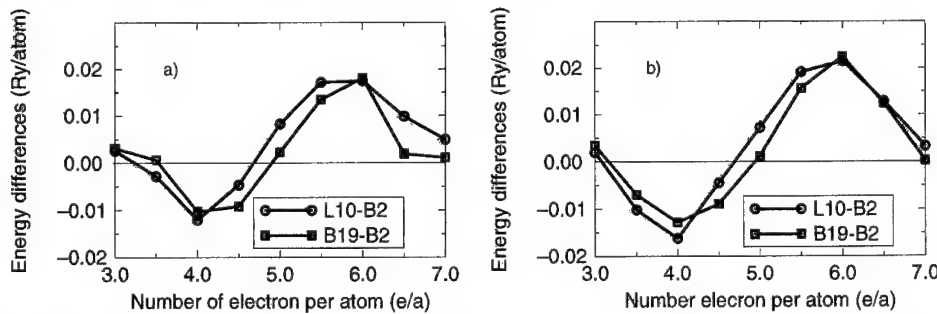


Figure 6. Structural energy differences between B19 and $L1_0$ relative to B2 calculated from (a) the B2-NiAl 'frozen-potentials' and (b) FP-LMTO method.

by comparing their band structure energies at the same atomic volume, namely

$$\Delta U_T \approx \Delta U_b = \Delta \left[\int_{E_F}^{E_F} E n(E) dE \right], \quad (2.4)$$

where E_F is the Fermi energy and $n(E)$ is the total electronic density of states.

Figure 6a shows the band energy differences between the HCP-like B19 and the FCC-like $L1_0$ structures compared to BCC-like B2 for the NiAl densities of states. We see that the structural energy differences are very similar to those obtained from the self-consistent FP-LMTO calculation in figure 6b. Very importantly, these calculations show that the band structure energy is a dominant factor in deter-

mining the structural stability of the transition metal aluminides. This factor is entirely quantum mechanical in origin.

3. Bond order potentials

(a) Many-atom expansion for the bond order

Within the two-centre orthogonal tight-binding approximation the covalent bond energy U_{bond}^{ij} between sites i and j may be written explicitly as (Pettifor 1989)

$$U_{\text{bond}}^{ij} = H_{ij} \Theta_{ji}(E_F), \quad (3.1)$$

where H_{ij} is the tight-binding Hamiltonian matrix linking sites i and j and $\Theta_{ji}(E_F)$ is the *bond order* (Coulson 1939). The bond order is the difference between the number of electrons in the bonding and antibonding states, respectively. It is a *non-pairwise* quantity since it depends on the local atomic environment about the bond and can be expressed *exactly* via the *moments of tight-binding Hamiltonian* as a many-atom expansion (Pettifor 1989; Aoki 1993).

The simplest approximation to the bond order retains only the first term in the many-atom expansion. This contribution takes into account the *second moment* only and gives immediately the embedding function introduced by Finnis & Sinclair (1984) in their embedded-atom potentials. The second moment about atom i can be written

$$\mu_2 = \sum_{j \neq i} H_{ij} H_{ji} = \sum_{j \neq i} H^2(R_{ij}). \quad (3.2)$$

The square root of the second moment is a measure of root mean square band width of the local density of states on atom i . The second term in the many-atom expansion for the bond order is dependent on the third moment μ_3 which sums over all the three-member ring contribution of type $i \rightarrow j \rightarrow k \rightarrow i$. This accounts for the asymmetric behaviour or skewing of the local density of states. The third term in the expansion is dependent on the fourth moment μ_4 which sums over paths such as the four member ring contribution $i \rightarrow j \rightarrow k \rightarrow l \rightarrow i$. The fourth moment defines the unimodal or bimodal shape of the density of states (see, for example, Bratkovsky *et al.* 1994).

The BOP formalism is an order N method, the computational time varying linearly with the number of atom N simulated. It is, therefore, significantly faster when applied to large systems than the methods using direct diagonalization of the Hamiltonian matrix where the time scales as the third power of the number of atoms N in the cell.

(b) Application for TiAl and NiAl

To develop the angularly dependent BOPs for transition metal aluminides, the *ab initio* binding energy curves are used to fit reliable transferable TB parameters.

(i) Titanium aluminide

Titanium has partially filled d-bands so that the atoms are non-spherical and the bonding is expected to display angular character. We first develop the BOP for elemental HCP-titanium using canonical tight-binding hopping integrals

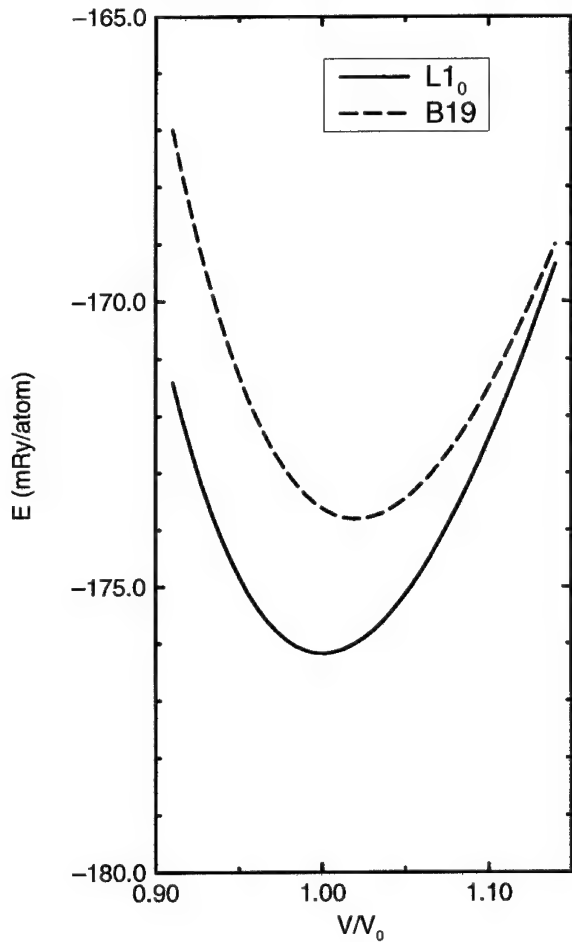


Figure 7. The binding energy curves from tight-binding model for TiAl for $L1_0$ and $B19$ structures.

$dd\sigma:dd\pi:dd\delta = -6:4:-1$. This potential correctly reproduces the *ab initio* structural energy-volume curves for HCP, FCC and BCC Ti within the sixth-moment approximation to the density of states. We then developed the BOP for compound TiAl. As stressed above directional bonding plays an important role in the structural stability of the group IV transition metal aluminides: whereas TiAl takes the $L1_0$ structure, ZrAl and HfAl take the complicated phase B33 structure (CrB type). This structure and the HCP-like $B19$ are the closest metastable phases to the $L1_0$ ground state of TiAl. Figure 5a shows that the Fermi level of TiAl is positioned in the middle of the d-band of Ti where the hybridization between the d(Ti) and the p(Al) states is strong. This situation is not captured by Embedded Atom type potentials. Figure 7 shows the tight-binding binding energy curves of TiAl with respect to the $L1_0$ and $B19$ using canonical parameters $pp\sigma:pp\pi = 2:-1$ and $pd\sigma:pd\pi = -3:3^{1/2}$. The transferrable tight-binding BOP gives the energy difference between $L1_0$ and $B19$ as 3.5 mRy per atom in good agreement with the *ab initio* calculations. We are currently predicting the binding energy curves for the other structure types of TiAl in figure 2.

(ii) *Nickel aluminide*

Unlike titanium the d-band of nickel is nearly full. The electronic density of states of nickel aluminide (figure 5d) shows that the Fermi level is positioned at the top of this d band, so that, the bonding is expected to have more spherical character than for the titanium aluminides. Nevertheless, there are two points which make us to believe that the angular bonding is still important in this intermetallic. Firstly, a very simple tight-binding calculation in which only the p orbitals on Al and d orbitals on Ni are retained, reproduces very well the shape of the density of states for B2-NiAl as shown in figure 5f. Thus, the particular shape of the density of states in NiAl can be explained by the strong covalent bonding between Ni and Al. Secondly, we note that PdAl takes the B20 structure type which is a distorted CsCl type lattice. Pd has the same number of d-electrons as Ni but PdAl takes the complex FeSi structure due to the covalent directional Al(p)-Pd(d) bonding. The directionality of the bonding is responsible for the B20 structure type being the closest metastable phase for NiAl. Preliminary results from BOPS calculations for NiAl show that these speculations are correct, as will be described elsewhere.

4. Conclusions

We have demonstrated the importance of a proper quantum mechanical description of the bonding for understanding the structural properties of the transition metal aluminides. In particular, we have shown that the closest competing structures types to the L1₀ ground state of TiAl and the B2 ground state of NiAl are the B33 (CrB) and B20 (FeSi) phases, respectively. The structural stability of these metastable phases is determined by the directional pd bonding between the sd-valent transition element and sp-valent aluminium.

Reliable atomistic simulation of the defect properties of the transition metal aluminides, therefore, requires the development of angularly dependent interatomic potentials. We have shown how it is possible to bridge the gap between the first principles quantum mechanical calculations at the *electronic* level and the simulations of defects at the *atomic* level by using the novel many-atom expansion for the bond order within the tight-binding description of the electronic properties. These potentials have been fitted to the band structure and binding energy curves of TiAl and NiAl and will be used in the near future for simulating defects in these intermetallics.

We are very grateful to Dr Tony Paxton for his help with the FP-LMTO calculations and many helpful discussions during this work. D.N.M. thanks the Japanese NEDO project for financial support, A.M.B. thanks the EPSRC. Computations were performed in the Materials Modelling Laboratory, Department of Materials, Oxford, which has been funded in part by the EPSRC under grant GR/H 58278-C80 and on SERC's Cray Y-MP at Rutherford Appleton Laboratory.

References

Aoki, M. 1993 Rapidly convergent bond order expansion for atomistic simulations. *Phys. Rev. Lett.* **71**, 3842–3845.
 Bratkovsky, A. M., Aoki, M., Horsfield, A. & Pettifor, D. G. 1994 Tight-binding calculations in real space: towards the bond-order potentials. Workshop on Bond-Order Potentials for Atomistic Simulations, University of Oxford, Oxford, 26–27 September.

Coulson, C. A. 1939 The electronic structure of some polyelenes and aromatic molecules. VII. Bonds of fractional order by molecular orbital method. *Proc. R. Soc. Lond. A* **169**, 413–428.

Darolia, R. 1991 NiAl alloys for high-temperature structural applications. *J. Metals* **43**, 44–49.

Dimiduk, D. M., Miracle, D. B. & Ward, C. H. 1992 Development of intermetallic materials for aerospace systems. *Mater. Sci. Technol.* **8**, 367–375.

Finnis, M. W. & Sinclair, J. E. 1984 A simple empirical N -body potential for transition metals. *Phil. Mag. A* **85**, 45–55.

Goodwin, L., Skinner, A. J. & Pettifor, D. G. 1989 Generating transferable tight-binding parameters: application to silicon. *Europhys. Lett.* **9**, 701–706.

Hohenberg, P. & Kohn, W. 1964 Inhomogeneous electron gas. *Phys. Rev.* **136B**, 864–871.

Kohn, W. & Sham, L. 1965 Self-consistent equations including exchange and correlation effect. *Phys. Rev.* **140A**, 1133–1138.

Methfessel, M. 1988 Elastic constants and phonon frequencies of Si calculated by a fast full-potential linear-muffin-tin-method. *Phys. Rev.* **38B**, 1537–1540.

Nguyen Manh, D., Paxton, A. T., Pettifor, D. G. & Pasturel, A. 1995 On the phase stability of transition metal trialuminides compounds. *Intermetallics* **3**, 9–14.

Nguyen Manh, D., Trambly de Lassardiere, J. J. P., Mayou, D. & Cyrot-Lackmann, F. 1992 Electronic structure and hybridization effect in the compounds Al_2Ru and Ga_2Ru . *Solid St. Commun.* **82**, 329–334.

Pettifor, D. G. 1989 New many-body potential for the bond order. *Phys. Rev. Lett.* **63**, 2480–2843.

Pettifor, D. G. 1992 Theoretical predictions of structure and related properties of intermetallics. *Mater. Sci. Technol.* **8**, 345–349.

Pettifor, D. G., Aoki, M., Gumbsh, P., Horsfield, A., Nguyen Manh, D. & Vitek, V. 1995 Defect modelling: the need for angularly-dependent potentials. *Mater. Sci. Engng A* **192/193**, 24–30.

Pettifor, D. G. & Podloucky, R. 1986 The structure of binary compounds. II. Theory of the pd-bonded AB compounds. *J. Phys. C* **19**, 315–330.

Pierce, F. S., Poon, S. J. & Biggs, B. D. 1993 Band-structure gap and electronic transport in metallic quasicrystals and crystals. *Phys. Rev. Lett.* **70**, 3919–3922.

Yamaguchi, M. & Inui, H. 1993 TiAl compounds for structural applications. *Structural intermetallics* (ed. R. Darolia, J. J. Lewandowski, C. T. Liu, P. L. Martin, D. B. Miracle & M. V. Nathal), pp. 127–142. The Minerals, Metals and Materials Society.

Zhang, B. & Soffa, W. A. 1994 The structure and properties of L1_0 ordered ferromagnets: Co–Pt, Fe–Pt, Fe–Pd and Mn–Al. *Scr. metall. Mater.* **30**, 683–688.

Discussion

A. R. C. WESTWOOD (*Sandia National Laboratories, USA*). What are the prospects for extending this approach to ternary and quaternary alloys with the ultimate objective of developing, from first principles, an intermetallic that exhibits significant ductility?

D. G. PETTIFOR. The approach of modelling defects using bond order potential is easily extendable to a treatment of ternary and quaternary alloys provided the appropriate tight binding parameters between the different chemical constituents are known. These calculations at the electronic and atomistic level would have to be linked to simulation of dislocation behaviour at the microstructural level before we have a truly ‘first principles’ modelling capability of ductile behaviour.

K. S. KUMAR (*Martin Marietta Laboratories, Baltimore, USA*). Given that the mechanical properties of intermetallic compounds are particularly sensitive to minor stoichiometric deviations as well as minor alloying additions, how realistically

can we expect atomistic modelling to serve as a predictive tool, since the number of atoms/cells that can be included is limited? Further, can defect population be included in the calculations?

D. G. PETTIFOR. The sensitivity of planar fault energies to alloying additions is already being modelled. As the interatomic potentials become more realistic and computers ever more powerful, we can expect that modelling will be able to provide new insight into the role of alloying additions and non-stoichiometry on mechanical properties.

R. W. CAHN (*University of Cambridge, UK*). Professor Pettifor showed, for certain intermetallic phases, that the energy differences between the stable and the next-most-favourable crystal structures are exceedingly small. Can he reliably predict which of such phases will exhibit stacking faults (polytypism), like SiC or Co?

D. G. PETTIFOR. Yes, even though the absolute energy may show sizeable error, relative energies are usually very reliable. The polytypism in SiC or Co has been successfully predicted by groups in the Cavendish Laboratory and the Technische Hochschule in Darmstadt.

Phase diagram calculations for high-temperature structural materials

BY N. SAUNDERS

*Thermotech Ltd, Surrey Technology Centre, 40 Occam Road,
The Surrey Research Park, Guildford, Surrey GU2 5YG, UK, and
Interdisciplinary Research Centre in Materials for High Performance
Applications, University of Birmingham, Edgbaston, Birmingham B15 2TT, UK*

Materials in use at high temperatures can reach states which are close to equilibrium and knowledge of the stable phase structure at fabrication and working temperatures can therefore be very important. The field of high-temperature structural materials provided one of the areas where thermodynamic phase diagram calculations were first used some two to three decades ago. However, although some general features of phase equilibria were predicted reasonably well, the early attempts were not able to provide sufficient accuracy for more general, practical use. Recent work has now shown that it is possible to make very accurate predictions for phase equilibria in a number of high-temperature structural materials and it is possible to demonstrate that predictions for phase equilibria in 'real' multicomponent alloys provide results close to those which are measured experimentally. This paper will present typical results which can now be obtained for γ -TiAl-based intermetallics and Ni-based superalloys and some specific examples of usage will be shown. A further advantage of the CALPHAD (calculation of phase diagrams) route is that other properties can be predicted using input data from the calculations, for example non-equilibrium solidification phenomena, time-temperature-transformation diagrams, antiphase domain boundary and stacking fault energies. This extension of the CALPHAD method will be briefly discussed.

1. Introduction

The calculation of phase equilibria using what has become known as the CALPHAD (calculation of phase diagrams) method is becoming increasingly popular. The method requires firstly a mathematical description of the thermodynamic properties of the system of interest. If the phases of interest are stoichiometric compounds, e.g. NaCl, the composition is defined and a mathematical formula is then used to describe fundamental properties such as enthalpy and entropy. Where phases exist over a wide range of stoichiometries, which is the usual case for metallic materials, other mathematical models are used which account for the effect of composition changes on free energy. All types of models require input of coefficients which uniquely describe the properties of the various phases and these coefficients are held in databases which are either in the open literature or are proprietary.

Once the thermodynamics of the various phases are defined, an applications

software package which performs a series of calculations based on the thermodynamic data is then used to calculate phase equilibria. This is usually done via a Gibbs free energy minimization process. There are now a variety of such software packages available which can perform complex multicomponent calculations and for more information the recent review by Bale & Eriksson (1990) provides a fairly comprehensive coverage of these.

The field of high-temperature structural materials provided one of the earliest testing grounds for phase diagram calculations of the CALPHAD type. Early work by Kaufman and co-workers (see, for example, Kaufman & Nesor 1974a, b, 1975) showed that it was possible to provide some guidance in the search for high-temperature eutectic reactions in Ni-based ternary alloys. This information could then be used in the search for directionally solidified eutectic materials. However, although Kaufman and co-workers produced datasets which could be used for calculations in a wide number of ternary systems, it has become increasingly clear that the assumptions made in their simple model types, i.e. regular and subregular solution, inherently limit accuracy and general applicability.

As newer models and software packages have come to the fore the CALPHAD method has advanced to the stage where it can be legitimately expected that predictions for phase equilibria in multicomponent systems should provide answers close to that which would be measured experimentally. An example of such work is the effort devoted over the last two decades to multicomponent ferrous alloys by the Scientific Group Thermodata Europe (Ansara & Sundman 1987), and in particular by the Royal Institute of Technology, Stockholm, Sweden, a member of this group. Results have clearly demonstrated the excellent levels of accuracy that can now be attained which in turn allows design engineers to model materials of this type with confidence.

Unfortunately, until very recently there have been very few, if any, databases of equivalent accuracy currently in existence for other material types. This has presented severe problems for CALPHAD calculations with high-temperature materials of current usage, for example Ni-based superalloys, Ti alloys and γ -TiAl-based alloys. The present paper discusses new work in the field of Ti- and Ni-based alloys and demonstrates that high levels of accuracy can be achieved in predicted equilibria for multicomponent alloys of these types. Furthermore, the same database which is used for equilibrium predictions can be used for the prediction of other effects not normally associated with CALPHAD type calculations: (i) non-equilibrium solidification behaviour of superalloys during casting, providing results for fraction of solid transformation as a function of temperature, microsegregation, formation of interdendritic phases, heat evolution, etc.; (ii) time-temperature-transformation (TTT) diagrams for σ -phase growth; (iii) antiphase domain boundary energies in γ and stacking fault energies in γ .

2. The CALPHAD approach

The basis of the CALPHAD approach is the mathematical description of the free energy of the various chemically distinct phases in an alloy system. There are now a variety of models available to describe the thermodynamic properties of phases which can be, for example, stoichiometric compounds, solution phases, gaseous species, ionic materials, intermetallic compounds, ceramic types, etc. Several these models are listed by Hillert (1986) and Eriksson & Hack (1989).

The integral free energy of formation (ΔG) of a pure species or stoichiometric compound is given simply by the equation

$$\Delta G = \Delta H + T\Delta S, \quad (2.1)$$

where ΔH is the enthalpy of formation, T is the temperature and ΔS is the entropy of formation. For the case of a 'solution' phase where mixing of the various components takes place its free energy (ΔG) can be written generally as

$$\Delta G = \Delta G^\circ + \Delta G_{\text{mix}}^{\text{ideal}} + \Delta G_{\text{mix}}^{\text{xs}}, \quad (2.2)$$

where ΔG° is the free energy contribution of the pure components of the phase, $\Delta G_{\text{mix}}^{\text{ideal}}$ is the ideal mixing term and $\Delta G_{\text{mix}}^{\text{xs}}$ is the excess free energy on mixing of the components. There are also terms associated with (2.1) the effect of pressure which is important to geological systems and (2.2) the effect of magnetism which is important to ferrous alloys. It is not the purpose of this paper to describe in detail the various models which are used to describe the thermodynamic properties of phases, but it is useful to briefly discuss some of the models which are available and where they are applied.

(a) *Ideal solution model*

The simplest model is the ideal solution model where interactions between components in the phase of interest are considered to be negligible and the free energy of mixing is given by

$$\Delta G_m = x_i \sum_i \Delta G_i^\circ + RT \sum_i \ln x_i, \quad (2.3)$$

where x_i is the mole fraction of component i , ΔG_i° defines the free energy of the phase in the pure component i and R is the gas constant. In gases, ideal mixing is often assumed and this assumption is usually quite reasonable. However, in solid phases the interactions between components are far more significant and cannot usually be ignored.

(b) *Non-ideal solution models*

To deal with non-ideal interactions a further term is added to (2.3) which becomes

$$\Delta G_m = x_i \sum_i \Delta G_i^\circ + RT \sum_i \ln x_i + \sum_i \sum_{j>1} x_i x_j \sum_v \Omega_v (x_i - x_j)^v. \quad (2.4)$$

The final term is based on a Redlich-Kister-Muggianu (RKM) equation which considers the free energy of a many-component solution phase to be a product of the summed binary interactions and Ω_v is an interaction parameter dependent on the value of v . In practice the value for v does not usually rise above 3. Equation (2.4) assumes higher-order interactions are small in comparison to those which arise from the binary terms but this may not be always the case. Ternary interactions are often considered but there is little evidence of the need for interaction terms of a higher order than this. Various polynomial expressions for the excess term have been considered other than the RKM equation (see, for example, the reviews by Ansara (1979) and Hillert (1980)). However, all are based on predicting the properties of the higher-order system from the properties of the lower-component systems.

Equation (2.2) is normally used in metallic systems for substitutional phases such as liquid, BCC, FCC, etc., and in this mode its use is extensive. It can also be used to a limited extent for ceramic systems and useful predictions could be found in the case of quasi-binary and quasi-ternary oxide (Kaufman & Nesor 1978) systems. However, for phases where components occupy preferential sites on crystallographic sublattices such as interstitial solutions, ordered intermetallics, ceramic compounds, etc., simple substitutional models are not generally adequate and sublattice models are now becoming increasingly popular.

(c) *Sublattice models*

One of the earliest treatments of phases with distinct sublattice occupation was by Hillert & Staffansson (1970) who considered the case of a phase with two sublattices. The sublattice occupancy is shown schematically below:

$$(A, B)_u (C, D)_v.$$

For the two sublattice model ΔG° is written as

$$\Delta G^\circ = y_A^1 y_C^2 \Delta G_{A:C} + y_A^1 y_D^2 \Delta G_{A:D} + y_B^1 y_C^2 \Delta G_{B:C} + y_B^1 y_D^2 \Delta G_{B:D}, \quad (2.5)$$

where

$$y_i^s = n_i^s / \sum_i n_i^s \quad (2.6)$$

and

$$\sum_i y_i^s. \quad (2.7)$$

The ideal entropy of mixing is written as

$$\Delta G_{\text{mix}}^{\text{ideal}} = RT[u(y_A^1 \ln y_A^1 + y_B^1 \ln y_B^1) + v(y_C^2 \ln y_C^2 + y_D^2 \ln y_D^2)]. \quad (2.8)$$

The $\Delta G_{\text{mix}}^{\text{xs}}$ term considers the interactions between the components on the sublattice and can be quite complex, see for example Ansara *et al.* (1988). More recently Sundman & Ågren (1981) extended this model to take into account multiple sublattices and their model is used extensively in the present work.

3. Results and discussion

(a) *Ti-Al-X systems*

The α_2 -Ti₃Al and γ -TiAl compounds have been the centre of considerable interest as a material which would extend the applicability of Ti-based alloys to higher temperature regimes and areas where good oxidation and burn resistance are important. Initially, materials based on Ti₃Al, the so-called super- α_2 class of alloys, were seen as new generation materials. They are potentially stronger than the γ -TiAl-based alloys and can be made more ductile. However, the superior oxidation resistance and comparable fracture toughness of the γ -TiAl based alloys has seen these materials come to the fore.

Similarly to conventional Ti-alloys, the properties of γ -TiAl based alloys are strongly controlled by their microstructure. The various microstructure types and their effect on mechanical properties are now well documented (Kim 1994). Basically this can be understood from the Ti-Al phase diagram (figure 1). Levels of Al usually lie in the range 45–50 at.% where it is possible to anneal at high temperatures to produce a structure that is fully α (HCP). The high temperature α decomposes both by precipitating γ in the $\alpha + \gamma$ two-phase region and

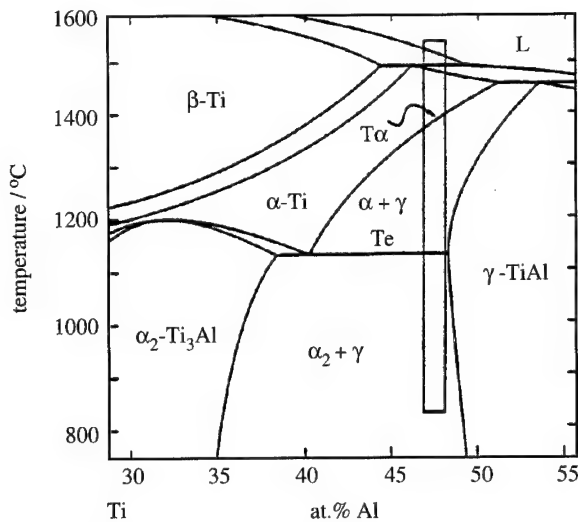


Figure 1. Ti-Al phase diagram (Kim 1991). Shaded area indicates Al composition of early γ -TiAl alloys.

importantly through decomposition by a eutectoid reaction to α_2 and γ . The microstructure then is a mixture of γ formed at high temperatures in the $\alpha + \gamma$ two-phase region and a lamellar structure of $\alpha_2 + \gamma$. By quenching from the α region it is also possible to bypass the precipitation of γ -TiAl and produce a fully lamellar structure. The ratio of primary γ to lamellar $\alpha_2 + \gamma$ is a critical factor in controlling mechanical properties and therefore phase diagram calculations have a potentially important part to play in the design of alloys, particularly with regard to thermo-mechanical processing schedules.

One of the major difficulties of the modelling is the Ti-Al binary system itself. In a recent Japanese report 42 versions of this diagram had been reported previous to 1990. With recent work this number is now well over 50. Phase diagram modelling for Ti-Al has been undertaken by the present author (Saunders 1990) and this forms the basis for Ti-Al-X systems now being modelled as part of a current COST 507 project (figure 2). Broadly speaking, the form of the diagram is quite well established now. The existence of the Ti_3Al and TiAl compounds is not disputed and their range of solubility reasonably well understood. The main outstanding problems lie in the determination of the exact position of the $\alpha + \gamma$ boundaries and whether the $\alpha + \beta$ phase boundary touches the α_2 phase field. The former problem relates to processing and microstructure formation and is therefore very important.

The extension to ternaries has been attempted by Kattner & Boettinger (1992) who used a two-sublattice model for the α_2 - Ti_3Al and γ - TiAl phases in their description of the Ti-Al-Nb system. They were able to produce a diagram which substantially agreed with that observed in the published literature up to that point. However, although the form of the diagram appears reasonable they did not take into account the ordering of the β phase to the B2 CsCl structure which is observed in almost all Ti-Al-X systems where X is one of the refractory metals such as Nb and V. Work by the present author on both Ti-Al-Nb and Ti-Al-V has shown the importance of including this ordering in the accurate representa-

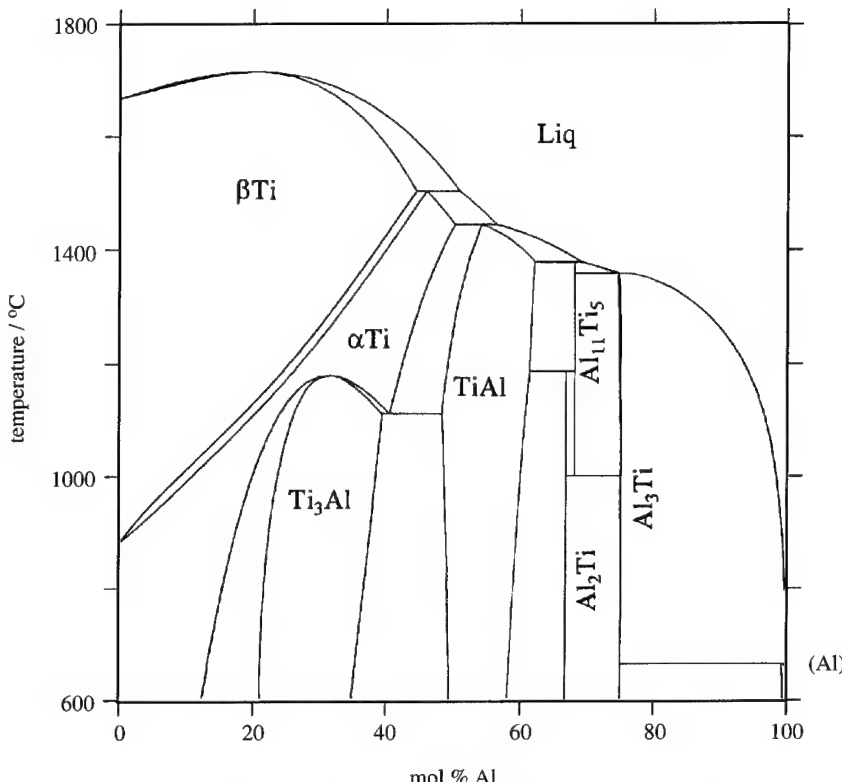


Figure 2. Calculated Ti-Al phase diagram (Saunders 1990).

tion of phase equilibria and it is of particular interest to be able to differentiate between the ordered and disordered form when considering mechanical properties.

Figures 3 and 4 show calculated isothermal sections at 1000 and 1200 °C for Ti-Al-Nb. They show the extension of the various intermetallic compounds, both Nb-Al based and Ti-Al based, into the ternary. The $\beta \rightarrow \text{B2}$ transformation is second order and its loci of composition at each temperature are shown by dashed lines. Of particular interest is the reappearance of the B2 phase as an isolated region close to γ -TiAl which is in excellent agreement with the detailed work of Hellwig (1992).

The B2 phase has been modelled using a two-sublattice ordering model first proposed by Ansara *et al.* (1988). The present author (Saunders 1989) then showed how this model could be made equivalent to a Bragg-Williams-Gorsky model which enables the correct model parameters to be used to produce the required second-order transformation. Further work on Ti-Al-V (Saunders *et al.* 1994) has confirmed the importance of taking into account the B2 ordering and initial work on Ti-Al-Mn-Nb has shown that the modelling is extendable to multicomponent alloys.

(b) Ni-based superalloys

Ni-based superalloys form one of the oldest class of high-temperature structural materials. They can be used at a higher value of T/T_m than almost any

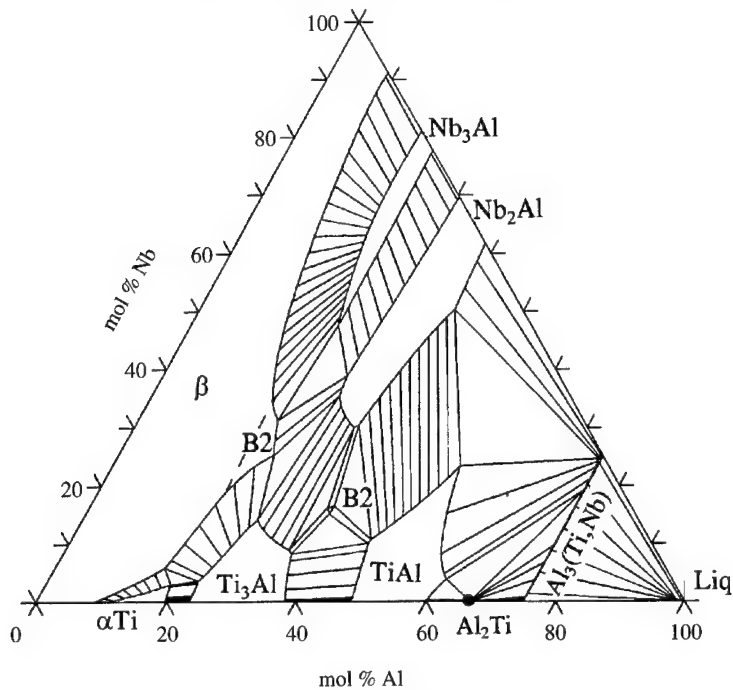


Figure 3. Calculated isothermal section for Ti-Al-Nb at 1000 °C.

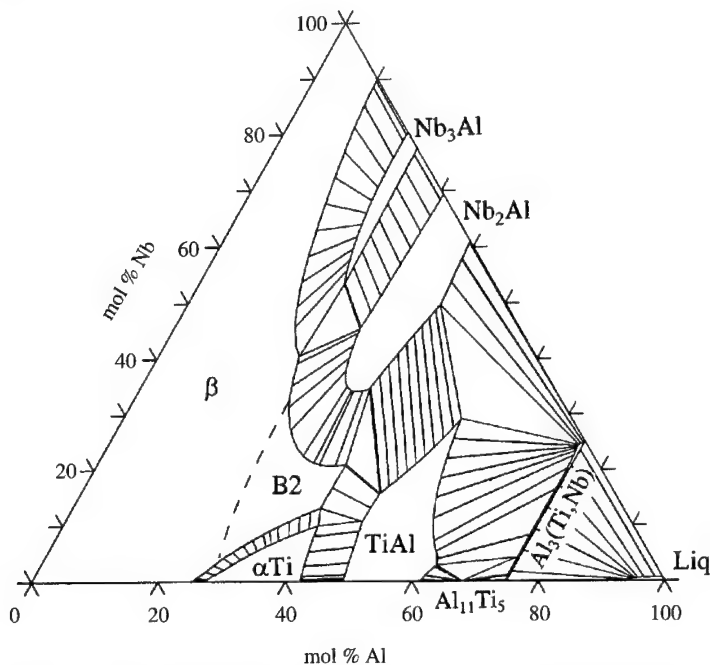


Figure 4. Calculated isothermal section for Ti-Al-Nb at 1200 °C.

other metallic material which allied to a high strength and excellent oxidation and corrosion resistance make them one the most widely used material types in aerospace and land-based gas turbine engines.

The strength of Ni-based superalloys comes from the precipitation of the ordered $L1_2$ compound (γ'), based on Ni_3Al , in a ductile FCC, Ni-based matrix (γ) and control of γ/γ' microstructure is one of the governing factors in choice of thermo-mechanical processing cycles. It is therefore of great interest to be able to predict γ/γ' equilibria accurately. Superalloys are also one of the most highly alloyed of all material types and with additions of elements such as Co, Cr, Mo and W the matrix becomes unstable with respect to embrittling TCP phases such as σ , μ and Laves phases, and the addition of C leads to the formation of a variety of carbide phases which can act as sites for TCP phases formation.

Both of the above factors are critical in the design and usage of Ni-based superalloys. Much work has been done via mathematical techniques such as regression analysis on γ/γ' equilibria (see, for example, Dreshfield & Wallace 1974) and (Harada *et al.* 1988), while the use of PHACOMP methods in predicting σ -phase formation is extensive. The limitations of regression analysis are straightforward. Firstly, the method relies on substantial previous experimentation which must be accurate. Secondly it is an interpolative technique and extrapolation outside the composition and temperature regime of the experiments used to provide the results for analysis can be quite unreliable.

PHACOMP relies on the simple concept of an average electron hole number, \bar{N}_v , which is made up of a weighted average of N_v values for the various elements. In itself the concept behind PHACOMP is theoretically simple and easy to use. However, there are a number of questions concerning its use and theoretical justification. For example the values of N_v used to calculate \bar{N}_v are usually empirically adjusted to fit experience and the model fails to explain why σ is not observed in the binary Ni-Cr or Ni-Mo systems but appears only in the Ni-Cr-Mo ternary. Furthermore, although it pertains to describe a line for the phase boundary of γ and σ it gives no information on the temperature range where σ may be stable, nor is there information on the interaction of this boundary with the γ/μ or γ /Laves boundaries.

Four years ago a development programme involving Thermotech and Rolls-Royce plc, Derby was begun to produce a multicomponent database for the prediction of phase equilibria in Ni-based superalloys. This work has now reached the stage where a database exists containing the following elements:

Ni Al Co Cr Hf Mo Nb Ta Ti W Zr B C

It is therefore at a point where real industrial superalloys can be routinely handled. As well as simple predictions concerning freezing ranges, γ' solvus temperatures, etc., the database allows the user to predict the composition and temperature conditions under which the various secondary phases such as σ , μ , Laves and η can form (successfully differentiating between them) and takes into account the various types of carbides found in superalloys.

Part of the project has involved a validation procedure for the accuracy of the database which, particularly with respect to γ/γ' equilibria, can be statistically quantified. Figure 5 shows the comparison between predicted and experimentally observed critical temperatures such as γ' solvus (γ'_s), liquidus and solidus where the average difference between predicted values and those observed experimentally is of the order of 10 °C. Extensive work has been done on measurements concerning γ/γ' equilibria and it is possible to compare in detail predicted values with those observed experimentally.

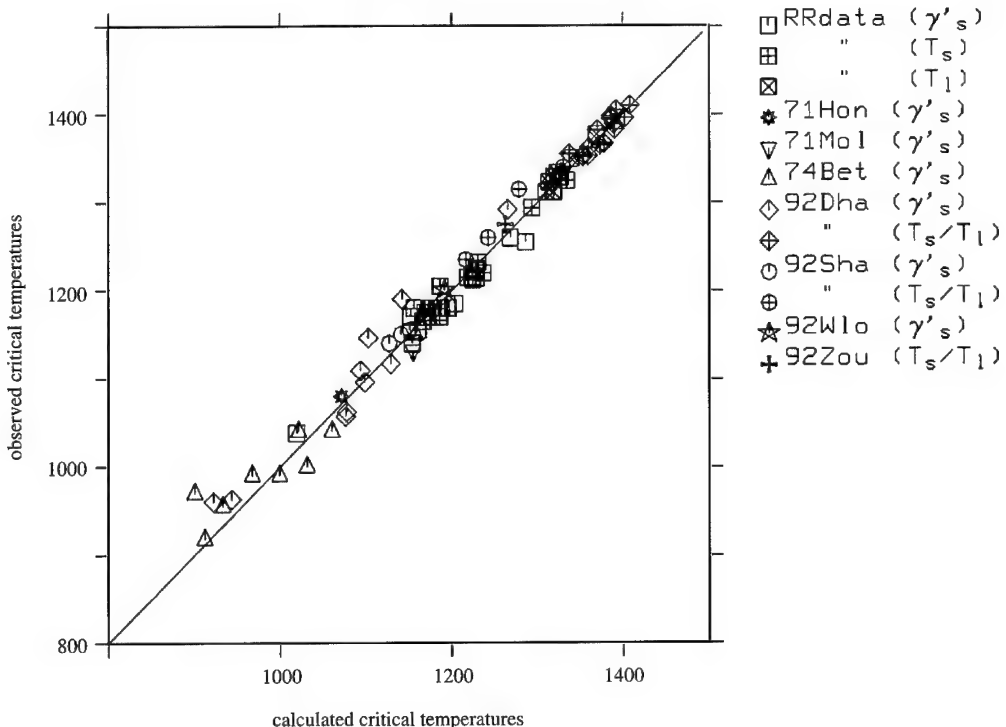


Figure 5. Comparison between calculated and experimentally observed critical temperatures in Ni-based superalloys.

Figure 6 shows a comparison between predicted and observed amounts of γ' in a variety of superalloys where the average difference between predicted values and those observed experimentally is of the order of 4%. In the comparison, results can be in either weight% or volume%. For the latter case, as lattice mismatches are so small, mole% values will give almost identical values to volume%. Figure 7a-g shows comparisons of the chemical compositions of γ and γ' . Where experimental results are given in weight% they have been converted to atomic% to provide a consistent basis for comparison. The average difference between predicted values and those observed experimentally is of the order of 1 at.% for Al, Co, Cr and 0.5 at.% for Mo, Ta, Ti and W. Table 1 gives some examples of superalloys used in the validation procedure.

Apart from its success in predicting liquid phase relationships and γ/γ' equilibria the database has been able to successfully predict transitions between the σ and μ phases and to differentiate between the different types of carbide that can be formed in Ni-base superalloys. It has also been strikingly successful at predicting the susceptibility to η phase formation, for example in alloys such as Nimonic 263 (Betteridge & Heslop 1974) and IN939 (Shaw 1992, personal communication).

Some of the ways in which the database can be used are shown by taking the specific example of Udimet 720 (U720). Figure 8 shows a calculated phase percent plot for this alloy which shows the various phases which exist in the alloy as a function of temperature; the alloy composition is given in table 2. The alloy was originally developed for land-based gas turbine applications and for long-term service at temperatures up to 900 °C. However, its excellent forging character-

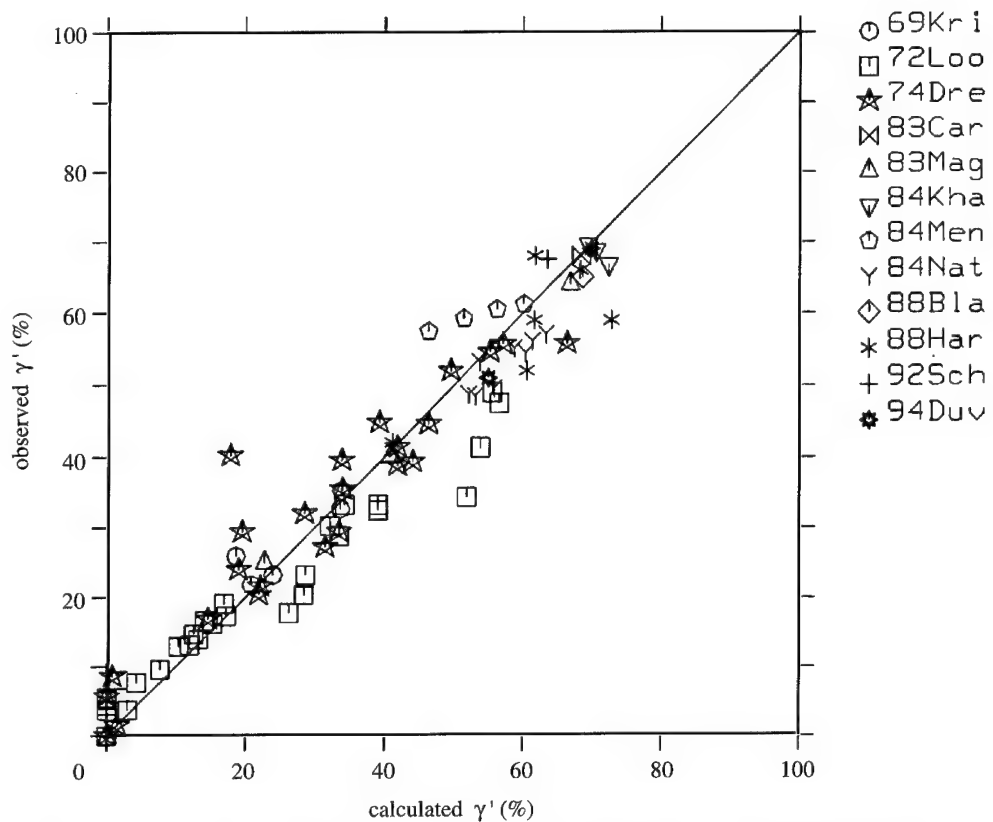


Figure 6. Comparison between calculated and experimentally observed amounts of γ' in Ni-based superalloys.

Table 1. Some alloys used in the validation of the Ni-based superalloy database

Inconel 700	Nimonic 263	MAR-M247
Nimonic 115	EPK 55	PWA 1480
René 41	EPK 57	IN738LC
Udimet 500	Udimet 520	SRR 99
Udimet 700	CMSX-2	AF2 1DA
Waspaloy	IN939	AP1
Nimonic 80A	IN 100	APK6
Nimonic 81	Udimet 710	CH88-A
Nimonic 90	MXON	Udimet 720
Nimonic 105	B1900	MC2

istics and mechanical properties suggested it could be used as a disc alloy. Unfortunately, although long-term exposure of the alloy at these high temperatures showed only a minor susceptibility to formation, tests done at 750 °C showed that σ formed very readily and in large amounts (Keefe *et al.* 1992). To overcome

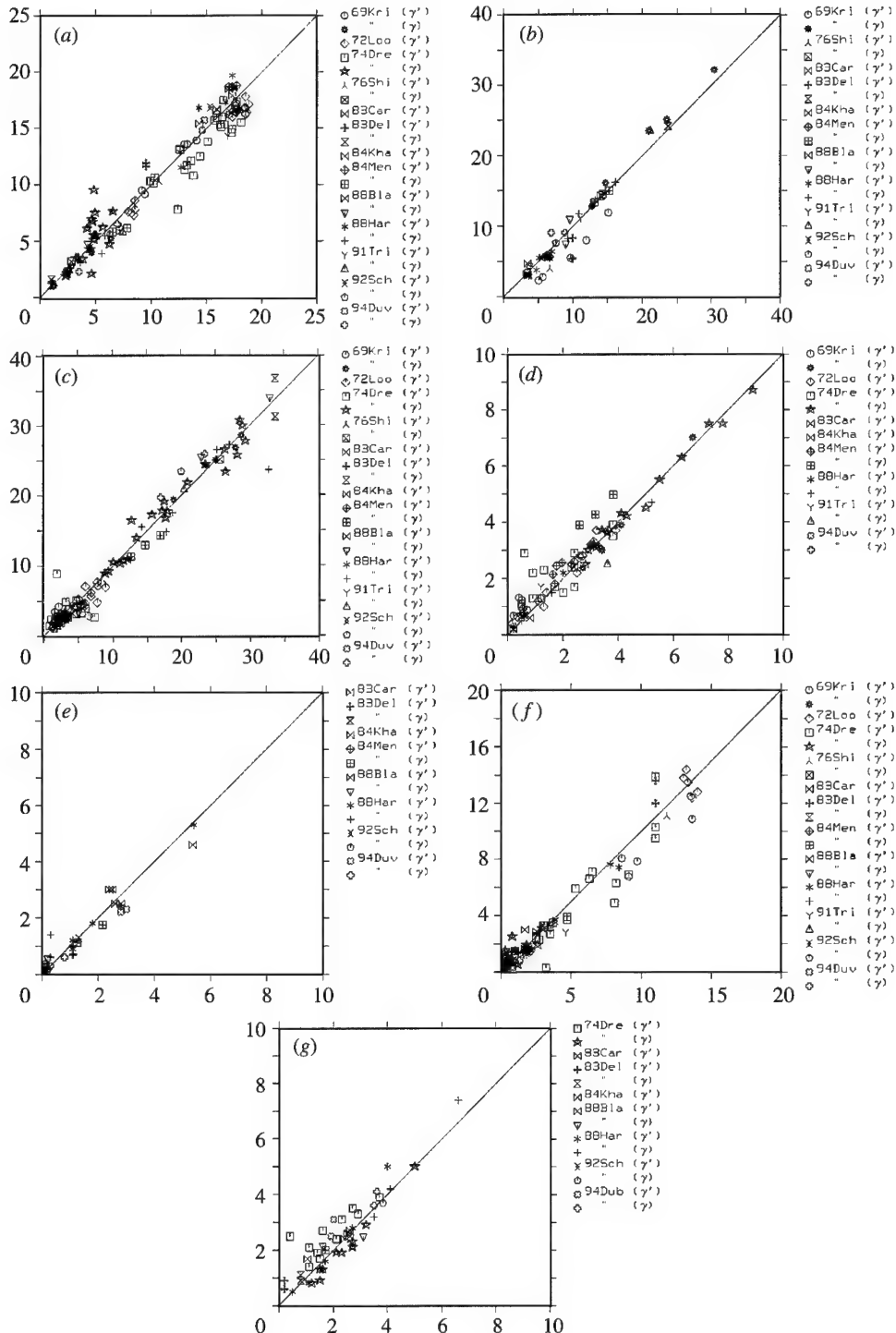


Figure 7. Comparison between calculated and experimentally observed compositions of γ' in Ni-based superalloys. (a) Al, (b) Co, (c) Cr, (d) Mo, (e) Ta, (f) Ti and (g) W.

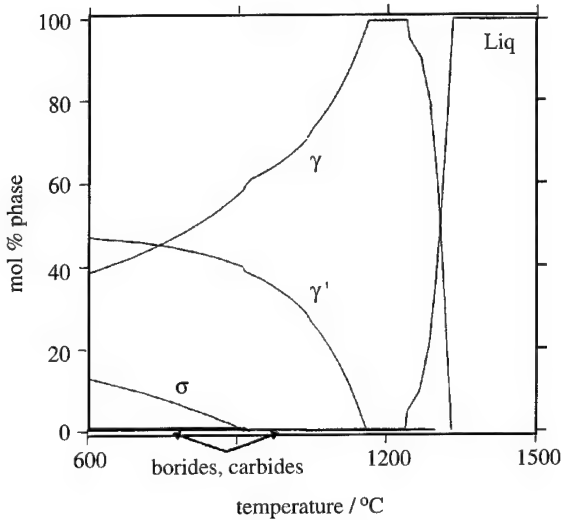
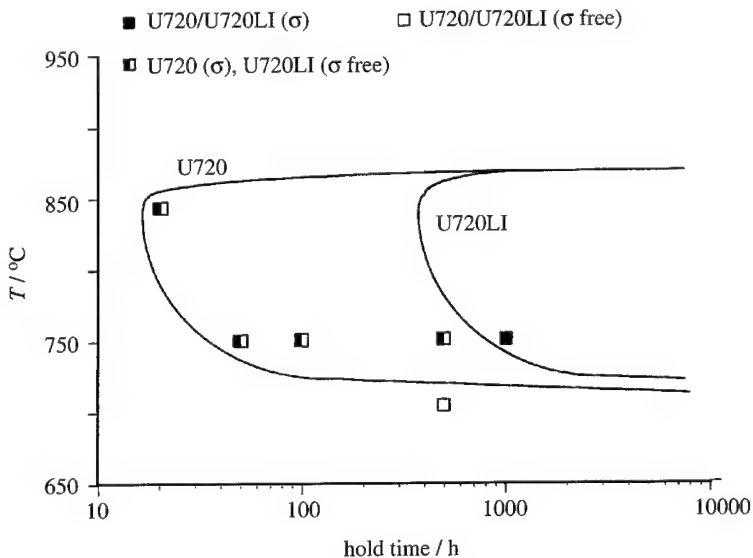


Figure 8. Calculated phase percent plot for U720.

Figure 9. Observation of σ in U720 and U720LI with TTT diagrams proposed by Keefe *et al.* (1992).

this, Udimet 720LI (U720LI), a low Cr version, was developed (table 2) which substantially reduced σ susceptibility at 750 °C. Keefe *et al.* (1992) suggested that a TTT diagram of the type shown in figure 9 could explain the difference in behaviour of the two variants. It is interesting to note that in their diagram the TTT curves for the two variants join at about 870 °C, but show substantially different behaviour below this temperature. Their diagram consequently suggests that the σ solvus temperature (σ_s) for both alloys is identical, which is unlikely as a change in composition must change this value.

It was therefore instructive to calculate the σ_s temperature for both alloys.

Table 2. Nominal compositions of Udimet 720 and Udimet 720LI
(After Keefe *et al.* 1992.)

	Cr	Co	Mo	W	Ti	Al	C	B	Zr
U720	18.0	14.7	3.0	1.25	5.0	2.5	0.035	0.033	0.03
U720LI	16.0	14.7	3.0	1.25	5.0	2.5	0.010	0.015	0.03

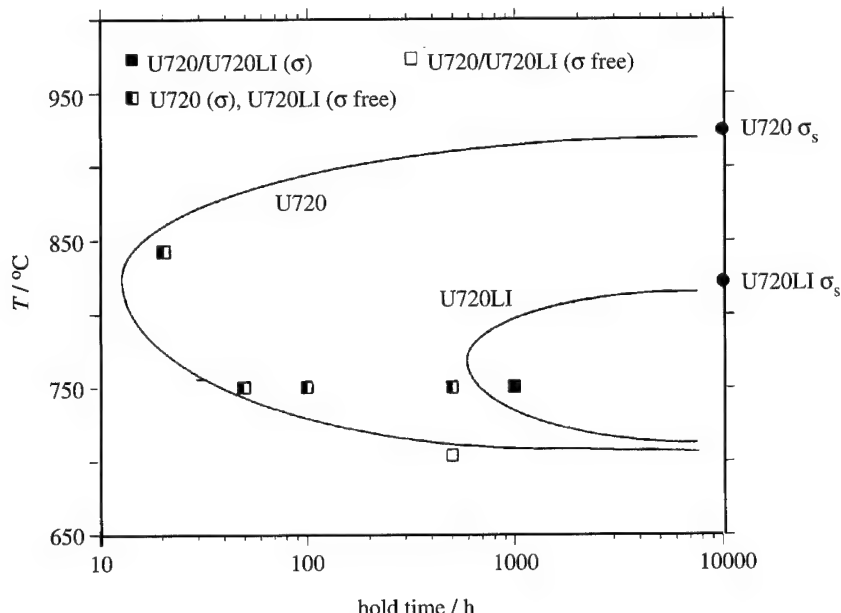


Figure 10. TTT diagrams proposed here for U720 and U720LI based on calculated σ_s values.

These are plotted on a similar diagram and also included are suggested TTT curves based on these results (figure 10). It can be seen that the difference in σ susceptibility can be almost completely explained by the 100 °C drop in σ_s when the Cr concentration is lowered.

It is now also possible to begin quantifying TTT diagrams such as this using a combined kinetic and thermodynamic approach. In recent years a European project has led to the creation of a software package, DICTRA, which links the simulation of diffusion-controlled processes in multicomponent systems with thermodynamic properties obtained directly and interactively from the phase diagram calculation package THERMO-CALC (Andersson *et al.* 1991; Inden *et al.* 1993). Work with DICTRA has mainly concentrated on ferrous-based alloys, for example the growth of ferrite from austenite, but preliminary work has shown that it is capable of simulating the growth of σ in a multicomponent Ni-based, γ matrix (Jönsson & Ågren 1993, personal communication).

It is also useful to know how variations in chemistry within proposed commercial specification limits affect σ_s and figure 11 shows the variation predicted as each element is changed between its maximum and minimum specification. What was at first surprising was the prediction that the greatest effect on σ_s was due to

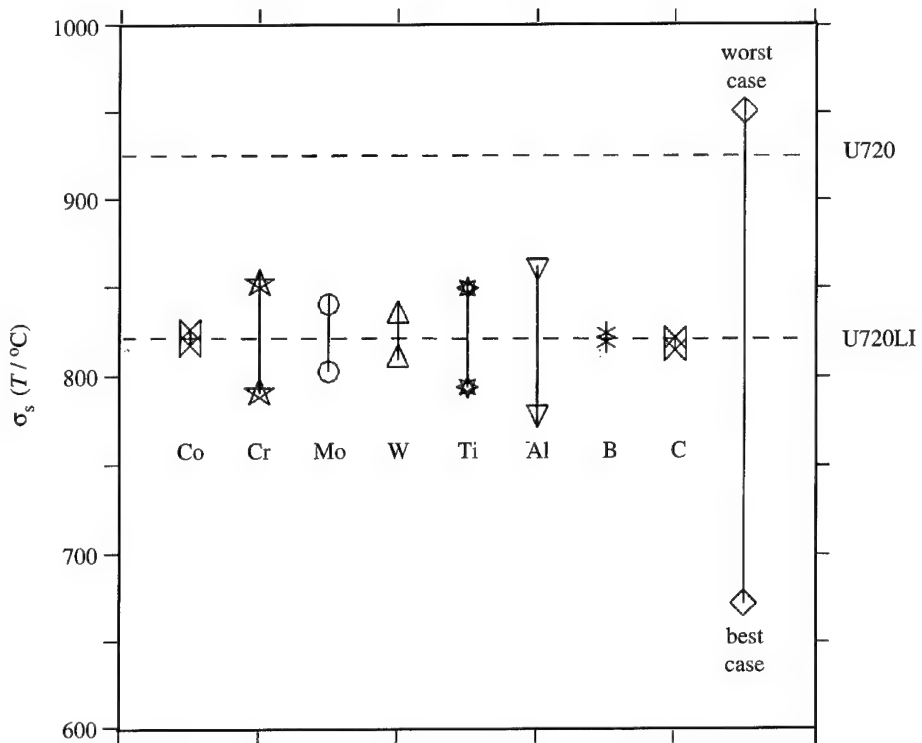


Figure 11. Variation in calculated σ_s as each element in U720LI is changed between its maximum and minimum specification.

Al and that variations within the Ti specification limit were nearly as potent as for Cr. This can be explained fairly readily. Al and Ti are powerful γ' formers and any increase in their levels increases the amount of γ' and reduces the amount of γ . As Cr and Mo strongly partition to γ , any increase in γ' levels markedly increases their concentration in γ hence making the alloy more susceptible to σ formation. It should be stressed that σ -sensitivity factors as shown in figure 11 are compositionally dependent and as such their values can significantly change depending on the alloy studied. However, the relative effect of the elements does seem to be maintained.

There is interest in understanding the solidification behaviour of Udimet 720 and to this end a 'single crystal' alloy was prepared at Rolls-Royce without B and C additions (Small 1993, personal communication). Initial examination appeared to show a familiar structure of Ni-rich γ dendrites with some γ' in the interdendritic regions. However, microprobe analysis across the interdendritic region showed many of the precipitates to have very high Ti and low Al levels and these were associated with a more needle-like morphology. It is possible to make predictions for non-equilibrium solidification assuming no back-diffusion in the solid using a standard Scheil-Gulliver simulation within the Thermo-Calc software package. The results from this clearly indicated that as well as γ' there would be a susceptibility for η formation in the interdendritic regions explaining the high Ti and low Al levels which were observed in needle-like precipitates.

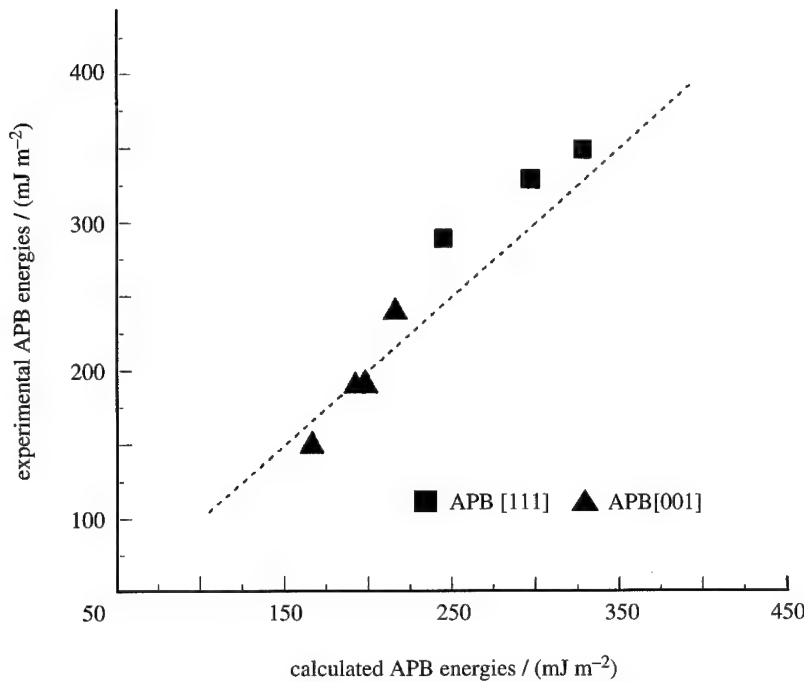


Figure 12. Comparison between calculated and experimentally observed APB energies for several Ni-based superalloys including U720.

There is also interest in being able to predict the mechanical behaviour of Ni-based superalloys. Several models exist but these rely on input data for properties such as stacking fault energies (SFE) in γ and antiphase domain boundary (APB) energies in the γ' . Although not readily associated with the CALPHAD method, such properties can be predicted, for example SFEs in Fe–Ni–Cr alloys were predicted by Miodownik (1978) based on $\Delta G^{\text{FCC} \rightarrow \text{CPH}}$ for alloys in this system. Clearly if similar data were available for Ni-based systems such a method could be applied for Ni-based superalloys.

APB energies have been predicted for a number of Ni-based superalloys including Udimet 720, using a model based on the calculation of bond energies across the APB (Miodownik & Saunders 1994). The method relies on calculating nearest neighbour interaction energies for the γ' phase, up to the third nearest neighbour. These can be estimated using the ordering energy of the γ' phase from the disordered FCC γ phase and the heat of formation of the FCC phase of the same composition. The treatment was applied to several selected alloys, including Udimet 720, and these were compared with subsequently determined experimental values (Small 1994, personal communication) for the APB[111] and APB[001]. The results are shown in figure 12 and the comparison is extremely satisfactory.

4. General comments and summary

It has not been possible within the scope of this paper to go into detail concerning many of the applications which are possible using the CALPHAD method, nor to describe recent work on conventional Ti-alloys (Saunders 1994). However, it should be stressed that complex alloys can now be routinely handled, and

with high degrees of accuracy. This leads to an ability to quantify and understand many issues of interest concerning materials for use in high-temperature applications.

For too long, materials such as superalloys have been considered too complex for modelling of this type. This has led to a reliance on approaches such as PHACOMP which are at best semi-quantitative and at worst inaccurate and has further led to a mystique surrounding the phase behaviour of such materials. It is to be hoped, now basic phase behaviour can be predicted with a high degree of confidence, that more quantitative modelling approaches can be applied for a variety of materials design and process issues, thus leading to a greater understanding of material behaviour, the optimization of properties and some quality control aspects in production.

The author gratefully acknowledges the use of the Thermo-Calc software package developed by the Division of Computational Thermodynamics, Department of Materials Science and Engineering, Royal Institute of Stockholm, S-100 44 Stockholm 70, Sweden.

References

Andersson, J.-O., Höglund, L., Knoop, U., Inden, G. & Ågren, J. 1991 In *Computer Simulation of Multicomponent Diffusional Transformations in Steel: Proc. Int. Symp. Fundamentals and Applications of Ternary Diffusion* (ed. G. R. Purdy). New York: Pergamon.

Ansara, I. 1979 *Int. Met. Rev.* **22**, 20.

Ansara, I. & Sundman, B. 1987 In *Computer handling and dissemination of data* (ed. P. S. Glaeser), p. 154. CODATA.

Ansara, I., Sundman, B. & Willemin, P. 1988 *Acta metall.* **36**, 977.

Bale, C. W. & Eriksson, G. 1990 *Can. metall. Q.* **29**, 105.

Betteridge, W. & Heslop, J. 1974 In *The NIMONIC alloys and other Ni-based high temperature alloys*, 2nd edn. Edward Arnold.

Blavette, D., Caron, P. & Khan, T. 1988 In *Superalloys 1988* (ed. S. Reichman, D. N. Duhl, G. Maurer, S. Antlovich & C. Lund), p. 305. Warrendale, PA: The Metallurgical Society.

Caron, P. & Khan, T. 1983 *Mat. Sci. Engng* **61**, 173.

Delargy, K. M. & Smith, G. D. W. 1983 *Metall. Trans. A* **14**, 1771.

Dharwadkar, S. R., Hilpert, K., Schubert, F. & Venugopal, V. 1992 *Z. Metallk.* **83**, 744.

Dreshfield, R. L. & Wallace, J. F. 1974 *Metall. Trans.* **5**, 71.

Duval, S., Chamberland, S., Caron, P. & Blavette, D. 1994 *Acta metal. mater.* **42**, 185.

Eriksson, G. & Hack, K. 1990 *Metall. Trans. B* **21**, 1013.

Guillermet, A. F. 1989 *Z. Metallk.* **80**, 83.

Harada, H., Ohno, K., Yamagata, T., Yokokawa, T. & Yamazaki, M. 1988 In *Superalloys 1988* (ed. S. Reichman, D. N. Duhl, G. Maurer, S. Antlovich & C. Lund), p. 733. Warrendale, PA: The Metallurgical Society.

Hellwig, A. 1992 Ph.D. thesis, University of Düsseldorf, Germany.

Hillert, M. & Staffansson, L.-I. 1970 *Acta chem. scand.* **24**, 3618.

Hillert, M. 1980 *Calphad* **4**, 1.

Hillert, M. 1986 In *Computer modelling of phase diagrams* (ed. L. H. Bennett), p. 1. Warrendale, PA: The Metallurgical Society.

Honnarat, Y., Davidson, J. & Duffaut, F. 1971 *Mem. Sci. Rev.* **68**, 105.

Inden, G., Franke, P. & Knoop, U. 1993 In *Computer aided innovation of new materials II* (ed. M. Doyama, J. Kihara, M. Tanaka & R. Yamamoto), p. 701. Amsterdam: Elsevier.

Kattner, U. R. & Boettinger, W. J. 1992 *Mater. Sci. Engng A* **152**, 9.

Kaufman, L. & Nesor, H. 1974a *Metall. Trans.* **5**, 1617.

Kaufman, L. & Nesor, H. 1974b *Metall. Trans.* **5**, 1623.

Kaufman, L. & Nesor, H. 1975 *Metall. Trans. A* **6**, 2115.

Kaufman, L. & Nesor, H. 1978 *Calphad* **2**, 35.

Keefe, P. W., Mancuso, S. O. & Maurer, G. E. 1992 In *Superalloys 1992* (ed. S. D. Antolovich, R. W. Stusrud, R. A. MacKay, D. L. Anton, T. Khan, R. D. Kissinger & D. L. Klarstrom), p. 487. Metals Park, OH: The Metallurgical Society.

Khan, T., Caron, P. & Duret, C. 1984 In *Superalloys 1984* (ed. M. Gell *et al.*), p. 145. Warrendale, PA: Metals Society AIME.

Kim, Y.-W. & Dimiduk, D. M. 1991 *J. Metals, N.Y.* **43**(8), 40.

Kim, Y.-W. 1994 *J. Metals, N.Y.* **46**(7), 30.

Kriege, O. H. & Baris, J. M. 1969 *Trans. ASM* **62**, 195.

Lasalmonie, A. & Lobradou, M. 1979 *J. Mater. Sci.* **14**, 2589.

Loomis, W. T., Freeman, J. W. & Sponseller, D. L. 1972 *Metall. Trans.* **3**, 989.

Magrini, M., Badan, B. & Ramous, E. 1983 *Z. Metallk.* **74**, 314.

Meng, Z.-Y. 1984 In *Superalloys 1984* (ed. M. Gell *et al.*), p. 563. Warrendale, PA: Metals Society AIME.

Miodownik, A. P. 1978 *Calphad* **2**, 207.

Miodownik, A. P. & Saunders, N. 1994 Presented at *The Metallurgical Society Fall Meeting, Rosemount, Illinois, 3-6 September 1994*.

Nathal, M. V. & Ebert, L. J. 1984 In *Superalloys 1984* (ed. M. Gell *et al.*), p. 125. Warrendale, PA: Metals Society AIME.

Saunders, N. 1989 *Z. Metallk.* **80**, 903.

Saunders, N. 1990 In *Measurement and valuation of thermochemical and thermophysical properties to provide a database for the development of new light alloys*. COST 507 Programme. (Submitted.)

Saunders, N. & Chandrasekaran, L. 1992 *J. Phase Equilibria* **13**, 612.

Saunders, N., Sheng, G.-Y. & Miodownik, A. P. 1994 In *Calphad XXIII, Madison, Wisconsin, USA, 12-17 June 1994*.

Saunders, N. 1994 *Ti-DATA, a thermodynamic database for calculation of phase equilibria in multi-component Ti-based alloys*. Guildford, UK: Thermotech Ltd.

Schmidt, R. & Feller-Kniepmeier, M. 1992 *Scr. metall. mater.* **26**, 1919.

Shimanuki, Y., Masui, M. & Doi, H. 1976 *Scr. metall.* **10**, 805.

Sims, C. T. 1987 In *Superalloys II* (ed. C. T. Sims, N. Stoloff & W. C. Hagel), p. 217. New York: John Wiley.

Sundman, B. & Ågren, J. 1981 *J. Phys. Chem. Solids* **42**, 297.

Trinckhauf, K. & Nembach, E. 1991 *Acta metall. mater.* **39**, 3057.

van der Molen, E. H., Oblak, J. M. & Kriege, O. H. 1971 *Metall. Trans.* **2**, 1627.

Wlodek, S. T., Kellu, M. & Alden, D. 1992 In *Superalloys 1992* (ed. S. D. Antolovich, R. W. Stusrud, R. A. MacKay, D. L. Anton, T. Khan, R. D. Kissinger & D. L. Klarstrom), p. 165. Metals Park, OH: The Metallurgical Society.

Discussion

R. W. CAHN (*University of Cambridge, UK*). My compliments on a most convincing demonstration of the power of the CALPHAD method as applied to 'real' industrial alloys! To complete this exposition, could Dr Saunders tell us something about the kind of experimental data that are needed as input for the sort of CALPHAD calculations he has exemplified.

N. SAUNDERS. The calculations for the multicomponent systems presented in

the paper are based on predicting the thermodynamic properties of higher-order systems from the thermodynamic modelling of the lower-component systems. In the present calculations these lower-component systems are binaries and ternaries. It is therefore necessary to have data such as the experimental determination of binary and ternary phase diagrams and experimental measurements of thermodynamic properties such as enthalpies of formation, activities, etc. Preferably such information should be of good quality.

R. W. CAHN. Dr Saunders hinted at a rather remarkable claim. When there are several distinct measurements of a phase equilibrium feature, you suggest you can pick out a faulty measurement by comparison with a CALPHAD calculation. But surely, the precision of such a calculation is linked to the precision of the thermochemical measurements which contribute your input. Shouldn't a curve calculated by CALPHAD actually show upper and lower confidence limits depending on your judgement of the reliability of the input measurements?

N. SAUNDERS. The answer to Professor Cahn's question is yes and no. In an ideal world, where all experimentation is reliable and of good quality, I would agree that the curve calculated by a CALPHAD calculation could have such confidence limits imposed. Unfortunately, this is not often the case and, for example, sets of measured datapoints for a liquidus in a simple binary system can vary considerably. In some high melting point systems it is not unusual for these differences to be of the order of 100 °C or higher. Sometimes a simple comparison of the original datapoints can show that one particular set of results is obviously inconsistent with other reported values and this forms the basis of experimental phase diagram assessment work by people such as Hansen. Unfortunately in other cases the position is not so clear cut. The CALPHAD calculation does impose a self-consistency between the underlying thermodynamics and the phase diagram and therefore can be used as an arbiter between conflicting values.

M. MCLEAN (*Imperial College, London, UK*). To what extent is the accuracy of the phase diagram calculation dependent on (a) the calculation methods used in the different software systems available and (b) the thermodynamic databases available? In particular, have there been round robins using the same data, but different software, to calculate the same information?

N. SAUNDERS. If I may I will try and answer Professor McLean's second question first. In Europe there is an organization called SGTE (Ansara & Sundman 1987), which is a grouping of several centres which are active in the CALPHAD area. Workers from this group use at least four different software packages for doing CALPHAD calculations. The programs rely on some form of Gibbs free energy minimization and a brief background to this can be found in a paper by Hillert (1979). Such techniques do not give unique solutions and, therefore, there will be differences in the answers. However, such differences are typically very small. It may be that some software packages have thermodynamic models which are unique to that package and, therefore, it would not be possible to do a similar calculation on another package. However, it would be reasonable to say that, given the same implementation of models, identical database input and the correct starting points to begin the calculation, the various software systems within SGTE will provide effectively identical answers.

To answer his first question, the accuracy of the phase diagram calculations

presented here relies solely on the thermodynamic database and is not a function of the software package that is used.

M. RAPPAZ (*EPFL, France*). Phase diagram calculations give volume fractions of phases which are at equilibrium (lever-rule). They can be easily adapted to the case of no-diffusion in the solid during a solidification experiment (Scheil) by 'freezing' the concentration at the newly formed interface. How easy (or difficult) is it to couple phase diagram computations with back-diffusion models?

N. SAUNDERS. There have been recent publications in the literature which have attempted to do just this with a good degree of success (see, for example, Matsumiya 1992). The DICTRA program mentioned earlier (Andersson *et al.* 1991; Inden *et al.* 1993) is also capable of accounting for backdiffusion during solidification.

D. G. PETTIFOR (*University of Oxford, UK*). In the prediction of the B2 phase field in the ternary Ti-Al-Nb system, was it necessary to readjust the accepted data for the binary systems?

N. SAUNDERS. No.

Additional references

Hillert, M. 1979 In *Calculation of phase diagrams and thermochemistry of alloy phases* (ed. Y. A. Chang & J. F. Smith), p. 1. Warrendale, PA: Metals Society AIME.
Matsumiya, T. 1992 *Mater. Trans. JIM* **33**, 783.

Process modelling and microstructure

BY M. RAPPAZ AND CH.-A. GANDIN

*Ecole Polytechnique Fédérale de Lausanne, Laboratoire de métallurgie physique,
MX-G, CH-1015 Lausanne, Switzerland*

Among the many routes which are used for the processing of high-temperature materials, solidification plays a key role. Several modelling tools are now available for the simulation of the interconnected macroscopic phenomena associated with any casting process (heat exchange, mould filling, convection, stress development, etc.). Based upon finite-difference (FD) or finite-element (FE) techniques, these models solve the continuity equations of mass, energy, momentum, solute species, averaged over the liquid and solid phases. As such, macroscopic models do not account for the detailed phenomena occurring at the scale of the microstructure. For that reason, a stochastic cellular automaton (CA) model has been developed recently for the prediction of the grain structure formation in solidification processes, in particular during the investment casting of superalloys. Such a microscopic model considers the heterogeneous nucleation of grains at the surface of the mould and in the bulk of the liquid, the growth kinetics and preferential growth directions of the dendrites and the microsegregation. The microscopic CA model has been coupled to FE heat flow computations in order to predict the grain structure at the scale of a casting. It is shown that microstructural features and crystallographic textures can be simulated as a function of the casting conditions and alloy composition.

1. Introduction

Numerical simulation has been first used by civil and mechanical engineers for the calculation of deformation, fluid dynamics and heat transfer. Based upon finite-difference (FD) or finite-element (FE) methods, these models solve the continuity equations of heat, mass and momentum. These tools were then transferred and adapted to the field of materials science. Therefore, it is not surprising that most of these 'macroscopic' models are primarily concerned with macroscopic entities such as the temperature, stress, strain or velocity fields. In a given process such as forming or solidification, these fields (e.g. the temperature distribution) can be related to the process parameters (e.g. the heat flow extracted from a cooling system). Such information might be useful to the process engineer, but it is only an 'intermediate' output: the materials scientist is interested in the characteristics (microstructure/defects) and final mechanical/functional properties/performances of the product.

To predict entities which are of some relevance to materials scientists, two approaches can be used. The first one is based on empirical relationships or expert systems (e.g. neural networks) whose input can be either the process parameters

or the 'intermediate' output. This method is straightforward but does not bring much insight into the microscopic mechanisms. The second approach, which is more tedious, is to simulate the various microscopic phenomena which cannot be accounted for by a continuum model. Such a *micro-macroscopic* approach will be illustrated in the present paper for the particular case of the grain structure formation in solidification processes (Rappaz 1989).

Solidification is an important route for the production of many parts and components, in particular in aerospace applications (turbine blades, diffuser cases, vanes, etc.). Solidification is also an illustration of the manifold lengthscales that intervene in materials science (process scale (cm–m), grain size (mm), dendrites/eutectic spacings (μm), atomistic scale ($< \text{nm}$)). After a short review of the macroscopic models used in solidification processes (§ 2), this contribution will present a stochastic model recently developed for the prediction of nucleation and growth of dendritic grains (§ 3). The coupling of these two scales is discussed in § 4 and the last section outlines some of the future developments that will be made in this area.

2. Macroscopic modelling

(a) Geometry description and enmeshment

Three-dimensional (3D) components are described nowadays by computer-aided design (CAD) files coming from the designer. The engineer in charge of the production of the component via a casting process must first read this file and then add several other domains: risers, ingates, mould parts, insulation, cooling devices, etc. Using these CAD files, the corresponding volumes must be then enmeshed in order to solve the continuum equations. This is done with grid points or elements for the FD or FE methods, respectively. It is beyond the scope of the present paper to discuss the advantages and disadvantages of these two numerical techniques but the enmeshment procedure is still a critical step. Figure 1a shows the enmeshment of a structural aircraft component. Only half of the piece is shown together with the risers and gating.

(b) Fraction of solid and solidification path

Because of the fineness of the microstructure that develops during solidification, the macroscopic models do not track the position of the solid–liquid interface but rather use continuity equations averaged over the two phases (Bennon & Incropera 1987; Voller *et al.* 1989; Ganesan & Poirier 1990; Ni & Beckerman 1991). This averaging procedure introduces a new field: the volume fraction of solid, f_s . Since there is no additional continuity equation governing the evolution of this entity, a local relationship, the solidification path, has to be found between f_s and the temperature, T . Such a relationship is given by a local solute balance (microsegregation model) and by the phase diagram of the alloy. Most of the macroscopic models of solidification use a unique solidification path, $f_s(T)$, which range from a linear interpolation between the liquidus and solidus temperatures, to more sophisticated models such as the lever rule, the Scheil–Gulliver or the Brody–Flemings models (Kobayashi 1988). All these models apply to a closed system, i.e. when there is no fluid flow.

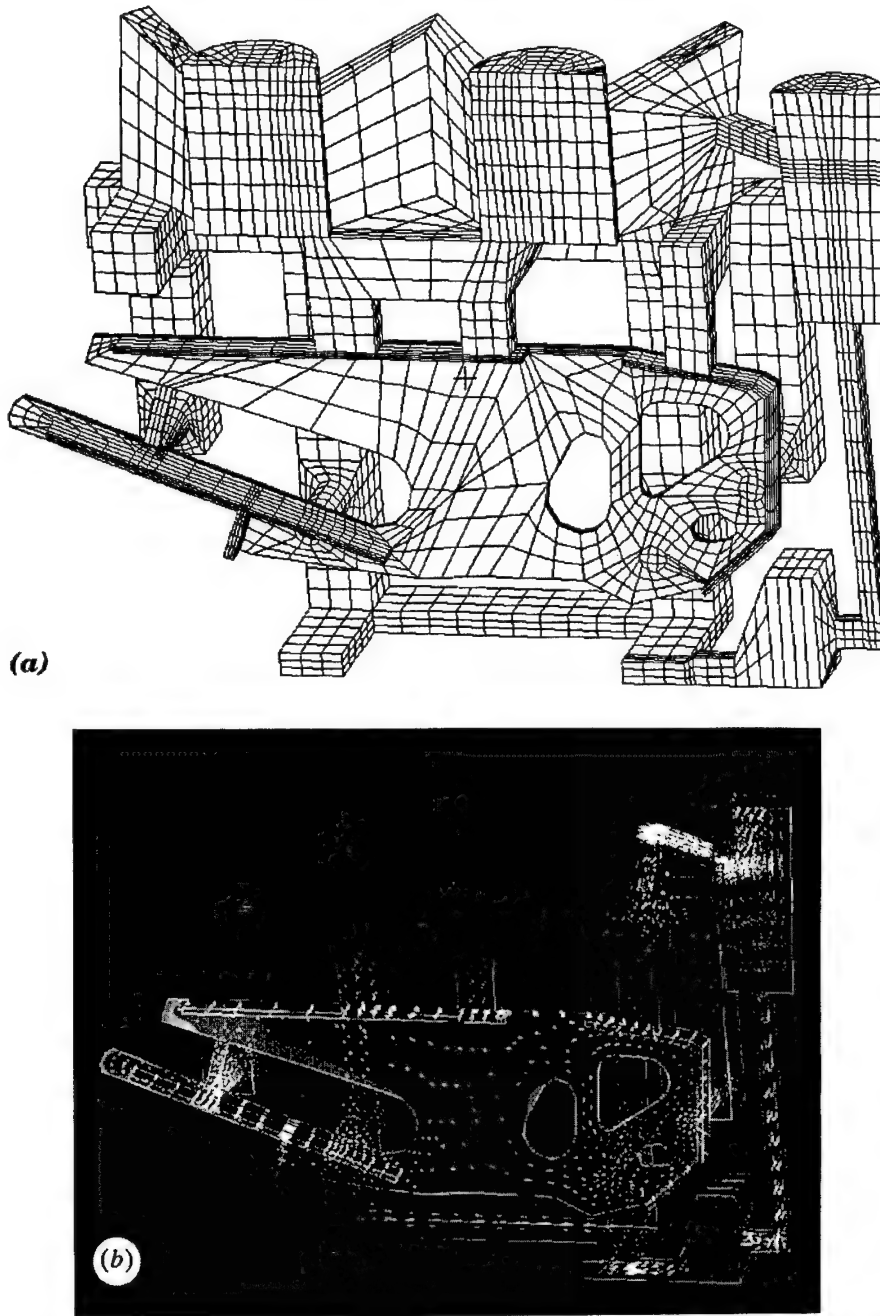


Figure 1. Structural aircraft component in Al-alloy (investment casting): (a) 3D enmeshment of a casting and (b) corresponding temperature and fluid flow velocities during mould filling (courtesy of CERCAST, calculation made with ProCASTTM).

(c) Heat and fluid flow calculations

Even though the convection associated with pouring effects, buoyancy, surface tension gradients or electromagnetic forces modifies the local solute balance

made within a small volume element of the enmeshment, most of the simulation codes developed for solidification processes assume a unique $f_s(T)$ relationship. The averaging of the continuity equations is usually made under the assumption that the solid skeleton is fixed. The permeability, K , of the mushy zone is introduced to simulate the interdendritic flow in the porous medium constituted by the dendrites array (Darcy equation). Detailed derivations of these equations can be found, for example, in Bennion & Incropera (1987), Voller *et al.* (1989), Ganesan & Poirier (1990), Ni & Beckerman (1991). As an example, the temperature distribution and fluid flow velocities calculated within the component of figure 1a are shown in figure 1b. The results have been computed with the software ProCAST™, taking into account heat flow and fluid flow with free surface (mould filling).

(d) *Prediction of macro- and mesosegregation*

Macro- and mesosegregation, two defects frequently encountered in castings, are solute concentration inhomogeneities observed at the scale of the casting or at a more localized scale (e.g. segregated channels or freckles). Both types of segregation are associated with the transport of solute species by convection. Neglecting the diffusion of solute species at the macro- and mesoscales, the local solute concentration is averaged over the solid and liquid phases using a microsegregation model. The simplest model makes the assumption of local equilibrium between the solid and liquid phases (lever rule). Scheil or back-diffusion microsegregation models, which are closer to the case of real alloys, are more difficult to handle for systems in which convection occurs (Rappaz & Voller 1990; Mo 1994).

As a result of convection (open system), the local average concentration is no longer constant and the solidification path, $f_s(T)$, is no longer unique. For example, the arrival of solute-rich liquid can partly remelt the solid even though the local temperature is decreasing monotonically. This phenomenon is typically associated with solutal convection in the mushy zone and may lead to the formation of segregated channels or freckles. The simulation result shown in figure 2 corresponds to the formation of such an instability in a large rectangular two-dimensional (2D) ingot of Ni-Al (Combeau & Lesoult 1993).

3. Microstructure modelling

(a) *Nucleation of grains*

The formation of primary phase grains during solidification starts with the heterogeneous nucleation of nuclei at the surface of the mould or within the bulk of the liquid. Convection can also play a significant role at this stage since it can transport grains and enhance the density of nuclei by dendrite fragmentation (Sato *et al.* 1987). Such effects will be ignored in the investment casting of superalloys considered in the present paper. Although the theory of heterogeneous nucleation is fairly well known (Turnbull 1950), the mechanisms are still unclear. For that reason, most simulation approaches consider that the heterogeneous nucleation of grains is described by a distribution of nucleation sites, $p(\Delta T)$, which become active as the undercooling, ΔT , is increased (Rappaz 1989). The parameters of this distribution are determined by comparison with experimental results obtained under different cooling rates but identical inoculation conditions. The density of grains in the bulk of the liquid, $n(t)$, at a given time, t , is then given

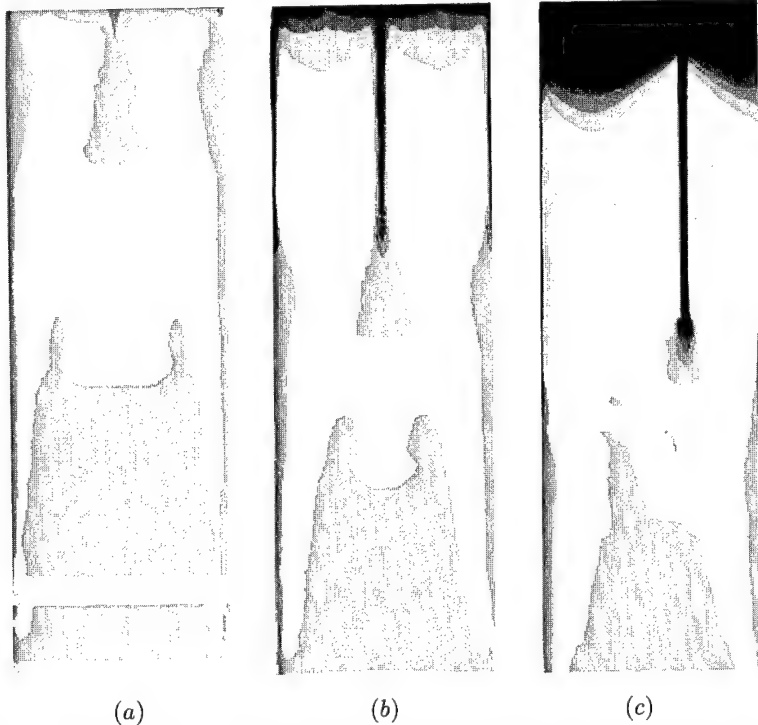


Figure 2. 2D Al concentration distribution and freckle formation in a large Ni-Al rectangular ingot after (a) 1 h, (b) 1 h 23 min and (c) 8 h (courtesy of Combeau *et al.* 1993).

by

$$n(t) = \int_0^{\Delta T(t)} p(\Delta T)(1 - f_s) d(\Delta T). \quad (3.1)$$

The factor $(1 - f_s)$ accounts for the disappearance of the nucleation sites which are trapped by the grains already formed (Hunt 1984). Equation (3.1) has been used originally for the formation of equiaxed grains in the bulk of the liquid, but the same approach can be adapted to the heterogeneous nucleation at a mould surface (Rappaz & Gandin 1993).

(b) Dendrite growth

For the sake of simplicity, let us first consider the situation of a uniform temperature field. After a grain has nucleated, it grows first as a sphere, then becomes unstable and later grows with a dendritic morphology. The growth velocity of the tips of the dendrites, $v(\Delta T)$, is a function of the local undercooling and can be estimated using various analytical models (Kurz & Fisher 1989). For cubic metals, the growth directions of the dendrite trunks and arms correspond approximately to $\langle 100 \rangle$ crystallographic directions (Chalmers 1964). Thus, in a uniform temperature field, a grain grows almost as an octahedron whose diagonals are given by the $\langle 100 \rangle$ directions of the parent nucleus. The situation illustrated in figure 3 corresponds to 2D dendritic grains growing in a plane with a square shape. Neglecting the initial stage of spherical growth, the half-length of the $\langle 100 \rangle$ diagonals of the grains, $L(t)$, is given by

$$L(t) = \int_{t_n}^t v(\Delta T(t)) dt, \quad (3.2)$$

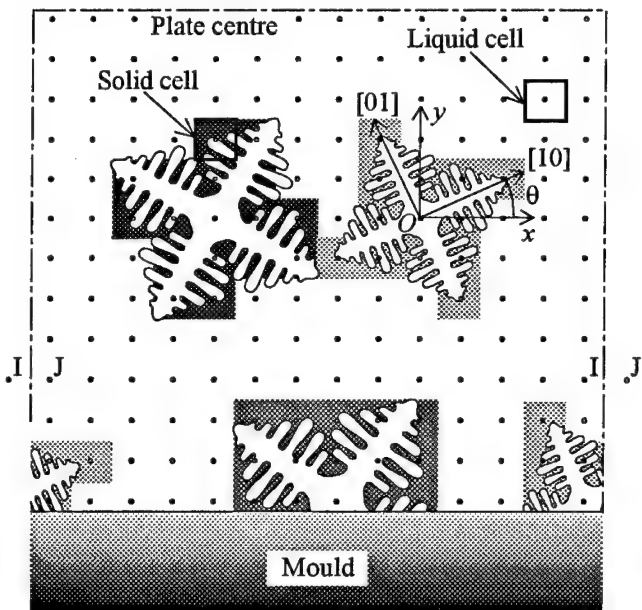


Figure 3. Schematic diagram of a 2D CA model for the nucleation/growth of grains in a uniform temperature field.

where t_n is the time of nucleation. Within the octahedron, the volume is mushy. A simple solute diffusion model can be used to predict the internal volume fraction of solid within the grains (Rappaz & Thévoz 1987).

Based upon these simple considerations, the simulation of grains growing in a thermal gradient can be calculated using the cellular automaton briefly described below (Rappaz & Gandin 1993; Gandin & Rappaz 1994).

(c) Cellular automaton

To predict the nucleation and growth of grains in any thermal environment, a physically based cellular automaton (CA) has been developed. For that purpose, the volume of the melt is divided into N_c regular square cells (figure 3). For each cell ν , a 'crystallographic' index, I_{C_ν} , is defined. It is equal to zero at the beginning of the simulation meaning that the cell is liquid. During solidification, this index can become a positive integer whose value corresponds to a given misorientation of the dendritic network with respect to the axes of the CA network. Furthermore, the cells which belong to the boundary of the domain are marked with an additional index and are referred to as 'boundary cells'.

For the nucleation in the bulk of the specimen, a certain number of nucleation undercoolings are randomly selected according to the pre-determined nucleation distribution $p(\Delta T)$ (e.g. Gaussian distribution). These undercoolings are spatially attributed to randomly chosen cells. The same procedure is applied to the boundary cells with the appropriate nucleation site distributions. All the cells which have been attributed a critical nucleation undercooling, $\Delta T_\nu^{\text{nuc}}$, are referred to as 'nucleation cells' in the following.

Let us assume now that the cooling curve, $T_\nu(t)$, at any cell location is known. This cooling history can be obtained from the cooling curve measured in a small specimen of nearly uniform temperature (figure 3) or it can be calculated using FE

heat flow computations, as explained in more detail in § 4. During a time-stepping calculation, a cell ν can make a transition from the liquid state ($Ic_\nu = 0$) to a dendritic state ($Ic_\nu \geq 1$) according to two mechanisms.

1. If the cell is a nucleation cell and is still liquid at time t , it can become a new nucleus if its undercooling becomes larger than the predetermined critical nucleation undercooling (i.e. if $\Delta T_\nu(t) = T_L - T_\nu(t) \geq \Delta T_\nu^{\text{nuc}}$). Its index Ic_ν giving the crystallographic orientation of the new grain is set to a randomly selected value.

2. Once a cell has nucleated, the corresponding grain is assumed to grow with the kinetics of the dendrite tips, $v(\Delta T_\nu)$ (Kurz *et al.* 1986). In two dimensions, it grows as a small square envelope (see figure 3). At a certain time, the dendrite envelope reaches the centres of the four nearest-neighbour cells. If these neighbours are still liquid, their indices are set to the value of the parent nucleus thus taking on the orientation of the grain. The growth procedure is then repeated for the neighbouring cells using the corresponding local undercooling.

The simple 'capture' procedure of the cells which is described above has a major drawback: it propagates the growth of dendritic grains from cells to cells but it biases their misorientations. This problem is well known in the application of cellular automata and Monte Carlo methods to grain growth (Toffoli & Margolus 1991; Anderson *et al.* 1984). A 2D growth algorithm which does not present this drawback is described by Gandin & Rappaz (1994). This algorithm has not yet been extended to 3D situations. However, a simple octahedron growth algorithm has been used for uniform temperature situations in three dimensions (Gandin *et al.* 1993).

(d) Results

Figure 4 shows the grain contours seen in a transverse section of an equiaxed turbine blade airfoil (Gandin *et al.* 1994). The superalloy was cast at the SNECMA foundry in a ceramic mould coated with inoculant particles. The grain boundaries, clearly revealed by the etching procedure, were redrawn to produce the grain structure of figure 4a. The result of the simulation which is shown in figure 4b has been obtained using the 3D stochastic model under the assumption of a uniform temperature field. For that purpose, a small length of the blade normal to the 2D section was considered and the final grain structure is shown in the same transverse section. The label 'equiaxed blade' used in the investment casting industry for such grain structures is somehow misleading since the grains shown in the simulated micrograph were assumed to nucleate only at the surface of the ceramic mould (i.e. columnar growth starting from the surface). However, since the octahedral grains may grow at some angle with respect to the transverse section plane, many of them are not directly connected to the edge of the airfoil and thus appear as 'equiaxed'. This simple example shows how the results of a simple 3D stochastic growth model can provide useful stereological information.

This simple 3D growth model can also predict the grain competition that occurs within the columnar zone of a casting. Since the dendritic network is constrained to grow along $\langle 100 \rangle$ directions, the grains which have one of their $\langle 100 \rangle$ orientations most closely aligned with the thermal gradient direction are selected by the growth process at the expense of less favourably oriented grains (Chalmers 1964). As a result of this grain competition, the grain density measured in a section par-

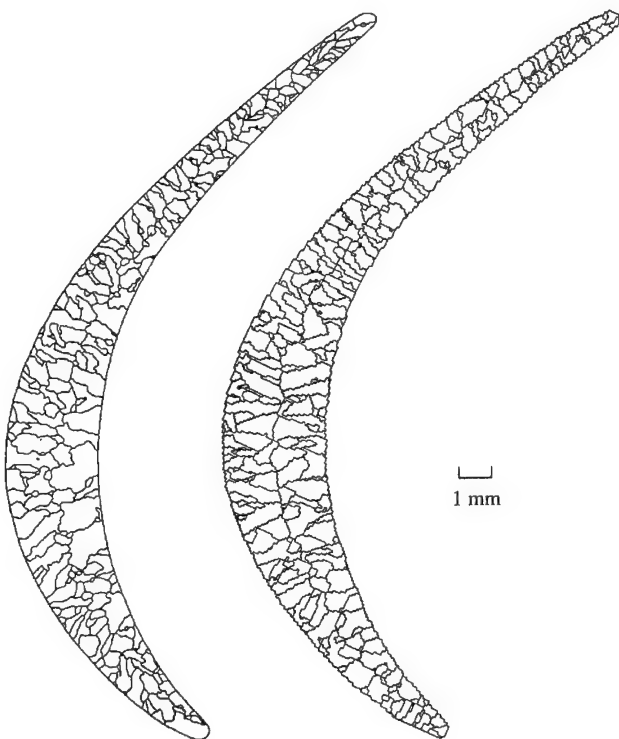


Figure 4. (a) Measured and (b) predicted grain structures in the cross section of an equiaxed turbine blade airfoil (Gandin *et al.* 1994).

allel to the surface of nucleation must decrease with the distance to this surface. This is shown in figure 5 for an Inconel X750 alloy (Gandin *et al.* 1995). This alloy was cast in a preheated ceramic mould attached to a copper chill plate. The mean linear grain boundary intercept normal to the growth direction was measured in a longitudinal section and is reported as a function of the distance to the chill. The same measurement was made for the grain structure computed with the 3D stochastic model. Although the assumption of uniform temperature made in the simulation is no longer valid near the chill, the correct trend is predicted by this simple model.

According to the mechanisms of heterogeneous nucleation, the orientation of the grains formed at the surface of the chill should be random. However, as the growth proceeds and eliminates the 'poorly' oriented grains, the orientation distribution should become closer to a $\langle 100 \rangle$ crystallographic texture. Figure 6 shows the measured and simulated evolutions of the $\langle 100 \rangle$ pole figures for the same Inconel X750 specimen. The centre of the pole figures corresponds nearly to the perpendicular to the copper chill surface. The experimental and simulated pole figures were obtained using an automatic indexing of electron backscattered diffraction patterns and the 3D growth model, respectively (Gandin *et al.* 1995). As can be seen, the crystallographic orientation of the grains is nearly random near the surface of the chill and is close to a $\langle 100 \rangle$ texture 2 mm from the chill. The most probable $\langle 100 \rangle$ orientation of the dendrite trunks at this distance was

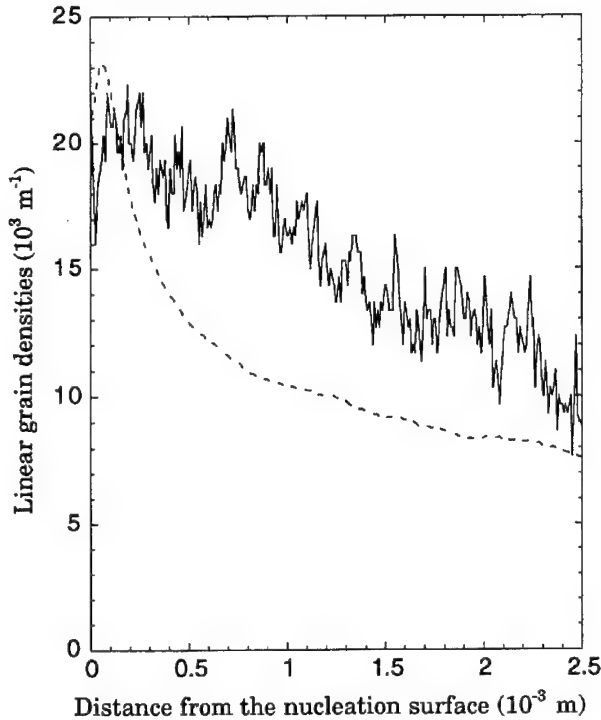


Figure 5. Measured (solid line) and calculated (dashed line) evolutions of the grain density in the columnar zone of an Inconel X750 alloy (Gandin *et al.* 1995).

calculated to be about 12° from the normal to the chill surface, a value which is very close to the experimental result.

4. Micro- and macroscopic modelling

(a) Principles

The simulation results presented in § 3d have been obtained with the 3D stochastic model under the assumption of a uniform temperature. However, in most practical situations, the thermal gradient within the specimen must be considered. Since the thermal diffusion layer is much larger than the scale of the microstructure, the heat flow equation should not be solved at the scale of the CA network but rather at a coarser scale (see figure 7). For that purpose, a 2D CA algorithm has been coupled with the FE heat flow code 3-MOS (Gandin & Rappaz 1994). This code is based upon an enthalpy formulation and an implicit time-stepping scheme (Thévoz *et al.* 1990). Using a linearization procedure, the variation of enthalpies, δH_i , during one time-step can be found at all the nodal points of the FE mesh. For the nodes located in the solidifying alloy, the δH_i variations are converted into specific heat, $c_p \delta T_i$, and latent heat contributions, $L \delta f_{s,i}$, using the finer CA network and the CA algorithm.

The known temperatures at time t , T_i^t , and variations of enthalpies, δH_i , at the FE nodes are first interpolated for each CA cell, ν . Knowing these entities, the CA algorithm is applied for the nucleation/growth of the grains. For each cell, several situations can be encountered: (i) the cell was liquid and remains liquid

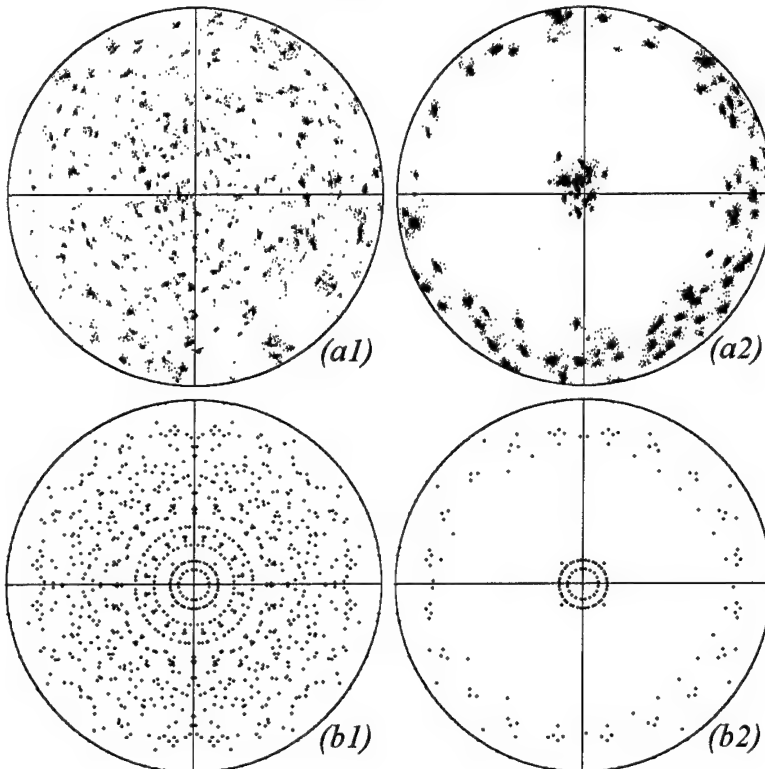


Figure 6. (a) Measured and (b) predicted $\{100\}$ pole figures of an Inconel X750 superalloy near the surface of (1) and at 2 mm from (2) the surface of the chill. The centre of the stereographic projection corresponds to the normal to the chill surface (Gandin *et al.* 1995).

or it was already fully solid; (ii) the cell was liquid and it becomes mushy by nucleation or capture of a growing grain (i.e. $I_{c,\nu}$ changes from zero to a positive value); (iii) the cell was mushy but not fully solid. To each case is associated a variation of the internal volume fraction of the cell, $\delta f_{s,\nu}$. Once the $\delta f_{s,\nu}$ of all the cells have been calculated using the CA, the values $\delta f_{s,i}$ at the FE node locations are summed up and the new temperatures $T_i^{t+\delta t}$ are then deduced according to the heat balance: $\delta H_i = c_p \delta T_i - L \delta f_{s,i}$.

(b) Results

Since the CAFE model is still 2D, figure 8 must be viewed as a 2D section of a blade. The grain selector has been highly idealized as a simple zigzag and an extra reservoir (riser) of molten metal at the top of the blade has been designed. Figure 8a shows the 2D FE enmeshment used for the heat flow computations and the enlargement view located on the left corresponds to the left corner of the bottom platform. This zoom shows both the FE enmeshment and the CA square grid, the latter being only defined for the metal part. The final grain structure calculated with the fully coupled CAFE model is shown in figure 8b with various grey levels. The various steps of the solidification process are shown in figures 8c–i.

Figures 8c and 8d show the temperature distribution and the grain structure at time $t = 30$ s in the bottom part of the grain selector. The temperature scale

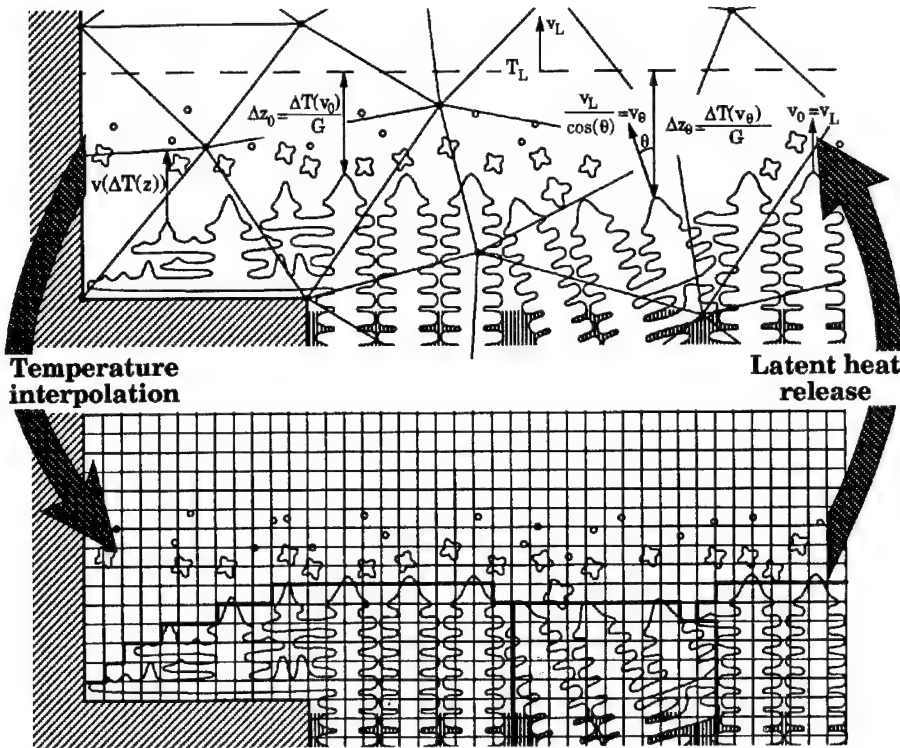


Figure 7. Coupling of the CA algorithm with FE heat flow computations.

was chosen so as to reveal the position of the liquidus front ($T_L = 1312^\circ\text{C}$) and to give an indication of the thermal gradient. From the many grains nucleated at the surface of the chill, only two grains remain after the zigzag of the selector (figure 8e, $t = 230\text{ s}$). Since most of the heat flow still goes through the grain selector, the isotherms are curved and the dendrite fronts of both grains are convex.

At time $t = 320\text{ s}$, the liquidus temperature is already above the first platform on the right of the blade and the left corner of the platform is also cooled below T_L (figure 8f). Since the dendritic network has to propagate in these open regions of liquid, the grain structure has the morphology shown in figure 8g. However, before the grain can reach the end of the platform on the right, a new grain has nucleated at this place. At time $t = 400\text{ s}$ (figure 8h), the right part of the platform is already filled by the dendrites but another stray crystal has nucleated at the left of the platform. The liquidus isotherm, T_L , is outlined by a nearly horizontal line and is already located within the airfoil.

Figure 8i is an enlargement of the final grain structure calculated in the airfoil. The $\langle 10 \rangle$ crystallographic orientation of the two crystals is indicated with arrows: the grain at the left has a misorientation of -14° with respect to the vertical axis of the blade whereas that of the right grain is $+14^\circ$. The position of the liquidus isotherm is also plotted on this figure for three different times of solidification. As can be seen, the liquidus front which was slightly convex at the exit of the first platform becomes flat and then concave as solidification proceeds. This change in

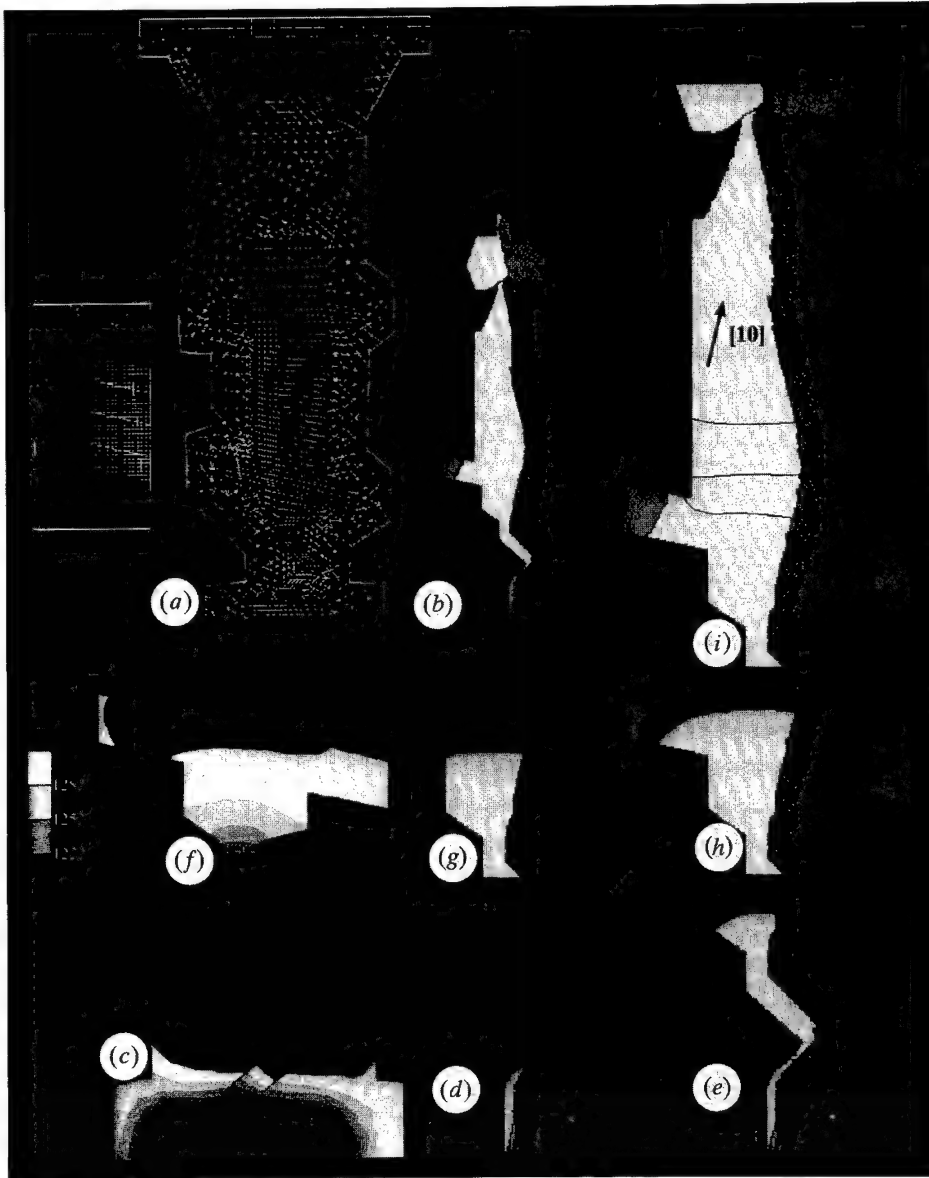


Figure 8. (a) Enmeshment, (b), (d), (e), (g), (h), (i) grain structure and (c), (f) temperature maps during and after solidification of an idealized 2D turbine blade.

the thermal gradient direction has a direct influence on the shape of the boundary between these two grains.

5. Conclusion

Although the full CAFE model presented here is still 2D, it brings valuable insights into the mechanisms of grain structure formation in various solidification processes. The grain selection mechanisms in the columnar zone of DS turbine blades, the transition from columnar-to-equiaxed structures, the formation of

stray crystals at section changes of the mould, the influence of the thermal gradient direction on the shape of the grain boundaries have been demonstrated for an investment cast turbine blade.

To use the full capability of the coupled CAFE model, it is necessary to extend it to three dimensions. Such an extension has been done under the limitation of uniform temperature situations (Gandin *et al.* 1993, 1994, 1995) and already has brought quantitative answers regarding the evolution of the grain density and texture. The full 3D CAFE model will be an important simulation tool for the optimization of the grain selector shape, of the casting conditions and of the yield rate of complex investment cast components.

The authors thank Dr Ph. Thévoz and Dr H. Combeau for providing figures 1 and 2 and the Commission pour l'Encouragement de la Recherche Scientifique (CERS), Bern, for its financial support.

References

Anderson, M. P., Srolovitz, D. J., Grest, G. S. & Sahni, P. S. 1984 Computer simulation of grain growth. I. Kinetics. *Acta metall.* **32**, 783–791.

Benson, W. D. & Incropera, F. P. 1987 A continuum model for momentum, heat and species transport in binary solid–liquid phase change systems. *Int. J. Heat Mass Transfer* **30**, 2161–2187.

Chalmers, B. 1964 *Principles of solidification*. New York: Wiley.

Combeau, H. & Lesoult, G. 1993 Simulation of freckles formation and related segregation during directional solidification of metallic alloys. In *Modeling of casting, welding and advanced solidification processes VI* (ed. T. S. Piwonka *et al.*), pp. 201–208. The Minerals, Metals and Materials Society.

Ganesan, S. & Poirier, D. R. 1990 Conservation of mass and momentum for the flow of interdendritic liquid during solidification. *Metall. Trans. B* **21**, 173–181.

Gandin, Ch.-A., Rappaz, Ch. A. & Tintillier, R. 1993 Three-dimensional probabilistic simulation of solidification grain structures: application to superalloys precision castings. *Metall. Trans. A* **24**, 467–479.

Gandin, Ch.-A., Rappaz, M. & Tintillier, R. 1994 Three-dimensional simulation of the grain formation in investment casting. *Metall. Trans. A* **25**, 629–635.

Gandin, Ch.-A. & Rappaz, M. 1994 A coupled finite element–cellular automaton model for the prediction of dendritic grain structures in solidification processes. *Acta metall. mater.* **42**, 2233–2246.

Gandin, Ch.-A., Rappaz, M., West, D. & Adams, B. L. 1995 Grain texture evolution during the columnar growth of dendritic alloys. *Metall. Trans. A* **26**, 1543–1552.

Hunt, J. D. 1984 Steady state columnar and equiaxed growth of dendrites and eutectic. *Mater. Sci. Engng* **65**, 75–83.

Kobayashi, S. 1988 Solute redistribution during solidification. *J. Cryst. Growth* **88**, 87–96.

Kurz, W. & Fisher, D. J. 1989 *Fundamentals of solidification*. Aedermannsdorf: Trans. Tech. Pub.

Kurz, W., Giovanola, B. & Trivedi, R. 1986 Theory of microstructural development during rapid solidification. *Acta metall. mater.* **34**, 823–830.

Mo, A. 1994 An internal variable description of solidification suitable for macrosegregation modeling. *Metall. Trans. B* **25**, 597–605.

Ni, J. & Beckermann, C. 1991 A volume-averaged two-phase model for transport phenomena during solidification. *Metall. Trans. B* **22**, 349–361.

Rappaz, M. & Thévoz, Ph. 1987 Solute diffusion model for equiaxed dendritic growth: analytical solution. *Acta metall. mater.* **35**, 2929–2933.

Rappaz, M. 1989 Modelling of microstructure formation in solidification processes. *Int. Mater. Rev.* **34**, 93–123.

Rappaz, M. & Voller, V. 1990 Modelling of micro-macrosegregation in solidification processes. *Metall. Trans. A* **21**, 749–753.

Rappaz, M. & Gandin, Ch.-A. 1993 Probabilistic modelling of microstructure formation in solidification processes. *Acta metall. mater.* **41**, 345–360.

Sato, T., Kurz, W. & Ikawa, K. 1987 Experiments on dendrite branch detachment in the succinonitrile–camphor alloy. *Trans. Jpn Inst. Metals* **28**, 1012–1021.

Thévoz, Ph., Rappaz, M. & Desbiolles, J. L. 1990 3-MOS: a general FEM code for the prediction of microstructures in castings. In *Light metals* (ed. Ch. M. Bickert), pp. 975–984. The Minerals, Metals and Materials Society.

Toffoli, T. & Margolus, N. 1991 *Cellular automata machines*. MIT Press.

Turnbull, D. 1950 Kinetics of heterogeneous nucleation. *J. chem. Phys.* **18**, 198–203.

Voller, V. R., Brent, A. D. & Prakash, C. 1989 The modelling of heat, mass and solute transport in solidification systems. *Int. J. Heat Mass Transfer* **32**, 1719–1731.

Discussion

A. M. STONEHAM (*Industrial Technology, Harwell, UK*). The end result of Professor Rappaz's very nice work is a structure (grain structure and dendrites). Some other workers have used the realizations from mesoscopic calculations to predict performance (e.g. John Harding's work on plasma-sprayed coating, where mechanical properties were predicted). Does he have plans of this sort?

M. RAPPAZ. Not at the moment. With the existing models of microstructure formation, the grain morphology and size, the fraction of phases, the dendrite/eutectics spacings can be calculated for as-cast components. However, the dependence of mechanical properties and performances of a component is a complex function of all these parameters. Furthermore, subsequent heat treatments (e.g. homogenization, γ' precipitation) modify the as-cast structures and the properties. The present models are therefore only one piece of the puzzle, but nevertheless essential for the process engineer.

M. MCLEAN (*Imperial College, UK*). What material data are required to allow the models of solidification to make quantitative predictions of the microstructure that develops? Also, how sensitive are these predictions to the uncertainties in these data?

M. RAPPAZ. The importance of thermophysical and other materials data is not emphasized enough in the modelling community. Together with boundary conditions, they are essential in any macroscopic calculations. The present model also requires reliable phase diagram data, diffusion coefficients, surface tension, etc. in order to calculate the solidification path and the growth kinetics of the dendrites. The nucleation parameters are certainly the most critical and can only be deduced from carefully controlled experiments. This shows that simulation and experiment really go together and cannot replace each other.

M. S. LOVEDAY (*Division of Materials Metrology, National Physical Laboratory, Teddington, UK*). Professor Rappaz has presented a very interesting example showing the importance of process control for the optimization of grain structure in an important technologically advanced component, i.e. a gas turbine blade. Processibility was recognized by the Department of Trade and Industry (UK)

as an important area when new research programmes were initiated about two years ago. There are now several research projects underway aiming to produce data of the appropriate precision for use in process control models, or to develop standard methodology for the procurement of such data. Projects are underway at the National Physical Laboratory, the National Engineering Laboratory, AEA Technology and the IRC Birmingham/Swansea to address problems such as (i) Measurement of heat capacities, enthalpies, melting ranges, densities, viscosities, surface tension and thermal conductivities for commercial alloys, (ii) viscosity and elasticity of polymers, (iii) phase changes, recrystallization kinetics, friction and heat transfer coefficients for rolling and forging of metals, (iv) optimization of soldered joints for the electronics industry, (v) rheology of fluid solid mixtures for moulding components, and (vi) physical and mechanical properties of liquid–solid mixtures for casting of metals.

Clearly most of the above activities have a direct relevance to the production of components many of which will see service in high-temperature structural applications. All of the projects are supervised by Industrial Advisory Committees, and it is intended to rapidly disseminate the findings to the relevant sections of industry.

Mechanical testing of high-temperature materials: modelling data-scatter

BY B. F. DYSON

Department of Materials, Imperial College of Science, Technology and Medicine, London SW7 2BP, UK

Scatter in mechanical property data of a metallic alloy derives from two sources: a variable microstructure or an inadequate and sometimes badly executed test method. A quantified example of each source of scatter is given in this paper by examining two important high-temperature properties: uniaxial tensile creep and low-cycle fatigue. Creep-lifetime data of engineering alloys often show scatter-bands much greater than can be accounted for on the basis of well-understood physics of testing-induced scatter. Bounds to this material-induced scatter have been computed for a low-alloy ferritic steel dataset using a physically based creep model incorporating damage state variables. High-temperature low-cycle fatigue demands a more complicated test procedure than does steady-load creep and the large interlaboratory scatter found in recent round robin data from 26 laboratories in Europe and Japan has highlighted inadequacies in the standardized test method. A simple material model and fracture criterion has been used, in conjunction with a previously introduced testpiece-bending model, to predict testing-induced interlaboratory scatter for the two nickel-base superalloys reported upon in the round robin exercise.

1. Introduction

Low-cycle fatigue and creep are two of the most important high-temperature mechanical properties in aero-engine applications and their laboratory-testpiece data often show a large scatter. Mechanical property data-scatter is universal and its degree depends on both the material and the testing procedures. Material-induced scatter is caused by gross spatial variability in the material's microstructure within a single 'cast' or to microstructural variability between different casts: the 'tightness' of the chemical specification; the shape and size of the component from which the testpiece is manufactured; and the component's thermo-mechanical processing route all contribute towards the extent of microstructural inhomogeneity. It is only through qualitative (or preferably quantitative) implementation within the processing technology of expensively acquired microstructural and kinetic knowledge that some control can be exerted on the magnitude of this cause of data-scatter. The more mature a material is in its engineering usage, the more likely there will be an adequate knowledge-base to facilitate close microstructural control. Whether implementation will be economically worthwhile is another matter; the specific product will certainly need to have sufficient added-value, which goes some way towards understanding why

microstructural control has progressed more in aero-engine applications than in, for example, petrochemical plant.

Data-scatter resulting from inadequacies in creep and low-cycle fatigue (LCF) testing has three main constituents: (i) random and systematic errors in measurements made during testing; (ii) random fluctuations in the magnitudes of the test control-parameters: force/stress, displacement/strain and temperature; (iii) errors in the computation of strain due to uncertainties in the magnitude of the operative gauge length and/or its local state of loading. Testing-scatter has received a high profile over the last decade as a consequence of the drive towards harmonization and accreditation of testing methods, aimed at removing potential barriers to trade in the global market. Research has been sponsored in Europe by the Community Bureau of Reference (BCR) and fostered internationally by the Versailles Project on Advanced Materials and Standards (VAMAS). *Repeatability* of a dataset within a single laboratory and *reproducibility* of the equivalent dataset between laboratories rely in the first instance, on the existence of Measurement Standards for length, mass, time, temperature, etc., and secondly on Documentary Standards. The latter contain not only methodologies for performing what are often highly complicated materials property tests, but provide a framework for *documented* traceability to Measurement Standards (Dyson *et al.* 1995; Hossain & Sced 1995).

Lack of precision in data is not always an issue when materials are being considered for structural applications – for example in the early stages of design (Ashby 1989, 1991) – but once a material class has been chosen for a particular application, data-scatter poses an obvious problem for a design engineer hoping to steal a competitive-edge in a global market place that is increasingly unforgiving of failure to deliver on time and to specification. In Europe, the harmonization process may itself cause an increase in data-scatter in the future, as a consequence of its ‘lowest common denominator’ policy towards test methods (Loveday 1992). This is ironic considering that the potential of cheap computer-based design and lifetime prediction will become more difficult to realise if the input data (condensed though it will be, as constitutive laws) is insufficiently precise.

Since data-scatter is a fact of life, its physical origins require quantitative understanding if full use is to be made of materials data in structural design, although this is not the route currently chosen by European Standards committees, which take a purely statistical stance, probably due to the fact that physically based methods of quantifying data-scatter are only now emerging. This paper focuses on two recent advances in predictive modelling of data-scatter: in creep, when the source of scatter lies primarily in ‘cast-to-cast’ microstructural differences; and in low-cycle fatigue, when scatter can be attributed to inadequacies in the test method.

2. Modelling materials-scatter in creep

(a) Background

Within an advanced and frequently accredited (Henderson & Thomas 1995) creep-testing laboratory, random and systematic errors in basic metrology should be small and contribute little to data-scatter: the resolutions of devices for measuring displacement, force and temperature, recommended in Documentary Standards, are usually more than adequate for the task. An exception being the de-

termination of Young's modulus using testpieces with a short (but still within standard) gauge length (Loveday 1992). Similarly, fluctuations in the control parameters (the so-called tolerances) can, using modern devices, be easily kept within the ranges allowed by Documentary Standards. In uniaxial creep testing (which accounts for the majority of creep strain data), there are systematic errors generated during the computation of strain from displacements made on testpieces having extensometer ridges, because the accompanying non-uniform strain fields give rise to an uncertain gauge length. Extensometer ridges are used world-wide in creep testing and a comprehensive finite element study has recently been published of the errors in strain that are predicted to occur when superalloy behaviour is simulated using a multiaxial material model with tertiary-damage variables (Lin *et al.* 1993a). Testpieces with nominal gauge lengths greater than approximately 40 mm – universally used to generate so-called high-sensitivity creep strain data – are predicted to have only small errors from this source and these can be reduced to negligible levels using a modified design for the ridge (Lin *et al.* 1993b).

Uniaxial creep data should therefore be procurable with a minimum of reproducibility errors caused by inadequacies in testing procedures. This conclusion is further justified by the relatively recent validation of a Creep Reference Material (Gould & Loveday 1992), where it was demonstrated that scatter in strain/time trajectories exhibited by the Reference Material could be accounted for by the tolerances on stress and (particularly) temperature specified in Documentary Standards. Figure 1 illustrates this with a set of six creep curves generated by a single laboratory and reported by Gould & Loveday (1992): the scatter markers shown in figure 1 were calculated from the tolerances specified in BS 3500 and ISO DIS783 using a simple power-law creep model with exponential temperature dependency. The sigmoidal primary creep displayed in figure 1 is unusual for this material (a specially prepared batch of Nimonic 75) but is a useful monitor of testing proficiency.

In spite of an adequate test procedure, scatter in creep lifetime data of engineering alloys is widespread and particularly bad in the extensive databases that have been generated for ferritic steels used as high-temperature structural components in electricity power plant. It is unlikely that scatter is caused by poor implementation of the creep test procedure and indeed the electricity supply industry devoted much effort in the 1960s establishing this point. Figure 2 is the only comprehensive systematic study known to the author that clearly and unambiguously relates thermally induced microstructural changes in an important engineering material with subsequent scatter in creep lifetimes. Toft & Marsden (1961) classified the microstructures of 1%Cr1/2%Mo steel tube components that had been exposed to a variety of thermal environments in service before laboratory creep testing; each symbol in figure 2 represents a particular microstructure, although in practice there was necessarily some subjectivity in the classification. Toft & Marsden made the very interesting point that individual extrapolation of each dataset using the empirical Manson-Haferd (1953) method predicts a common lifetime of 10^5 h for all microstructures at a stress of approximately 30 MPa. It is suggested here that the connection between Toft & Marsden's work and the scatter exhibited by ferritic steel creep data in general lies in the fact that the processing route for these materials naturally results in a spectrum of microstructures between casts and that this is the underlying cause

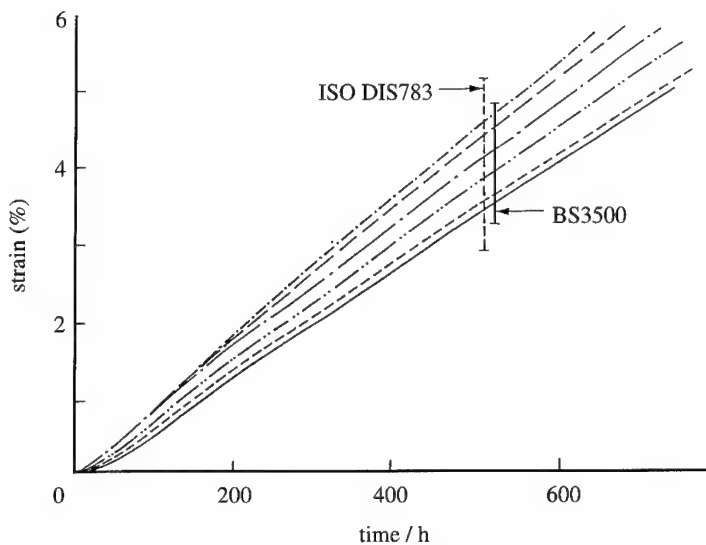


Figure 1. Illustrating the adequacy of uniaxial tensile creep testing practice using a Nimonic 75 Creep Reference Material (Gould & Loveday 1992).

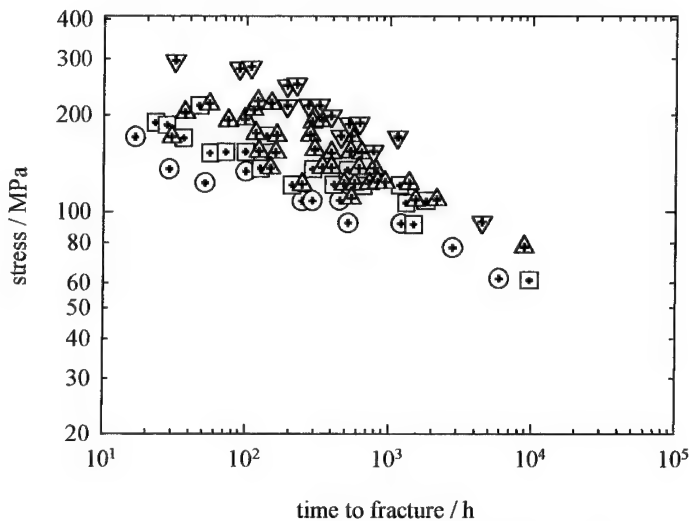


Figure 2. Time to fracture as a function of stress for four different batches of 1%Cr1/2%Mo steel (replotted data of Toft & Marsden 1961).

of the data-scatter. The working hypothesis in this paper is that the primary detailed micromechanism of material-scatter in ferritic steels lies in the volume fraction and dispersion characteristics of the main carbide-strengthening particles and that efficient extrapolation procedures will only emerge through quantitative creep modelling.

(b) Material model

The uniaxial creep behaviour of precipitation hardened alloys has recently been modelled by Dyson & Osgerby (1993). Creep is hypothesized as being rate-limited by the drift of dislocations surmounting a spherical particle distribution which

Table 1. Model material creep parameters for a 1%Cr_{1/2}%Mo ferritic steel

$\dot{\epsilon}_0/\text{h}^{-1}$	σ_0/MPa	h'/MPa	H^*	K'/h^{-1}
$1.4 \times 10^9 \sigma_0^{-1} e^{-31000/T}$	$8 \times 10^{-3} e^{6000/T}$	10^5	0.4	$1.4 \times 10^{12} \sigma_0^3 e^{-36000/T}$

is spatially homogeneous. Drift occurs by climb and glide occurring in parallel along any dislocation segment and leads to an activation-area that reflects the state of precipitate dispersion, thus predicting an effect of coarsening and/or volume fraction which manifests itself either as tertiary creep or as an initial weakening when the material has been given a prior thermal exposure. Creep behaviour is given by the constitutive and damage evolution equation-set:

$$\left. \begin{aligned} \dot{\epsilon} &= \dot{\epsilon}_0 \sinh \frac{\sigma(1-H)}{\sigma_0(1-S)(1-\omega)}, \\ \dot{H} &= h'(1-H/H^*)\dot{\epsilon}/\sigma, \\ \dot{S} &= \frac{1}{3}K'(1-S)^4, \\ \dot{\omega} &= D\dot{\epsilon}. \end{aligned} \right\} \quad (2.1)$$

Equation-set (2.1) differs in two ways from previous attempts (reviewed by Dyson & McLean 1990; McLean *et al.* 1991) to provide physically based constitutive and damage evolution equations for predicting creep behaviour: the new creep mechanism has a sinh stress-function, rather than the more familiar power-law and thereby models minimum creep rates well; the effect of particle coarsening enters the strain rate equation as a stress multiplier, rather than as the usual threshold stress.

The first term in equation-set (2.1) defines the true creep rate, $\dot{\epsilon}$, in terms of (i) the uniaxial stress, σ ; (ii) the hardening parameter, H , causing primary creep due to internal stress redistribution; (iii) the softening parameter, S , causing tertiary creep by the Lifshitz-Slyozov (1961) particle-coarsening equation; and (iv) the softening parameter, ω , causing tertiary creep and fracture. The unusual form of the Lifshitz-Slyozov (1961) equation is a consequence of the parameter S being defined by $S = 1 - p_i/p$ to range between zero and unity; p is the interparticle spacing and the subscript denotes an initial value. Explicit expressions for $\dot{\epsilon}_0$ and σ_0 , given by Dyson & Osgerby (1993), are not sufficiently accurate for lifetime prediction and were treated, along with h' , K' and H^* , as model parameters to be determined from creep data analysis, but constrained by physics to lie within certain ranges. Table 1 gives the parameters derived by Dyson & Osgerby, from 1%Cr1/2%Mo steel data generated in a COST 501 programme of the European Community.

The activation energy in $\dot{\epsilon}_0$ is nominally that of self-diffusion, while that for K' additionally contains the heat of solution of carbon in iron. The COST programme used material that had been either newly processed or service-exposed for 250 000 h at 525 °C; table 1 applies to new material and to material service-exposed at temperatures greater than 883 K. For material service-exposed at temperatures greater than 800 K but less than 883 K, $|\sigma_0|$ is replaced by the

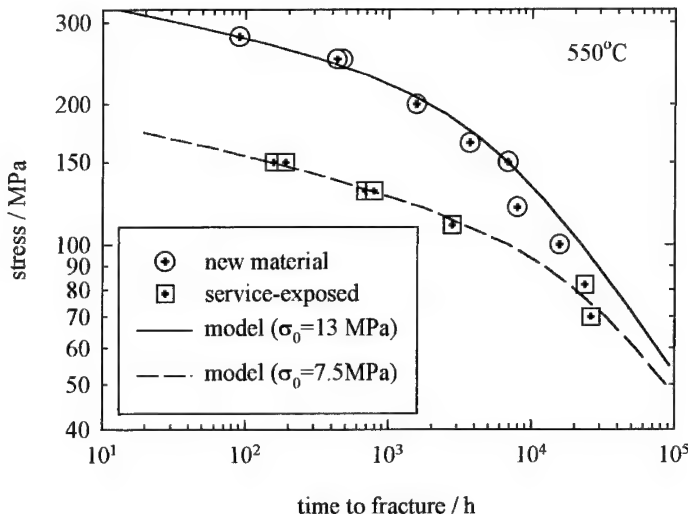


Figure 3. Illustrating the ability of equation-set (2.1) to model the substantial differences in fracture lifetimes between new 1%Cr1/2%Mo steel and serviced-exposed material. The only model parameter to be changed is σ_0 , which quantifies the coarsening of the particles.

following:

$$\sigma_0 = 1.62 \exp[1300/T] \text{ MPa.} \quad (2.2)$$

Equation (2.2) reflects the effect of thermal ageing during service exposure on the initial carbide particle spacing, while the activation energy is believed to be related to the temperature dependence of the particulate volume fraction. Table 1 and equation (2.2) have been used as input parameters in equation-set (2.1) to generate the solid and dashed curves in figure 3 which, in qualitative agreement with the empirical calculations of Toft & Marsden (1961), predict convergence of behaviour in new and service-exposed material at times of the order of 10^5 h.

(c) Predicted creep data-scatter

Figure 4 compares the lifetime/stress data of Toft & Marsden (1961) with the behaviour predicted using the COST model material parameters given in table 1, from which a value of $\sigma_0 = 10.5$ MPa can be calculated at a temperature of 565 °C. The predicted behaviour lies not only within but, more importantly, towards the top of the scatter band (consistent with the Toft & Marsden data being service-exposed) and so gives confidence in the underlying physics of the model. Its potential usefulness in extrapolating data that are scattered primarily because of large-scale material inhomogeneities is illustrated in figure 5: the two solid lines bounding the data were calculated using values of $\dot{\epsilon}_0$, K' , h' and H^* given in table 1 calculated at 565 °C, with two values of σ_0 to reflect the extremes of microstructure.

3. Modelling testing-scatter in low-cycle fatigue

(a) Background

In 1985, an intercomparison programme on high-temperature low-cycle fatigue (LCF) was sponsored by BCR, with the UK's National Physical Laboratory (NPL)

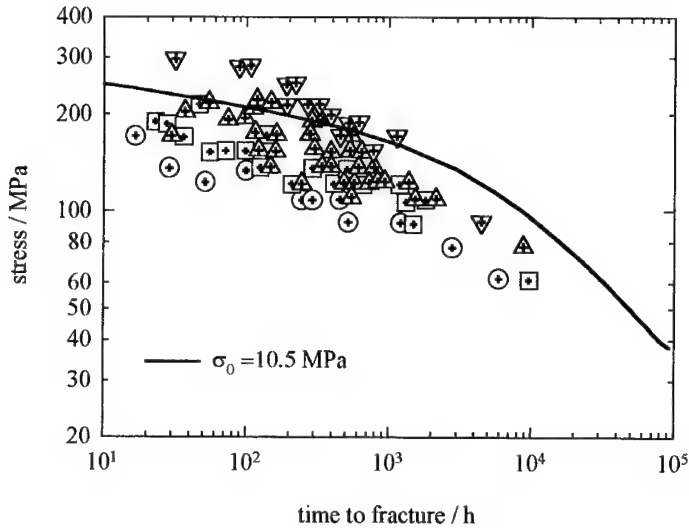


Figure 4. Comparison of Toft & Marsden (1961) data with predictions using equation-set (2.1) and COST model parameters.

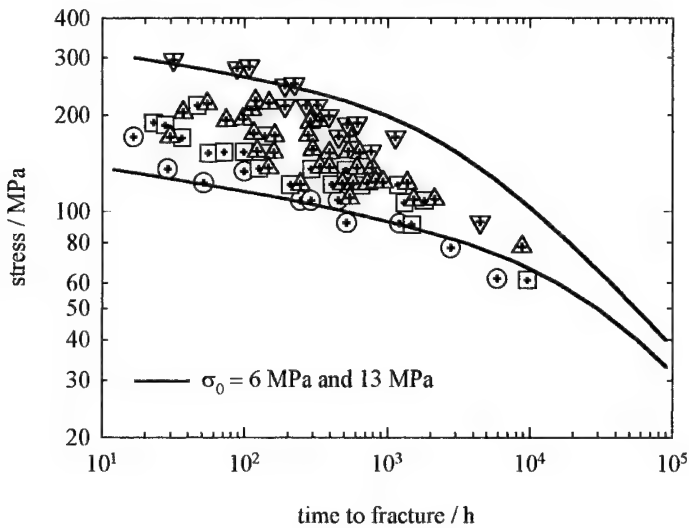


Figure 5. Bounding of Toft & Marsden (1961) data using equation-set (2.1) and COST model parameters with two values of σ_0 .

taking the lead. The proposal had evolved from an initiative by the UK's High Temperature Mechanical Testing Committee to prepare a code of testing practice (Thomas *et al.* 1989), based upon an emerging European consensus on best practice. Four types of metallic alloy were tested: AISI 316L steel, 9Cr1Mo steel and IN 718 at 550 °C; and Nimonic 101 at 850 °C. Twenty-six laboratories in Europe and Japan produced 61 sets of LCF data which were subsequently analysed by Thomas & Varma (1992). Laboratories were requested to test three testpieces at each of 3 prescribed strain ranges for every alloy: in the event, not all laboratories tested every alloy and some used more than one type of extensometer in order to explore their differences. The results within any one laboratory showed little

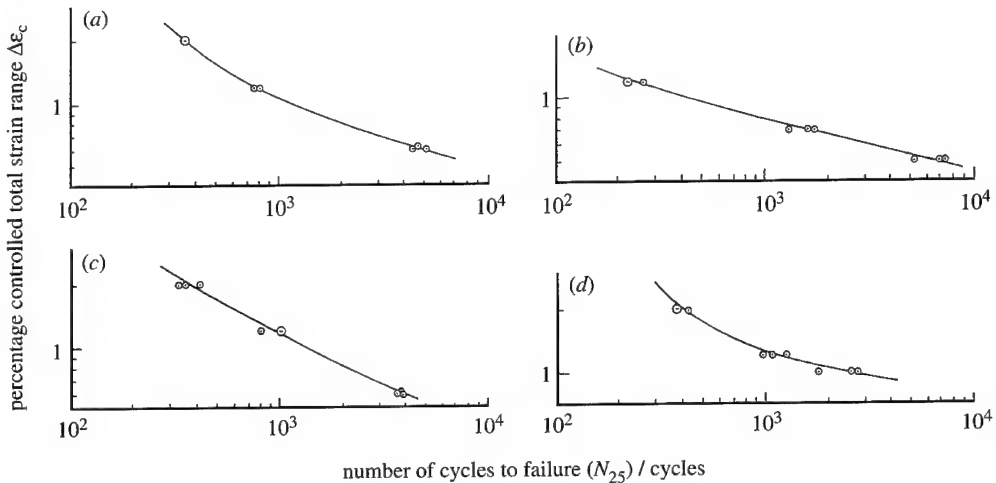


Figure 6. Four sets of low-cycle fatigue test results from a single laboratory in the BCR round robin exercise (original data from Thomas & Varma 1992).

scatter and examples of this good repeatability are given in figure 6. In contrast, reproducibility of data between laboratories for all four materials was extremely poor, as illustrated in figure 7 with results for the nickel-base superalloy Nimonic 101. The results given in figure 7 are in the form of a box plot; thus although only three strain ranges have been used, each is expanded for the purpose of identifying the relatively small repeatability scatter within each laboratory. Figure 7 underestimates the magnitude of the data-scatter because Thomas & Varma had to leave out datasets whenever their analysis showed that the detailed guidelines covering test conditions and reporting requirements had not been followed. Since repeatability scatter was small compared to reproducibility scatter and testpiece samples had been issued randomly to minimize effects due to material-scatter, the problem was clearly one of inadequate testing. By detailed argument, Thomas & Varma (1992) reduced the large number of conceivable reasons for the poor reproducibility to a possible three: (i) bending of the testpiece; (ii) uncertainties in the measurement of strain range; (iii) uncertainties in the measurement and control of temperature.

LCF data are plotted in the engineering literature with lifetime, N_f , as a function of total strain range, $\Delta\epsilon$. Over small strain ranges, the following empirical law adequately approximates behaviour:

$$N_f \Delta\epsilon^\beta = K, \quad (3.1)$$

where K and β are constants for a given material only.

Equation (3.1) can be differentiated to give the lifetime uncertainty, dN_f/N_f :

$$\frac{dN_f}{N_f} = -\beta \left[\frac{d\Delta\epsilon}{\Delta\epsilon} \right]. \quad (3.2)$$

Over larger strain ranges, K and β are found to vary systematically, demonstrating that equation (3.1) does not represent the correct physics; a more physically realistic model will be used in § 3b.

Contributions to the uncertainty in strain range $d(\Delta\epsilon)/\Delta\epsilon$ can occur from

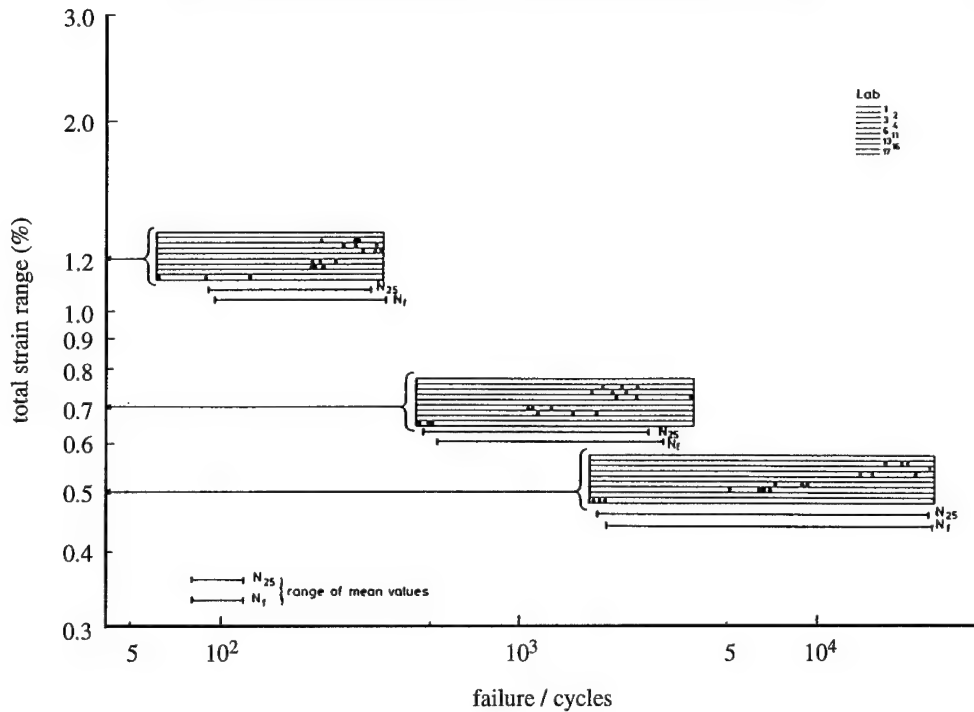


Figure 7. Illustrating the extent of interlaboratory scatter in the BCR round robin exercise, using Nimonic 101 at 850 °C as an example (Thomas & Varma 1992).

measurement-errors alone but these are unlikely to be of any great significance when modern contact extensometers are used correctly. Kandil & Dyson (1993a, b) considered in considerable detail the influence of testpiece-bending on LCF lifetimes and proposed two new mechanisms that would lead to uncertainties in the value of the control strain range. The major contributing mechanism of testpiece-bending was suggested to be due to a lateral offset of the centrelines of the load train with respect to the machine's frame. This 'load-train-offset' model of bending predicted not only a linear increase in bending strain with load, but a reversal in curvature of the (induced) banana-shaped testpiece between tension and compression loading. As a consequence, the uncertainty in strain range becomes twice the magnitude of the maximum fractional bending strain, $\epsilon_b/\Delta\epsilon_c$, measured in the setting-up procedure. The maximum bending strain ϵ_b is defined as half the difference between the maximum and minimum strains measured across the plane of maximum bending; $\Delta\epsilon_c$ is the control strain range of the test. For a test set up according to ASTM Standard E606-80 (1980), the maximum uncertainty in strain range becomes 10%, rather than 5%, which manifests itself in a potentially larger repeatability-scatter within a single laboratory. The other proposed new source of strain uncertainty is specific to the now almost universal use of a single side-entry extensometer to measure and control displacements and leads to reproducibility errors. Because of the procedures used in LCF testing (bending being invariably measured with a separate strain-gauged testpiece) the location of the extensometer on the testpiece will be randomly related to the plane of maximum strain, induced by the bending. This means that even though the control strain may be set accurately at a constant value in a series of tests, resultant

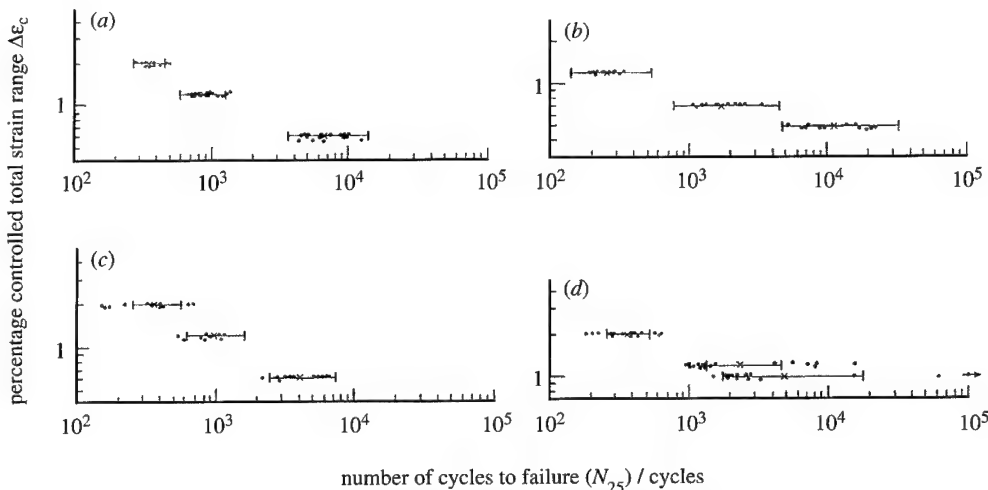


Figure 8. Comparison of predicted scatter in LCF lifetimes with BCR datasets conforming to the ASTM bending criterion (Kandil & Dyson 1993b).

lifetimes will depend on the angular position of the extensometer around the circumference of the testpiece, even when bending is kept constant. For example, when the extensometer is positioned in the plane of maximum bending, the maximum strain range, $\Delta\epsilon_{\max}$, is equal to the control strain range, $\Delta\epsilon_c$; whereas, when the extensometer is positioned diametrically opposite, $\Delta\epsilon_{\max} = \Delta\epsilon_c + 4\Delta\epsilon_b$. Since test data are compared on reported values of $\Delta\epsilon_c$ and yet failure is often thought to initiate at the point of maximum strain, it is clear that the use of a single extensometer will lead to interlaboratory differences in lifetime. To quantify the consequences for interlaboratory scatter, Kandil & Dyson (1993a) made the reasonable assumption that the angular position of the extensometer relative to the plane of maximum bending would remain sensibly constant from test to test within a single laboratory (provided that only a single machine were used). The maximum uncertainty in the strain range between laboratories conforming to ASTM Standard E606-80 (1980) now becomes 20% ($4\epsilon_b$). Figure 8 is taken from Kandil & Dyson (1993b) to illustrate the reasonably good agreement between their predicted reproducibility-scatter and data obtained from several laboratories participating in the BCR exercise. The data selected for use in figure 8 was a fraction of the whole database, restricted by the constraint that each laboratory should provide evidence that bending conformed to ASTM E606-80. Many data were excluded for this reason, from which it is reasonable to infer that this inability to control the test procedure contributed significantly to the larger scatter of the whole database.

Kandil & Dyson (1993b) predicted the scatter-bands in figure 8 by using information derived from the BCR round robin experimental datasets: values of β and K (equation (3.1)) were determined for each strain range from curves of the type shown in figure 6. Lifetime scatter-bands at a prescribed total strain range, such as those presented in figure 8 were calculated using equation (3.1) with the appropriate levels of uncertainty predicted by the 'load-train-offset' model of bending. The procedure demonstrated the potential of the 'load-train-offset' model in understanding scatter in LCF data but its reliance on specific experimen-

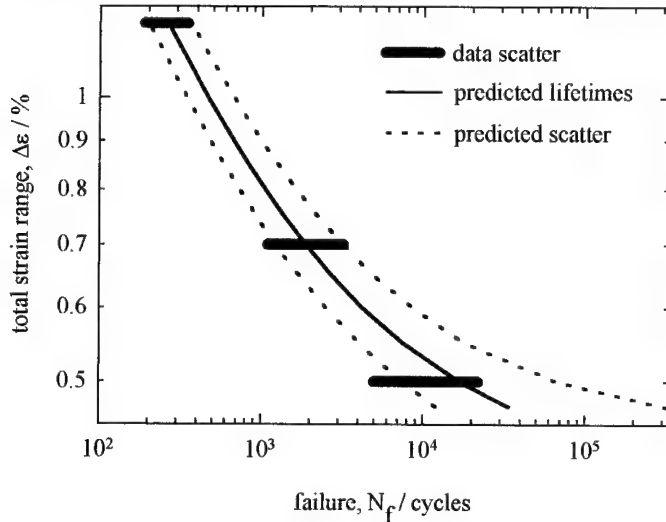


Figure 9. Comparison of LCF data-scatter for Nimonic 101 at 850 °C with lifetime and associated scatter-band predictions calculated from equation (3.5).

tal data precludes general applicability. An alternate and more general procedure, explored in the following section, is to use the 'load-train-offset' model of bending in conjunction with a material-behaviour model and data from independent sources.

(b) *A model-based prediction of LCF scatter-bands*

Although complex empirical constitutive models of material behaviour under reversed loading, similar in construction to equation-set (2.1), have been aired in the literature, their detailed application to nickel-base superalloys is still debatable. A very simple material-behaviour model will be used here: uniaxial loading; no transients; no time-dependency; and linear cyclic hardening. The stress range, $\Delta\sigma$, in the LCF cycle is then related to the plastic strain range, $\Delta\epsilon_p$, by:

$$\Delta\sigma = \Delta\sigma_y + h\Delta\epsilon_p, \quad (3.3)$$

where $\Delta\sigma_y$ and h are respectively, the material's cyclic yield stress and work-hardening coefficient.

Rather than using equation (3.1), material failure in LCF is better represented by relating lifetime to plastic strain range (Tavernelli & Coffin 1959):

$$N_f \Delta\epsilon_p^\nu = C, \quad (3.4)$$

where C and ν are constants, approximately independent of material. For predictive purposes in engineering, equation (3.4) has to be put in terms of the total strain range $\Delta\epsilon$, controlling the test. Using equations (3.3) and (3.4) and $\Delta\epsilon = \Delta\epsilon_p + \Delta\sigma/E$, where E is Young's modulus, gives

$$N_f \left[\frac{E}{E+h} (\Delta\epsilon - \Delta\epsilon_y) \right]^\nu = C, \quad (3.5)$$

where $\Delta\epsilon_y$ is the strain range at yield.

Equation (3.5) has been used to construct figures 9 and 10, which plot the predicted number of cycles to failure, N_f , at total strain range, $\Delta\epsilon$ (thin solid

Table 2. Model parameters used in equation (3.5) to construct lifetime and associated scatter-bands in figures 9 and 10

v	C	h/MPa	$d(\Delta\epsilon)/\Delta\epsilon$	$\Delta\epsilon_y$
2	10^{-2}	$0.3E$	± 0.1	4×10^{-3} (Nim 101 at 850°C) 9×10^{-3} (IN 718 at 550°C)

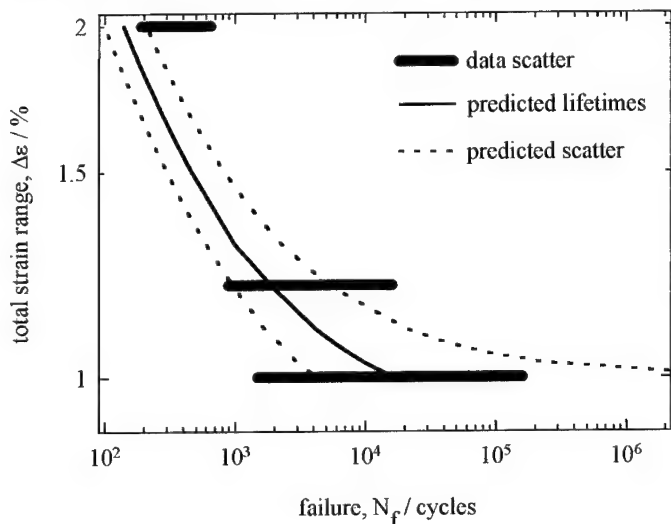


Figure 10. Comparison of LCF data-scatter for IN 718 at 550°C with lifetime and associated scatter-band predictions calculated from equation (3.5).

line) and the associated scatter-bands (dashed lines) for Nimonic 101 at 850°C and IN 718 at 550°C , respectively. The BCR data, plotted as thick horizontal lines are the same as those shown in figure 8. The model parameters are shown in table 2.

The values used for the hardening parameter, h , and the yield strains, $\Delta\epsilon_y$, were deduced from experimental data on the two alloys given by Thomas & Varma (1992): there was much scatter in these stress/strain data and so the values quoted are only approximate. The value of $v = 2$ is the same as that reported by Tavernelli & Coffin (1959) for a different set of alloy systems. Strictly, the uncertainty in the strain range, $d(\Delta\epsilon)/\Delta\epsilon$, should be used as a range term (operating only to reduce model-based predicted lifetimes) and not as a '±' term. However, since the model parameters have been derived from averaged data and the material behaviour parameters from approximate data, this seems justifiable. A value of $\pm 10\%$ has been used since the maximum uncertainty range predicted by the 'load-train-offset' model in § 3a is 20%, assuming that ASTM Standard E606-80 (1980) is obeyed.

Figures 9 and 10 demonstrate that this simple model has all the necessary components for successfully predicting lifetime and scatter, but requires fine-tuning to get detailed agreement between experiment and theory. However, fine-tuning is hardly worthwhile because the main message concerns the inevitability

of large deterministic scatter bands when the control strain range is reduced towards that of the yield strain range. Such deterministic scatter is in addition to probabilistic scatter associated with the intrinsic inability to define yield stress precisely in a polycrystal.

4. Discussion and conclusions

Scatter in mechanical property data has always posed a problem for designers of load-bearing components and has been accounted for historically by so-called factors of safety. A more descriptive term would be factors of ignorance since their magnitudes evolved, quite properly, through experience of disastrous failures. Factors of safety also reflect early inadequacies in the design process and should now be an anachronism in an age when lifetime prediction of complex components using finite element analysis (FEA) is a reality although not yet by any means common-place. The limitation on FEA lifetime prediction lies not in computing power but in (i) improving the physical basis for quantitatively understanding materials' behaviour so that adequate constitutive equations can be developed and (ii) ensuring that the chosen material has been manufactured consistently and the properties measured to an adequate precision. Point (ii) has been addressed in this paper using creep and LCF as case studies, although 'adequate precision' never seems to have been quantified by structural designers.

The paper has attempted to put a scientific framework around this area which, despite its fundamental importance to efficient and cost-effective structural design, has received relatively little attention. Perhaps in the past, steady advances in materials processing and performance have enabled the design engineer to persist in his use of 'factors of ignorance', but an era of 'materials-limited design' can now be foreseen in power engineering applications and this will encourage a better use of the existing materials resource. The continuing dramatic fall in the cost of computing power when offset against the spiralling cost of prototype testing has similarly tilted the balance in favour of better quality databases or, at least, databases of known pedigree. An example of the usefulness of good pedigree data is the creep case-study where the understanding and potential predictability of materials-scatter was enabled only by the systematic experimental work of Toft & Marsden (1961).

The disappointing quality of the interlaboratory data arising out of the BCR round robin exercise on high-temperature LCF has been rationalized by Thomas & Varma (1992) as due to certain inadequacies in the test method. Whether the necessary improvements in testing practice will emerge in the near future remains to be seen, but the work of Kandil & Dyson (1993a, b) has quantitatively accounted for a large fraction of the scatter and provided guidance on the experimental path to follow to effect such improvements. Perhaps one of the most important conclusions to emerge from the analysis is that large deterministic scatter-bands are inevitable as the cyclic yield strain is approached. This is just the region of most interest to the design engineer and any scatter is usually attributed to materials processing. Perhaps a rethink is required in the whole area of usage in design of data from strain-controlled LCF tests at high temperatures!

Dr S. Osgerby (NPL) kindly supplied digitised data of creep lifetime as a function of stress, derived from the paper by Toft & Marsden (1961). Comments by Dr F. A. Kandil (NPL) on a draft of the manuscript have been incorporated into the final text.

References

Ashby, M. F. 1989 Materials selection in conceptual design. In *Materials and engineering design* (ed. B. F. Dyson & D. R. Hayhurst), Part I, ch. 2, London: Institute of Metals

Ashby, M. F. 1991 Materials and shape. *Acta metall. Mater.* **39**, 1025–1039.

ASTM Standard E606-80 1980 Standard recommended practice for constant-amplitude low-cycle fatigue testing. *1991 Annual Book of ASTM Standards*, Part 3.01, pp. 609–621, Philadelphia, PA: American Society for Testing and Materials.

Dyson, B. F. & Osgerby, S. 1993 Modelling and analysis of creep deformation and fracture in a 1Cr1/2Mo ferritic steel. *NPL Rep. DMM(A)116*

Dyson, B. F., Loveday, M. S. & Gee, M. G. 1995 Materials metrology and standards: an introduction. In *Materials metrology and standards for structural performance* (ed. B. F. Dyson, M. S. Loveday & M. G. Gee), ch. 1. London: Chapman and Hall.

Dyson, B. F. & McLean, M. 1990 Creep deformation of engineering alloys: developments from physical modelling. *ISIJ Int.* **30**, 802–811.

Gould, D. & Loveday, M. S. 1992 A reference material for creep testing. In *Harmonisation of testing practice for high temperature materials* (ed. M. S. Loveday & T. B. Gibbons), ch. 6. London: Elsevier Applied Science.

Henderson, W. T. K. & Thomas, G. B. 1995 Accredited testing and reference materials. In *Materials metrology and standards for structural performance* (ed. B. F. Dyson, M. S. Loveday & M. G. Gee), ch. 10. London: Chapman and Hall.

Hossain, M. K. & Sced, I. R. 1995 Metrology for engineering materials. In *Materials metrology and standards for structural performance* (ed. B. F. Dyson, M. S. Loveday & M. G. Gee), ch. 9. London: Chapman and Hall.

Kandil, F. A. & Dyson, B. F. 1993a The influence of load misalignment during uniaxial low cycle fatigue testing. I. Modelling. *Fatigue Fract. Engng Mater. Struct.* **16**, 509–527.

Kandil, F. A. & Dyson, B. F. 1993b The influence of load misalignment during uniaxial low cycle fatigue testing. II. Applications. *Fatigue Fract. Engng Mater. Struct.* **16**, 529–537.

Lifshitz, I. M. & Slyozov, V. V. 1961 *J. Phys. Chem. Solids* **19**, 35–50.

Lin, J., Hayhurst, D. R. & Dyson, B. F. 1993a The standard uniaxial testpiece: computed accuracy of creep strain. *J. Strain Analysis* **28**(1), 20–34.

Lin, J., Hayhurst, D. R. & Dyson, B. F. 1993b A new design of uniaxial creep testpiece with slit extensometer ridges for improved accuracy of strain measurement. *Int. J. Mech. Sci.* **35**(1), 63–78.

Loveday, M. S. 1992 Towards a tensile reference material. In *Harmonisation of testing practice for high temperature materials* (ed. M. S. Loveday & T. B. Gibbons), ch. 7. London: Elsevier Applied Science.

Manson, S. S. & Haferd, A. M. 1953 A linear time–temperature relation for extrapolation of creep and stress rupture data. *Nat. Advisory Committee Aeronautics Tech. Note* 2890.

McLean, M., Dyson, B. F. & Ghosh, R. N. 1991 Recent evolution of gas turbine materials and the development of models for life prediction. In *Mechanical behaviour of materials. VI* (ed. M. Jono & T. Inoue), vol. 12, pp. 49–58. Pergamon Press.

Tavernelli, J. F. & Coffin, L. F. 1959 A compilation and interpretation of cyclic strain fatigue tests on metals. *Trans. ASM* **51**, 438–453.

Thomas, G. B., Hales, R., Ramsdale, J., Suhr, R. W. & Sumner, G. A. 1989 A code of practice for constant-amplitude low cycle fatigue testing at elevated temperature. *Fatigue Fract. Engng Mater. Struct.* **12**, 135–153.

Thomas, G. B. & Varma, R. K. 1992 Review of the BCR/VAMAS low cycle fatigue intercomparison programme. In *Harmonisation of testing practice for high temperature materials* (ed. M. S. Loveday & T. B. Gibbons), ch. 8. London: Elsevier Applied Science.

Toft, L. H. & Marsden, R. A. 1961 The structure and properties of 1Cr1/2Mo steel after service in CEGB power stations. In *Structural processes in creep*, 276–294. London: Institute of Metals.

Discussion

P. HIRSCH (*Department of Materials, University of Oxford, UK*). I am deeply concerned about the quality of the data quoted on low cycle fatigue. The spread of the results from different laboratories exceeds the safety factor of 25 usually applied in safety assessments to allow for various uncertainties. This is potentially serious because when making such assessments data from different laboratories, which might indicate the presence of systematic errors, are not always available. It is to be hoped that the efforts of those engaged in BCR and other projects will soon lead to a tightening of the specifications governing measurement techniques, so that these systematic errors can be reduced to negligible values.

B. F. DYSON. I hope that Sir Peter Hirsch's concern will soon be allayed. My former colleague at NPL, Dr F. A. Kandil, is now leading an investigation sponsored by BCR and aims to develop a theoretical and experimental framework for quantifying uncertainties in low cycle fatigue lifetime data due to errors in measurement during testing. The ultimate objective is to provide a robust methodology that will reduce interlaboratory data-spread to a factor less than about five in lifetime. Although this is not negligible as Sir Peter clearly wishes, it is still an extremely ambitious target because of the difficulties inherent in this test.

M. MCLEAN (*Imperial College, London, UK*). Professor Dyson's model incorporates the effect of the coarsening of a fixed volume fraction of strengthening particles, and it clearly gives a good representation of the high-temperature behaviour of this class of alloy. In others there can be significant changes in phase chemistry. For example, we have recently shown in a 12CrMoNbV steel that MC transforms to $M_{23}C_6$ during service. This reduction in the volume fraction of MC leads to a reduction in strength.

R. C. THOMSON (*Cambridge University, UK*). Professor Dyson described the data presented (Toft & Marsden) by a single coarsening parameter, S . However, the particles present in the $1Cr\frac{1}{2}Mo$ steel microstructure undergo transformations from cementite to alloy carbides M_7C_3 and $M_{23}C_6$, etc. It is known in the literature that these Cr rich alloy carbides coarsen much more slowly than cementite. Could he comment on how these transformations and subsequent changes in coarsening rate might be incorporated into the coarsening parameter, and secondly on whether he thinks there is a need to do so in terms of explaining the macroscopic creep behaviour?

B. F. DYSON. Professor McLean and Dr Thomson state quite correctly that the present model is concerned only with the effect on creep rate when a spherical particulate dispersion of fixed volume fraction coarsens according to the Lifshitz-Slyozov equation. Real materials are usually more complicated and this is particularly the case with low-alloy ferritic steels, which is the point of commonality between the two comments. A succession of coarsening carbides could in principle be incorporated into the present model by introducing a damage parameter with its appropriate evolution equation for each carbide. However, it is debatable whether the effort involved in producing such a sophisticated model would be worthwhile, except as an academic exercise. A better first attempt in my view is to assume the dominance of a single carbide particle for all but the shortest times, particularly since one important aim of developing physically based constitutive equations is to predict behaviour at stresses giving lifetimes of the order 10^5 h.

Professor McLean suggests that in the currently important 12CrMoNbV steel, the reduction in volume fraction with time of one of the carbides is life-limiting. In such a situation, the Lifshitz-Slyozov coarsening relationship in equation-set (2.1) would need to be replaced by one containing the evolution rate of volume fraction, with suitable changes also being made to the strain-rate equation to accept volume fraction as a damage parameter.

M. S. LOVEDAY (*Division of Materials Metrology, National Physics Laboratory, Teddington, UK*). Professor Dyson has highlighted in a very clear manner the importance of assessing measurement uncertainty, and, in particular, the role of modelling a material's behaviour to provide a clearer means of identifying the causes of scatter in experimental data.

The need for a statement of uncertainty of measurement is now a requirement for International (ISO) and European (CEN) testing standards; in addition accreditation agencies such as NAMAS (National Measurement Accreditation Service) now require an assessment of uncertainty of measurement, whether it be for determining material properties, or for any other physical, chemical or electrical measurements. A recently published document – 'A guide to the expression of uncertainty in measurement' – has been issued by ISO, IEC, OIML and BIPM which provides an approach for assessing total uncertainty. Although this document is comprehensive and based on sound statistical methods, it is difficult to see how the majority of technical staff in testing laboratories would be able to understand and implement its recommendations; however, simplified guidelines in the UK are being prepared by NAMAS and the BMTA (British Measurement and Testing Association).

B. F. DYSON. I agree with the sentiments expressed about the document; its incomprehensibility certainly extends to me. I wish NAMAS and BTMTA well in their endeavour to provide us all with a translation!

Effect of matrix cracking on the overall thermal conductivity of fibre-reinforced composites

BY T. J. LU AND J. W. HUTCHINSON

Division of Applied Sciences, Harvard University, Cambridge, MA 02138, USA

The longitudinal thermal conductivity of a unidirectional fibre-reinforced composite containing an array of equally spaced transverse matrix cracks is calculated. The cracked composite is modelled by a cylindrical cell which accounts for altered heat transfer across the matrix cracks as well as through debonded portions of the fibre-matrix interface. Heat transfer mechanisms across the cracks and debonded interfaces considered are contact, gaseous conduction, and radiation, and the relative importance of these mechanisms is discussed. Approximate closed form solutions to the cell model for the overall thermal conductivity are obtained using an approach reminiscent of the shear lag analysis of stiffness loss due to matrix cracking and debonding. Selected numerical results from a finite-element analysis of the cell model are presented to complement the analytical solutions. Both matrix cracking and interfacial debonding have the potential for significantly reducing the longitudinal thermal conductivity.

1. Introduction

The rule of mixtures holds rigorously for the overall longitudinal thermal conductivity k_z^0 of a crack-free composite reinforced by continuous unidirectional fibres: $k_z^0 = \rho k_z^f + (1 - \rho)k_m$, where ρ is the fibre volume fraction, k_z^f is the axial thermal conductivity of the fibre and k_m is the matrix conductivity. This result continues to apply when fibre debonding occurs (i.e. when a thermal barrier of negligible thickness emerges at the debonded portion of the fibre-matrix interface) but fails if the matrix develops cracks perpendicular to the fibres which impede the heat flow. Such matrix cracking may occur in intermetallic and ceramic matrix composites, arising from excessive stressing in the vicinity of notches or other sources of stress concentrations. Thus, the presence of these matrix cracks will degrade the thermal conductivity of the composite and thereby alter heat flow. In the extreme, heat transfer through the matrix can be fully interrupted by a combination of matrix cracking and interfacial debonding such that the overall longitudinal thermal conductivity of the composite is due entirely to heat conducted by the intact fibres. It is evident, therefore, that the longitudinal conductivity will range from k_z^0 for the uncracked composite to as little as ρk_z^f when matrix cracking and interface debonding reduce the effective heat flow in the matrix to zero. Matrix cracking also strongly affects other thermo-mechanical properties of the compo-

site such as stiffness, coefficients of thermal expansion (CTE), thermal diffusivity, etc. These issues are now receiving increased attention in connection with the application of composite materials to environments involving high temperatures and temperature gradients.

Several analytical procedures have been developed for the evaluation of the overall thermal conductivity of a homogeneous, isotropic matrix containing distributed, weakly interacting cracks or voids (e.g. Hasselman 1978; Hoenig 1983; Tzou 1991; Tzou & Li 1993). For a unidirectional fibre-reinforced matrix composite suffering no matrix cracking, the influence of fibre-matrix debonding on the overall transverse thermal conductivity of the material has been studied by Benveniste (1987), Hasselman & Johnson (1987), Bhatt *et al.* (1990) and Fadale & Taya (1991), among others. In the case where the fibres are perfectly bonded to the matrix with intimate thermal contact across their interface or in the case where full debonding along the fibre-matrix interface occurs, the presence of matrix cracking perpendicular to the fibres does not affect the thermal conductance capability of the composite in the transverse direction. Thus in the analysis to follow the focus is on the overall longitudinal thermal conductivity of the unidirectional composite as influenced by matrix cracking and interface debonding.

The key element in building up a solution to the titled problem is the determination of the disturbance to the temperature distribution in each composite constituent due to the matrix cracks and the debonded interfaces. The thermal conductance mechanisms that are in play across the cracks and the debonded interfaces will be discussed. The same cylindrical cell is used to model the conductivity of the cracked composite as was used by He *et al.* (1994) to predict tensile stress-strain behaviour and by Lu & Hutchinson (1995) to study CTE changes. The present study will focus on a composite comprised of transversely isotropic fibres in an isotropic matrix such that the effective properties of the composite are transversely isotropic relative to the fibre direction. Attention is mainly directed to systems where the matrix has a larger thermal expansion coefficient than those of the fibres, such that upon cooling from the processing temperature, residual tension builds up in the matrix parallel to the fibres while compression develops across the fibre-matrix interfaces. As a consequence, once formed, the matrix cracks remain open, and debonded portions of the fibre-matrix interfaces remain nominally closed but with reduced thermal contact. The thermal barrier at the debonded interfaces is modelled by an equivalent interfacial heat transfer coefficient comprised of the sum of three conductances: fibre-matrix contact across the interface, gaseous conduction and radiation heat exchange. Only the latter two mechanisms operate to transfer heat across the matrix cracks. Based on the analogy between the variables describing elasticity and those for steady-state heat conduction, an approximate analytical solution for the effective thermal conductivity as a function of crack density is obtained by an approach analogous to the well-known shear lag analysis of stiffness loss due to matrix cracking and interface debonding. The accuracy of the approximations introduced in the analysis of the cell model will be assessed with the aid of selected finite-element calculations.

The organization of the paper is as follows. In § 2, the problems are formulated with discussion of the heat transfer boundary conditions. Solutions for the overall thermal conductivity of the cracked composite with perfect fibre-matrix bonding are derived in § 3. These results are extended in § 4 to account for the combined effects of matrix cracking and interface debonding.

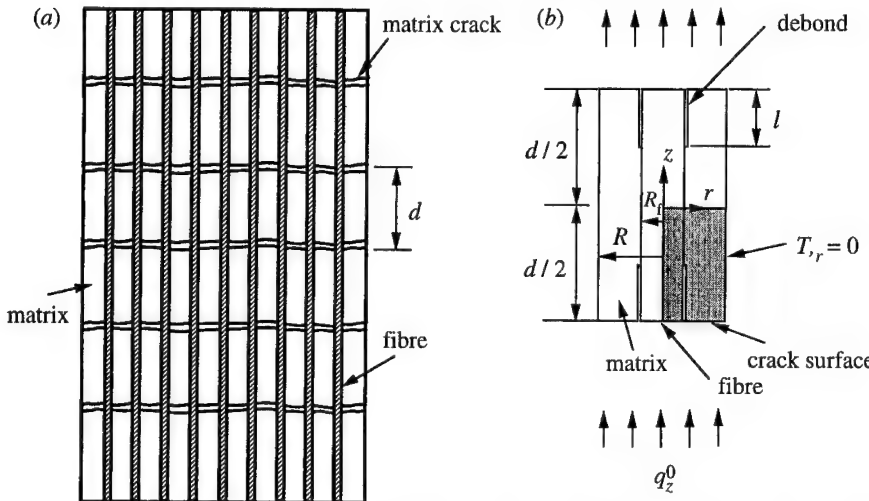


Figure 1. (a) A unidirectionally reinforced fibre-matrix composite with an array of uniformly spaced matrix cracks; and (b) a single unit cell of the periodically cracked composite.

2. Formulation of the problems

A unidirectional, continuous fibre-reinforced composite has through-the-thickness, periodically distributed matrix cracks with spacing d , as depicted in figure 1a. For cases in which fibre-matrix debonding has occurred, the debonds extending from the matrix crack surfaces will be assumed to have a common length l such that the periodicity is preserved. The average heat flux in the composite parallel to the fibres is denoted by q_z^0 . The cylindrical cell shown in figure 1b is introduced to model one of the periodic cells of the cracked composite. Boundary conditions appropriate to the cylindrical cell will be discussed below. A set of cylindrical polar coordinates (r, θ, z) is chosen such that the z -axis coincides with the axis of the fibre and increases in the direction of the heat flow, with $z = 0$ at the cell centre. The radius R of the cylindrical cell is related to the fibre radius R_f via $R = R_f/\sqrt{\rho}$. Debonding over a cylindrical portion of the fibre-matrix interface, if present, is modelled by an interfacial crack extending a distance l on either side of each matrix crack surface. It follows that $l = \frac{1}{2}d$ represents complete debonding, whereas $l = 0$ corresponds to no debonding.

(a) Basic heat conduction equations

By cylindrical symmetry, the temperature and temperature gradient fields in the cell depend only on r and z . For fibres with transversely isotropic properties, Fourier's law reads

$$\begin{Bmatrix} q_r^f \\ q_z^f \end{Bmatrix} = - \begin{bmatrix} \gamma k_z^f & 0 \\ 0 & k_z^f \end{bmatrix} \begin{Bmatrix} T_{f,r} \\ T_{f,z} \end{Bmatrix}, \quad (2.1)$$

where $q_r^f(r, z)$ and $q_z^f(r, z)$ are flux components in the radial and axial directions, k_r^f ($= \gamma k_z^f$), k_z^f are transverse and longitudinal thermal conductivities of the fibre, $T_f(r, z)$ is the current temperature in the fibre, $T_{f,r} \equiv \partial T_f / \partial r$, etc. The corresponding relation for the isotropic matrix is

$$\begin{Bmatrix} q_r^m \\ q_z^m \end{Bmatrix} = - \begin{bmatrix} k_m & 0 \\ 0 & k_m \end{bmatrix} \begin{Bmatrix} T_{m,r} \\ T_{m,z} \end{Bmatrix}, \quad (2.2)$$

with k_m designating the thermal conductivity of the matrix. In the analysis, (k_m, k_r^f, k_z^f) are taken to be temperature-independent constants.

In the absence of internal heat sources, conservation of heat in association with Fourier's law (2.1) leads to the following steady-state equation of heat conduction in the fibre:

$$\frac{1}{r} \frac{\partial}{\partial r} \left(\gamma r \frac{\partial T_f}{\partial r} \right) + \frac{\partial^2 T_f}{\partial z^2} = 0. \quad (2.3)$$

This equation also holds for the matrix material except for the replacement of fibre temperature $T_f(r, z)$ by matrix temperature $T_m(r, z)$ and $\gamma = 1$. For isotropic fibres, equation (2.3) reduces to the more familiar Laplace equation.

The perfectly bonded portion of the interface is assumed to have no thermal resistance, requiring

$$\gamma k_z^f T_{f,r} = k_m T_{m,r} \quad \text{on } r = R_f, \quad |z| \leq \frac{1}{2}d - l, \quad (2.4)$$

$$T_f = T_m \quad \text{on } r = R_f, \quad |z| \leq \frac{1}{2}d - l, \quad (2.5)$$

Symmetry with respect to the z -axis implies:

$$T_{f,r} = 0 \quad \text{on } r = 0, \quad |z| \leq \frac{1}{2}d. \quad (2.6)$$

The appropriate condition on the outer surface of the cell which models the periodic structure of the solution expected for the cracked composite of figure 1a is that no heat is transferred there, i.e.

$$T_{m,r} = 0 \quad \text{on } r = R, \quad |z| \leq \frac{1}{2}d. \quad (2.7)$$

Inside the cylindrical cell, on every cross-section transverse to the axis of the fibre, the following heat balance condition is satisfied:

$$(1 - \rho) k_m \hat{T}_{m,z} + \rho k_z^f \hat{T}_{f,z} = -q_z^0 \quad \text{for } |z| < \frac{1}{2}d, \quad (2.8)$$

where

$$\hat{T}_{f,z} = \frac{2}{R_f^2} \int_0^{R_f} r T_{f,z} dr, \quad \hat{T}_{m,z} = \frac{2}{R^2 - R_f^2} \int_{R_f}^R r T_{m,z} dr \quad (2.9)$$

are temperature gradients averaged over the cross-sectional areas of the fibre and matrix, respectively. Simple arguments based on the periodicity and linearity of the temperature field of the cracked (and possibly debonded) composite cell model disclose that the temperature distribution is independent of r on each of the transverse planes half way between the matrix cracks such as those at $z = 0$ and $z = d$. It is also independent of r within the fibre on all planes containing matrix cracks such as $z = \frac{1}{2}d$. Denote by ΔT the temperature change between $z = 0$ and $z = d$. The overall longitudinal thermal conductivity k_z is defined by

$$k_z = -\frac{q_z^0}{\Delta T/d}. \quad (2.10)$$

Apart from the conditions on the matrix crack surfaces and on the debonded portions of the fibre-matrix interface, which will be discussed immediately below, these equations fully specify the problem for k_z .

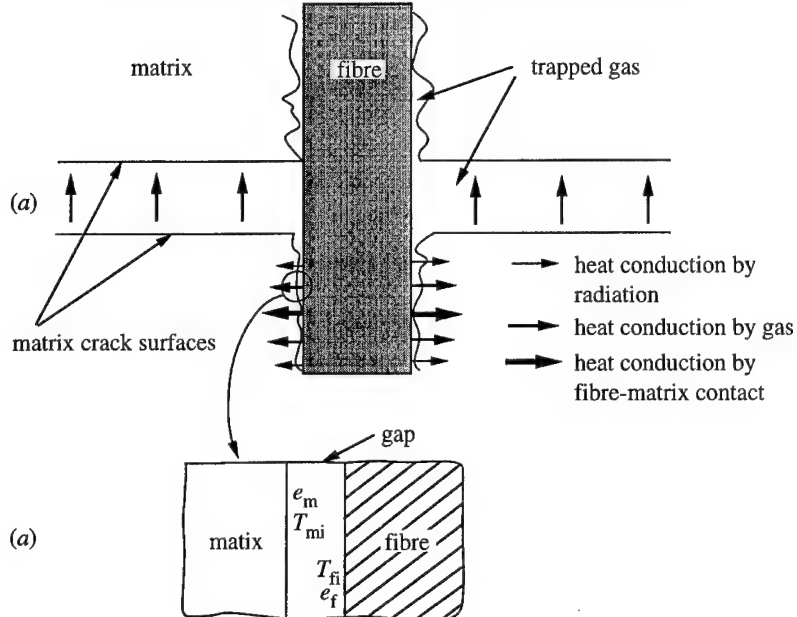


Figure 2. (a) Schematics of the heat conductance mechanisms across the matrix crack surfaces and the debonded portions of the fibre-matrix interface; and (b) model representation of the radiative heat exchange between fibre and matrix over a typical gap at the interface.

(b) Boundary condition at the debonded interfaces

Heat flow will be impeded on portions of the fibre-matrix interface which have debonded. Assume the heat flow through the interface is proportional to the temperature jump across it. Let h_i be the *interfacial thermal conductance* defined such that

$$\gamma k_z^f T_{f,r} = k_m T_{m,r} = h_i (T_{mi} - T_{fi}) \quad \text{on} \quad r = R_f, \quad \frac{1}{2}d - l \leq |z| \leq \frac{1}{2}d, \quad (2.11)$$

where $T_{fi}(z)$ and $T_{mi}(z)$ denote respectively the temperatures of the fibre and matrix at the interface. If the mechanisms of heat transfer through the interface operate independently, h_i can be written as (Leung & Tam 1988; Bhatt *et al.* 1990)

$$h_i = h_c + h_g + h_r, \quad (2.12)$$

where h_c is the component contributed by heat transfer through contacting points between the fibre and matrix, h_g is due to the interfacial gaseous heat transfer, and h_r is attributable to the radiative heat transfer across the non-contacting portions of the interface (figure 2a). The subject of thermal resistance is itself a complex one, and no complete theory is available. Several theoretical models as well as experimental results for solid-solid interfaces are reviewed recently by Swartz & Pohl (1989).

Assuming the matrix has a larger thermal expansion coefficient than that of the fibre, the fraction of interfacial conductance due to fibre-matrix contact h_c depends in a complicated manner on both on the surface roughness of the debonded portion of the interface and on the clamping pressure σ_r acting over the interface. Since the latter scales with thermal expansion mismatch between fibre and matrix, it is expected that h_c should increase with mismatch. Quantitative estimates

of h_c are difficult to establish theoretically, but may often be inferred from the measurement of the total conductance h_i in vacuum, as will be discussed.

The detailed mechanism underlying the transfer of heat by the gas filling the spaces of the interface is controlled by the Knudsen number N_K , defined as the ratio of the mean free path of the gas to the characteristic width of the interfacial gap. When $N_K \ll 1$, the continuum theory of heat conduction in the gas applies. If $N_K \gg 1$ the energy exchange involves collisions of gas molecules and the interfacial surface with relatively few intervening interatomic or intermolecular collisions. For intermediate values of N_K , the two processes are in transition. Since the mean free path of a gas depends on both temperature and pressure, the mechanism controlling h_g may shift as environmental conditions imposed on the composite change.

To gain insight into the radiative heat transfer mode, consider radiative heat exchange between two parallel surfaces with emissivities e_m and e_f and absolute surface temperatures T_{mi} and T_{fi} , respectively, as depicted in figure 2b. The net rate of radiative heat exchange between the two surfaces is given by

$$q = \frac{\sigma(T_{fi}^4 - T_{mi}^4)}{1 - e_m e_f (e_m + e_f)}, \quad (2.13)$$

where $\sigma = 5.67 \times 10^{-8} \text{ W m}^{-2} \text{ K}^{-4}$ is the Stefan–Boltzmann constant of radiation. The temperature jump $T_{fi} - T_{mi}$ across the thin interfacial gap is expected to be small compared to either of the two surface temperatures. With \bar{T}_i denoting the average of T_{mi} and T_{fi} , (2.13) can be approximated by

$$q_{ri} = \frac{4\sigma(\bar{T}_i)^3}{1 - e_m e_f (e_m + e_f)} (T_{fi} - T_{mi}), \quad (2.14)$$

which, in the light of (2.11) and (2.12), yields

$$h_r \propto \frac{4\sigma(\bar{T}_i)^3}{1 - e_m e_f (e_m + e_f)}. \quad (2.15)$$

As an estimation of the relative significance of the radiative effect, take $e_m = e_f = 0.9$ and $\bar{T}_i = 1200 \text{ K}$ in (2.15) to get $h_r \approx 7.1 \times 10^2 \text{ W m}^{-2} \text{ K}^{-1}$. This is a very small value compared to values such as $10^5 \text{ W m}^{-2} \text{ K}^{-1}$ or larger expected for most ceramic and intermetallic matrix composites maintaining nominally closed debonded interfaces or even gas-filled open interfaces. One point of calibration is the value of h_i measured experimentally by Bhatt *et al.* (1990) for debonded interfaces of a composite consisting of double-coated SCS-6 SiC fibres within a reaction-bonded silicon nitride matrix. The thermal expansion mismatch of this composite system is such that the debonded interface is fully opened. Nevertheless, h_i was found to be in the range 10^4 to $10^5 \text{ W m}^{-2} \text{ K}^{-1}$, with h_g overwhelming h_r . Thus it can be reasonably expected that the radiative component h_r will generally be negligible for temperatures as large as 1200 K and probably higher, especially for composites for which the debonded interface surfaces maintain nominal contact.

The competition between heat transfer by surface asperity contact and gaseous conduction vanishes under vacuum conditions with the gaseous phase removed. (Bhatt *et al.* (1990) used vacuum testing to elucidate the role of gaseous conduction in their study.) Thus, to a good approximation, the interfacial thermal

conductance measured in vacuum represents the contact conductance h_c . Then to obtain the component h_g , one may measure the total interfacial conductance h_i in the gaseous phase of interest and subtract h_c from it.

(c) *Boundary condition on the crack surfaces*

As has been already emphasized, attention is focused on composite systems where the CTE of the matrix exceeds that of the fibre. For composites with either a ceramic or intermetallic matrix, the fibres are usually bonded to the matrix at relatively high temperatures. Under cooling from the fabricating temperature, the matrix develops residual tension in the direction of the fibre while a clamping pressure acts across the fibre-matrix interface. When matrix cracks form they remain completely open even under no applied load. Residual crack openings are generally in the range 0.01–1 μm , depending on many factors including residual stress, extent of fibre debonding and sliding, and fibre diameter.

Assuming negligible heat loss due to flow of gas through the cracks (which is justified for crack openings as large as 0.1 mm), it follows that heat transfer across the crack surfaces is realized by two mechanisms: gaseous conduction and crack surface radiation. Hence, with H_c denoting the total conductance across the matrix crack,

$$H_c = H_g + H_r, \quad (2.16)$$

where H_g and H_r are defined in the same way as h_g and h_r . The qualitative arguments advanced above for the relative importance of the two conductance contributions apply here as well. Specifically, it can be expected that H_r will often play a minor role. In general, the boundary condition governing heat transfer across the matrix crack surface is

$$k_m T_{m,z} = H_c (T_m^+ - T_m^-) \quad \text{on} \quad |z| = \frac{1}{2}d, \quad R_f \leq r \leq R, \quad (2.17)$$

where the flow of heat is taken to be in the positive z -direction, and T_m^+ and T_m^- are temperatures on the upper and lower surfaces of the crack, respectively. Under the limiting condition in which negligible heat passes across the crack, the boundary condition becomes

$$k_m T_{m,z} = 0 \quad \text{on} \quad |z| = \frac{1}{2}d, \quad R_f \leq r \leq R. \quad (2.18)$$

Under this limit when the cracks act as perfectly insulating barriers, and, for the cell model, all the heat then passes the plane at $z = \frac{1}{2}d$ through the fibre, i.e.

$$\frac{2}{R_f^2} \int_0^{R_f} r T_{f,z} \, dr = -\frac{q_z^0}{\rho k_z^f} \quad \text{on} \quad |z| = \frac{1}{2}d. \quad (2.19)$$

3. Thermal conductivity of cracked composites with perfectly bonded interfaces

The set of governing equations of steady-state heat conduction in a unidirectional fibre-reinforced composite, (2.1)–(2.3), is formally analogous to that of the elasticity problem for the same composite, if q_i , $T_{,i}$, k_{ij} are respectively replaced by ϵ_{ij} , σ_{ij} , S_{ijkl} . The so-called shear lag approximations (Laws & Dvorak 1988; McCartney 1990; Lu & Hutchinson 1995), which are very effective for estimating stiffness loss due to matrix cracking and debonding, can be adapted to the

thermal conductivity problem. Details of this approximate solution procedure are elaborated in an expanded version of this paper available from the second author as report MECH-239.

For perfectly bonded fibre-matrix interfaces, the governing differential equation which emerges for the average fibre temperature gradient in the presence of matrix cracking is

$$\frac{d^2\hat{T}_{f,z}}{dz^2} = \left(\frac{\xi}{R_f}\right)^2 \left(\hat{T}_{f,z} + \frac{q_z^0}{k_z^0}\right) \quad \text{for } |z| \leq \frac{1}{2}d, \quad (3.1)$$

where the non-dimensional coefficient is defined by

$$\xi = \{8\gamma k_z^0 / (1 - \rho) k_m\}^{1/2}. \quad (3.2)$$

The relevant solution to (3.1) is

$$\hat{T}_{f,z} = -q_z^0 / k_z^0 + A_1 \cosh(\xi z / R_f) \quad \text{for } |z| \leq \frac{1}{2}d, \quad (3.3)$$

where A_1 is a constant to be determined from the boundary condition. The first term is recognized as the uniform temperature gradient in the uncracked composite. The disturbance to the uniform field by the matrix cracks is represented by the second term. This same type of solution for this geometry carries over to problems of elasticity, thermal expansion, electrical conduction, electrostatics, and magnetostatics owing to the well known mathematical analogy that exists between the subjects (Batchelor 1974).

(a) Thermally insulated crack surfaces

If the matrix crack surfaces are thermally insulated under condition (2.18) discussed earlier, (3.3) together with (2.19) yields

$$\frac{d\hat{T}_f}{dz} = -\frac{q_z^0}{k_z^0} \left\{ 1 + \frac{1 - \rho}{\rho} \frac{k_m}{k_z^f} \frac{\cosh(\xi z / R_f)}{\cosh(\xi d / 2R_f)} \right\} \quad \text{for } |z| \leq \frac{1}{2}d. \quad (3.4)$$

The overall longitudinal thermal conductivity k_z is defined by (2.10) where $\Delta T = \hat{T}_f(d) - \hat{T}_f(0)$, since T is uniform with respect to r on $z = 0$ and $z = d$. Geometric symmetry with respect to $z = \frac{1}{2}d$ then gives

$$\Delta T = 2(\hat{T}_f(\frac{1}{2}d) - \hat{T}_f(0)) = 2 \int_0^{d/2} \frac{d\hat{T}_f}{dz} dz. \quad (3.5)$$

(Equation (3.5) applies to the cell model for all boundary conditions considered in this paper.) By (2.10),

$$k_z = k_z^0 \left\{ 1 + \frac{1 - \rho}{\rho} \frac{k_m}{k_z^f} \frac{\tanh(\xi d / 2R_f)}{\xi d / 2R_f} \right\}^{-1}. \quad (3.6)$$

Figure 3 gives curves of k_z/k_z^0 against normalized crack density R_f/d for five values of fibre volume fraction ρ : 0.1, 0.2, 0.3, 0.4 and 0.5. The constitutive parameters used in this example are $k_z^f/k_m = 2$ and $\gamma = 1$.

Also included in figure 3 are numerical results from a finite-element analysis of the boundary value problem for the cell as posed above for $\rho = 0.1, 0.3, 0.5$. The finite-element discretization is made for a quarter of the cell (the shaded region of figure 1b) with eight-node quadratic axisymmetric elements. Quarter-point elements are used to simulate the singular behaviour of the temperature

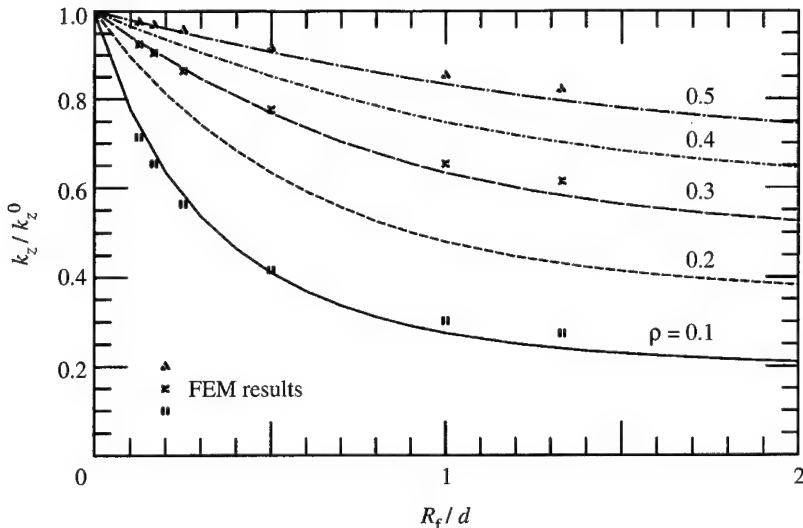


Figure 3. Cell model predictions and finite-element results for normalized longitudinal conductivity k_z/k_z^0 as functions of normalized crack density R_f/d for five selections of fibre volume fraction ρ : 0.1, 0.2, 0.3, 0.4 and 0.5. Other constitutive parameters used are $k_z^f/k_m = 2$, $\gamma = 1$ and $B_c = 0$.

gradient and heat flux fields in the vicinity of the crack tip. The agreement between the approximate solution and the finite-element results is clearly very good. For $d/R_f > 3$, the dependence of k_z on crack density is nearly linear. This is the density range in which interaction between neighbouring cracks is weak. At higher crack densities, k_z/k_z^0 decays relatively slowly and gradually approaches the asymptote $\rho k_z^f/k_z^0$. In the limit $d = 0$, all the heat flows through the fibre so that $k_z = \rho k_z^f$. The finite-element results are relatively insensitive to the details of the mesh around the crack tip when the crack density is low. They become more sensitive to mesh refinement at high densities, but, in any case, crack spacings less than about $2R_f$ are rare.

In passing, it is worth noting that (3.6) is similar in form to the shear lag approximation for the longitudinal elastic modulus E_z of the cracked unidirectional composite,

$$E_z = E_z^0 \left\{ 1 + D_1^0 \frac{R_f}{d} \tanh \left(\frac{S}{D_1^0} \frac{d}{R_f} \right) \right\}^{-1}, \quad (3.7)$$

where E_z^0 is the axial elastic modulus of the uncracked composite, and where D_1^0 and S are dimensionless functions of ρ and moduli ratios (Lu & Hutchinson 1995). Application of the shear lag approach to the stiffness problem requires some numerical analysis to evaluate D_1^0 . Similar numerical work is unnecessary for the lower order heat conduction problem.

(b) The effect of gaseous heat conduction within matrix cracks

Gaseous conduction is expected to be the most important mechanism for heat transfer across the open matrix cracks, as previously discussed. Condition (2.17) is assumed to hold on the cracks where H_c is the heat conductance coefficient. This coefficient will be taken to be independent of the temperature in the analysis,

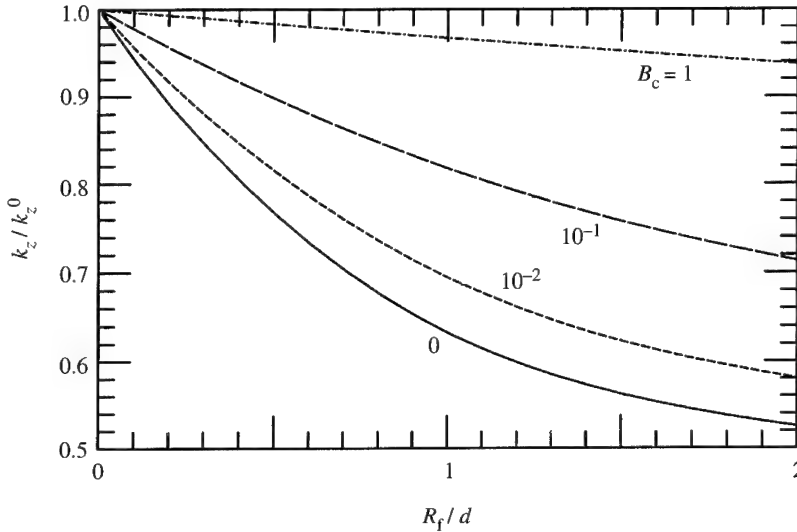


Figure 4. The effect of varying the Biot number for matrix cracking on the overall longitudinal thermal conductivity for $k_z^f/k_m = 2$, $\gamma = 1$ and $\rho = 0.3$.

but clearly its value should be assigned consistent with the ambient temperature in the composite.

The temperature gradient averaged across the fibre is still given by (3.3). From (2.8) and (3.3), the temperature gradient in the matrix immediately follows as

$$\hat{T}_{m,z} = -\frac{q_z^0}{k_z^0} - \frac{\rho k_z^f A_1}{(1-\rho)k_m} \cosh\left(\xi \frac{z}{R_f}\right) \quad \text{for } |z| \leq \frac{1}{2}d. \quad (3.8)$$

Given that the temperature is *uniform* with respect to r at $z = 0$ and $z = d$, it follows that the temperature drop across the crack can be expressed as

$$\begin{aligned} \hat{T}_m^+ - \hat{T}_m^- &= \Delta T - 2 \int_0^{d/2} \frac{d\hat{T}_m}{dz} dz = 2 \int_0^{d/2} \left[\frac{d\hat{T}_f}{dz} - \frac{d\hat{T}_m}{dz} \right] dz \\ &= \frac{2A_1 R_f k_z^0}{(1-\rho)\xi k_m} \sinh\left(\xi \frac{d}{2R_f}\right). \end{aligned} \quad (3.9)$$

When (2.17) is rewritten in terms of \hat{T}_m , and (3.8) and (3.9) are substituted into the result, one finds

$$A_1 = -\frac{q_z^0 (1-\rho) k_m}{\rho k_z^f} \left\{ \cosh\left(\xi \frac{d}{2R_f}\right) + \frac{2k_z^0 H_g R_f}{\rho \xi k_m k_z^f} \sinh\left(\xi \frac{d}{2R_f}\right) \right\}^{-1}. \quad (3.10)$$

Finally, the overall longitudinal thermal conductivity of the composite is obtained from relations (2.10), (3.3) and (3.10) as

$$k_z = k_z^0 \left\{ 1 + \frac{(1-\rho)k_m}{\rho k_z^f} \frac{\tanh(\xi d/2R_f)/(\xi d/2R_f)}{1 + (2k_z^0 B_c / \rho \xi k_m) \tanh(\xi d/2R_f)} \right\}^{-1}, \quad (3.11)$$

where $B_c = H_c R_f / k_z^f$ is the Biot number for matrix cracking. Relation (3.11) reduces to (3.8) for adiabatic crack surfaces ($H_c = 0$).

The effect of B_c on the normalized overall thermal conductivity, k_z/k_z^0 , is il-

Table 1. The properties of dry air at atmosphere pressure

(The dimension of H_g is $\text{W m}^{-2} \text{K}^{-1}$.)

T (K)	l_m (10^{-8} m)	k_g ($\text{W m}^{-1} \text{K}^{-1}$)	$\delta = 0.01 \mu\text{m}$	$\delta = 0.1 \mu\text{m}$	$\delta = 1 \mu\text{m}$
300	5.69	0.032	$N_K = 5.69$	$N_K = 0.57$	$N_K = 0.057$
			$H_g = 3.2 \times 10^6$	$H_g = 3.2 \times 10^5$	$H_g = 3.2 \times 10^4$
1273	11.1	0.085	$N_K = 11.1$	$N_K = 1.11$	$N_K = 0.11$
			$H_g = 8.5 \times 10^6$	$H_g = 8.5 \times 10^5$	$H_g = 8.5 \times 10^4$

lustrated in figure 4, for $k_z^f/k_m = 2$, $\gamma = 1$ and $\rho = 0.3$. The limit for $B_c = 0$ corresponds to perfectly insulating cracks for which results have been displayed previously, while the limit for $B_c = \infty$ leaves the overall conductivity unchanged at k_z^0 . The value of B_c characterizing the transition midway between these two extremes is about 0.1. To acquire some feel for the significance of crack thermal conductance, consider a ceramic composite with a fibre of radius, $R_f = 10 \mu\text{m}$, and conductivity in the range 10^2 – $10^3 \text{ W m}^{-1} \text{ K}^{-1}$ expected for SiC fibres. If B_c is to be greater than 0.1, the crack conductance parameter, H_c , must be larger than 10^6 – $10^7 \text{ W m}^{-2} \text{ K}^{-1}$. As already discussed, the contribution of H_r to H_c is likely to be orders of magnitude smaller than this. To gain some insight into the contribution from H_g , consider the parameter values for dry air at a pressure of one atmosphere given in table 1 for $T = 300 \text{ K}$ and $T = 1273 \text{ K}$, taken from Sears (1967). The mean free path of the molecules in the gas, l_m , is on the order of $0.1 \mu\text{m}$ at both temperatures giving rise to the Knudsen number, N_K , shown for each of the three values of the crack opening, δ . The continuum conductance of the gas k_g is not applicable to the two smallest crack openings at $\delta = 0.01 \mu\text{m}$ and $0.1 \mu\text{m}$. Nevertheless, even for these cases, the continuum formula $H_g = k_g/\delta$ should give a rough estimate of the heat conductance across the crack, an estimate which is expected to be somewhat below the value appropriate in the regime of intermediate to large Knudsen numbers. It can be seen from the values of H_g given in table 1 that B_c is likely to be as large as 0.1 when the crack openings are in the range from $0.01 \mu\text{m}$ to somewhat less than $0.1 \mu\text{m}$, but B_c should be well below 0.1 for ‘large’ openings of $1 \mu\text{m}$. From this example, we conclude that composite thermal conductivity may be sensitive to conductance by the gas in the matrix cracks, with cracks with openings well above $0.1 \mu\text{m}$ acting as barriers to thermal conduction and those with openings below $0.1 \mu\text{m}$ having less effect on the overall heat flow.

4. Thermal conductivity of cracked composites with partly or fully debonded interfaces

In this section the combined effects of matrix cracking and thermal contact resistance due to fibre–matrix debonding on the overall longitudinal thermal conductivity of the composite are considered. The thermal barrier at the debonded interface may be modelled either by an equivalent interfacial heat transfer coefficient h_i or by introducing a thin cylindrical layer of poor conductivity between the fibre and the matrix. The concept of interfacial heat transfer in the form of

(2.11) will be adopted below due to its simplicity. As discussed, the coefficient h_i depends on surface asperities, thermal expansion mismatch, gas in the interface, interface temperature and possibly other factors. As in the study of the effect of matrix crack conductance, h_i will be taken to be independent of temperature in the analysis.

For the bonded portion of the fibre, the differential equation (3.1) governing the longitudinal temperature gradient has a solution in the form,

$$\hat{T}_{f,z} = -q_z^0/k_z^0 + A_2 \cosh(\xi z/R_f) \quad \text{for } |z| \leq \frac{1}{2}d - l, \quad (4.1)$$

where the unknown coefficient A_2 will be determined from the continuity of $\hat{T}_{f,z}$ at the debond tip. For the debonded portion of the fibre, the analysis gives

$$\frac{d^2 \hat{T}_{f,z}}{dz^2} = \left(\frac{\zeta}{R_f} \right)^2 \left(\hat{T}_{f,z} + \frac{q_z^0}{k_z^0} \right) \quad \text{for } \frac{1}{2}d - l \leq |z| \leq \frac{1}{2}d, \quad (4.2)$$

where the dimensionless coefficient ζ is related to ξ by

$$\zeta = \xi \left\{ \frac{1}{1 + 4\gamma/B_i} \right\}^{1/2}, \quad (4.3)$$

and $B_i \equiv h_i R_f / k_z^f$ is the Biot number for the debonded interface. The limiting case of $B_i \rightarrow 0$ represents the *adiabatic* boundary condition in which the debonded portion of the fibre-matrix interface is perfectly insulated. The other limit $B_i \rightarrow \infty$ refers to the case where *intimate thermal contact* obtains between the fibre and matrix with $T_{fi} = T_{mi}$ everywhere across the debonded interface; then, (4.2) reduces to (3.1). The general solution to (4.2) for a gradient which is symmetric with respect to $z = 0$ is

$$\hat{T}_{f,z} = -q_z^0/k_z^0 + A_3 \cosh(\zeta z/R_f) \quad \text{for } \frac{1}{2}d - l \leq |z| \leq \frac{1}{2}d, \quad (4.4)$$

where the unknown coefficient A_3 will be determined from the boundary condition on the matrix crack surface.

(a) Thermally insulating matrix cracks

If debonding of length l has occurred at the fibre-matrix interface and no heat is being transferred across the matrix cracks, combination of relations (4.1), (4.4) with relations (2.8), (2.11) and (2.18) gives the following distribution of average temperature gradient within the fibre

$$\hat{T}_{f,z} = \begin{cases} -\frac{q_z^0}{k_z^0} \left\{ 1 + \frac{1-\rho}{\rho} \frac{k_m}{k_z^f} \frac{\cosh[\zeta(\frac{1}{2}d-l)/R_f]}{\cosh[\xi(\frac{1}{2}d-l)/R_f]} \frac{\cosh(\xi z/R_f)}{\cosh(\zeta d/2R_f)} \right\}, \\ \quad \text{for } |z| \leq \frac{1}{2}d - l, \\ -\frac{q_z^0}{k_z^0} \left\{ 1 + \frac{1-\rho}{\rho} \frac{k_m}{k_z^f} \frac{\cosh(\zeta z/R_f)}{\cosh(\xi d/2R_f)} \right\}, \\ \quad \text{for } \frac{1}{2}d - l \leq |z| \leq \frac{1}{2}d. \end{cases} \quad (4.5)$$

The resulting expression for the effective overall longitudinal thermal conductivity of the composite becomes

$$k_z = k_z^0 \left\{ 1 + \frac{1-\rho}{\rho} \frac{k_m}{k_z^f} \left[\frac{\tanh(\zeta d/2R_f)}{\zeta d/2R_f} + F\left(\xi, \zeta, \frac{l}{R_f}, \frac{d}{R_f}\right) \right] \right\}^{-1}. \quad (4.6)$$

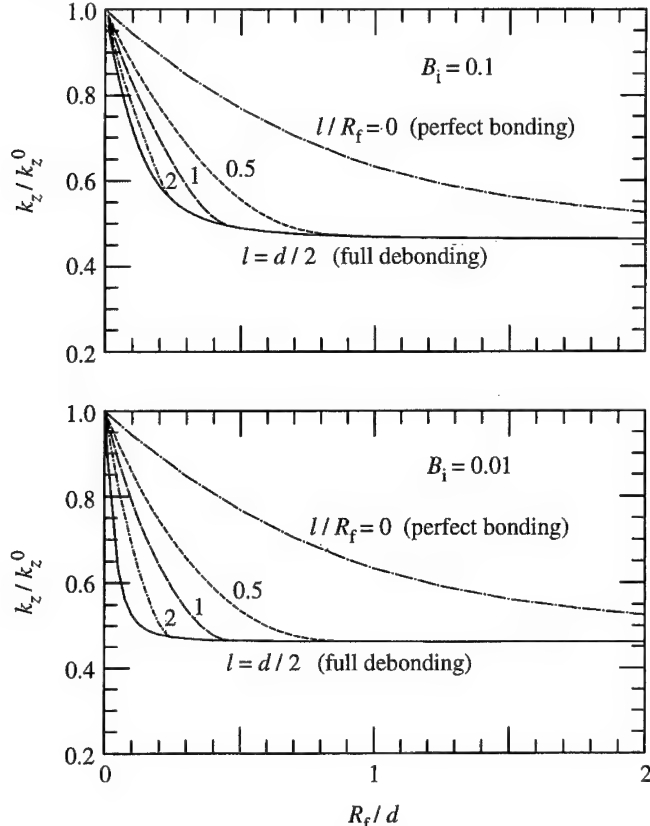


Figure 5. Effect of fibre-matrix debonding on the overall longitudinal thermal conductivity of the cracked unidirectional composite for (a) $B_i = 0.1$ and (b) $B_i = 0.01$. The constitutive parameters used are $k_z^f/k_m = 2$, $\gamma = 1$, $\rho = 0.3$ and $B_c = 0$.

Here, F is a dimensionless function defined by

$$F\left(\xi, \zeta, \frac{l}{R_f}, \frac{d}{R_f}\right) = \frac{\cosh[\zeta(\frac{1}{2}d - l)/R_f]}{\cosh(\zeta d/2R_f)} \left\{ \frac{\tanh[\xi(\frac{1}{2}d - l)/R_f]}{\xi d/2R_f} - \frac{\tanh[\zeta(\frac{1}{2}d - l)/R_f]}{\zeta d/2R_f} \right\}. \quad (4.7)$$

The predicted values of k_z/k_z^0 are plotted in figure 5 against R_f/d for five choices of normalized debond length: $l/R_f = 0, 0.5, 1, 2, d/2R_f$, and two values of the interface Biot number: $B_i = 0.01$ and 0.1 . The parameters $k_z^f/k_m = 2$, $\rho = 0.3$ and $\gamma = 1$ have been used in plotting these curves. Compared with the case of matrix cracking unaccompanied by fibre-matrix debonding where a fairly high density of cracks is needed to cause a significant reduction in the axial thermal conductivity k_z , the results in figure 5 clearly show that debonding associated with a low Biot number can reduce k_z to the lowest limit, ρk_z^f , even at relatively low crack densities.

At full debonding, when $l = \frac{1}{2}d$, F vanishes in (4.6), yielding

$$k_z = k_z^0 \left\{ 1 + \frac{1 - \rho}{\rho} \frac{k_m}{k_z^f} \left[\frac{\tanh(\zeta d/2R_f)}{\zeta d/2R_f} \right]^{-1} \right\}, \quad (4.8)$$

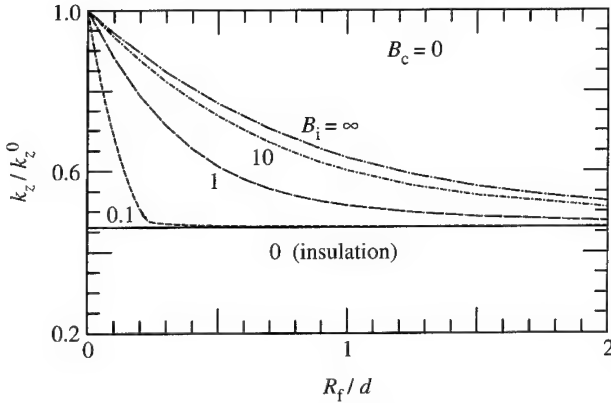


Figure 6. The effect of varying the interfacial Biot number B_i on the overall longitudinal thermal conductivity of the cracked unidirectional composite with complete debonding over the fibre-matrix interface. The constitutive parameters used are the same as those listed in figure 5.

which has the same form as that of (3.8) for the case of perfect bonding except that the coefficient ξ there is now replaced by ζ . Moreover, (4.8) reduces to (3.6) when the fibre and matrix are in intimate contact across the debonded portion of the interface ($B_i = \infty$). If the debonded interfaces are perfectly insulating ($B_i = 0$), k_z reduces to ρk_z^f for all crack spacing d . For intermediate values of B_i , the curve of k_z/k_z^0 against R_f/d is plotted in figure 6, again with $k_z^f/k_m = 2$, $\rho = 0.3$ and $\gamma = 1$. For composite systems having values of $B_i < 0.1$, the conclusion to be drawn from figure 6 is that the debonded portion of the interface can be safely taken to be perfectly insulating.

(b) The combined effect of B_i and B_c

If heat is transmitted across the matrix crack surfaces ($B_c > 0$), the solution for A_2 and A_3 follows along the lines outlined in § 3 and for the case just discussed. The result is

$$A_2 = A_3 \frac{\cosh[\zeta(\frac{1}{2}d - l)/R_f]}{\cosh[\xi(\frac{1}{2}d - l)/R_f]}, \quad (4.9)$$

$$A_3 = -\frac{q_z^0}{k_z^0} \frac{(1-\rho)k_m}{\rho k_z^f \cosh(\zeta d/2R_f)} \left\{ 1 + \frac{2k_z^0 H R_f}{\zeta \rho k_m k_z^f} \tanh\left(\frac{\zeta d}{2R_f}\right) \right\}^{-1}. \quad (4.10)$$

The corresponding solution for the overall conductivity k_z is

$$k_z = k_z^0 \left\{ 1 + \frac{(1-\rho)k_m}{\rho k_z^f} \frac{\tanh(\zeta d/2R_f)/(d/2R_f) + F(\xi, \zeta, l/R_f, d/R_f)}{1 + (2k_z^0 B_c / \zeta \rho k_m) \tanh(\zeta d/2R_f)} \right\}^{-1}, \quad (4.11)$$

where ζ depends on B_i as given by (4.3) and F is still given by (4.7). In the case of complete debonding along the interface ($l = \frac{1}{2}d$), $F = 0$ and (4.11) becomes formally identical to (3.11) except for the replacement there of ξ by ζ .

With B_i fixed at 0.1 and with $k_z^f/k_m = 2$, $\rho = 0.3$ and $\gamma = 1$, the values of k_z/k_z^0 from (4.11) are displayed in figure 7 for several choices of B_c , assuming that full debonding has taken place along the fibre-matrix interface. They are bracketed by the two limiting cases $B_c = 0$ and $B_c = \infty$ corresponding to $k_z = \rho k_z^f$ and $k_z = k_z^0$, respectively. Apparently, if the magnitudes of both B_i and B_c are

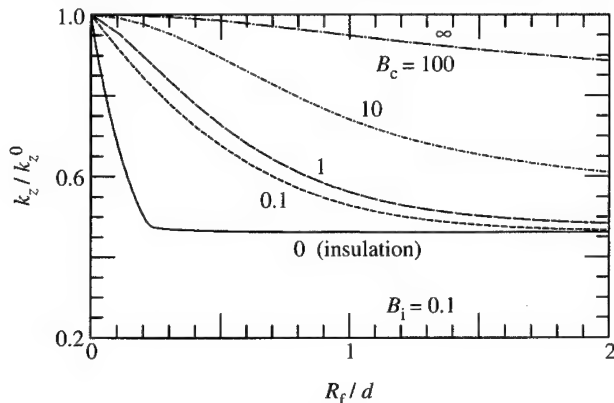


Figure 7. The effect of varying the matrix cracking Biot number B_c on the overall longitudinal thermal conductivity of the cracked unidirectional composite with complete debonding over the fibre-matrix interface. The constitutive parameters used are $k_z^f/k_m = 2$, $\gamma = 1$, $\rho = 0.3$ and $B_i = 0.1$.

less than 0.1, then the approximations of *adiabatic* crack surfaces and *adiabatic* debonded interfaces can be justified.

5. Concluding remarks

Matrix cracking in combination with interfacial debonding can reduce the overall longitudinal thermal conductivity of a unidirectional fibre-reinforced composite to a level where essentially all the heat is conducted through the fibres. The reduction can be as large as 50–70% if the fibre conductivity is comparable to that of the matrix and the volume fraction of the fibre is in the range of 0.3–0.5. Significantly, this can be achieved at relatively low crack densities when extensive debonding occurs, if the relevant Biot numbers for the matrix cracks and the debonded interfaces are both less than about 0.1. In the case where matrix cracking is not accompanied by fibre debonding, correspondingly large reductions in the thermal conductivity of the composite are not seen until the cracks reach a relatively high density rarely observed in practice. Matrix cracking perpendicular to the fibres does not affect the transverse heat-carrying capability of the composite if the fibres are perfectly bonded to the matrix.

Insightful discussions by one of the us (T.J.L.) with Professor H. W. Emmons and Professor J. L. Sanders, Jr, concerning heat transfer boundary conditions have been very helpful. Financial support from ARPA University Research Initiative (Subagreement P.O. #KK 3007) with the University of California, Santa Barbara, ONR Prime Contract N00014-92-J-1808, and from the Division of Applied Sciences, Harvard University, is gratefully acknowledged. The finite-element code, ABAQUS, was used to provide selected numerical solutions to the cell model.

References

Batchelor, G. K. 1974 *A. Rev. Fluid Mech.* **6**, 227–251.
 Beyerle, D., Spearing, S. M., Zok, F. W. & Evans, A. G. 1992 *J. Am. Ceram. Soc.* **75**, 2719–2725.
 Bhatt, H., Donaldson, K. Y., Hasselman, D. P. H. & Bhatt, R. T. 1990 *J. Am. Ceram. Soc.* **73**, 312–316.
 Benveniste, Y. 1987 *J. appl. Phys.* **61**, 2840–2843.
 Fadale, T. D. & Taya, M. 1991 *J. Mater. Sci. Lett.* **10**, 682–684.

Hasselman, D. P. H. 1978 *J. Comp. Mater.* **12**, 403–407.

Hasselman, D. P. H. & Johnson, L. F. 1987 *J. Comp. Mater.* **21**, 508–512.

He, M. Y., Wu, B.-X., Evans, A. G. & Hutchinson, J. W. 1994 *Mech. Mater.* **18**, 213–229.

Hoenig, A. 1983 *J. Comp. Mater.* **17**, 231–237.

Hutchinson, J. W. & Jensen, H. M. 1990 *Mech. Mater.* **9**, 139–163.

Laws, N. & Dvorak, G. J. 1988 *J. Comp. Mater.* **22**, 900–916.

Leung, W. P. & Tam, A. C. 1988 *J. appl. Phys.* **63**, 4505–4510.

Lu, T. J. & Hutchinson, J. W. 1995 *Composites*. (In the press.)

McCartney, L. N. 1992 *J. Mech. Phys. Solids* **40**, 27–68.

Sears, F. W. 1967 *Introduction to thermodynamics: the kinetic theory of gases and statistical mechanics*. Cambridge, MA: Addison-Wesley.

Swartz, E. T. & Pohl, R. O. 1989 *Rev. mod. Phys.* **61**, 605–668.

Tzou, D. Y. 1991 *J. Comp. Mater.* **25**, 1064–1084.

Tzou, D. Y. & Li, J. 1993 *Int. J. Heat Mass Transfer* **36**, 3887–3895.

Discussion

D. J. RÖDEL (*GDP, Darmstadt, Germany*). Could Professor Hutchinson get an insight into asperity contact and especially into the change of asperity contact after cyclic loading from thermal conductivity measurements in transverse directions on uniaxial debonded reinforcements?

J. W. HUTCHINSON. This seems quite possible. There is only one set of data, from Hasselman. They measured transverse conductivity in vacuum and argon and from the data in argon one could get an insight into asperity contact. The micromechanics would not help much—you would have to calibrate.

High-temperature mechanism-based design

BY F. A. LECKIE

Department of Mechanical and Environmental Engineering, College of Engineering, University of California, Santa Barbara, CA 93106-5070, USA

The historical development of the procedures used in high-temperature design using isotropic materials is described. It is illustrated how knowledge of the mechanisms causing time-dependent deformation and damage can help to describe the influence of the multi-axial states of stress occurring in practice and to provide rational procedures for extrapolating the results of short-term tests. Since the procedures are based on mechanisms, their structure lends itself readily to a concurrent engineering approach.

Procedures which support the application of composites to high-temperature designs are much less well developed but the progress to date supports the notion that mechanism-based design procedures are practical, economic and amenable to concurrent engineering.

1. Introduction

The procedures of design with monolithic metals are now well established having been in a state of constant development for over a century. The concept of ductility (Fairbairn 1856) enabled engineers, if only intuitively, to use plastic deformations to design efficient and reliable components. The experiments of Wöhler (1860) demonstrated that the application of many cycles of load could cause failure at levels which are fractions of those causing short-time failure. The theory of elasticity (Love 1892) provided the theoretical support for its practical application by means of strength of materials. The rules of design gradually developed from experience combined with the results of experiments on large complex components (Blair 1946). By the middle of the century, the theory of plasticity was established definitively (Hill 1950) and the results were being applied to civil engineering (Baker *et al.* 1956) and pressure vessel technology stimulated by the demands of nuclear power (Kennedi 1960). The combination of economic and technological factors encouraged the increased use of high-strength steels. Experience with the use of high-strength steels pointed to the importance on performance of defects introduced during the process of manufacture and construction. These circumstances stimulated renewed interest in the previous studies of Griffith (1920) and resulted in the theory of fracture (Irwin 1958) which is now widely practised as a design tool.

The availability of these concepts provides a box of design tools which are sharp enough to be used across a spectrum of applications from electronic components to offshore structures. Each application has its own set of nuances but the uniformity of language eases communication between the disciplines of materials science, design and manufacture. Design involves many decisions which

are easier to make when supported by a small number of robust concepts. Their application must avoid complex procedures which encumber the creative process. As design progresses, more emphasis and effort may be expended on details and refinement, but these must be compatible with the overall thrust of the original design concept.

The design concepts using the new breed of materials, such as those proposed for future aircraft engines remain to be established. There are several difficulties. Material development is characterized by rapid change so that only small amounts are available, for even the simplest tests. Specimens which duplicate the complex states of stress occurring under operating conditions are extremely expensive, even if sufficient material is available. Information from a build and test experience base will not be available. Drawing blindly from experience with monolithic metals is likely to result in failures, which are the consequence of unsuspected mechanisms. Under these circumstances, new design procedures must include the role of material mechanisms on component performance. This has been possible in high-temperature design with metals. The procedures described in R5 (1991) are simple, robust, science-based and provide a common language between materials scientist and designer. In this paper, an abbreviated account is given of attempts to establish design procedures for new high-temperature composite materials.

2. The mechanics and mechanisms of current high-temperature design

The mechanics of design for components which operate at high temperature are already in place and have been incorporated into working design codes (R5 1991). Because the life and deformation of high-temperature components are dictated by the time-dependent failure mechanisms, it has been essential that the results of materials science be integrated into the design process. Material properties establish the connection between materials science and the continuum mechanics as described in the text of Ashby & Jones (1980).

Mostly, but not always, components operate in the elastic range. The elastic moduli of the material which are the consequence of interatomic forces are the parameters needed to complete the elastic analysis of a component. Hence, the properties provide the means of relating the microscale to the scale of components according to the relation shown below.

mechanism → property → continuum mechanics → design concepts

interatomic force	E, G	theory of elasticity (Love 1892)	strength of materials stress concentration factor finite element
-------------------	--------	-------------------------------------	--

In addition to connecting scales, the properties provide information about the response to the multi-axial stress states occurring in practice. Hence, in the case of isotropic materials, both Young's modulus E and shear modulus G are required to

activate the theory of elasticity. Elasticity theory can, in principle, be used to solve problems. However, the theory of elasticity is an enormous intellectual edifice and it is the simplified methods known as strength of materials that designers use to estimate quickly, deformations and stress levels. Stress concentration values are also important in helping to determine design limits and these have been catalogued. For more complex, unusual problems, the finite-element method is a well-developed design tool.

An elastic response is normally expected when the component operates under normal working conditions. However, under unusual and infrequent operating conditions, it is common to exceed the conditions for which elasticity is valid. It is then necessary to include the influence of irreversible plastic deformations. The yield stress σ_y , is then the appropriate material property which relates dislocation mechanics to the continuum theory of plasticity as indicated below.

mechanism → property → continuum mechanics → design concepts

dislocation mechanics	σ_y, J_2	theory of plasticity (Hill 1950)	limit load bounds
-----------------------	-----------------	----------------------------------	-------------------

The second stress tensor invariant J_2 defines the influence of three-dimensional stress states. This is the simplest description and does not include important effects, such as work-hardening, but design procedures must be simple, and such concerns are left to a more detailed level of design. The application of the theory of plasticity has been a fertile ground for design because the application of the bounding theorems allows decisions to be made on the basis of quite simple calculations and can be part of the creative process.

Fracture has also been integrated into the design process and in addition to evaluating the influences of defects introduced during manufacture can also be used as a creative design tool. The relationship between mechanisms and design is indicated below.

mechanism → property → continuum mechanics → design concepts

voids	K_{IC}	fracture mechanics (Irwin 1958)	critical crack length
debonding	K_{IIC}		leak before break
	K_{IIIC}		test procedures

When two different mechanisms operate simultaneously, the conditions are set for the appearance of additional phenomena. For example, under cyclic loading conditions, when both elastic and plastic deformations occur, then the shake-down concept provides valuable insight into component behaviour. Comparison of the limit and fracture loads suggests the 'leak before break' concept defining the condition when contained fluid can leak before failure, providing additional safety to the design. The material parameter describing this mechanism parameter $(K_{IC}/\sigma_y)^2$, which is a particular example of the material indices studied extensively by Ashby & Jones (1980).

The methods for high-temperature design fit into a similar framework by using

Table 1. *High-temperature design*

identifier	→	mechanism	→	material property	→	continuum mechanics	→	design concepts
creep deformation maps		diffusion dislocation		σ_D ϕ		theory of creep		bounding methods
creep rupture maps		void growth		σ_R		continuum damage mechanics		modification of limit load shakedown bounding methods
creep ductility index		microstructural growth		Δ				

the reference stress as a material property which removes time from the design process. The deformation reference stress, σ_D , is defined usually as that stress which, when applied to a uniaxial specimen for time equal to the design life causes a strain of 1%. The rupture stress is that uniaxial stress which causes rupture at the design life. The need to extrapolate data and identify mechanisms necessitates the addition of a column headed Identifier so that the chart for high temperature is shown in table 1.

The effect of multi-axial states of stress on creep deformation is defined by the function ϕ . The function ϕ is usually taken to be the second stress invariant J_2 , but under conditions dominated by diffusion ϕ is the maximum stress. The studies of deformation creep mechanics have identified deformation bounds, so that deformations can be estimated for constant and cyclic loads and temperature. As it is for plasticity theory, the bounding principles are the basis of design procedures. When the function $\phi = J_2$, many of the calculations for plasticity can be used directly with the reference deformation stress σ_D replacing the yield stress σ_D . This means that the extension of the design methods of plasticity can be extended to creep and this is the basis of the R5 procedure.

The mechanics which describes component behaviour when the material deteriorates with time is known as continuum damage mechanics. This subject is of more recent origin and it is only recently that the first text on the subject has been published by Lemaitre (1992). The function Δ , which describes the effect of three-dimensional stress states on damage growth, is dependent on the underlying damage mechanism. In diffusional creep rupture, Δ tends to be the maximum stress, σ_{\max} , whereas for materials with changing internal dislocation state, Δ is the second stress invariant J_2 . The functional form of ϕ and Δ can be determined from experiment, but the tests are demanding, expensive and time consuming. Clearly, the ability to define Δ from a knowledge of the underlying mechanism offers substantial benefits. This need has led to the interest in mechanism identifiers. The most commonly used are the high-temperature mechanism maps (Frost & Ashby 1982), which identify the operating limits of different damage mechanisms. Another identifier is the creep ductility index which is defined as the creep strain at rupture divided by the product of the steady-state creep

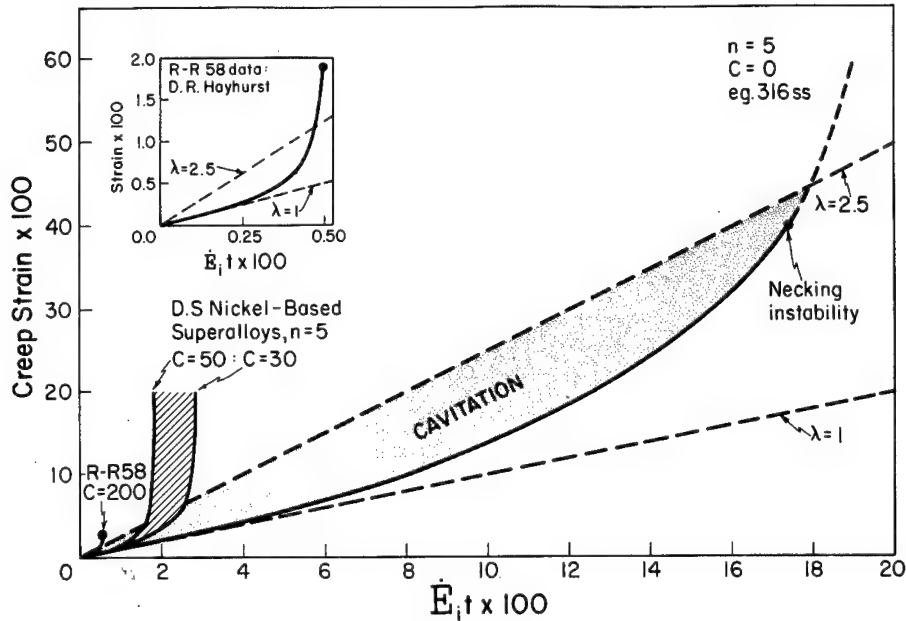


Figure 1. Diagnostic diagram.

rate and the time to rupture. The deformation is illustrated in figure 1. Dyson & Leckie (1988) have shown that, when $\lambda \approx 1$, the mechanism is diffusion controlled and $\Delta = \sigma_{\max}$. When λ is large ($\lambda = 10$), then $\Delta = J_2$.

It is a constant problem in high-temperature design that the experiments are accelerated and failure times measured in the laboratory are orders of magnitude less than the design life. It is then necessary to use some form of extrapolation to estimate the reference stress corresponding to the life of the component. A knowledge of the mechanism and the conditions under which they operate can direct an efficient test program and add confidence to the extrapolation techniques. Knowledge of the mechanism also helps to provide a mathematical description needed for design calculations. Finally, the mechanism growth laws can be expressed in terms of dimensionless groups. It has been established by Frost & Ashby (1982) that data obtained for one material may be used to describe the behaviour of another, provided they fall within defined material groupings. This implies that the results of long-term tests obtained for one material may be modified to provide information of another material within the same classification for which test data are not available.

Codes of practice define those design procedures which result in a reliable and functioning product without the need for expensive build and test verification. This latter requirement is especially important in complex systems. The most recent attempt to define design procedures, for high temperature operation comes from the Assessment Procedures R5 from Nuclear Electric plc (1991). The procedures are based on the framework described above, relating mechanisms and mechanics by means of the reference stress. Extensive use is made of bounding theorems, so that only elastic analysis is required. In this way, complex and time-consuming analyses, which impede design decisions, can be avoided. The overall

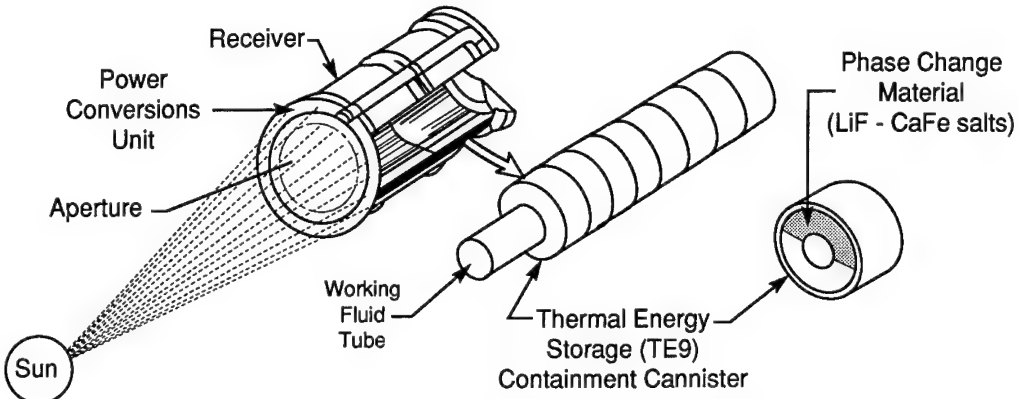


Figure 2. Space Station Freedom solar dynamic power module.

clarity of the approach also provides the flexibility necessary for integrating the effort needed to solve complex technological problems. The design methods have been formulated with large mechanical components in mind which operate up to 600 °C. The procedures used to design aircraft engines are the closely guarded results of industrial competitors, but it is clear in discussions with designers that the same ingredients govern the design process.

An illustration of the flexibility of the R5 procedure is the design of the power plant for a space station to circle the Earth for 30 years. The proposal uses LiF-CaFe salt, as the heat source of a Brayton thermodynamic cycle. When the spacecraft is facing the Sun, the rays are directed onto pellets, containing the salt eutectic which melts at 750 °C (figure 2). When the spacecraft passes behind the Earth away from the Sun, the melted salts solidify and supply the latent heat required to operate the power system during the darkened portion of the flight while maintaining a constant temperature heat source. The design life is 30 years, the cycle time around the Earth is 90 min, so that there are 175 000 operating cycles. The pressure of the working fluid is 308 kPa and operates at 750 °C. Upset conditions include the plant shutdown, followed by restart when the a temperature increase is 1000 °C. The proposed material is the cadmium alloy Haynes 88. Following the systematic interpretation of the R5 procedure reveals that the most critical mechanism is the creep rupture of the containment vessel operating at 750 °C. An instinctive reaction might have suggested that it is the severe upset conditions which are critical. It is an advantage of the R5 procedure that there is no pre-judgement of the failure mechanism and each must be systematically investigated. The biggest unknown is long-term creep strength and the need to extrapolate rupture tests lasting 30 000 h to the 263 000 h life of the component. It is then that the mechanism approach allows rational and effective interpretation of available information and the selection of the reference stress.

3. Some observations on the use of composite material

In addition to the ability to operate at high temperatures, weight saving is an important design consideration for aero-engines so that the strength/density ratio features in material selections. However, since multi-axial stress states are the

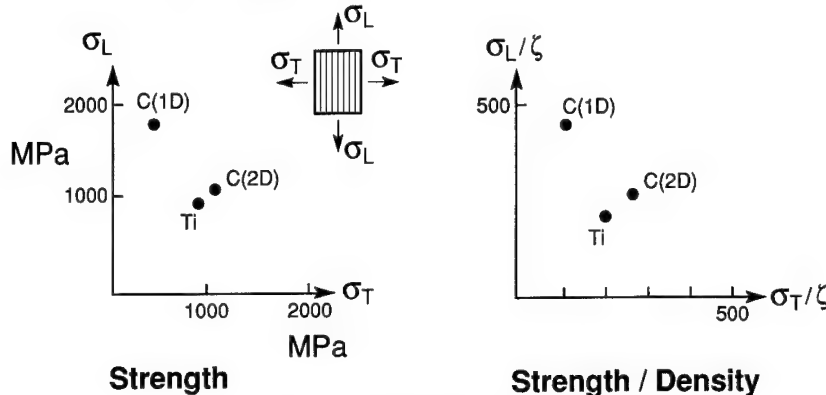


Figure 3. Bi-axial strength.

normal conditions in engineering components, the axial strength/density values may be an insufficient indicator of material behaviour.

The longitudinal transverse strength and strength/density properties of the MMC SiC-Ti, with unidirectional continuous fibres, are shown in figure 3a, b. The strength in the fibre direction is σ_L and σ_T in the transverse direction. Also plotted in the diagram are the strength and the strength/density values of the metal matrix. It can be readily seen that the addition of fibres to the titanium matrix improves the strength of the matrix in the fibre direction, but reduces it in the transverse. However, in circumstances when the stress state is uniformly biaxial and there is equal reinforcement in two directions, the resulting strength and strength/density values indicated in figure 3 are scarcely better than those of the matrix. The message is clear. To gain advantage of the strength/weight properties of the MMC, the loading anisotropy should match that of the material. An appropriate application of MMCs is the boron-aluminum uniaxial members proposed for a space station (figure 4). The selection of a monolithic material for the joints is appropriate on two counts. The stress states in the joint are multi-axial so there is no strength/density advantage to be gained by using a composite. Furthermore, the technology of monolithic joints is much more advanced. The interface properties between composite and monolithic are a new unknown introduced into the problem. The struts proposed to position nozzles in aero-engines is also illustrated in figure 4, with the SiC-Ti composite being bonded to a monolithic titanium joint. When designing the joint, the load is assumed to be transferred entirely in shear between the joint and MMC. It is assumed no stress is carried across the normal interface. This assumption results in heavier joints and creates interfaces which may fail by fatigue.

Another application to be discussed later is the composite ring of an aero-engine, compressor, in which the dominant stress is in the hoop direction (figure 4). The centrifugal loads introduce transverse stresses into the ring which must be taken into consideration when attempting to determine the flow of the load into the fibres in the circumferential direction.

A basic concern is the decrease of composite performance in the presence of the stress concentrations which occur at holes and intersections. Experiments performed by Connell *et al.* (1994) on SiC-Ti MMC plates indicate that the introduction at holes and slits greatly reduce strength. The tensile strength of the

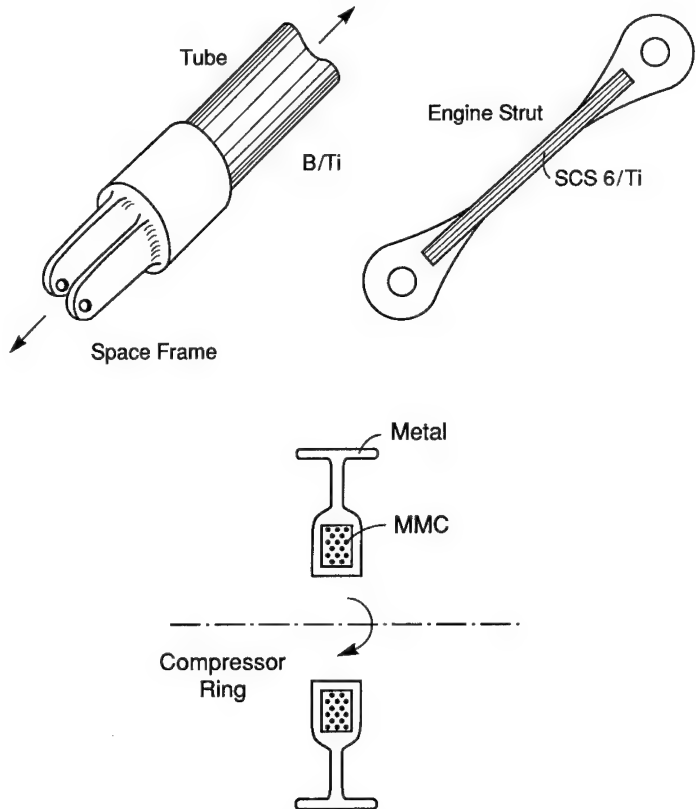


Figure 4. Typical metal-matrix composite component.

composite is 1800 MPa and the introduction of a 1 mm diameter hole reduces the strength to 1100 MPa. This result is consistent with a toughness of approximately 100 MPa, which agrees quite closely with the results of the detailed analysis by Connell *et al.* (1994). The design implication is evident. In the longitudinal direction the MMC is brittle, so that stress concentration must be avoided or special attention given to reinforcement. It is of little surprise then, that current applications appear to be limited to simple shapes which avoid the stress concentrations associated with holes or intersections. Similar experiments on panels of CMCS with notches (Cady 1994) indicate that these materials are tough and notch insensitive so that failure occurs when the average stress at the point of minimum cross section equals the ultimate strength of the CMC. During such tests, it is observed that there is multiple matrix cracking, which is the likely source of the negligible effect of stress concentration. CMCS must have multi-directional reinforcement and since they are notch insensitive, the presence of stress concentrations is of little importance. The CMC component shown in figure 5 is the exhaust chamber of an aero-engine. The mechanical load from internal pressure is small but the component has a complex shape with many points of stress concentrations.

The MMC rotor ring and the CMC exhaust chamber represent examples of the application of composites to specialized aero-engine components. Other presentations in these proceedings deal with ceramic matrix composites, so that further discussion is restricted to metal matrix composites.

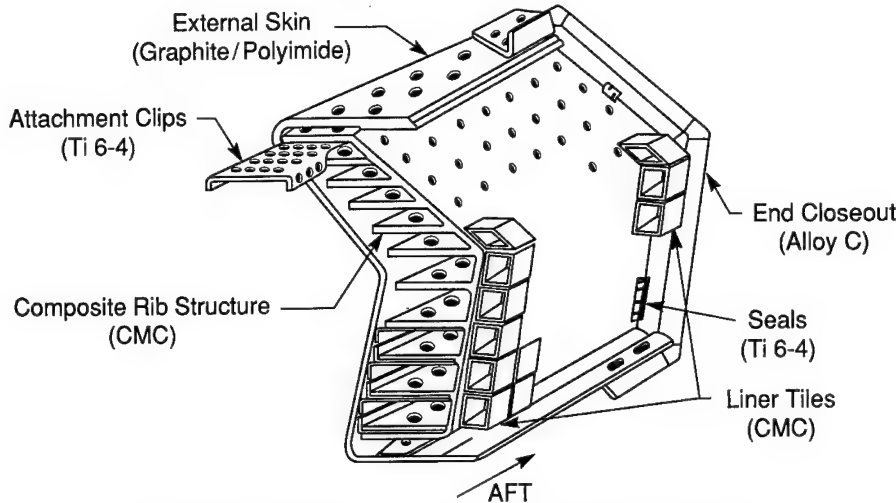


Figure 5. Typical ceramic-matrix composite component.

4. Behaviour of metal matrix composites

The behaviour of MMCs is strongly dependent on the strength of the interface between the fibre and matrix. The MMC SiC-Ti usually has a weak interface, while Al_2O_3 -Al has a strong interface. A weak interface ensures that the strength of the fibres can be fully utilized, but this is achieved at the expense of transverse properties. By contrast, the MMCs with strong interface have relatively poor longitudinal strength but good transverse properties.

Because the effective use of MMCs implies unidirectional reinforcement, it is this form of reinforcement which is considered. In practice however, the operating stress states are multi-axial and it is necessary to determine the modes of deformation and failure for all stress states. Since the availability of materials under development is usually limited to a small number of small plates, it is not possible to perform the number or kind of tests used to characterize isotropic metals. A compensation is that the microstructure is usually well defined and the results of computation using homogenization methods can help to investigate stress states which are difficult experimentally (Gunawardeena *et al.* 1993). Although the properties of MMCs have been investigated in the fibre direction, perpendicular to the fibres and in shear, only the effect of transverse stress is covered for the present. It is the response to this loading which influences the behaviour of the rotor ring discussed later.

The maximum stress observed in the transverse stress-strain relationship (figure 6) for the SiC-Ti composite reaches only 40% of the strength of the matrix. The weak fibre-matrix interface is the source of this behaviour. There is thermal mismatch between fibre and matrix, so that the HIPing process used in production introduces compressive thermal stresses across the interface. On application of the transverse stress, the compressive interface stress is reduced until the residual stresses are overcome when the interface debonds. The presence of the debond decreases the transverse elastic modulus and strength, since the composite now behaves as titanium penetrated by holes the size of the fibres. These features are seen in the transverse stress-strain curve shown in figure 6, with debond occurring when the applied stress is 200 MPa. The reduction in the elastic modulus is

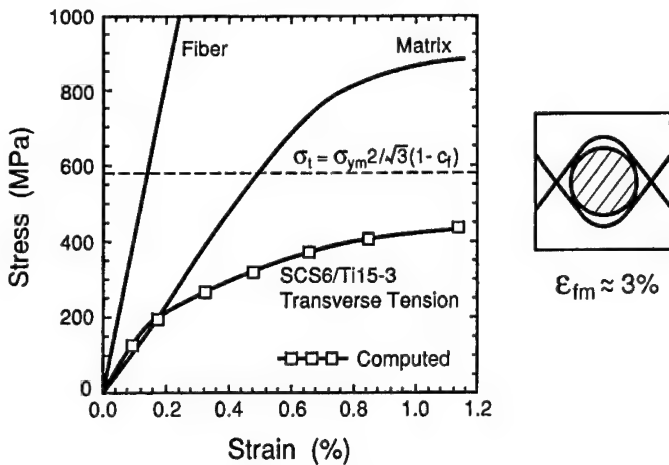


Figure 6. Transverse stress-strain relationship for SCS6-Ti composite.

substantial and the strength is only 40% of the strength of the matrix. Since there is no build-up of triaxial stresses, the failure strain of 1% is not dramatically less than the 3% observed for the matrix material.

5. Rotor design

Because of the high mechanical loads, the rotor of the compressor presents a demanding design problem. By replacing the conventional rotor by an MMC ring, it has been suggested that the weight of the compressor may be decreased by as much as 50%. A first attempt of a rotor design for study purposes is shown in figure 7. The rotor consists of a SiC-Ti composite ring in a Ti cladding. There are 25 blades attached to the outer diameter. The rotor speed is 1900 r.p.m. and the total centrifugal load from the blades is 1.3 MN.

The rings are manufactured using the HIPing procedure at 900 °C. Because of the thermal mismatch between fibre and matrix and the MMC ring and the cladding, thermal residual stresses are introduced into the microstructure of the composite and the ring.

The distribution of blade loading is not uniform along the perimeter and introduces troublesome multi-axial stress states into the MMC ring. This difficulty can be avoided by noting the load can be divided into components, one of which is uniform and equal to the average load. The other loading is periodic, being alternatively positive and negative, repeating itself over a distance equal to the circumferential pitch l . When the loading has the periodic form indicated in figure 8, it is known from elasticity theory that at a depth equal to the circumferential pitch l the stress has been reduced to less than 5% of the magnitude of the periodic loading component. Hence, provided the distance between the blades and the MMC ring is greater than the circumferential pitch of the blades the load applied to the ring is uniform and the irregularities of blade loading removed. It can be seen in the present design that the blade spacing is substantially less than the distance between blades and ring so that an immediate weight gain should be possible.

To understand how the centrifugal blade load is transferred into the ring, constitutive equations have been developed which describe the behaviour of the SiC-Ti

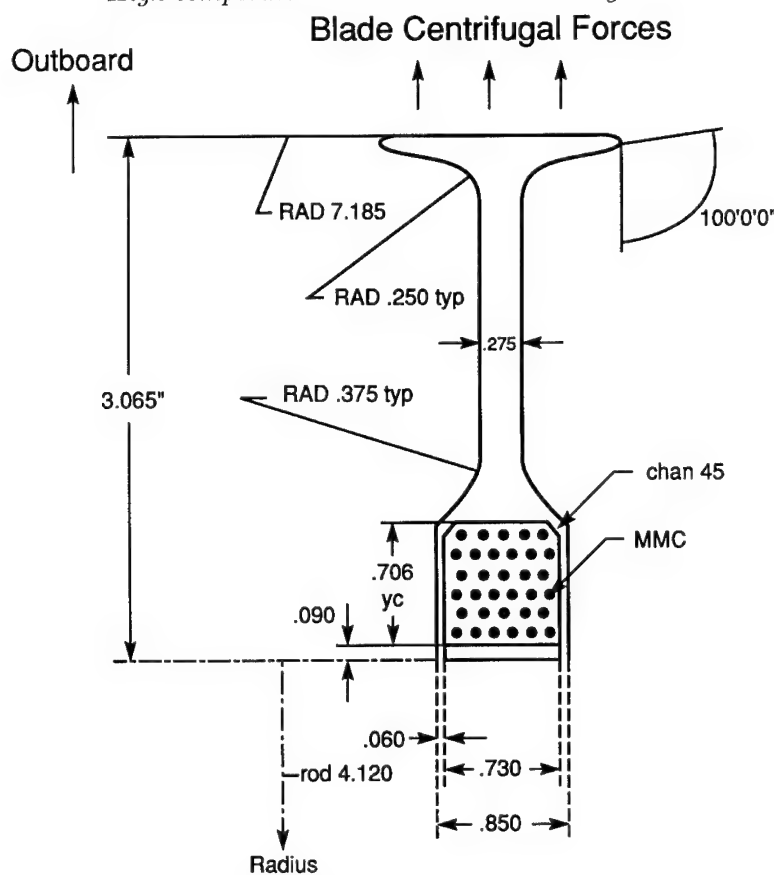


Figure 7. Compressor disc with MMC ring.

Blade Loading P

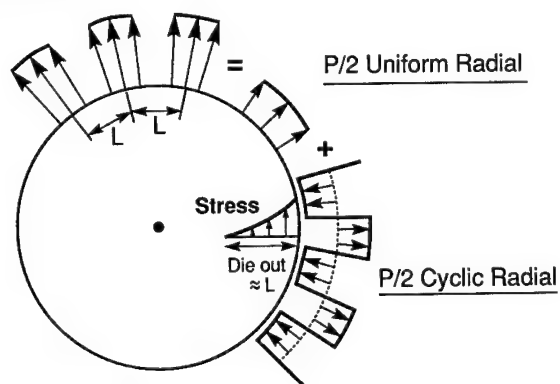


Figure 8. Components of blade loading.

MMC and can be used in finite-element calculations. The constitutive equations take into consideration the changes in the elastic and plastic deformations following debonding at the fibre-matrix interface.

The tensile stresses in the fibre direction are shown in figure 9. Because of the debonding (the debond angle is also shown in figure 9), the radial loading does

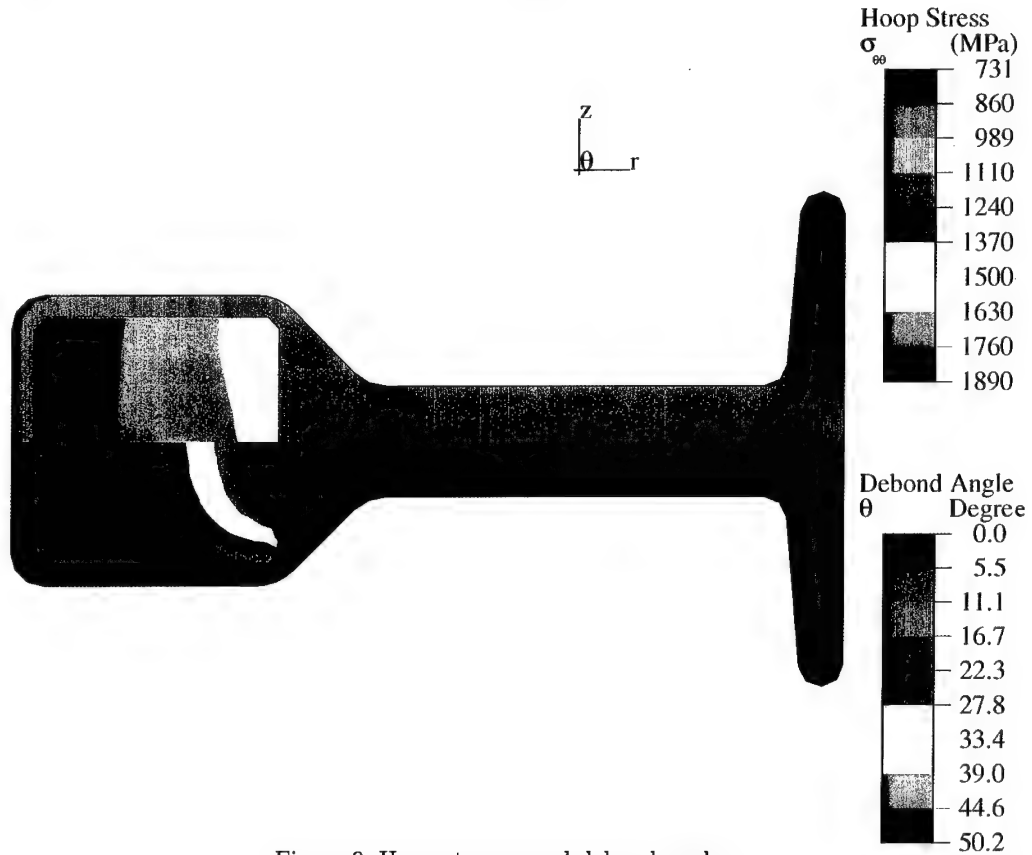


Figure 9. Hoop stresses and debond angle.

not pass smoothly into the ring with some of the load being transferred down the outside cladding. Consequently, the tensile stress in the MMC ring is not uniform, being a maximum at the bore. This lack of uniformity in stress means that the ring is not used efficiently. Furthermore, when fibres begin to break, failure is catastrophic, which is clearly undesirable. By adjusting the shape of the cross-section, it is possible to achieve more uniform stress in the ring and at the same time, arrange that substantial plastic deformation occurs in the metal ligament before fibre failure. With this arrangement, plastic deformation occurs before the onset of general failure, thereby introducing a safety mechanism.

The constitutive equations are complex and need the results of non-standard tests together with micro-mechanics models. Their application is unlikely to appeal to designers and for that reason, something simpler is required. It has been observed in this study that the most important influence is the effect of debond of the fibre-matrix interface on the elastic properties. Hence, elastic calculations which at the outset assume the elastic properties of the MMC with debonded interface give a good indication of how the flow of stress supports the transverse loads. These calculations are very much simpler than those which follow the debonding process. Apart from any computational advantage, it is prudent to assume that the compression stresses following processing are eliminated by small amounts of creep so that the continuity of the fibre-matrix interface is broken and transverse properties are reduced.

6. Summary and conclusions

The design methodology for metals operating at high temperature is well developed. The procedures are based on the results of continuum mechanics and the role of materials is defined by a small number of material properties and functions which describe the behaviour under three-dimensional stress states. When the temperatures are such that time-dependent phenomena dominate, the selection of material properties and the dependence on multi-axial stress are dictated by the physical mechanisms. The organizational table 1 provides a comprehensive understanding of the role of each mechanism and the framework needed for concurrent engineering. High-temperature mechanics is nonlinear and the calculations required to predict component behaviour are expensive, lengthy and impede design decisions. Codes based on bounding methods have been formulated on the basis of elastic calculations which are completed with much greater ease.

A comparable framework for high-temperature design with composite materials is emerging but the material properties are dependent on the mix and geometry of the constituents on the composites. The increased choice adds complexity and emphasizes the need for a mechanisms-based methodology which increases understanding and avoids crushing knowledge overload. Some examples have been covered which show that it is possible to connect mechanism indicators with component performance. Generally speaking, understanding of the mechanisms is improving and the procedures are available to formulate constitutive equations which provide faithful representation of the controlling mechanisms. However, the calculations are complex and indicate the need for simple procedures which can be used in design.

References

Ashby, M. F. & Jones, S. R. 1980 *Engineering materials*. Oxford: Pergamon Press.

Baker, J. F., Horne, M. R. & Heyman, J. 1956 *The steel skeleton*. Cambridge University Press.

Blair, J. S. 1946 *Reinforcement of branch pieces*. Engineering 162.

Cady, C., Evans, A. G. & Perry, K. E. 1994 Attachments in ceramic matrix composites. *Composites*. (In the press.)

Connell, S. J., Zok, F. W., Du, Z. Z. & Suo, Z. 1994 On the tensile properties of a fiber reinforced titanium matrix composite. II. Influence of notches and holes. *Acta metall. Mater.* **42**, 35–51.

Dyson, B. & Leckie, F. A. 1988 Physically based modelling of permanent creep life. *Mater. Sci. Engng A* **103**.

Fairbairn, W. 1856 On the resistance of tubes to collapse. *Phil. Trans. R. Soc. Lond.* **148**.

Frost, H. S. & Ashby, M. F. 1982 *Deformation-mechanism maps*. Oxford: Pergamon Press.

Griffith, A. A. 1920 The phenomena of rupture and flow in solids. *Phil. Trans. R. Soc. Lond. A* **221**.

Gunawardena, S. R., Jansson, S. & Leckie, F. A. 1993 Modeling of anisotropic behavior of weakly bonded fiber reinforced MMC. *Acta metall. Mater.* **41**.

Hill, R. 1950 *The mathematical theory of plasticity*. Oxford: Clarendon Press.

Irwin, G. R. 1958 Fracture. In *Encyclopedia of physics* (ed. S. Flügge), vol. 6, pp. 551–590. Springer.

Kennedy, R. J. 1960 *Nuclear reactor containment buildings and pressure vessels*. London: Butterworth.

Lemaitre, J. 1992 *A course on damage mechanics*. Springer.

Love, A. E. H. 1892 *The mathematical theory of elasticity*. Cambridge University Press.

Wöhler, A. 1860 Versuche über die Festigkeit der Eisenbahn-wagen-Achsen. *Z. Bauwesen* **10**.

INSTRUCTIONS TO AUTHORS

1. Scope

Philosophical Transactions series A is published monthly. Individual issues contain either (i) submitted papers, or (ii) commissioned articles on a topic ('Theme'), or (iii) papers presented at a Royal Society Discussion Meeting. The journal welcomes the submission of papers on any aspect of the physical sciences and engineering, including mathematics and Earth sciences. Submitted papers should treat their subject in depth (up to 12 000 words is normal) and should be likely to prove of lasting value.

2. Submission

Submitted papers must not have been published previously, nor be under consideration for publication elsewhere. Authors will be asked to assign to the Society the copyright in any article published in the journal. In assigning copyright, authors will not be forfeiting the right to use their original material elsewhere subsequently. This may be done without seeking permission and subject only to normal acknowledgement to the journal, although it would be appreciated if authors informed the Society.

The Society is concerned to preserve the integrity of the work of those publishing in its journals and to avoid misrepresentation caused by selective quotation of texts or by the redrawing of illustrations. Accordingly, where copyright has been assigned to the Society, it will give permission for a figure to be reproduced without reference to the original authors *only* if the figure will be reproduced photographically in full and with the complete original caption. Requests for reproduction of partial texts or redrawn figures will always be referred to authors, as will any doubtful cases. Requests for facsimile reproductions of complete papers will not be referred to authors.

Papers may be submitted either (i) directly to the Editorial Office, The Royal Society, 6 Carlton House Terrace, London SW1Y 5AG, or (ii) to a Regional Editor of the journal. Three copies (double-sided) of the typescript (and of any figures, together with original drawings and prints) are required. The extra copies of any photographs should be prints rather than photocopies. Authors should include details of their address, and their telephone, fax, and email addresses.

Authors may suggest the names of referees on the understanding that the Society has the final decision on the selection of referees.

3. General preparation of papers

All papers must be clearly typed, serially numbered, and divided into sections, described by short headings.

The title should be as concise as possible, and followed by the names of the authors (in full if preferred) and the addresses where the work described was

carried out. The current addresses of authors, where different to these, should be clearly indicated.

Each paper must be accompanied by an abstract, which should follow the list of addresses.

Spelling should conform to the preferred spelling of the *Shorter Oxford English Dictionary*.

For notes on the preparation of papers on disk, see the following two sections.

4. Preparation of **T_EX** papers

The Society encourages authors to use **L_AT_EX** for the preparation of all papers submitted for publication, especially those with a large amount of mathematics. Although **L_AT_EX** is the preferred macro package, any **T_EX** source code will be accepted.

A style file, **rs.sty**, is available from the Production Office, either on disk or via email (**ezrs002@vmsfe.ulcc.ac.uk**). It is not essential that this style file is obtained before the paper is written (one advantage of **L_AT_EX** is the interchangeability of style files). However, authors should set the width of the text to 13.5 cm,

The source code (files with the extension **.tex**) corresponding to the final version should be sent *only when the paper is accepted*. It can be sent either by post or email, and should include any specially defined macros. The source code should also be contained within a *single* file, whose root name should be the name of the paper; e.g. the source code for the paper 94PA99 should be labelled **94PA99.TEX**.

5. Preparation of non-**T_EX** papers

Authors preparing their papers using packages other than **T_EX** should still submit the files on disk, which will be converted to **L_AT_EX** where possible. To increase the likelihood of the Society being able to use the file, authors should minimize the formatting of their document and avoid the use of special packages for the setting of mathematics.

6. Units and symbols

As far as possible the recommendations – based on the International System of Units (SI) – contained in *Quantities, units, and symbols* (1975, The Royal Society, £3.00) should be followed.

Units are always set in roman type, even in an italic environment, and **T_EX** authors should note that the spaces separating units must be unbreakable.

7. Illustrations

Line drawings

Descriptions should be placed whenever possible in the legends and not on the figures themselves. Labels should be brief, e.g. (a), (b), (i), (ii), etc., and explained in the legend. All lettering of words should be in lower case except

for proper names, and mathematical symbols must follow the style of the text. Authors may provide unlettered artwork.

Photographs

Authors should supply unmounted glossy prints marked on the back with the author's name and the number of the figure, and with top and bottom indicated. Colour figures will be published on scientific merit but authors will be asked to make a financial contribution to the extra printing cost.

Illustrations in electronic form

Where Adobe IllustratorTM has been used to prepare the figures, these should be supplied on disk in PostScriptTM form. Where Illustrator has not been used but PostScript figures are still available, these should also be supplied in encapsulated form, i.e. with a tight bounding box, and care should be taken to ensure any labelling conforms to the journal's style. Please contact the Journals Production Office if in any doubt.

8. Tables

Tables should be numbered in arabic numerals and referred to in the text by their numbers (e.g. 'see table 3'). Captions to tables should be brief. Column headings should be in lower-case lettering except for the initial capitals of proper names. The units of measurement and any numerical factors should be placed unambiguously at the head of the column, e.g. F/MHz , $10^{28}\sigma/\text{m}^3$, or $q/(\text{kg mol}^{-1})$.

9. References

References to the literature cited must be given in alphabetical order at the end of the paper, and should be arranged as follows.

1. Name(s) with initials of the authors.
2. Year of publication of the paper or book.
3. The title of the paper or book.
4. The title of the periodical, abbreviated where possible.
5. Volume number in bold.
6. First and last page numbers.
7. For a book, the number of the edition, the place of publication and the name of the publisher should be given.

For example:

Bellman, R. 1959 Asymptotic behaviour of solutions of differential-difference equations. *Mem. Am. Math. Soc.* **35**, 123-134.

Bellman, R. & Cooke, K. L. 1963 *Differential-difference equations*, 2nd edn, pp. 342-348. New York: Academic Press.

Bellman, R., Dyson, A. & Cooke, K. L. 1964 *The deficiency index problems*. Lecture Notes in Mathematics, vol. 621. Heidelberg: Springer-Verlag.

Bellman, R., Cooke, K. L. & Dyson, A. 1965 Shock dynamics in metals. In *Proc. Int. Conf. on Mechanical Behaviour of Materials* (ed. J. L. Miller & R. F. Smith), vol. 2, pp. 173-183. Oxford: Pergamon Press.

For \TeX authors, the source code for these references is:

```
\begin{thebibliography}{}
\bibitem[]{}
Bellman, R. 1959 % Author and year
Asymptotic behaviour of solutions of % Title
differential-difference equations.
{\em Mem. Am. Math. Soc.} {\bf 35}, % Journal details
123-134.
\bibitem[]{}
Bellman, R. \& Cooke, K. L. 1963
{\em Differential-difference equations}, % Title and book details
2nd edn, pp.~342--348.
New York: Academic Press. % Place and publisher
\bibitem[]{}
Bellman, R., Dyson, A. \& Cooke, K. L. 1964
{\em The deficiency index problems.}
Lecture Notes in Mathematics, vol.~621.
Heidelberg: Springer-Verlag.
\bibitem[]{}
Bellman, R., Cooke, K. L. \& Dyson, A. 1965
Shock dynamics in metals. % Title of paper
In {\em Proc. Int. Conf. on Mechanical % Title of conference
Behaviour of Materials\}}
(ed. J. L. Miller \& R. F. Smith), % Editors
vol.~2, pp.~173--183.
Oxford: Pergamon Press.
\end{thebibliography}
```

References in the text are made by giving the names of the authors and the date of publication, e.g.

Brown (1994) showed how all equations are now transformed from (s, z) as independent variables to (s', z') and are replaced by conservative finite difference equations (see also Smith & Brown 1994a, b; Brown *et al.* 1994).

Authors using the `\cite` command in \LaTeX should take care to follow this style.

[November 1994]

Indexes to Volume 351 (A)

Author index

Abel, C. A. *See* Ashby & Abel.

Ashby, M. F. & Abel, C. A. Materials selection to resist creep, 451.

Balakotaiah, V. & Chang, H.-C. Dispersion of chemical solutes in chromatographs and reactors, 39.

Bona, J. L., Dougalis, V. A., Karakashian, O. A. & McKinney, W. R. Conservative, high-order numerical schemes for the generalized Korteweg-de Vries equation, 107.

Brady, M. *See* Mukherjee *et al.*

Bratkovsky, A. M. *See* Nguyen Manh *et al.*

Cahn, R. W. Multiphase intermetallics, 497.

Chang, H.-C. *See* Balakotaiah & Chang.

Claussen, N. *See* Knechtel *et al.*

Dougalis, V. A. *See* Bona *et al.*

Dyson, B. F. Mechanical testing of high-temperature materials: modelling data-scatter, 579.

Evans, A. G. Ceramics and ceramic composites as high-temperature structural materials: challenges and opportunities, 511.

Gandin, Ch.-A. *See* Rappaz & Gandin.

Hutchinson, J. W. *See* Lu & Hutchinson.

Karakashian, O. A. *See* Bona *et al.*

Knechtel, M., Claussen, N. & Rödel, J. Reliability of structural ceramics, 469.

Leckie, F. A. High-temperature mechanism-based design, 611.

Lu, T. J. & Hutchinson, J. W. Effect of matrix cracking on the overall thermal conductivity of fibre-reinforced composites, 595.

McKinney, W. R. *See* Bona *et al.*

McLean, M. Nickel-base superalloys: current status and potential, 419.

Morrison, L. V. *See* Stephenson & Morrison.

Mukherjee, D. P., Zisserman, A. & Brady, M. Shape from symmetry: detecting and exploiting symmetry in affine images, 77.

Naslain, R. R. Ceramic matrix composites, 485.

Nguyen Manh, D., Bratkovsky, A. M. & Pettifor, D. G. Quantum mechanical predictions in intermetallics modelling, 529.

Pettifor, D. G. *See* Nguyen Manh *et al.*

Priest, E. R., Titov, V. S. & Rickard, G. The formation of magnetic singularities by time-dependent collapse of an X-type magnetic field, 1.

Rappaz, M. & Gandin, Ch.-A. Process modelling and microstructure, 563.

Rickard, G. *See* Priest *et al.*

Rödel, J. *See* Knechtel *et al.*

Saunders, N. Phase diagram calculations for high-temperature structural materials, 543.

Stephenson, F. R. & L. V. Morrison, L. V. Long-term fluctuations in the Earth's rotation: 700 BC to AD 1990, 165.

Titov, V. S. *See* Priest *et al.*

Williams, J. C. Materials requirements for high-temperature structures in the 21st century, 435.

Zisserman, A. *See* Mukherjee *et al.*

Subject index

ab initio database, 529.
adaptive grid refinement, 107.
air-surface exchange, 279.
aircraft engines, 435.
aircraft measurements, 357.
ammonia fluxes, 261.
ammonia, plant-atmosphere exchange, 261.
ammonium, 339.
atmospheric, 397.
atmospheric carbon, 297.
atmospheric chemistry, 279.
atmospheric diffusion, 383.

balloon, 357.
biogenic emissions, 279.
bond order potentials, 529.
boundary layer, 357.
burning, vegetation, 297.

CALPHAD, 543.
carbon dioxide, 249.
carbon monoxide, 219.
carbonyl sulphide, 219.
cellular automaton, 563.
ceramic matrix composites, 511.
chemical reactions, 231.
chromatography, 39.
composite materials, 435, 611.
composites, mechanical behaviour, 485.
computer vision, 77.
correction procedures, 231.
cost, 435.
cracked composites, 595.
creep anisotropy, 419.
creep-limited design, 451.
current sheet, 1.

debonded interfaces, 595.
defect modelling, 529.
dendrite growth, 563.
dislocation injection, 497.
dry deposition, 231.

Earth's rotation, 165.
eclipses, 165.
effective dispersion coefficient, 39.
enmeshment, 563.
error estimates, 107.

fatigue, 435.
fertilizer, 313.
fire, gas emissions, 297.
flux chamber, 327.
fluxes, atmospheric trace gas, 371.

fracture and ductility, 435.
fracture-limited design, 451.
fracture mechanics, 469.

gas analysis, 327.
gas turbines, 419.
geometric invariance, 77.
greenhouse effect, 327.

hydrogen, 219.
hydroxyl radical, 205.

inelastic deformation mechanisms, 511.
intermetallic alloys, 497.
interphase texture, 485.
isoprene, 279.

Lagrangian dispersion, 383.
land use, 313.
low-cycle fatigue, 579.
lunar ephemerides, 165.
lunar occultations, 165.

magnetohydrodynamics, 1.
mass balance, 383.
material indices, 451.
matrix cracks, 595.
metal-matrix composites, 611.
methane, 219, 249, 371, 397.
methane fluxes, 357.
methane oxidation, 313.
microbial adaptation, 313.
micrometeorology, 339.
microstructure modelling, 563.
mirror symmetry, 77.
monolithic ceramics, 511.

Ni base superalloys, 435.
nickel aluminides, 497.
nitric acid, 371.
nitric oxide, 219.
nitrogen, 313.
nitrogen oxides, 231.
nitrous oxide, 219, 327, 339, 371.
nonlinear dispersive waves, 107.
nucleation of grains, 563.
numerical modelling, 397.

ordered-matrix alloys, 497.
oxidation embrittlement, 511.
ozone layer, 327.

peatland, 249.
perfectly bonded interfaces, 595.
photochemistry, 205.

plasma, 1.
pollution, atmospheric, 413.
pre-telescopic observations, 165.

quadrupole mass spectrometry, 249.

relaxation-limited design, 451.

scatter, 579.
SiC–SiC composites, 485.
single crystals, 419.
singularity, 1.
singularity formulation, 107.
SODAR, 357.
soil, 327.
soil acidity, 313.
soil microbiology, 413..
solar ephemerides, 165.
solitary waves, 107.
sources & sinks, 383.

spatial averaging, 39.
stratospheric ozone, 397.
structural stability, 529.
Sun, 1.
superalloys, 419.
symmetry, skewed, 77.

Taylor dispersion, 39.
Taylor–Aris dispersion, 39.
temperate forests, 279.
titanium aluminides, 497.
trace gas budgets, 397.
transition metal aluminides, 529.
troposphere, 205.
tunable diode laser, 371.
turbulence, 383.

uniaxial tensile creep, 579.

Weibull distribution, 469.

Philosophical Transactions of The Royal Society of London

**Series A
Physical Sciences and
Engineering**

**VOLUME 351
1995**

Published by
THE ROYAL SOCIETY
6 Carlton House Terrace, London SW1Y 5AG

ISSN 0962-8428

The three numbers in this volume can be obtained separately
from the Royal Society, 6 Carlton House Terrace, London
SW1Y 5AG.

Copyright
© 1995 The Royal Society

Except as otherwise permitted under the Copyright, Designs and Patents Act, 1988, this publication may only be reproduced, stored or transmitted, in any form or by any means, with the prior permission in writing of the publisher, or, in the case of reprographic reproduction, in accordance with the terms of a licence issued by the Copyright Licensing Agency. In particular, the Society permits the making of a single photocopy of an article from this issue (under Sections 29 and 38 of the Act) for an individual for the purposes of research or private study.

The text paper used in this publication is alkaline sized with a coating which is predominantly calcium carbonate. The resultant surface pH is in excess of 7.5 which gives the maximum practical permanence.

Contents

Series A Volume 351

No. 1695 15 April 1995

The formation of magnetic singularities by time-dependent collapse of an X-type magnetic field

By E. R. Priest, V. S. Titov and G. Rickard	<i>page</i> 1
Dispersion of chemical solutes in chromatographs and reactors	
By V. Balakotaiah and H.-C. Chang	39
Shape from symmetry: detecting and exploiting symmetry in affine images	
By D. P. Mukherjee, A. Zisserman and M. Brady	77
Conservative, high-order numerical schemes for the generalized Korteweg-de Vries equation	
By J. L. Bona, V. A. Dougalis, O. A. Karakashian and W. R. McKinney	107
Long-term fluctuations in the Earth's rotation: 700 BC to AD 1990	
By F. R. Stephenson and L. V. Morrison	165

No. 1696 16 May 1995

The exchange of trace gases between land and atmosphere

A discussion organized and edited by D. Fowler, D. S. Jenkinson, J. L. Monteith and M. H. Unsworth	205
--	-----

No. 1697 15 June 1995

High-temperature structural materials

A discussion organized and edited by R. W. Cahn, A. G. Evans and M. McLean	417
Instructions to authors	625
Indexes	629

Proceedings: Mathematical and Physical Sciences

Series A Volume 447 Number 1937 8 June 1995

B. J. LOWRY & P. H. STEEN

Capillary surfaces: stability from families of equilibria with application to the liquid bridge

C.-Y. WANG & J. D. ACHENBACH

Three-dimensional time-harmonic elastodynamic Green's functions for anisotropic solids

D. N. RIAHI

Finite amplitude thermal convection with spatially modulated boundary temperatures

S. P. HASTINGS, J. B. MCLEOD & W. C. TROY

Static spherically symmetric solutions of a Yang-Mills field coupled to a dilaton

H. S. SIDHU, L. K. FORBES & B. F. GRAY

Analysis of the unified thermal and chain branching model of hydrocarbon oxidation

J. F. NYE, J. H. HANNAY & W. LIANG

Diffraction by a black half-plane: theory and observation

ZHENYU ZHOU, C. E. SYNOLAKIS, R. M. LEAHY & S. M. SONG

Calculation of 3D internal displacement fields from 3D X-ray computer tomographic images

N. C. BURTON, J. E. BUTLER, A. R. LANG & J. W. STEEDS

On a characteristic misorientation structure within (001) facets of CVD-grown diamond crystallites: an analysis by optical microtopography, interferometry, electron diffraction and cathodoluminescence

R. J. A. TOUGH, D. BLACKNELL & S. QUEGAN

A statistical description of polarimetric and interferometric synthetic aperture radar data

F. M. BORODICH

Integral properties of solutions to some boundary initial-value problems in linear anisotropic elastodynamics

W. B. FRASER, L. FARRELL & D. M. STUMP

Effect of yarn non-uniformity on the stability of the ring-spinning balloon

B. PALMER

The Bao-Ratiu equations on surfaces

P. A. BOASMAN & J. P. KEATING

Semiclassical asymptotics of perturbed cat maps

S. RAMASAMY, P. B. DESHPANDE, S. S. TAMBE & B. D. KULKARNI

Robust nonlinear control with neural networks

D. DEUTSCH, A. BARENCO & A. EKERT

Universality in quantum computation

A. BARENCO

A universal two-bit gate for quantum computation

THE ROYAL SOCIETY

Philosophical Transactions: Physical Sciences and Engineering

Series A Volume 351 Number 1697 15 June 1995

CONTENTS

High-temperature structural materials

A Discussion organized and edited by R. W. Cahn, A. G. Evans
and M. McLean

M. McLEAN	
Nickel-base superalloys: current status and potential	pages 419-433
J. C. WILLIAMS	
Materials requirements for high-temperature structures in the 21st century	435-449
M. F. ASHBY & C. A. ABEL	
Materials selection to resist creep	451-468
M. KNECHTEL, N. CLAUSSEN & J. RÖDEL	
Reliability of structural ceramics	469-483
R. R. NASLAIN	
Ceramic matrix composites	485-495
R. W. CAHN	
Multiphase intermetallics	497-509
A. G. EVANS	
Ceramics and ceramic composites as high-temperature structural materials: challenges and opportunities	511-527
D. NGUYEN MANH, A. M. BRATKOVSKY & D. G. PETTIFOR	
Quantum mechanical predictions in intermetallics modelling	529-542
N. SAUNDERS	
Phase diagram calculations for high-temperature structural materials	543-561
M. RAPPAZ & CH.-A. GANDIN	
Process modelling and microstructure	563-577
B. F. DYSON	
Mechanical testing of high-temperature materials: modelling data-scatter	579-594
T. J. LU & J. W. HUTCHINSON	
Effect of matrix cracking on the overall thermal conductivity of fibre-reinforced composites	595-610
F. A. LECKIE	
High-temperature mechanism-based design	611-623
INSTRUCTIONS TO AUTHORS	625-628
INDEXES	629-632

* * *

VOLUME TITLE PAGE AND CONTENTS

All the papers in this issue were produced from the authors' disks by using the *TeX* typesetting system.

Published by the Royal Society, 6 Carlton House Terrace, London SW1Y 5AG

Printed in Great Britain for the Royal Society by the University Press, Cambridge